

Tropospheric formaldehyde retrievals with GOME-2

Thesis submitted for the degree of
Doctor of Philosophy at the
University of Leicester

by

Will Hewson
Department of Physics and Astronomy
University of Leicester

December 18, 2013

© Will Hewson, December 18, 2013

This thesis is copyright material and no quotation from it may be published without proper acknowledgement.

Declaration

I hereby declare that no part of this thesis has been previously submitted to this or any other University as part of the requirement for a higher degree. The work within this document has been conducted by the undersigned except for contributions where acknowledged in the text.

Will Hewson, December 18, 2013.

Tropospheric formaldehyde retrievals with GOME-2

by Will Hewson

Abstract

Biogenic Volatile Organic Compounds (BVOCs) emitted by terrestrial ecosystems impact air quality and climate. The most important BVOC for global tropospheric composition is isoprene, whose annual global emissions (400–600 Tg C/year) account for ~50% of the total global BVOC budget. Tropical ecosystems are generally thought to be responsible for 70–90% of the global isoprene budget. Satellite observations of formaldehyde (CH_2O), a high-yield, short lifetime product of isoprene oxidation, provide top-down constraints on surface isoprene emissions.

Errors in retrieved satellite slant column densities (SCD – trace gas concentration along the instrument’s line of sight) are typically in the region of 40% for scenes with little cloud and aerosol contamination. Error sources arise from instability in the differential optical absorption spectroscopy (DOAS) retrieval procedure, largely due to low signal to noise ratios frequently encountered with space-borne UV spectrometers, coupled to CH_2O ’s faint absorption signal. The essential conversion of SCDs to vertical column densities (VCDs – vertical trace gas concentration extending from the Earth’s surface), needed for application of retrieved CH_2O values to geochemical modelling schemes, is a further significant contributor to product error (30–60%), being strongly influenced by aerosol, cloud and albedo inhomogeneities at sub-pixel level.

A new global 5 year CH_2O product (2007–2011) generated with global ozone monitoring experiment 2 (GOME-2) satellite radiance data is presented. SCDs for this are generated with optimised spectroscopic fit settings derived from an extensive sensitivity study of input retrieval parameters for the DOAS portion of the retrieval. SCDs are then converted to vertical column densities VCDs using air mass factors calculated with a significantly upgraded retrieval scheme, accounting for atmospheric radiative transfer due to viewing geometry, surface albedo and atmospheric scattering. New GOME-2 CH_2O VCDs are then evaluated against GEOS-Chem modelled CH_2O VCDs, and compared to a suite of associated environmental parameters.

Acknowledgements

I am grateful to my ever patient supervisors Hartmut Bösch and Michael Barkley, being constantly on hand to guide me through my project. Their scientific knowledge and technical assistance paved the way for a thoroughly enjoyable 4 years.

Additionally, thanks are extended to those who assisted in the retrieval work. The GOME-2 team at the Belgian Institute for Space Aeronomy; in particular Caroline Fayt, Isabelle De Smedt and Nicolas Theys; whose advice and technical guidance provided greatly needed assistance at several points throughout my project. At the Rutherford Appleton Laboratory; Georgina Miles and Richard Siddans provided technical support in the early stages.

Finally, I reserve a special mention for Rachael, Mum, and the Boys (Michael, David, Titus, Pig and Carl); all of whom I owe an incalculable debt of gratitude for their support, encouragement and care.

Table of Contents

Chapter 1: Introduction	4
Chapter 2: Formaldehyde's Role in Atmospheric Chemistry	10
2.1 Overview of atmospheric chemistry	10
2.1.1 Atmospheric vertical structure and composition	11
2.1.2 Stratospheric chemistry	14
2.2 Tropospheric chemistry	15
2.2.1 Radiative forcing	15
2.2.2 Chemical forcing	16
2.2.3 Atmospheric pollution	16
2.2.4 Ozone sources and sinks	17
2.2.5 Tropospheric radical chemistry	19
2.2.6 Methane	21
2.2.7 Non-methane volatile organic compounds	23
2.3 Isoprene	24
2.3.1 Production	24
2.3.2 Emission	25
2.3.3 Function	26
2.3.4 Chemical significance	27
2.3.5 Role of isoprene for Earth's climate	28
2.3.6 Isoprene measurement	33
2.4 Formaldehyde	39
2.4.1 Sources and sinks	40
2.4.2 Formaldehyde measurements and distribution	40
2.5 Summary	44
Chapter 3: Retrieval Methods and Instrumentation	46
3.1 Atmospheric radiative transport	46
3.1.1 Absorption	47
3.1.2 Scattering	48
3.1.3 Beer-Lambert law	51
3.2 Differential optical absorption spectroscopy	52
3.2.1 Passive DOAS application	54
3.2.2 Reference spectra	56
3.2.3 Slant to vertical column conversion	60
3.3 Space-borne remote sensing of trace gases	60
3.3.1 GOME	61
3.3.2 SCIAMACHY	63

3.3.3	OMI	64
3.3.4	GOME-2	64
3.4	Practical DOAS considerations	67
3.4.1	Instrument line shape	67
3.4.2	Wavelength calibration	69
3.4.3	I_0 effect	71
3.4.4	Undersampling	72
3.4.5	Radiometric degradation	74
3.5	Summary	76
Chapter 4: DOAS Parameter Testing		78
4.1	DOAS parameter sensitivities	81
4.1.1	Spectral fit range	81
4.1.2	Absorber effects	87
4.1.3	Polynomial degree	93
4.1.4	Instrument corrections	94
4.1.5	SCD error	97
4.2	Earthshine I_0 reference	99
4.2.1	Earthshine I_0 selection	100
4.2.2	EI_0 retrieval results	102
4.2.3	EI_0 analysis	104
4.3	SCD post processing	105
4.3.1	Cloud fraction	105
4.3.2	Reference sector method	108
4.3.3	Homogenisation of CH_2O vertical columns	109
4.4	Summary	112
Chapter 5: Air Mass Factors		115
5.1	Air mass factors in a scattering atmosphere	116
5.2	AMF implementation	121
5.2.1	GEOS-Chem overview	121
5.2.2	LIDORT overview	122
5.2.3	Baseline UoL AMF	124
5.3	UoL AMF input parameter comparisons	125
5.4	UoL AMF development	128
5.4.1	A-priori input grid resolution	132
5.4.2	Weighted pixel means	136
5.4.3	Updated surface albedo	138
5.4.4	Pressure correction	140
5.4.5	LIDORT absorption cross sections	144
5.4.6	O_3 vertical mixing ratios	146
5.5	Updated AMF algorithm	147
5.6	AMF error	150
5.7	Summary	152
Chapter 6: VCD Evaluation and Comparison		154
6.1	Five year CH_2O VCD product	154
6.1.1	VCD seasonal means	155
6.1.2	VCD trend	157

6.1.3	Model comparisons	158
6.1.4	Fire screening	160
6.1.5	Retrieval comparisons	162
6.2	Environmental correlations	164
6.2.1	Aerosol	165
6.2.2	Precipitation	167
6.2.3	Land surface temperature	170
6.2.4	Chlorophyll fluorescence	172
6.3	Summary	178
Chapter 7: Discussion and Conclusions		180
7.1	DOAS parameter testing	181
7.2	Air mass factors	184
7.3	CH ₂ O VCD evaluation and comparisons	186
7.4	Conclusions	188
References		189
Peer reviewed publication		217

Chapter 1

Introduction

Trends in the Earth's long term climate record are controlled by the balance of radiation received from the Sun, offset by losses from the Earth system through re-radiation back into space. Adjustment of this radiation balance caused by anthropogenic modification of Earth's naturally regulated environment has contributed to recent changes in climate (Forster et al., 2007). Since the industrial revolution at around the turn of the 18th century, the atmospheric environment in particular has undergone significant changes in the magnitude and distribution of its constituent components (Isaksen et al., 2009). The influence of atmospheric chemistry on global climate is seen through adjustments to levels of greenhouse gases resident in the atmosphere, directly affecting the insolation and irradiation balance through absorption and scattering processes (Collins et al., 2006).

Atmospheric chemistry is a dynamic system primarily driven by photochemistry (solar radiation exciting and breaking chemical compound bonds), whose variation around the Earth determines availability of catalysts for chemical reactions (Monks et al., 2009). These catalysts are more commonly known as the radical species HO_x and NO_x , molecules with an unpaired electron endowing them with a particularly high level of reactivity. Photolysis of the trace gas ozone (O_3) in proximity to water generates the hydroxyl radical OH, a free radical whose propensity for participation in chemical reactions and acceleration of chemical decomposition, frequently leads to its moniker as the detergent of the troposphere (Monks, 2005). OH's importance in

the troposphere hinges on its capacity for removal and conversion of a great variety of trace gases and pollutants. Over time, the atmosphere reaches a semi-steady state of stable oxidised substances resulting from this initial radical oxidation of trace gas species. Such stable species are un-reactive, thereby allowing them long residence times in the atmosphere on the order of decades to centuries (Wayne, 1990). With an increasing concentration of anthropogenically induced trace gas emissions, the balance of these gases is changing, affecting global climate through direct and indirect radiative forcing.

The tropics is a key region of the Earth for global atmospheric chemistry (Seinfeld and Pandis, 2006). Due to the phenologically advantageous climatic conditions at tropical latitudes, trace gas biogenic compound emissions are greatly enhanced in these regions (Guenther et al., 2006; Müller et al., 2008). The isoprene compound is a major component of these emissions (~50% globally), playing a role in the regulation of direct and indirect radiative forcing (Forster et al., 2007; Pacifico et al., 2009; Arneth et al., 2010). Isoprene is emitted globally from vegetation, with emission dependencies on temperature, light and water availability (Rinne et al., 2002). In the tropics, where none of these factors are in short supply, isoprene emissions can be greatly enhanced above global background levels year round. The environmental stimuli governing regulation of isoprene emission from vegetation are poorly understood; however the current consensus postulates emission as a stress response, acting as a safety valve in high heat and / or low moisture availability events to increase efficiency of membrane activity (Sharkey et al., 2008).

Isoprene's radiative forcing capacity is related to the compound's influence on tropospheric O₃ production, and regional pollution in the form of secondary organic aerosol (van Donkelaar et al., 2007; Fiore et al., 2011). Once emitted to the planetary boundary layer, the interaction of isoprene with the local and regional atmospheric chemistry can follow several pathways depending on the prevailing trace gas composition. Isoprene is identified as a key component in tropospheric ozone production, whereby in the presence of sunlight, molecules (typically nitrogen compounds – NO_x)

are split into inert nitrogen and an oxygen atom, quickly combining with an adjacent O_2 molecule to form ozone. Complicating this simplified tropospheric ozone production mechanism, isoprene is oxidised by OH to H_2O and CO_2 , with intermediate peroxy radical oxidation products reacting with NO to form another OH radical, and NO_2 . The isoprene compound therefore displays a sensitivity to local NO_x levels – serving to increase tropospheric ozone in high NO_x situations, and decrease ozone with low NO_x availability (Atkinson and Arey, 2003; Paulot et al., 2012). In addition to being an emission precursor of the greenhouse gas ozone, isoprene is also identified as a precursor to secondary organic aerosol production (Carlton et al., 2009). Karl et al. (2009) outline isoprene to aerosol conversion mechanisms; including gas-phase photo oxidation under both high and low NO_x conditions, acidification of isoprene oxidation products, and polymer formation directly from isoprene. High levels of OH in the tropical troposphere means isoprene’s lifetime is typically short at under 1 hour (Palmer et al., 2003), however its overall effect on tropospheric chemistry through O_3 regulation is thought to be significant at a global scale (Sanderson et al., 2003). Isoprene affects global climate through regulating greenhouse gas budgets available for radiative forcing (Paulot et al., 2012). The compound also bears implications for human health through its interaction in pollution episodes via tropospheric ozone production and aerosol pollution (Brunekreef and Holgate, 2002). Expected dynamic isoprene emission feedbacks due to climate change are expected, but the sign of such changes are uncertain. Increased global CO_2 concentrations coupled to expansion of savannah grassland type biomes will lead to increases in isoprene emitting vegetation (Hardacre et al., 2013; Squire et al., 2013), whilst some authors suggest a reduction in isoprene caused by elevated CO_2 concentrations inhibiting emissions (Young et al., 2009).

Measurements of isoprene are currently limited to in-situ observations, for which the logistical expense of data gathering in remote, but chemically reactive tropical regions (e.g. the Amazon rainforest) precludes isoprene measurements being made in any great quantity (Kuhn et al., 2007; Eerdekens et al., 2009; Jones et al., 2011).

Formaldehyde (CH_2O) represents a major trace gas sink for isoprene oxidation, and is detectable from space-borne UV spectrometers, albeit with great difficulty, due to its extremely weak absorption signal (Chance et al., 2000; Wittrock, 2006; De Smedt et al., 2008). Its balance in the troposphere is largely determined by sources of oxidation of the global methane background, and elevated concentrations due to biogenic isoprene sources, and sinks of conversion to CO and the hydroxyl radical via photolysis (Cooke et al., 2010). Localised direct CH_2O sources include biomass burning events, industrial and urban pollution (Stavrakou et al., 2009b; Gonzi and Palmer, 2010; Parrish et al., 2012). Satellite observations of CH_2O can be used to infer global isoprene emissions through application of a linear regression from formaldehyde observations to chemical transport model estimated isoprene emissions (Palmer et al., 2003; Shim et al., 2005; Palmer et al., 2006; Fu et al., 2007; Barkley et al., 2008, 2013).

Continuing a heritage of satellite mounted UV spectrometers beginning with GOME-1, through SCIAMACHY and to OMI, GOME-2 was launched on October 19th 2006 on board the European MetOp-A satellite (Munro et al., 2006). The polar orbit of MetOp-A has a local equator crossing time of 09:30, whilst the 1920 km swath of GOME-2 allows for global coverage every 1.5 days. GOME-2's wavelength range extends through 240–790 nm, recording Earthshine radiances on four channels each constructed of 1024 pixels. Scanning the sensor's field of view across the satellite ground track's swath width of 1920 km, standard mirror rotation speed generates data at a spatial resolution of $80 \text{ km} \times 40 \text{ km}$ per scan – a significant increase on its predecessor's $320 \text{ km} \times 80 \text{ km}$. Designed with the ability to discriminate between atmospheric absorbers whose absorption cross sections possess rapidly varying features, the spectral resolution of the instrument ranges from 0.26 nm to 0.51 nm.

Work presented here is motivated by a need to increase the knowledge of atmospheric chemistry's interactions with global climate. In the context of constraining the effects of isoprene on tropical tropospheric chemistry, significant improvements

on current CH_2O retrieval accuracy are necessary to improve poorly understood isoprene emission estimates (Barkley et al., 2012a). This translates to a requirement for a formaldehyde product whose spectral fitting parameters are thoroughly understood, and optimised specific to the GOME-2 instrument. Critical to the application of satellite measured formaldehyde is the error prone conversion from line of sight measurements to vertical columns whose values are directly applicable to chemical transport models (CTM). For this, an air mass factor (AMF) must be derived, accounting for instrument viewing geometry, cloud, aerosol surface albedo, and absorber profile of the measurement (Palmer et al., 2001). In an effort to derive CH_2O columns whose measurements are as reliable as currently possible, the accuracy of highly sensitive formaldehyde AMFs must also be improved upon the current generation of models for applicability to GOME-2. Comparison of satellite formaldehyde products against CTM columns provides a two-way evaluation of both CTM and satellite data, whilst new data can be correlated with environmental parameters known to be of relevance to isoprene emission (Zhang et al., 2010).

This thesis begins in Chapter 2 with a briefing on the scientific background of tropospheric chemistry, and significantly for this work, isoprene's interaction with atmospheric chemistry. A summary of isoprene monitoring methods is continued with the introduction of formaldehyde, its relevance to isoprene and atmospheric chemistry, and a discussion of existing monitoring methods for its distribution and magnitude. Chapter 3 examines the methodology and instrument used for detection of formaldehyde from space in this work. The Global Ozone Monitoring Experiment 2 (GOME-2) spectroscopic instrument is detailed, and complemented by an introduction to the principles of the differential optical absorption spectroscopy (DOAS) method used for CH_2O 's detection from space. Limitations of the DOAS method when applied to GOME-2, as well as issues surrounding the radiometric degradation of the instrument are noted.

Conducting a comprehensive suite of sensitivity tests on a month's GOME-2 data, the 4th chapter details the characterisation of an optimal CH_2O retrieval using

the DOAS technique with radiance measurements from the GOME-2 instrument. Further experiments are conducted in an effort to reduce instrumental degradation effects, and spectroscopic retrieval dependence on the latitudinal bias correction known as the reference sector method. Chapter 5 looks at the generation of AMFs pertinent to the preceding GOME-2 CH₂O retrieval, focussing on the development and upgrade of an existing AMF algorithm. This incorporates the state of the art in the field of AMF generation, whilst advancing the method with the introduction of several novel components to the algorithm. Chapter 6 brings together work from chapters 4 and 5 to present a brand new global 5 year (2007–2011) CH₂O vertical column product. This provides the data for subsequent quantitative comparison and evaluation of the new columns against model generated CH₂O columns from GEOS-Chem, and an existing CH₂O dataset. Correlations are then drawn between CH₂O concentrations and external geophysical datasets associated with elevated formaldehyde (and by extension, isoprene) concentrations. Chapter 7 concludes the thesis with a critical appraisal and summary of the work, as well as discussion on future directions for tropospheric CH₂O retrieval research.

Chapter 2

Formaldehyde's Role in Atmospheric Chemistry

2.1 Overview of atmospheric chemistry

The atmosphere is essential for life on Earth, providing a protective shield to reflect and absorb harmful ultra-violet (UV) radiation, as well as providing an invisible blanket for the biosphere; serving to maintain temperatures within a habitable range for much of the Earth's surface. Atmospheric chemistry groups the study of chemical processes occurring above Earth's crust, and extending through various layers of gases enveloping the Earth, up to the boundary of space, at approximately 100 km from the Earth's surface. Atmospheric chemistry is intimately connected to the Earth system through dynamic feedbacks with the biosphere and hydrosphere, with changes in magnitudes and distributions of chemical compounds resident in the atmosphere affecting geochemical and geophysical processes at the Earth's surface (Wayne, 1990; Fowler et al., 2009). The role of atmospheric chemistry in regulating Earth's climate is significant, with direct effects occurring due to reflection and absorption of radiation by greenhouse gases in the atmosphere. Indirect effects on climate change arise due to the regulation of quantities of these first order climate effectors by highly reactive chemicals in the atmosphere (Forster et al., 2007).

The majority of research into atmospheric chemistry has historically been of a reactionary nature, investigating anthropogenically initiated pollution events related to air quality (Monks et al., 2009). Examples of such events include the London smog, arising from lack of control on industrial emissions from the 1700's onwards, allowing large urban scale accumulations of soot and fog to form over the capital. In tandem with rapid industrialisation experienced globally over the last century, photochemical smog has formed over large conurbations (e.g. Los Angeles, Mexico City) on a regular basis, becoming a common feature of life over the last 20 years for residents in the rapidly developing urban centres of East Asia. Discovery of the ozone hole over Antarctica provided evidence of the global impact of humans on atmospheric chemistry (Farman et al., 1985), whose rapid diagnosis has allowed policy makers to implement legislation to ameliorate and reverse the problem over the coming years. Contemporary focus on anthropogenically induced climate change has led to a co-ordinated effort to better understand the processes of atmospheric chemistry on a global scale. In order to provide policy makers with more accurate information on probable causes and effects in the climate system, monitoring and modelling of atmospheric chemistry is now at the forefront of the climate change agenda (IPCC, 2001).

Within this chapter, an overview of the basics of atmospheric chemistry is presented, acting as a primer for the following discussion of the volatile organic compound isoprene, and its significance for atmospheric chemistry. As a first order decomposition product of isoprene, formaldehyde is subsequently examined together with an appraisal of its global distribution, magnitudes, and a review of space-borne monitoring methods.

2.1.1 Atmospheric vertical structure and composition

The atmosphere is a stratified medium, whose distinct layers are formed by pressure and temperature gradients as a result of radiation balancing between the Solar source and Earth's radiative emission. At least in the lower reaches of the atmo-

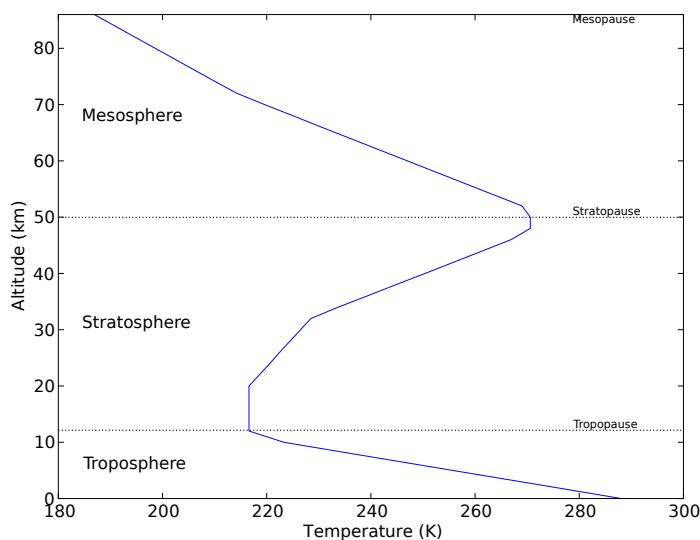


Figure 2.1: Vertical composition of the atmosphere, showing the temperature gradient as a function of height. Data from the 1976 U.S. standard atmosphere.

sphere, these layers are identifiable by the reactivity of gases found within them due to available radiation with which to encourage chemical reactions (Finlayson-Pitts and Pitts, 2000). Directly above the Earth’s surface lies the troposphere, typically extending upwards to between 8–15km at mid-latitudes, and accounting for approximately 80% of atmospheric mass (Seinfeld and Pandis, 2006). This layer consists of turbulent air masses, directly influenced by surface albedo and diurnal variation in the radiation balance, and friction of its air masses against the Earth’s surface. Weather systems are generated by turbulence in the troposphere, facilitating significant chemical mixing within this layer, contributing to the dynamic cocktail of chemical composition in this region. Decreasing temperatures are experienced as a function of height throughout the troposphere, as air parcels become less subject to the influence of the radiation reflected and emitted by the Earth’s surface. This encourages vertical mixing between systems of ascending and descending parcels of air, influencing pressure and temperature at the surface, serving to form weather systems of wind and cloud.

The stratosphere is defined by a gradual increase in temperature from the top of the troposphere, upwards to approximately 50 km at mid latitudes. It is less

<i>Constituent</i>	<i>Chemical formula</i>	<i>Mole fraction in dry air</i>	<i>Major sources</i>
Nitrogen	N ₂	78.084%	Biological
Oxygen	O ₂	20.948%	Biological
Argon	Ar	0.934%	Inert
Carbon dioxide	CO ₂	360 ppm	Combustion, ocean, biosphere
Neon	Ne	18.18 ppm	Inert
Helium	He	5.24 ppm	Inert
Methane	CH ₄	1.7 ppm	Biogenic, anthropogenic
Hydrogen	H ₂	0.55 ppm	Biogenic, anthropogenic, photochemical
Nitrous oxide	N ₂ O	0.31 ppm	Biogenic, anthropogenic
Carbon monoxide	CO	50–200 ppb	Photochemical, anthropogenic
Ozone (troposphere)	O ₃	10–500 ppb	Photochemical
Ozone (stratosphere)	O ₃	0.5–10 ppm	Photochemical
NMHC	C _x H _y	5–20 ppb	Biogenic, anthropogenic
Chlorofluorocarbon 12	CF ₂ Cl ₂	540 ppt	Anthropogenic
Chlorofluorocarbon 11	CFCl ₃	265 ppt	Anthropogenic
Methylchloroform	CH ₃ CCl ₃	65 ppt	Anthropogenic
Carbon tetrachloride	CCl ₄	98 ppt	Anthropogenic
Nitrogen oxides	NO _x	10 ppt–1 ppm	Soils, lightning, anthropogenic
Ammonia	NH ₃	10 ppt–1 ppb	Biogenic
Hydroxyl radical	OH	0.05 ppt	Photochemical
Hydroperoxyl radical	HO ₂	2 ppt	Photochemical
Hydrogen peroxide	H ₂ O ₂	0.1–10 ppb	Photochemical
Formaldehyde	CH ₂ O	0.1–1 ppb	Photochemical
Sulfur dioxide	SO ₂	10 ppt–1 ppb	Photochemical, volcanic, anthropogenic
Dimethyl sulfide	CH ₃ SCH ₃	10–100 ppt	Biogenic
Carbon disulfide	CS ₂	1–300 ppt	Biogenic, anthropogenic
Carbonyl sulfide	OCS	500 ppt	Biogenic, volcanic, anthropogenic
Hydrogen sulfide	H ₂ S	5–500 ppt	Biogenic, volcanic

Figure 2.2: Chemical composition of the atmosphere (Table 1., Prinn (2003))

affected by fluctuations in the radiation balance of the Earth's surface, depending primarily on incoming solar radiation for its energy receipt, and as such is much less turbulent than the troposphere in terms of weather systems. Ascending temperature gradients in this region are caused by photochemical oxidation of oxygen molecules by UV radiation forming the ozone layer.

Beyond the stratosphere lie the mesosphere, thermosphere, and exosphere, continuing into the ionosphere, collectively termed the upper atmosphere, these regions extend towards Earth's boundary with space at approximately 600 km. At these heights very low air densities are encountered, with the few chemicals in this region forced to highly volatile states owing to high levels of unmodulated solar energy. Due to its inaccessibility (too high for aircraft and balloon measurements, and too low for orbiting spacecraft), the upper atmosphere has been the subject of comparatively little research compared with efforts applied to the lower reaches of the atmosphere.

Air within the atmosphere is composed predominantly of nitrogen (N₂ - 78%), oxygen (O₂ - 20.9%) and argon (Ar - 0.9%), with the remainder constituting the trace gases, which although only present in minute amounts, account for the majority of

activity in atmospheric chemistry (Figure 2.2). Trace gases of interest include O_3 in the stratosphere, the greenhouse gases – responsible for climate forcing via direct adjustment of Earth’s radiation balance in the troposphere (e.g. H_2O , CO_2 and CH_4), and traces gases responsible for indirect forcing via altering greenhouse gas concentrations (CO , NO_2 , O_3 and volatile organic compounds such as isoprene). Aerosols represent the final important constituent of the atmosphere, whose particle size and weight allow these solid particles to be uplifted from the Earth’s surface and held in suspension in the atmosphere. Whilst not classed as gases, aerosols nevertheless exhibit many key interactions with atmospheric chemistry.

2.1.2 Stratospheric chemistry

Providing the first significant buffer of gaseous molecules between space and the Earth’s surface, the stratosphere acts to absorb the vast majority of UV radiation through photochemical oxidation (Rowland, 2006). An excited $O(^1D)$ atom from photolysis of O_2 at wavelengths <290 nm rapidly combines with an adjacent O_2 molecule to form O_3 , itself susceptible to further photolysis in the UV, ensuring the cycle is continued (Chapman, 1932). This ozone-oxygen cycle maintains a layer of stratospheric ozone absorbing approximately 98% of incoming UV radiation from the Sun, which in its lower wavelengths (< 280 nm) is extremely harmful to life (Diffey, 1991). With an increase in ozone monitoring facilities, it has been shown that ozone amounts estimated solely with the Chapman formalism have been incorrectly estimated at approximately twice their actual concentrations.

Extra catalytic ozone removal processes have since been inferred which align modelled ozone with the measured reality. Hydrogen, nitrogen, chlorine and bromine are known to offer pathways for ozone removal, all being emitted in not insignificant quantities globally - BrO released from melting snowpacks at the poles, OH from water vapour and vegetation, and chlorine emission via CFCs. In addition to absorption of harmful UV radiation, displaced energy from this process acts to maintain broad temperature gradients throughout the atmosphere. The thickness,

and therefore quantity of ozone in the stratosphere, can be directly linked to climatic changes for the Earth system (Aghedo et al., 2011). Greater amounts of ozone lead to a greater interception of UV radiation and higher levels of photolysis, in turn liberating larger amounts of heat from energy, warming the stratosphere. Whilst lesser amounts of ozone allow for fewer reactions, encouraging a cooler stratosphere. Ozone is distributed globally, with layer depth varying on a broadly latitudinal scale, thinning towards the poles as a result of Brewer–Dobson circulation.

2.2 Tropospheric chemistry

The troposphere lacks the ozone layer seen in the stratosphere (accounting for 90% of the atmosphere’s O₃) due to an insufficient number of photons with enough energy (<240 nm) reaching the troposphere to initiate the Chapman cycle. This region therefore relies on a multitude of complex chemical processes for OH sources with which to initiate chemical reactions. Typically exhibiting a lifetime of between 1 week in the tropical planetary boundary layer to several months closest to the tropopause (Jacob, 2000), ozone’s interaction with atmospheric chemistry at these lower levels are markedly different to its role in the stratosphere. Tropospheric ozone is of major interest as a direct influence on climate change via radiative forcing of the Earth’s climate, and for its indirect effects through influence on the oxidative capacity of the troposphere (Brasseur et al., 1998).

2.2.1 Radiative forcing

The most recent IPCC report ranks tropospheric ozone’s radiative forcing effect (the difference between energy received at the top of the atmosphere to that which is reflected back into space) behind only CO₂ and CH₄, with an estimated total sky radiative forcing of 0.35 W m⁻², noting the level of scientific understanding on the topic as medium (Forster et al., 2007). More recent evaluations taking into account upgraded model schemes, place ozone’s direct radiative effect at 0.40 W m⁻²

(Stevenson et al., 2012). Uncertainties for attribution of ozone forcing remain, in part influenced by temporal and spatial variability in the tropospheric O₃ column. These uncertainties are affected by poorly quantified cloud screening effects on ozone forcing, in the short wave acting to increase radiation path lengths, and in the long wave decreasing outgoing long wave radiation (Joiner et al., 2009). Varying spatial and vertical distributions of the gas also impart errors on attempts to constrain O₃'s radiative effect, with Aghedo et al. (2011) finding significant biases between model estimations due to uncertainties in tropopause height and O₃ vertical columns over Earth's mid-latitudes.

2.2.2 Chemical forcing

The complex web of chemical pathways leading to generation and de-composition of chemical species plays a large role in moderation of the Earth's radiation budget. That these pathways are so numerous, and for the most part unknown, makes this area of tropospheric chemistry source and sink attribution so uncertain. With anthropogenic increases of CH₄, reductions in tropospheric OH are expected, encouraging further accumulation of CH₄ as part of the CH₄ oxidation chain (Logan et al., 1981). Elevated O₃ production as a result of CH₄ photolysis provides an additional element to CH₄'s radiative forcing capacity. IPCC estimates indicate extra tropospheric O₃ will add ~30% to CH₄ radiative forcing of approximately 0.11 W m⁻² (Collins et al., 2006; Forster et al., 2007).

2.2.3 Atmospheric pollution

Tropospheric ozone clearly has the potential to provide a significant element in climate change (Ainsworth et al., 2012; Stevenson et al., 2012); however its effects are often felt more immediately in the form of pollution in the very lowermost levels of the troposphere. Ozone pollution has major effects on the biosphere in natural and agricultural contexts (Chameides et al., 1999; Fuhrer, 2003; Ashmore, 2005), where an excess of the molecule causes injury to vegetation by forcing the closure

of stomata, usually open for the diffusion of CO_2 and H_2O into tissues, thereby reducing photosynthesis, plant re-generation and growth (Heggstad and Middleton, 1959; Reich and Amundson, 1985). These effects on plant productivity are thought to offer an indirect forcing on climate change by adjusting levels of carbon fixation through vegetation, possibly accounting for a greater contribution to global warming than expected for ozone’s radiative effects alone (Sitch et al., 2007; Ainsworth et al., 2012).

Ozone can cause damage to living tissue including that of humans, with the molecule ingested via the respiratory system causing a multitude of health issues related to cell damage in this part of the body (Kim et al., 2011). The impact for humans is exacerbated by the fact that anthropogenic activities often have a tendency to promote an excess of tropospheric ozone to form, through incomplete combustion of fossil fuels in industrial processes and vehicle engines (via NO_x initiated O_3 production), as well as a greatly increased likelihood for the presence of anthropogenic VOCs.

2.2.4 Ozone sources and sinks

The tropospheric ozone budget is derived from a number of sources (Table 2.1). Most obviously, the sinking of stratospheric air through the tropopause accounts for approximately 610 Tg yr^{-1} (Hsu and Prather, 2009) of an estimated tropospheric

	Natural emissions	Anthropogenic emissions
CH_4	100–230 Tg y^{-1} 10 Tg y^{-1} oceans 5 Tg y^{-1} freshwater 5 Tg y^{-1} CH_4 hydrates 20 Tg y^{-1} termites	299 Tg y^{-1}
NMVOC (all)	–	139 Tg y^{-1}
NMVOC (isoprene)	500–600 Tg y^{-1}	
NO_x	7–20 Tg NO-N y^{-1} soil 2–20 Tg N y^{-1} lightning 20 Tg N y^{-1} pyrogenic, agriculture	(all sources) 31 $\text{Tg NO}_x\text{-N y}^{-1}$
CO	Negligible	549 Tg y^{-1}

Table 2.1: Global natural and anthropogenic tropospheric ozone precursor estimates (Table 4.1, Royal Society (2008)).

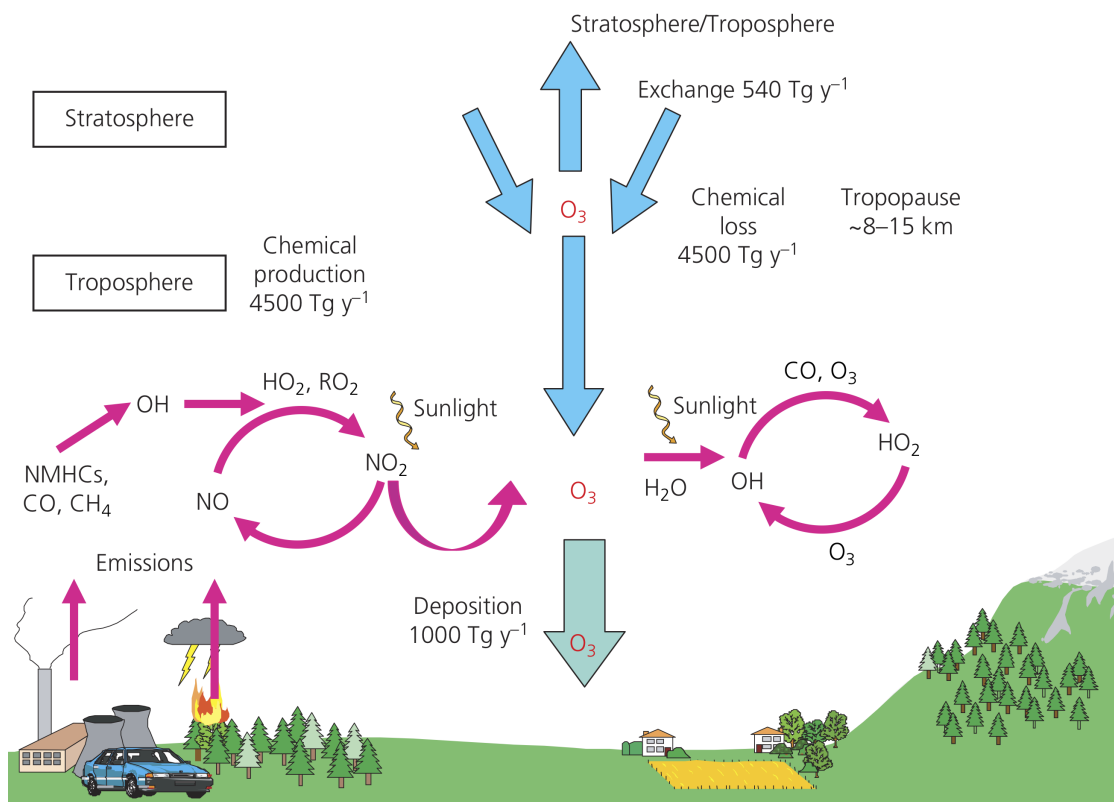


Figure 2.3: Tropospheric ozone sources and sinks, including global O₃ fluxes. (Figure 3.1, Royal Society (2008))

ozone budget of $4974 \pm 223 \text{ Tg yr}^{-1}$ (Stevenson et al., 2006). The remainder of the budget is highly dependent on the chemical conversion of trace gases in the planetary boundary layer (Holton et al., 1995; Lelieveld and Dentener, 2000). These contributing trace gases are primarily composed of variable NO₂ concentrations photolysing with carbon monoxide (CO) (Holloway et al., 2000), and the class of trace gases known as volatile organic compounds (VOCs) (Logan et al., 1981). Naturally occurring VOC emissions are found in vast quantities, which despite an increasing influence from anthropogenic activities in recent years, still dwarf the human component globally (Jacob and Wofsy, 1988; Guenther, 1995; Atkinson and Arey, 2003; Warneke et al., 2007). CO sources are primarily composed of anthropogenic emissions, together with oxidation of VOCs including CH₄ and biogenic VOCs (Duncan et al., 2007). Figure 2.3 provides an illustrated view of the O₃ cycle in terms of its global sources and sinks.

CO and CH₄ combine to provide a significant component of tropospheric chem-

istry in clean, remote regions lacking significant BVOC and anthropogenic VOC sources, together with additional oceanic sources of BVOCs (?). The extent of their influence on the remote troposphere is due to the gases high residence times prior to chemical degradation, allowing for thorough mixing and distribution to regions beyond the lifetime of more reactive trace gases. Significant non-methane VOCs (NMVOCs) are emitted primarily by vegetation, and include isoprene, monoterpenes, and aromatics (Guenther et al., 2006). Localised NMVOC budget contributions are seen from anthropogenic sources associated with fossil fuel combustion. Aside from VOCs, nitrogen oxides (NO_x) play a key role in tropospheric ozone formation (Sillman et al., 1999), being naturally released through decomposition of plant matter within soil (Bertram et al., 2005), as well as production from lightning (Price et al., 1997). The anthropogenic contribution to the NO_x budget is derived again from fossil fuel combustion, as well as a significant portion from biomass burning (Jaegle et al., 2005). As ozone is an unstable compound, its primary sink of $\sim 4500 \text{ Tg y}^{-1}$ is photolytic reaction in the troposphere (Jenkin and Clemitshaw, 2000), whilst deposition and ingestion by vegetation also accounts for approximately 1000 Tg y^{-1} of ozone removal (Ainsworth et al., 2012).

2.2.5 Tropospheric radical chemistry

Availability of free radicals determines the degradation pathways of many organic compounds in the atmosphere (Monks, 2005). Radicals including hydroxyl (OH), nitrates (NO_x), excited oxygen ($\text{O}(\text{D}^1)$), and hydroperoxys and peroxy (HO_2 and RO_2) control the rate of these reactions. Radical's ability to rapidly react with the vast majority of trace gases arises from a free electron forcing the molecule to an unbalanced state. The role of radicals in the troposphere, and OH in particular, is often likened to that of a detergent, providing the oxidation capacity to cleanse the troposphere of an excess of pollutants (Lelieveld et al., 2008).

Although radiation $\leq 290\text{nm}$ is largely filtered out by the stratospheric ozone layer, photolysis still occurs less frequently, at wavelengths $\geq 290\text{nm}$. Following

the nomenclature of Atkinson (2000), the single excited oxygen atom ($O(^1_D)$) from this reaction is available to combine with water vapour (H_2O) and produce an OH radical. The OH pathway operates in competition with de-activation of the oxygen free radical to a ground state - ensuring that for each $O(^1_D)$, approximately 0.2 OH molecules are generated.



Tropospheric VOC concentrations are reduced via deposition processes or chemical transformation as a result of interaction with NO_3 , OH and O_3 . These VOC transformations typically make use of the alkyl degradation pathway, entailing the creation and destruction of the alkyl (R), alkyl peroxy (RO_2), and alkoxy (RO) intermediary radicals. With the large number of VOC species present in the troposphere, in the following general description of VOC oxidation, R is used to denote a generic VOC. Hydroxyl initiates the oxidation chain by reacting with R, generating water, which reacts with oxygen to form peroxy radicals (RO_2):



The atmospheric pollutant NO_2 is generated after RO_2 's reaction with NO, allowing accumulation of O_3 through NO_2 generation, without requiring a further O_3 molecule:



Of relevance to work presented here, the organic formaldehyde (CH_2O) compound permits further R formation through photolysis, and as such represents an

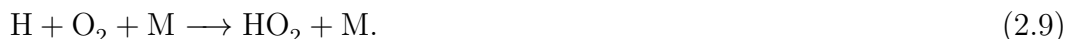
important intermediate in atmospheric O₃ cycling through release of free radicals (Calvert et al., 1972; Cantrell et al., 1990):



With the product of Equation 2.6 quickly reacting with oxygen leading to the generation of forming the hydroperoxyl radical:



Which in concert with a stabilising molecule of N₂ or O₂ (referred to as M), assists in the O₃ cycle:



2.2.6 Methane

CH₄ is of major importance for climate change for its properties as both a chemical and radiative forcer on the climate system (Wuebbles and Hayhoe, 2002). It plays an active role in regulating background tropospheric OH concentrations (Cicerone and Oremland, 1988), and contributes to the greenhouse effect through radiation absorption and reflection (Lashof and Ahuja, 1990). From a global emission source estimated at 600 Tg yr⁻¹, anthropogenic sources are thought to account for approximately 70% of methane released to the atmosphere (Lelieveld et al., 1998). These man-made sources occur in the form of agriculture, predominantly rice cultivation (Redeker et al., 2000), and coal and natural gas processing for use as fossil fuels. Naturally occurring methane is emitted from wetlands such as peat bogs and swamps (Whiting and Chanton, 1993). In all cases, the bulk of methane is emitted by bacteria acting on the decomposition of organic matter (Conrad, 1996; Hanson

and Hanson, 1996).

Removal processes for CH_4 are predominantly composed of loss to the tropospheric OH sink (507 Tg yr^{-1}), with minor stratospheric losses (40 Tg yr^{-1}), and subsumption by soil (30 Tg yr^{-1}) (Mikaloff Fletcher et al., 2004). To illustrate the OH decomposition pathway of CH_4 , the Atkinson (2000) nomenclature is used again:



The methyl peroxy radical product of the above reactions react with NO or HO_2 depending on availability:



Methyl radicals (CH_3O) from the NO based reaction are converted to CH_2O :



Whilst the CH_3OOH product from OH reaction can be photolysed, yielding CH_3O , which feeds into the above reaction:



Alternatively, reactions may be descendants of methyl, which on scavenging by OH leads to CH_2O generation, and OH recycling:

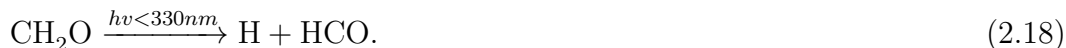


Or for descendants of hydroperoxy reactions, peroxy radicals are formed, feeding

back into the pathway at the NO / HO₂ level illustrated above (Equations 2.12 and 2.13):



From the above equations it is shown all CH₄ is eventually converted to CH₂O. In turn, CH₂O is converted to CO on a timescale of 4–6 hours, and then on to CO₂ over a matter of months. The HCO radical used in the conversion to CO is produced by photolysis below 330 nm:



Or through reaction with the OH radical:



And on to CO and HO₂:



2.2.7 Non-methane volatile organic compounds

The above mechanisms operate in a relatively uniform fashion across the globe due to the lifetime of CH₄. Less well distributed are NMVOCs, adjusting the balance of tropospheric ozone production, and the oxidising capacity of the atmosphere over vegetated continental regions. NMVOCs tend to have short atmospheric lifetimes of hours to days, rather than weeks, allowing large variations in spatial distribution across the globe to occur dependent on localised emission sources. Unlike direct ozone, CO₂ and CH₄ radiative forcing mechanisms, NMVOCs indirectly affect climate (Pacifico et al., 2009), adjusting the availability of ozone (Sanderson et al., 2003; Fiore et al., 2011; Paulot et al., 2012), influencing regional OH budgets

(De Arellano et al., 2011; Taraborrelli et al., 2012), and assisting in the production of secondary organic aerosol (SOA), a direct radiative forcer (Claeys et al., 2004; Henze and Seinfeld, 2006; van Donkelaar et al., 2007; Forster et al., 2007).

2.3 Isoprene

The NMVOC grouping is predominantly composed of isoprenoids, monoterpenes, alkanes and alkenes, amongst others (Kesselmeier and Staudt, 1999). Guenther et al. (2000) estimate that of the tens of thousands of organic compounds generated by vegetation, less than 40 are likely to be emitted in significant enough quantities to affect the atmospheric OH balance. Anthropogenic activities are thought to account for 145 Tg yr⁻¹ of the NMVOC budget (EDGAR, 2011), dwarfed by a further 1150 Tg yr⁻¹ of emissions from biogenic sources, primarily vegetation (Atkinson and Arey, 2003); hereafter referred to as biogenic volatile organic compounds (BVOCs). Here, the focus is placed on the most dominant BVOC, isoprene (C₅H₈). Thought to account for approximately 50% of the BVOC grouping, isoprene's estimated emissions are between 500–750 Tg yr⁻¹ (Guenther et al., 2006). Given the propensity for emission from vegetation, strong regional enhancements are masked by the global mean, with the Tropics accounting for 75% of the global total (Figure 2.4). In the following section, isoprene's significance for atmospheric chemistry is discussed, examining emission function and the effects of the compound on the tropospheric oxidation budget (Figure 2.5).

2.3.1 Production

Trace gas emissions from vegetation are identified as a key interface between the biosphere and atmosphere (Sharkey and Yeh, 2001). Isoprene production occurs in the chloroplast, undergoing no storage, and is immediately emitted directly to the planetary boundary layer through leaf stomata. Isoprene's emission from vegetation is known to be strongly dependent on light and temperature in the first instance,

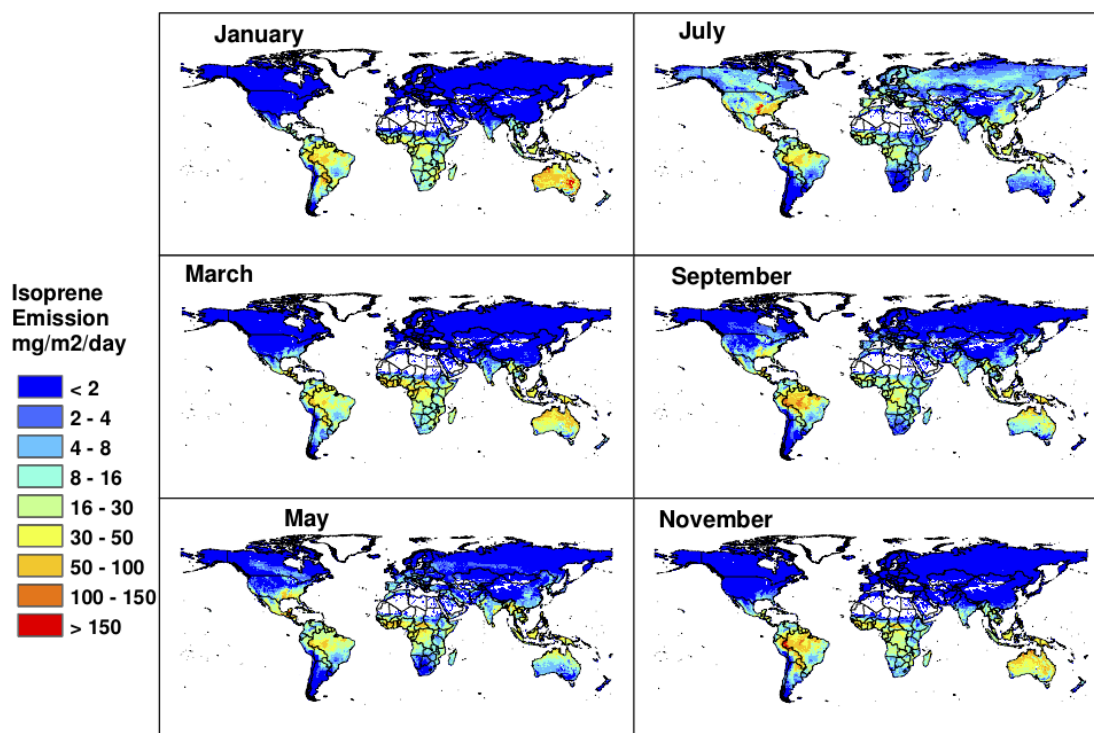


Figure 2.4: MEGAN estimated mean isoprene emission rates for 2003 (Figure 10, Guenther et al. (2006)).

as well as exhibiting more complicated relationships with environmental stress and growth stages (Pacifico et al., 2009). Occurring naturally, isoprene accounts for 2–8% of carbon fixation in vegetation, dependent on environmental factors and plant type (Kesselmeier and Staudt, 1999).

2.3.2 Emission

Isoprene emission is not common to all vegetation, but present in a large number of measured species, particularly woody biomass in temperate regions, which goes some way to explaining the prevalence of tropical rainforests in isoprene emission inventories (Guenther, 1995; Guenther et al., 2006; Müller et al., 2008; Arneth et al., 2011). It is widely reported that the fundamental controls on its emission are light and temperature (Sharkey and Singsaas, 1995; Sharkey et al., 1996). With the temperature dependency of isoprene production directly linked to photosynthesis, via isoprene synthase activity (Monson et al., 1992), emission rates and the climatic factors controlling isoprene emissions are intricately linked (Figure 2.6). Variations

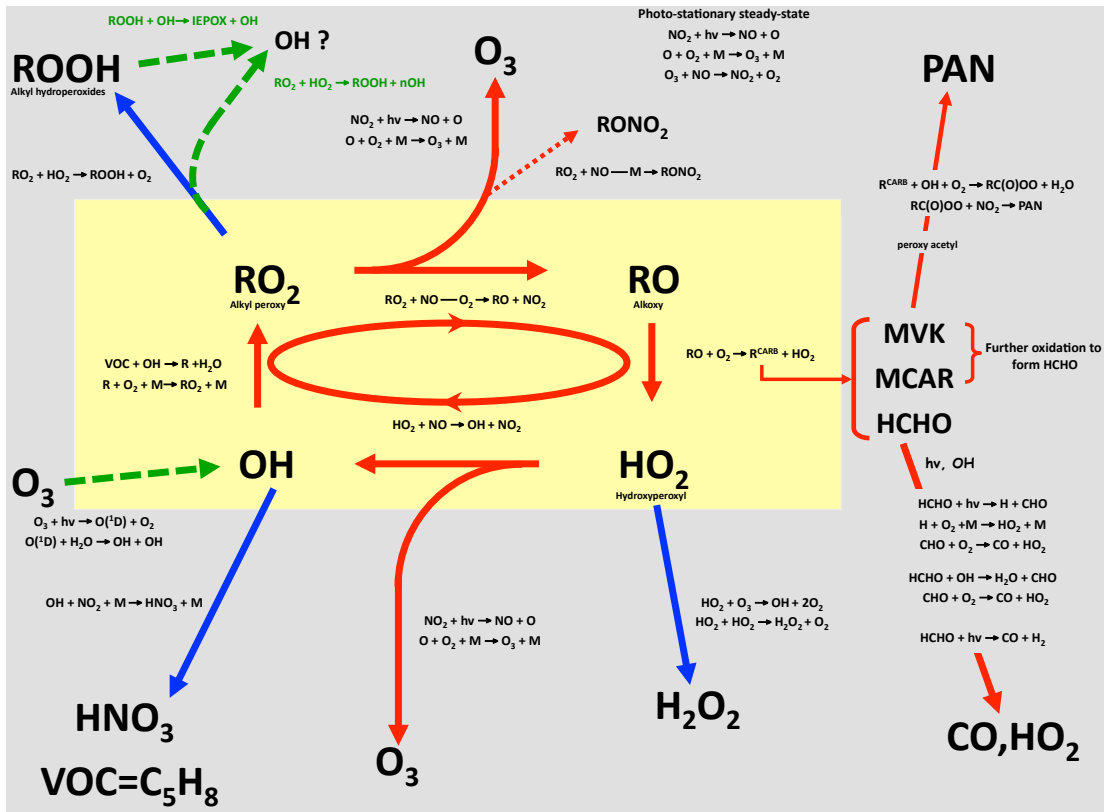


Figure 2.5: Overview of isoprene’s interaction for tropospheric chemistry (Barkley, personal communication, 2013).

in isoprene production occur between a range of minimum and maximum emission activation temperatures, above these maximum temperatures, emissions are seen to rapidly drop off, indicating a significant degradation in leaf biochemistry (Singsaas and Sharkey, 2000). Regional extrapolation studies using satellite datasets have been used to infer isoprene plant response to insolation and temperature, with results broadly confirming expected responses to air temperature (Abbot et al., 2003; Duncan et al., 2009).

2.3.3 Function

Leaf age and plant development also play a part in isoprene production, with work by Kuzma and Fall (1993) linking emissions to leaf growth stage and isoprene synthase activity, showing old and young leaves to emit isoprene at reduced rates. The work of Sharkey and Loreto (1993) extends this hypothesis, suggesting emissions are synchronised with leaf maturity, going on to show water availability maintains

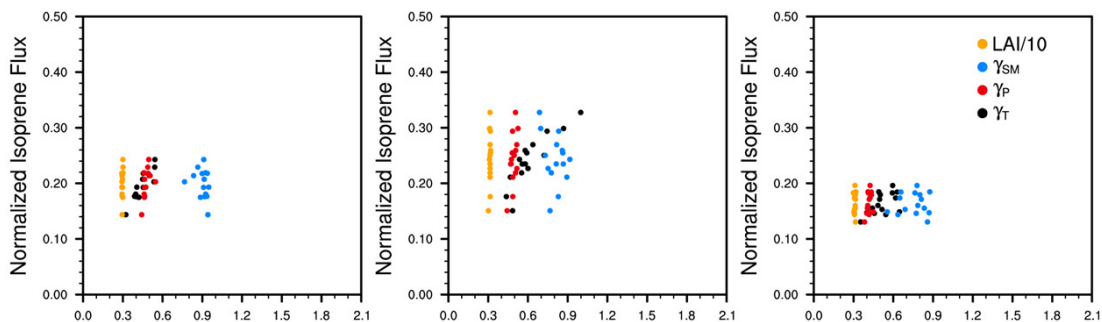


Figure 2.6: Modelled monthly mean (left to right: June, July, August averages over 1994–2008) isoprene fluxes for the north east U.S.A. plotted as a function of model parameter: LAI (yellow), soil moisture (blue), leaf temperature (black), photosynthetically active radiation (red). (Figure 4, Tawfik et al. (2012)).

a control on isoprene emission. Localised ozone pollution events affect plant health, with Loreto and Velikova (2001) postulating an anti-oxidant role for isoprene emissions, protecting photosynthetic membrane apparatus in plants from ozone damage. Isoprene is thought to offer a large degree of thermo-tolerance to leaves during extreme heat episodes, noting isoprene production greatly increases throughout such events, protecting leaves from cellular necrosis at otherwise unsustainable temperatures (Singsaas et al., 1997; Siwko et al., 2007). Further proposed functions of VOC emissions from vegetation include compounds facilitating communication between plants (Baldwin and Shultz, 1983; Kessler et al., 2006), and discouraging herbivore grazing (Baldwin et al., 2006; Kost and Heil, 2006). Oxidation of VOCs in the planetary boundary layer also creates variations in trace gas concentrations visible to some insect species, linking isoprene emission and plant pollination (Pichersky and Gershenzon, 2002; Andrews et al., 2007).

2.3.4 Chemical significance

Isoprene mixing within forest canopies is subject to a series of complex transport and decomposition pathways, all the more so in tropical regions where species diversity is high, and associated chemical reactions largely unknown. Following emission from leaves, isoprene’s escape efficiency to the atmosphere is determined primarily by its height in the boundary layer – for biomes composed predominantly of trees, these

emission rates increase towards the top of the canopy (Guenther et al., 1996; Helmig et al., 1998). For isoprene emitted within and below the canopy, significant amounts of isoprene are thought to be oxidised prior to reaching the canopy surface (Jardine et al., 2011), increasing variability in mixing gradients under the canopy. Despite this, studies have shown that on reaching the canopy ceiling, isoprene is reasonably well mixed on entrainment into the planetary boundary layer (Kuhn et al., 2007). Vertical mixing is time dependent, tied to diurnal cycles of mesoscale convection created by insolation receipt throughout the day to initiate within canopy movement (De Arellano et al., 2011). Once elevated to the troposphere, isoprene exhibits a high reactivity, with a tropical atmospheric lifetime expected to be in the region of 1–2 hours prior to its removal (Atkinson and Arey, 2003), although large variability is noted depending on compound height and associated temperature and pressure (Kuhn et al., 2007; Apel et al., 2012). Several of the chemical pathways followed in the breakdown of isoprene (Figure 2.7) are known to bear significant effects on regional atmospheric chemistry, with associated implications for global climate.

2.3.5 Role of isoprene for Earth’s climate

In a pristine atmosphere, ozone formation is regulated by NO_x and relative VOC concentrations (Jenkin and Clemitshaw, 2000). The key to isoprene’s interaction with ozone formation lies in the climatic predisposition for regions of elevated isoprene to sustain high atmospheric temperatures, leading to an efficient reaction with NO_x , whereby a single isoprene molecule can lead to several ozone molecules forming. This becomes a problem in urban areas where high NO_x levels from anthropogenic activities prevail (mainly combustion engine emissions) to produce unnaturally high O_3 concentrations (Ryerson et al., 2003).

OH regulation – Isoprene’s significance in the tropical atmosphere relates to its role in OH regulation (Stone et al., 2011), and subsequent provision for tropospheric ozone formation (Atkinson and Arey, 2003; Archibald et al., 2011; Fiore et al., 2011; Paulot et al., 2012). With isoprene decomposition pathways

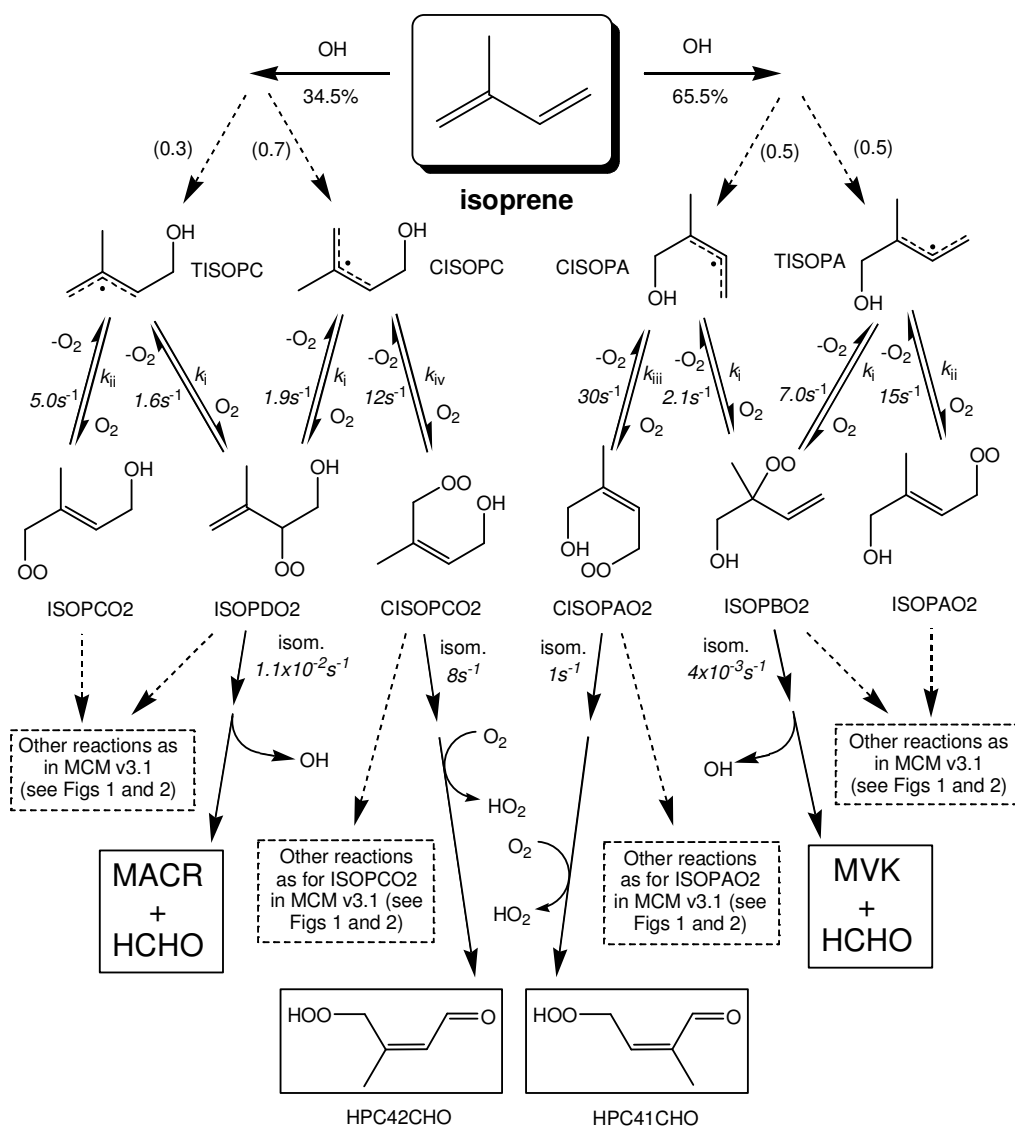


Figure 2.7: Isoprene's primary OH initiated decomposition pathways (Figure 6, Archibald et al. (2010)).

to numerous to detail here, the reader is referred to Atkinson and Arey (2003) and Archibald et al. (2010) for a detailed description of the predominant isoprene reactions. In short, isoprene is rapidly scavenged from the troposphere by OH, resulting in generation of peroxy radicals. Local concentrations of NO then determine the fate of these products - low concentrations allowing HO₂ to preferentially react with O₃, reducing the tropospheric ozone source. Conversely, high NO allows for recycling of OH, coincident with an increase in tropospheric O₃ (Atkinson, 2000; Sharkey et al., 2008), from which the majority of tropical boundary layer ozone is thought to be derived (Jacob and Wofsy,

1988). Recent work suggests an overlooked regeneration OH pathway in tropical environments, whereby in low NO situations, isoprene itself is recycled to OH without the need for NO interaction, reducing the previously stipulated influence of isoprene on OH depletion (Lelieveld et al., 2008; Taraborrelli et al., 2012).

Regardless of which pathway freshly emitted isoprene compounds follow, the cumulative effect ensures a rapid removal of BVOCs from the atmosphere, tropospheric ozone generation, and promotion of regional OH levels (Pacifico et al., 2009). Its net effects become more complex in pristine atmospheric environments with low NO_x levels such as remote tropical ecosystems, where isoprene is able to react directly with O₃, factors which contribute to large uncertainties in deriving previous extents of tropospheric greenhouse gas interactions (Beerling et al., 2007, 2011).

Secondary Organic Aerosols – Isoprene was first identified as a precursor to secondary organic aerosol (SOA) formation (Claeys et al., 2004). SOAs are formed in the boundary layer and troposphere through photo-oxidation of isoprene, at low enough vapour pressures to separate the compound into gas and aerosol components (Kanakidou et al., 2005; Hallquist et al., 2009). While the isoprene compound is not a large SOA yielding product itself, the magnitude of isoprene emissions (as a result of the extent of Tropical biomes), means a substantial portion of the global SOA budget is likely to be derived from isoprene photo-oxidation (Henze and Seinfeld, 2006). Carlton et al. (2009) list global SOA contributions from isoprene in the range of 14 Tg yr⁻¹ (Hoyle et al., 2007) to 19 Tg yr⁻¹ (Heald et al., 2008), out of a suggested total of 12–70 Tg yr⁻¹ SOA from all biogenic emissions (Hallquist et al., 2009).

The aerosol products resulting from the photo-oxidation of VOCs, including isoprene, are currently the least well understood of all organic aerosol formation mechanisms (Kroll and Seinfeld, 2008). As with all aerosols, SOA bears a wide range of impacts on the Earth system; influencing the insolation receipt

at the surface through modification of scattering and absorption processes (Paredes-Miranda et al., 2009; Morgan et al., 2010), as well as representing an important mechanism for cloud condensation nuclei, due to SOAs capacity for hygroscopic growth (Wex et al., 2009). With the majority of SOA formation occurring in the free troposphere, isoprene derived SOA also has the potential to be transported well away from its emission zones, expounding its effects to regional and global scales (van Donkelaar et al., 2007; Karl et al., 2009).

Pollution – Atmospheric levels of isoprene and its O₃ and SOA products are of critical relevance for human health. At enhanced concentrations in meteorologically stable conditions, these airborne chemicals and products form photochemical smogs (Chameides et al., 1988). Particularly over urban areas, human exposure to toxic airborne matter stresses cardiovascular and respiratory systems (Gold et al., 2000; Brunekreef and Holgate, 2002), being linked to increased mortality rates in affected regions (Samet et al., 2000). Ozone is also known to have detrimental effects on agriculture, affecting growth rates and reducing crop yield through leaf damage (Fuhrer et al., 1997). Further effects of isoprene on regional and global pollution have been identified through its pathway as a precursor, along with other VOCs such as acetaldehyde, to the peroxy acetyl nitrate (PAN) compound. PAN contributes to the ozone budget in the troposphere, although has a much longer lifetime than that of isoprene, allowing it to be entrained into cooler stratospheric airflows, where its reactivity is decreased and transported long distances. Upon descent into a warmer air mass, reactivity increases, thereby increasing tropospheric ozone levels over the subsiding region (Fiore et al., 2011).

Climate Change – Predicting isoprene’s overall contribution to the changing climate is hampered by the multitude of connections the trace gas makes with direct and indirect radiative forcers in chemistry, climate and the biosphere (Pacifico et al., 2009). However, increasing temperatures as a result of global climate change are expected to increase the latitudinal bounds of large biomass

2.3.6 Isoprene measurement

Direct isoprene emission measurement techniques take a variety of methodologies depending on the scale of observation desired. A brief outline of some of the more regularly applied techniques are outlined in order of measurement resolution, from leaf level to ecosystem scale. Table 2.2 lists a sample of isoprene mixing ratios across the globe taken with some of the below measurement techniques.

Emission observation

At leaf level, detailed measurements are made by sampling air adjacent to vegetation followed by subsequent application of gas chromatography to derive gaseous concentrations of the air mass (Goldan et al., 2000). Detailed measurements of this nature are limited by the proximity required to the vegetation being sampled, necessitating supporting structures for the suspension of equipment when making measurements away from the ground.

Sampling larger areas for isoprene emissions requires a modification to the leaf level approach, frequently entailing the use of tower and balloon mounted instruments. Harley et al. (2003) performed canopy isoprene emission measurements of the South African savannah with tower mounted sampling equipment, collecting air samples via absorbent cartridges, followed by laboratory based gas chromatography

Location	Mean conc. (ppbv)	Reference
Hong Kong, China (urban, tropical)	0.109	Guo et al. (2012)
Crete, Greece (mediterranean, semi-desert)	0.0015–0.1375	Liakakou et al. (2007)
N.E. Spain (mediterranean, semi-desert)	~1	Peñuelas et al. (2013)
Rondonia, Brazil (tropical, forested)	4–10	Kesselmeier et al. (2000)
West Africa (tropical, forested)	0.604	Murphy et al. (2010)
Taipei, Taiwan (sub-tropical, urban)	0.72	Wang et al. (2013)
Alaska, U.S.A. (clean, tundra)	1.5	Potosnak et al. (2013)
Southern Indian Ocean (clean, marine)	0.04	Colomb et al. (2009)

Table 2.2: Selected in-situ measurements of isoprene mixing ratios across the globe under varying environmental conditions, demonstrating the range of concentrations to be expected. Isoprene concentrations measured by Potosnak et al. (2013) are notable for their apparent high values when considering the lack of significant biomass stores in the region.

analysis. Balloons are used to sample air masses for isoprene studies in a similar fashion to canopy schemes, with Wiedinmyer et al. (2001) making isoprene measurements from balloon-borne samples at heights of 25 m over central Texas, U.S.A. Further extrapolation of isoprene measurement for regional study is made possible by mounting equipment on aircraft. Airborne isoprene measurements provide regional scale data for model validation and calibration, with successful campaigns over Borneo (Hewitt et al., 2010), south east U.S.A. (Goldan et al., 2000), and the northern Amazon (Eerdeken et al., 2009) highlighting the utility of large scale observations.

Increasing measurement capacity for isoprene observations at regional and continental scales necessitates application of geophysical models relating isoprene to its environmental precursors such as light, temperature and vegetation type. Construction of such models follows one of two pathways, with bottom-up models using available data on isoprene emission factors and meteorology, and top-down models constraining isoprene emissions with the use of a-posteriori emission data and satellite proxy emission datasets.

Bottom-up emission estimates

Bottom-up modelling schemes take databases of known isoprene emission dependencies (such as light availability, temperature and vegetation type) as inputs to isoprene mechanism parameterisations (determined from laboratory and field experiments) in order to derive spatial representations of the global isoprene emission flux. The Guenther et al. (2006, 2012) Model of Emissions and GAses from Nature (MEGAN) applies such a scheme to produce widely quoted global estimates of isoprene emissions from field measurements using the following equation:

$$Emission = \epsilon \gamma \rho. \tag{2.21}$$

The origin of the equation components are defined in Guenther (1995); here, ϵ represents the emission rate of a desired compound in $\text{mg m}^{-2} \text{h}^{-1}$ at a predefined set

of standard environmental measurement conditions, γ denotes the emission activity factor, modulating the emission rate as a function of climate and location, whilst ρ details within canopy sources and sinks. Despite species heterogeneity making this difficult to perform with a high degree of accuracy (particularly within tropical rainforests), evaluation of the MEGAN inventory has shown the model to produce isoprene emission estimates broadly inline with satellite derived estimates (Müller et al., 2008).

Building on a dynamic global vegetation model (DGVM) in the first instance, the Lund-Potsdam-Jena (LPJ) GUESS model takes a different approach to calculating isoprene emissions modelling from MEGAN. Taking into account plant functional types and atmospheric CO₂ (amongst other variables) to generate a model of vegetation patterns, isoprene fluxes are derived as a function of temperature and light with regards to electron requirements for isoprene generation at leaf level (Smith et al., 2001; Arneth et al., 2007, 2011). The Biogenic Volatile Organic Compound Emission Model (BVOCEM) represents a recent development for MEGAN, tying the driving inputs of the model to a DGVM (Lathière et al., 2010). Applying the same gridded inputs as applied in MEGAN (leaf area index, plant functional type, and dynamic meteorology) for derivation of isoprene emissions, BVOCEM incorporates model dependencies on MEGAN ϵ , γ and ρ parameters.

Future directions for BVOC emissions modelling include model integration to Earth system modelling schemes (Guenther et al., 2012), as well as the need for an improvement of leaf level emission factor definitions (Niinemets et al., 2010). With small scale measurements observing isoprene emission fluxes at a high spatial and temporal resolution, there is an implied tendency for canopy fluxes to exhibit specificity to vegetation types observed. When incorporated in global isoprene emission models, this uncertainty in leaf and canopy level emission observations allows for the propagation of error imparted through species un-captured species heterogeneity, for which the standardisation of observation techniques is attempting to address Niinemets et al. (2011). Despite emission estimate uncertainties for the latest gener-

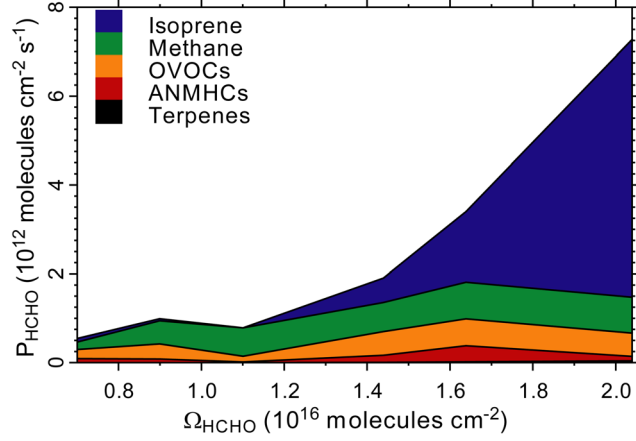


Figure 2.9: CH_2O 's production rate (P_{HCHO}) from the largest BVOC sources plotted against the measured CH_2O column (Ω_{HCHO}) (Figure 6, Millet et al. (2006)).

ation of isoprene models being of the order of a factor of 2 (Guenther et al., 2012), the similarity of parameterisations within modern isoprene emission models is causing a convergence for modern isoprene emission estimates (Arneth et al., 2008).

Top-down emission estimates

The top-down modelling approach constrains emission estimates with databases of isoprene oxidation products, stepping backwards through the isoprene oxidation chain based on assumptions of BVOC decomposition pathways. To mitigate for issues of model's temporal and spatial resolution failing to capture detail required to accurately simulate emissions, a top down approach to emission monitoring has been developed (Palmer et al., 2003, 2006); linking CTM BVOC outputs (E_i) (scaled to CTM CH_2O production rate Y_i), to CH_2O columns (Ω):

$$\Omega = \frac{1}{k_{\text{CH}_2\text{O}}} \sum_i Y_i E_i, \quad (2.22)$$

with $k_{\text{CH}_2\text{O}}$ denoting the CH_2O sink via photolysis and oxidation gases (primarily relevant to O_3 and NO_x reactions).

The key component of the above equation is the linking of CH_2O to BVOC outputs, as satellite measurements of CH_2O are available from 1996 to the present day (De Smedt et al., 2012). To ensure the applicability of satellite CH_2O columns

as a proxy for isoprene emissions, Palmer et al. (2006) demonstrated isoprene is the largest contributor to satellite measured CH_2O columns over south east U.S.A., showing the yield from longer lived BVOCs to be negligible within the measurement sensitivity of satellite spectrometers (also see Figure 2.9 and Millet et al. (2006)). Formaldehyde’s 2–8 hour lifetime is dependent on spatial and temporal gradients of reaction rates with OH, photolysis, and NO_3 (Frost et al., 2002; Cooke et al., 2010; MacDonald et al., 2012). This lifetime is thought to preclude significant horizontal transport prior to CH_2O removal, inferring satellite observed CH_2O at moderate ground footprint sizes (40–400 km) are not expected to be contaminated with signal from adjacent scans (Abbot et al., 2003).

Isoprene emissions are estimated with a linear regression from CTM isoprene emissions (E_{isop} , modelled for time and location of the satellite measurement) to modelled CH_2O columns:

$$\Omega = S E_{isop} + B, \quad (2.23)$$

with B representing a modelled CH_2O background (primarily as a function of CH_4 oxidation), and S the slope of the fitted regression, detailing CH_2O produced via isoprene oxidation (Figure 2.10) (Palmer et al., 2006). The slope S is then used to transfer satellite measured CH_2O columns (Ω_{meas}), less the model background B , to an isoprene emission estimate (E_{meas}):

$$E_{meas} = \frac{\Omega_{meas} - B}{S}. \quad (2.24)$$

Various studies making use of satellite CH_2O data have estimated the geographic distribution of isoprene emission quantities for all major vegetated biomes using this inversion technique (Table 2.3). Initial analysis of North America by Palmer et al. (2006) suggested the region to be responsible for as much as $15.4 \text{ Tg C month}^{-1}$ at the height of the growing season, with Shim et al. (2005) extending the study to a global scale translating this value to an annual isoprene emission mean of 25.7

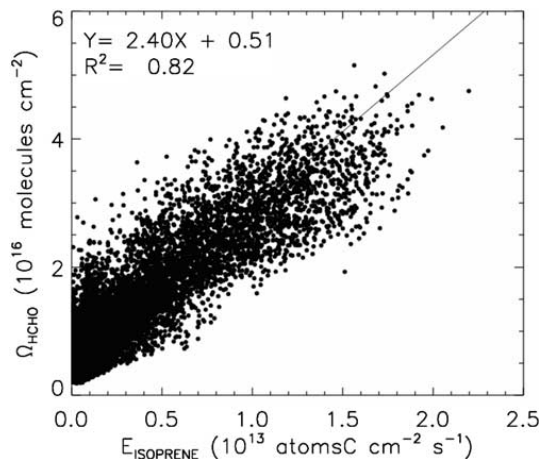


Figure 2.10: GEOS-CHEM modelled isoprene vs. GEOS-CHEM modelled CH_2O for North America, Summer 2006 (Figure 10, Millet et al. (2008)).

Tg C^{-1} . Emissions derived from ensuing studies using the technique are detailed in Table 2.3, although most notably the global inversion model proposed by Shim et al. (2005) predicts a global total of 566 Tg C^{-1} . As would be expected, the largest isoprene emission fluxes are found for tropical biomes, with estimated emissions for Europe around an order of magnitude lower. Despite all groups constraining their inversions with similar methodologies, differences are found for the same regions when using alternate satellite CH_2O datasets, pointing towards an additional source of error in the isoprene inversion.

CH_2O columns from satellite instruments represent one of the two major inputs to the inversion (the other being the CTM); the accuracy of this constraining

Region	Instrument	Time period	Mean emissions	Reference
S.E. Asia	GOME	1996–2001	$56 \pm 30 \text{ Tg C}^{-1}$	Fu et al. (2007)
Africa	OMI	2005–2009	60 Tg C^{-1}	Marais et al. (2012)
Europe	SCIAMACHY	6–8/2003	2.7 Tg C^{-1}	Dufour et al. (2009)
Trop. S. America	GOME	1–12/2000	$31\text{--}38 \text{ Tg C}^{-1}$	Barkley et al. (2008)
Trop. S. America	SCIAMACHY	1–12/2006	$31\text{--}38 \text{ Tg C}^{-1}$	Barkley et al. (2013)
Trop. S. America	OMI	1–12/2006	$28\text{--}38 \text{ Tg C}^{-1}$	Barkley et al. (2013)
N. America	GOME	7/2000	15.4 Tg C^{-1}	Palmer et al. (2006)
N. America	OMI	6–8/2006	11.5 Tg C^{-1}	Millet et al. (2008)

Table 2.3: Selected isoprene emissions derived from application of satellite formaldehyde data for constraining model isoprene inversions. Values given represent means over the time period denoted, multi year values detail annual values for the time period.

input dataset is identified as a key contributor the inversion’s accuracy Barkley et al. (2013), for which two sets of error sources exist. Firstly, measurement of the formaldehyde column from space is hampered by the low signal to noise ratio of UV spectrometers - particularly in the wavelength region formaldehyde’s extremely faint absorption signal is sensed in. Secondly, conversion of measurements along the instrument’s line of sight (slant columns – SC) to vertical columns (VCs – density of the absorber in a vertical column extending from the surface) are needed for application of retrieved CH_2O values to geochemical models. This represents a further significant contributor to product error (30–60%), being strongly influenced by aerosol, cloud and albedo inhomogeneities at sub pixel level. Over Tropical land-masses, the above limitations combine to make satellite retrievals of tropospheric gases particularly difficult due to persistent cloudiness (especially during the wet season) and high aerosol loading (from biomass burning and to an unknown extent, secondary organic aerosol).

2.4 Formaldehyde

The vast majority of tropospheric formaldehyde (CH_2O) is formed as an intermediate product in the VOC oxidation chain. A global background of CH_2O is maintained by CH_4 oxidation, described in equation 2.16. Regional enhancements are seen as a result of the compound being the major high yield product of isoprene oxidation (Palmer et al., 2003; Guenther et al., 2006), biomass burning (Gonzi et al., 2011) and industrial sources (Millet et al., 2008) (see Table 2.4). The release of isoprene from vegetation maintains CH_2O hotspots over the worlds major biomes, correlating the molecules short lifetime of 2–8 hours prior to photolysis and radical reactions, with isoprene’s source regions. That isoprene is identified as the major contributor to regional enhancements is readily confirmed by knowledge that direct CH_2O emissions by vegetation are negligible in a global context (Rottenberger et al., 2004). Direct anthropogenic VOC sources also contribute a small amount to the global CH_2O budget (Fu et al., 2007; Stavrou et al., 2009b).

2.4.1 Sources and sinks

Localised enhancements of CH_2O due to isoprene emissions occur via OH oxidation of isoprene yielding the peroxy radical RO_2 , which depending on adjacent NO_x concentrations, reacts to follow one of two pathways. For high NO_x situations, CH_2O , methacrolein (MACR) and methyl vinyl ketone (MVK) are formed in less than one hour in the first series of decomposition reactions (Palmer et al., 2006; Liu et al., 2012), followed by a second generation of further CH_2O from OH oxidising with the MVK and MACR. The alternate isoprene pathway for a low NO_x environment allows the reaction of RO_2 and HO_2 , encouraging peroxide deposition as well as CH_2O generation on a slightly longer timescale, on the order of a day, rather than 3–4 hours in the high NO_x pathway. Sinks of CH_2O are reaction with radicals OH and NO_3 , as well as photolysis (Cooke et al., 2010; MacDonald et al., 2012), with HCO producing hydroperoxy radicals and CO from reaction with O_2 , indicating the compound’s importance in contributing to the CO budget (see equations 2.18–2.20).

2.4.2 Formaldehyde measurements and distribution

Observations of atmospheric formaldehyde concentrations are made possible by the unique absorption cross section of the gas, permitting the derivation of column concentrations from measurements of light (Platt et al., 1979). Measurements from ground, airborne, and space-based instruments have proven invaluable in the cali-

Location	Mean conc. (ppbv)	Reference
Greenland (clean, Arctic)	0.12	Jacobi et al. (2002)
Northwest Canada (clean, Arctic)	0.15	Sumner and Shepson (1999)
Cape Verde (clean, marine)	0.35–0.55	Carpenter et al. (2010)
Mauna Loa (clean, marine)	0.2–0.9	Zhou et al. (1996)
Agra, India (clean, rural)	0.8	Khare et al. (1997)
Po Valley, Italy (polluted, rural)	0.7–4.2	Heckel et al. (2005)
Beijing, China (polluted, urban)	5.54–8.72	Li et al. (2010)
Bukit Atur, Borneo (tropical, forested)	2–3	MacDonald et al. (2012)
Florida, U.S.A. (tropical, forested)	0.3–5	Herndon et al. (2007)

Table 2.4: Selected in-situ measurements of formaldehyde mixing ratios across the globe under varying environmental conditions.

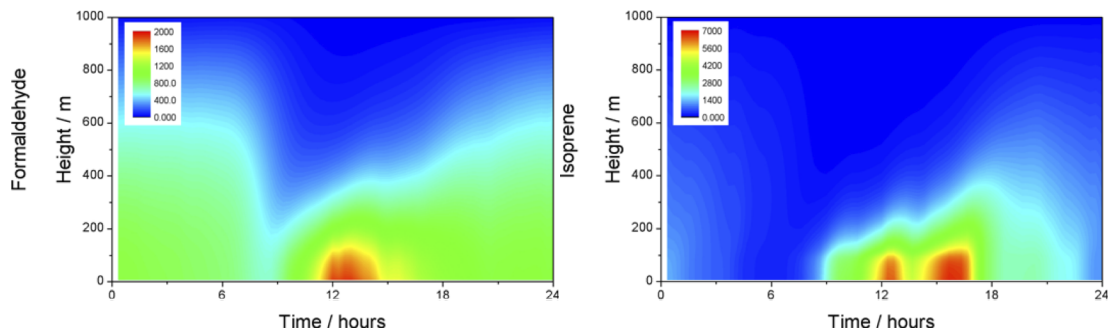


Figure 2.11: Modelled diurnal variation in vertical CH_2O and isoprene profiles above a South East Asian tropical rainforest (Figure 11, MacDonald et al. (2012)).

bration and validation of chemical transport model (CTM) formaldehyde estimates.

As part of the OP3 field campaign (Hewitt et al., 2010), boundary layer CH_2O concentrations were measured with a ground based MAX-DOAS instrument over Borneo in April and August 2008 (MacDonald et al., 2012). Shown in Figure 2.11, measurements and modelling of CH_2O and its isoprene precursor detail the diurnal cycle expected in response to isoprene's emission as a function of temperature and light. In use for validation of SCIAMACHY satellite CH_2O observations, Fourier transform infrared and MAX-DOAS measurements conducted at Réunion Island (Indian Ocean) offered good agreement between the two differing CH_2O observation sets, with comparison 1σ of 20–30%.

Aircraft campaigns have shown the majority of BVOC generated CH_2O to reside in the lower troposphere, with Martin et al. (2004) identifying ~60% of the tropospheric CH_2O column below 1500m over the south east U.S.A., reflecting the compound's short atmospheric lifetime prior to removal at low altitude. More aircraft measured CH_2O data from the south east U.S.A. provided input for comparison and validation between space-borne OMI CH_2O measurements and GEOS-Chem chemical transport model estimations (Boeke et al., 2011) (GEOS-Chem modelled monthly mean CH_2O concentrations for January 2009 are presented in Figure 2.12). Results from the study showed OMI data to exhibit a very small mean negative bias (-3%) compared to aircraft measurements.

Ship-borne campaigns offer the opportunity to measure formaldehyde over remote oceans, with the work of Peters et al. (2012) measuring background CH_2O

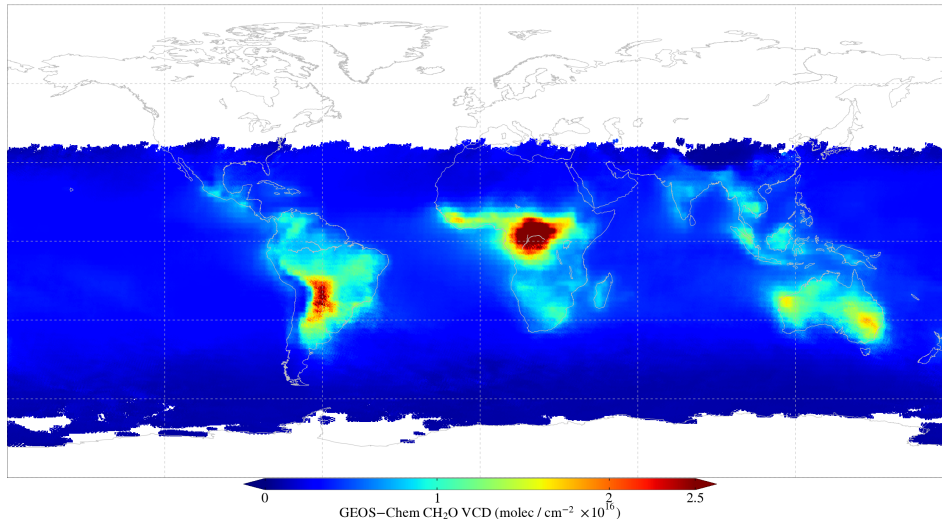


Figure 2.12: GEOS-Chem modelled mean CH_2O vertical columns for January 2009, constrained to the viewing geometry and scan pattern of the GOME-2 satellite instrument.

concentrations due to CH_4 oxidation with MAX-DOAS instrumentation. Typical CH_2O vertical columns from these observations over the western Pacific Ocean of $\sim 0.3 \times 10^{16}$ molecules cm^{-2} found strong agreement when used to validate co-located space-borne measurements from SCIAMACHY and GOME-2. An aircraft mounted laser absorption spectrometer was employed to measure CH_2O over the North Atlantic and North America as part of the INTEX field campaign (Fried et al., 2008). Observing throughout the troposphere to an altitude of 12.5 km allowed correlations between CH_2O 's vertical variability and temperature and pressure profiles to be drawn. CH_2O in the remote troposphere displays a more regular decline in mixing ratios with height, being a function of CH_4 oxidation temperature dependency (Millet et al., 2006). Convection contributes to the vertical profile of CH_2O depending on prevailing meteorology (Fried et al., 2008), or in certain cases, pyrogenic uplift (Gonzi and Palmer, 2010).

Use of instruments mounted onboard satellites mitigates many of the spatial sampling limitations inherent to in-situ observations, providing a global picture of the Earth's CH_2O emissions in as little as 1.5 days. With the launch of the Global Ozone Monitoring Experiment (GOME) UV spectrometer in 1996, satellite based measurement of tropospheric formaldehyde columns ushered in a new era of trace

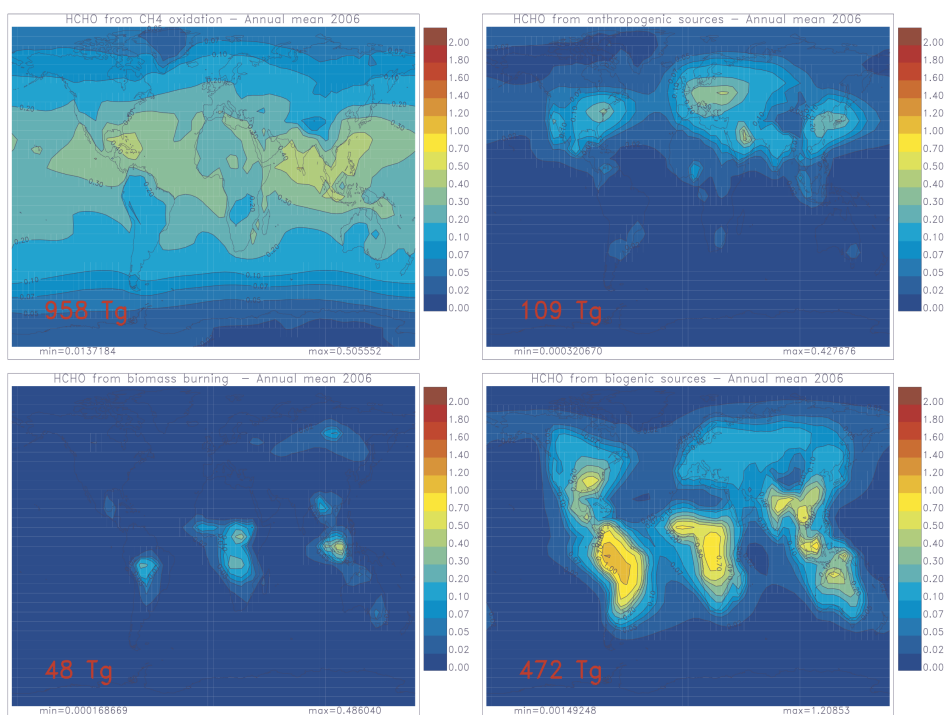


Figure 2.13: Modelled annual mean CH₂O emissions segregated into a: CH₄ oxidation, b: anthropogenic, c: pyrogenic, and d: biogenic NMVOC oxidation (Figure 2, Stavrou et al. (2009c)).

gas emission monitoring (Thomas et al., 1998; Chance et al., 2000), paving the way for isoprene emission estimation via model inversion (Palmer et al., 2003).

The formaldehyde budget is estimated from modelling studies by Stavrou et al. (2009b) at 1587 Tg yr⁻¹ (global mean for 2006). With a relatively homogenous global background determined by CH₄ of 958 Tg yr⁻¹, elevated formaldehyde concentrations are found at regional and continental scales in concert with significant biomass stores, providing a global mean from BVOCs of 472 Tg yr⁻¹ (Figure 2.13). Inevitably, Tropical rainforests are the highest emission sources given their year round growing season. Seasonal variations in isoprene emissions are noted, with the south east U.S.A. presenting a significant CH₂O emission hotspot from BVOCs during the summer months, and a small contribution from boreal regions of Northern latitudes for a brief period during the summer.

Localised contributions to the CH₂O budget are emitted from anthropogenic sources, estimated at 109 Tg yr⁻¹ (Stavrou et al., 2009c). In the anthropogenic signal, petrochemical industry emissions over Houston, USA, are identifiable (Millet

et al., 2008). The rapid industrialisation of Asia has provided noticeable increases in CH_2O concentrations over China and India from power plant and industrial emissions (Fu et al., 2007; De Smedt et al., 2008). With increasing global trade, associated transport of goods has also become a contributor, with Marbach et al. (2008) identifying formaldehyde from shipping emissions over the Indian Ocean. Although biomass burning is the smallest contributor to the global CH_2O mean, accounting for 48 Tg yr^{-1} , rapid convection of trace gases via pyrogenic uplift from burning sources to the upper troposphere plays an important role in upper tropospheric chemistry (Gonzi and Palmer, 2010).

2.5 Summary

The atmosphere is key to the presence of life on Earth. The closest two layers to the surface of the planet are the stratosphere (descending from approximately 50 km to the tropopause at 8–15 km), responsible for filtering out harmful ultra-violet radiation; and the troposphere (from the tropopause to the surface), playing host to the majority of chemical reactions and assisting in maintaining air in a sufficiently amenable state for all life on Earth to survive.

The hydroxyl radical OH is known as the detergent of the atmosphere, and tropospheric O_3 is key in the atmospheric production of OH. NO_x is seen to be a significant component of basic tropospheric chemistry, in high quantities acting to reduce OH recycling, whilst a reduction encourages CH_4 to act as an OH sink. The availability of NO_x also offers a control on ozone formation; NO_2 photolysis yields the free oxygen molecule required to react with O_2 , allowing formation of O_3 . The long lived greenhouse gases CH_4 and CO, both significant for climate change through direct and indirect forcing, act as sources and sinks for CH_2O , the trace gas of interest in this project.

In addition to these basic components of atmospheric chemistry, there are many NMVOCs with varying lifetimes and distributions. Isoprene accounts for ~50% of them, and can be monitored via its high yield oxidation product formaldehyde

(CH_2O). The complexity of emitted isoprene's chemical fate in the troposphere prevents an accurate quantification of its interaction with tropospheric chemistry, particularly in tropical regions where reactivity is high, leaving large errors on estimates of the magnitude and distribution of its effect. Furthermore, large gaps remain in knowledge on basic isoprene emission control functions from plants, with speculation continuing on fundamental factors such their relationship with light and temperature, and more complicated dependencies on vegetation growth and external stresses.

Formaldehyde's distribution can be summarised on three scales – a global background from CH_4 oxidation, regional concentrations from oxidation of BVOCs (primarily isoprene), and localised contributions from biomass burning, and to a lesser extent, anthropogenic sources. Sampling problems for the measurement of formaldehyde from space are identified as the area in which the following work is proposed to improve upon.

Chapter 3

Retrieval Methods and Instrumentation

In this chapter, basic principles of the transfer of electro magnetic radiation through the atmosphere are examined, followed by a discussion of the application of these properties to the spectroscopic measurement of trace gases in the atmosphere. Instrumentation used to measure ultra violet radiation with this technique from space is then detailed, together with an examination of the mitigative techniques applied to minimise impacts of instrumental shortcomings.

3.1 Atmospheric radiative transport

Light is accurately described as having the properties of both waves and particles, however for the discussion of radiative transport here, the concept of light as photons allows for a more convenient description. During transport from source (in our instance, the Sun) to detector (e.g. the cones and rods of an eye, or silicon diode of a spectrometer's detector array), the photon is likely to be subjected to a number of events acting to alter the intensity of energy emitted from the source. Collectively referred to as radiative transport, the processes of scattering and absorption force a transaction of energy between the photon and molecules lying in the path of transmission.

3.1.1 Absorption

Absorption describes the wavelength dependent reduction in intensity of radiation, due to transfer of energy from photon to incident molecule. The basic measure of a molecule's likelihood of radiation absorption is referred to as an absorption cross section (σ), in areal units of cm^2 . Underlying processes governing the absorption of radiation by a molecule relate electrons orbiting their nucleus at discretised energy levels (fixed by the nucleus electrical field) to their capacity to undergo excitation.

In order to effect this excitation, photons are required to impart sufficient energy to an opposing molecule to exactly equal the difference between a molecule's discretised energy levels. Those photons not bearing the required energy continue with no effect on the absorber or incident radiation. These energy transitions give rise to readily discernible structures in a molecule's absorption spectrum. Molecules with closely spaced energy levels exhibit wide absorption lines with a broad absorption cross section, indicating the probability of an excitation is increased. Conversely, individual absorption lines are evident for molecules with widely spaced energy transitions. In this instance, highly structured absorption cross sections are characteristic, due to the decreased number of photons possessing equal energy to effect an absorption response. Several key atmospheric trace gas species possess these latter characteristics, enabling us to fingerprint them with a unique absorption cross section (Figure 3.1).

Depending on radiation wavelength and molecular excitation at the time of absorption, energy imparted will act on the molecule in one of the following ways. Molecules may be split in a process known as photolysis, when energy levels are high enough to break chemical bonds in a molecule (e.g. stratospheric O_3). Collision of molecules encourages absorption and removal of energy from the atmospheric path. Absorption may also act as a catalyst for chemical reactions, providing energy for two or more adjacent molecules to break and reform bonds with one another. A further pathway for absorption processes is the re-radiation by an excited molecule of a portion of the incident photon's energy via fluorescence, with a reduction in the

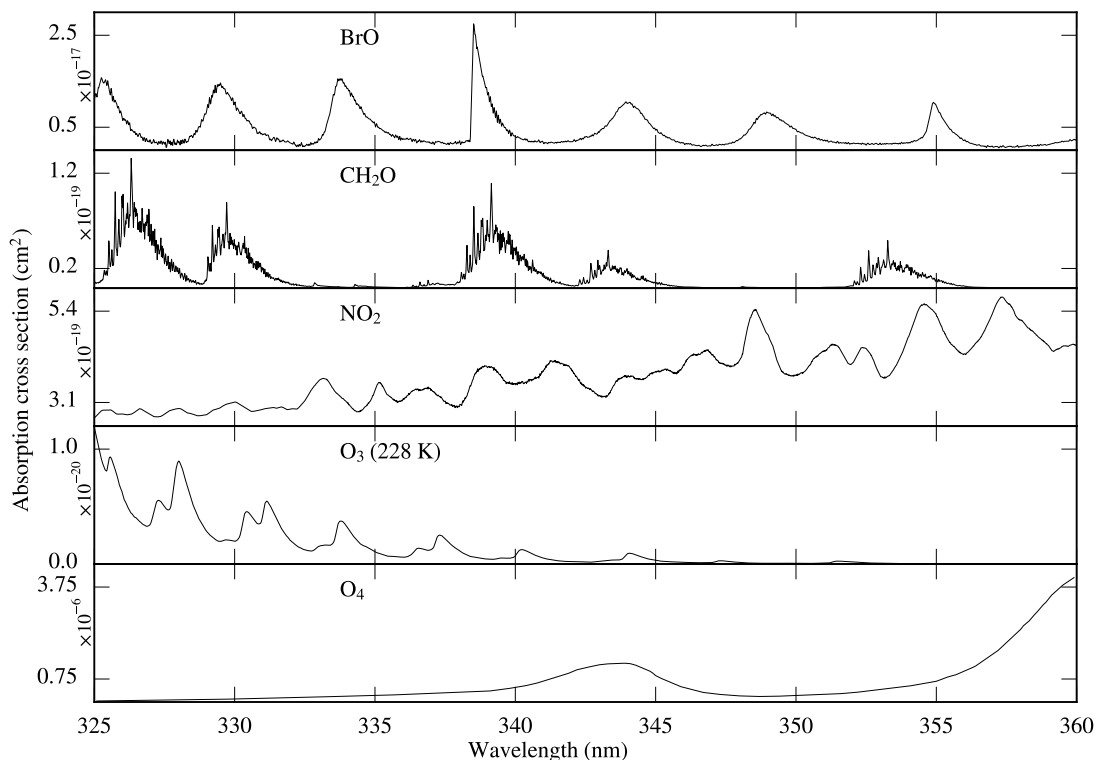


Figure 3.1: Trace gas absorption cross sections related to CH_2O retrievals.

photon's frequency according to the energy required to raise the molecule to a state of fluorescence.

3.1.2 Scattering

Scattering describes the processes resulting in a change of radiation direction due to interaction with an opposing particle. This causes energy to be re-radiated in any number of directions, depending on the scattering properties of the scatterer. Scattering can be further divided into elastic and inelastic scattering events, the former of which serves to re-direct incident radiation without significant transfer of energy. With inelastic scattering, part of the incident energy is conceded to the scatterer, whose properties are modified by the additional energy, causing an excitation. The probability of singular and multiple scattering events are related to atmospheric state at the time of transmission. Scattering greatly complicates the accurate solution of radiative transfer for a given light path due to the vast number of unknowns in the definition of a molecules scattering properties, and subsequent

unpredictability for the directions of reflected radiation.

Scattering is a wavelength dependent phenomenon, highly dependent on size of the scatterer. Consequently scattering events can be divided into one of three modes according to the ratio (α) of incident radiation wavelength (λ) to the scattering particle's spherical radius (r):

$$\alpha = \frac{2\pi r}{\lambda}. \quad (3.1)$$

Rayleigh scattering

For instances of $\alpha \leq 1$, typically found in the UV and visible wavelengths for scattering molecules, Rayleigh scattering permits redirection of radiation with no loss or conversion of photon energy. This redirection can be safely treated as an absorbing process due to the scattering of light away and out of its incident path. Known as Rayleigh scattering, the highly wavelength dependent Rayleigh scattering cross section (σ_R) is approximated following Platt and Stutz (2008):

$$\sigma_R(\lambda) = \frac{8\pi^3}{3\lambda^4 N_{air}^2} \cdot (n_0(\lambda)^2 - 1)^2 \cdot F_K(\lambda) \quad (3.2)$$

with n_0 representing air's refractive index, N_{air} as air's particle concentration, and F_K detailing the polarisability of air molecules. This shows us Rayleigh scattering is most effective towards shorter wavelengths, and causes the colour of the Earth's atmosphere as viewed from the ground.

Mie scattering

Mie scattering is an asymmetric scattering and absorption process describing the re-direction and change in intensity of radiation effected by interaction with the asymmetric surfaces of particulate matter. Active for a size parameter of ≥ 1 , this scattering type is most applicable to larger particles in the atmosphere such as aerosols and liquid droplets. Its effects are visible to the naked eye, with liquid droplets large enough to scatter visible radiation wavelengths equally, giving the

white appearance (all components of the visible spectrum) to clouds. Modelling of Mie scattering is particularly problematic when the scattering properties of non-spherical particles are taken into account, due to the number of scattering directions permitted by asymmetric objects.

The effects of Mie scattering are particularly relevant to the work covered in this project, with all tropospheric air parcels containing some amount of aerosol and water vapour. The modelling and measurement of suspended particulate matter is an extremely active research field, given the topic's implications for radiative transfer.

Briefly presented are the standardised terms used in describing a scattering particles properties:

Extinction coefficient – Denotes the fractional depletion of radiation per unit of path length, providing a measure of the ability of light to pass through the atmosphere following scattering and absorption by suspended particles. When considered over the entire vertical column of a light path, this extinction efficiency is more commonly referred to as optical depth.

Effective radius – To account for the non-sphericity of particles, an area weighted mean radius (measured in microns), representing an effective radius of a particle is used to describe particle size; with a division between fine and coarse mode particulate matter recognised at $2.5\mu m^{-1}$.

Single scattering albedo – Measurements of a particle's effectiveness at scattering versus extinction are described as a dimensionless figure; the single scattering albedo (w) simply refers to the ratio of an AOD to that of a radiance measurement's total optical depth.

Phase function – Given the tendency for Mie scattering to redirect incident light to a large number of angles, the phase function is used to describe the proportion of radiation scattered in each direction. With particles smaller than incident radiation's wavelength, there is a tendency for light to be scattered

away from the direction of photon's path of travel; whilst for particles with a larger effective radius than incident radiation's wavelength, there is a tendency for the majority of light to be scattered in the direction of travel.

Raman scattering

Raman scattering is an inelastic scattering process, occurring when a molecule's excitation state is modified by collision with a photon, along with a transmission of energy from the photon to the molecule. Rotational and vibrational excitations can be affected, although depending on the transfer of energy occurring the excitation may only be rotational (known as rotational Raman scattering), or vibrational (vibrational Raman scattering). Raman scattering causes a frequency shift on the incident photon, and is particularly significant in Earth's atmosphere due to the inelastic scattering caused by large quantities of O₂ and N₂ present, acting to fill in narrowband structures (known as Fraunhofer lines) of the solar irradiance spectrum by as much as 10%.

3.1.3 Beer-Lambert law

Forming the basis of all absorption spectroscopy measurements (the analysis of radiation's absorption by particles), the Beer-Lambert law provides a description for light's transmission through a volume, with exiting radiation subject to the influence of absorption (and scattering) by any particles within the volume. Light I_0 is emitted from a source (the Sun) at a wavelength λ , having passed through a medium of interest (the atmosphere, with a thickness dimension L), the intensity of light sampled by a detector (be it the eye or a spectrometer) ($I(\lambda)$) exponentially decreases as a function of scattering and absorption by molecules (σ) of concentration c :

$$I(\lambda) = I_0(\lambda) \cdot \exp(-\sigma(\lambda) \cdot c \cdot L). \quad (3.3)$$

The quantity of absorbing medium c , can be derived assuming the other quantities are known:

$$c = \frac{-\log\left(\frac{I_0(\lambda)}{I(\lambda)}\right)}{\sigma(\lambda) \cdot L}. \quad (3.4)$$

Where the logarithmic ratio of the original emitted light, to that of the light after passing through the absorber, is also known as an absorber's optical density τ , along the measured line of sight:

$$\tau = -\log\left(\frac{I_0(\lambda)}{I(\lambda)}\right). \quad (3.5)$$

3.2 Differential optical absorption spectroscopy

Using the Beer-Lambert law as a basis, it is possible to separate a measured UV absorption spectrum into broadband and narrowband components, allowing the identification of trace gas 'fingerprints' and their concentrations. Known as the differential optical absorption spectroscopy (DOAS) technique (Platt, 1994), the method is applied in this work for deriving CH₂O concentrations in the troposphere.

The basic concept of spectroscopic measurements for absorbing particles uses the optical density τ of a measurement to derive c . Scattering and absorption processes effected at wavelength λ are known from the properties of σ . For measurements taken in the open atmosphere, τ is difficult measure accurately due to the effect on the measured spectrum by an unknown quantity of absorber and aerosol scatterers extraneous to the desired trace gas measurement. Therefore, equation 3.3 is extended to include multiple absorbers c_j , light extinction due to Rayleigh and Mie scattering ($\epsilon_R(\lambda)$ and $\epsilon_M(\lambda)$), as well as additional effects imparted by the measurement device ($A(\lambda)$):

$$I(\lambda) = I_0(\lambda) \cdot \exp\left[-L \cdot \left(\sum(\sigma_j(\lambda) \cdot c_j + \epsilon_R(\lambda) + \epsilon_M(\lambda))\right)\right] \cdot A(\lambda). \quad (3.6)$$

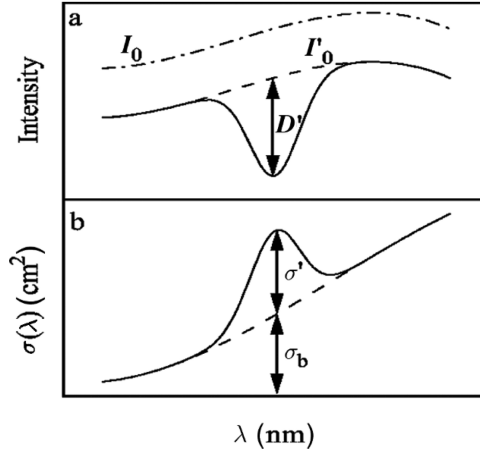


Figure 3.2: DOAS fitting principle (Figure 6.3, Platt and Stutz (2008)), with I_0 and σ separated into narrow and broadband components.

However, this extended Beer-Lambert equation still fails for remote sensing measurements of the atmosphere, as we have a measurement incorporating the sum of several absorbers, and for measurements from space, radiation is modified by the albedo of the surface it has reflected from back towards the sensor. To overcome these issues the differential portion of the DOAS technique is applied, comparing the intensity of light measured at multiple wavelengths with trace gas absorbers at the same wavelengths, themselves identifiable and separable by their unique wavelength dependent absorption cross section. To ease distinction between the various absorbers contributing to the measured spectrum, $I(\lambda)$ is separated into broadband ($\sigma_{j0}(\lambda)$) and narrowband components ($\sigma'_j(\lambda)$) (Figure 3.2). $\sigma_{j0}(\lambda)$ consists of smoothly varying ϵ_R and ϵ_M , whilst the high frequency $\sigma'_j(\lambda)$ spectrum represents the fine scale features of our expected absorption cross sections in the wavelength interval of interest, also known as the differential absorption spectrum.

Typically a low order polynomial designed to approximate $\sigma_{j0}(\lambda)$ is subtracted from $I_0(\lambda)$ to leave just $I'(\lambda)$ - the spectrum due to absorption processes. This allows the derivation of a differential optical density (τ'), providing the logarithmic ratio for the amount of I removed with σ_j (absorption processes), as well as removing

Fraunhofer structures in the Earthshine and Reference spectrums:

$$\tau' = \log \frac{I'_0(\lambda)}{I(\lambda)} = L \cdot \sum_j \sigma'_j(\lambda) \cdot c_j. \quad (3.7)$$

The concentration c of absorber $\sigma'_j(\lambda)$ is commonly calculated using linear regression (amongst other techniques), fitting laboratory measured absorption spectra to the narrowband $\sigma'_j(\lambda)$ spectrum. For multiple absorbers, fitting several absorption spectra ($\sigma'_{j_1 \dots j_n}(\lambda)$) over the same wavelength range to just one measured spectrum is made possible by differences in each absorbers absorption structure (Figure 3.1) at different wavelengths. In deriving c , we are able to arrive at a density for the absorber along the path L , which for satellite instruments, is typically an off nadir, slanted line of sight, referred to as a Slant Column Density (SCD):

$$SCD = \tau' / \sigma_j. \quad (3.8)$$

3.2.1 Passive DOAS application

Practical applications apply residual minimisation procedures such as linear least square fits, to reconcile the Earthshine spectrum measured looking down at the Earth from space ($I(\lambda)$) with quantities of trace gas absorbers, adjusting trace gas SCDs to reduce the fit residual to an absolute minimum. Spectrometers measure at a finite resolution, downgrading the recorded spectrum from a perfect representation, via passage through the instrument's optics and gratings in order to separate radiation into required wavelength intervals (the instrument line shape - ILS). Conversion of the analogue spectrum to a digital representation suitable for numerical analysis is performed via convolution with the instrument transfer function (ITF) at the ILS-ITF interface (H):

$$I^*(\lambda, L) = I(\lambda, L) * H. \quad (3.9)$$

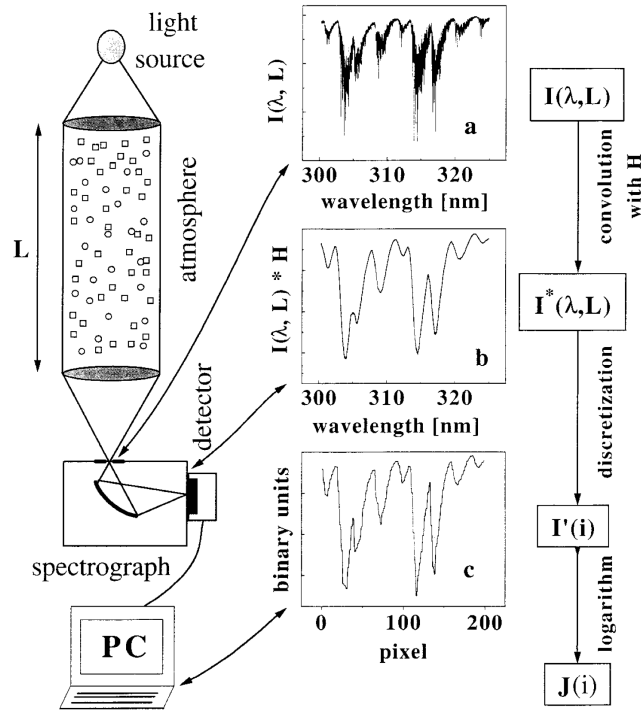


Figure 3.3: Convolution (H) and digitisation of a measured spectrum ($I(\lambda)$) over the light path L (Figure 1, Stutz and Platt (1996)).

This process assigns wavelength intervals of the measured range to individual pixels of the spectrometer detection array. Each pixel records the intensity of light integrated over its mapped wavelength range, according to its detector response (Stutz and Platt, 1996). Detector response over the whole detector array is denoted as the instrument line shape (ILS). Critical to the performance of an accurate DOAS retrieval is an accurate definition of H , which can change over short timescales (due to temperature variation in materials along the optical train) and significantly affect fitting accuracy when wavelength scales are not absolutely aligned with the spectrum being measured.

Instrumental dependencies such as the wavelength to pixel mapping, can be accounted for in the DOAS equation, where convolution of spectra by the ILS is now included, along with measured absorbers pressure (p) and temperature (T)

dependencies at point l along measured light path L , in a layer of thickness dl :

$$\begin{aligned}
I^*(\lambda, L) &= I(\lambda, L) * H \\
&= \int_{-\Delta\lambda}^{\Delta\lambda} I_0(\lambda - \lambda', L) \exp \\
&\quad \left(\int_0^L \sum_j (\sigma_j(\lambda - \lambda', p, T) \cdot c_j(l)) + \epsilon_R(\lambda - \lambda', l) + \epsilon_M(\lambda - \lambda', l) dl \right) \cdot (3.10) \\
&\quad \cdot H(\lambda') d\lambda'.
\end{aligned}$$

For the purpose of the DOAS retrieval, an integration over the entire atmospheric path L is safe to perform when the path of photons to the detector can be assumed to be linear within a scan, which is generally the case for clear sky situations. Finally, resolution of the light path L is required to account for scattering processes and instrument viewing geometry. The radiative transfer properties of L are largely unknown from the radiance measurement alone, instead requiring numerical solution of the scattering processes with the calculation of a scattering air mass factor.

3.2.2 Reference spectra

Parameters fitted to the narrowband differential absorption spectrum $\sigma'_j(\lambda)$ include absorption cross sections of trace gases expected in the measured wavelength range, modelled Ring spectra, and instrumental corrections, such as undersampling (section 3.4.4). Here, absorption cross section preparation and the Ring effect, common to all DOAS retrievals in the UV, are discussed. Instrumental corrections vary from instrument to instrument, therefore their discussion is omitted until examination of the instrument in use for this work.

Absorption cross sections

Formaldehyde exhibits a highly structured set of absorption features in the lower UV, between 320 and 360 nm. Figure 3.1 shows the interfering absorbers in this wavelength range which need to be accounted for in a CH₂O DOAS retrieval. These

cross sections were measured in laboratories, with equipment designed to capture the spectral detail at the highest resolution possible. For use in later retrievals, selected reference spectra should ideally be an order of magnitude higher in sampling than the resolution of the Earthshine measurement they are to be applied to (Platt and Stutz, 2008). The enhanced resolution of such lab measured spectra allows their application to a broad range of DOAS retrievals later on, regardless of the instrument transfer function for the space-borne instrument. In using lab measured reference spectra, care must be taken to ensure all spectra used in analysis (including Earthshine) are corrected to their equivalent wavelengths in a vacuum, and so account for wavelength shifting due to temperature and pressure within Earth's atmosphere (Edlén, 1966). For comparability between reference spectra and the measured spectrum, reference spectra must be downgraded to match the sampling of I , applying a convolution of the known instrument line shape to the reference spectra.

Wavelength to detector mapping

Knowledge of the central wavelength for each pixel in the detector array is essential for the matching of reference and Earthshine spectra (I). For spectral measurements from space, a rigorous interrogation of each pixel is not possible due to instrumental limitations. However a daily measurement of solar irradiance can provide the necessary quantification of wavelength to detector mapping. On emission from the Sun, light must pass through the solar atmosphere, where portions of the emitted radiation are removed by absorption in this region. A characteristic set of reductions in the solar spectrum were first noted by Joseph von Fraunhofer (1787–1826), with the solar line shape seen to be constructed of a number of very fine peaks and troughs. Correlation of a selection of these lines in smooth, man-made calibration light sources (from onboard lamps or LEDs), allows for alignment of the two measured light sources, thereby providing an accurate quantification of wavelength–detector mapping. Reference trace gas absorption spectra should not need calibrating in this manner, as in theory, they are perfectly aligned with a laboratory

calibrated absolute wavelength scale.

Remaining minor spectral mis-alignments due to the finite resolution of the measuring spectrometer, can be corrected in the DOAS retrieval procedure (Fayt et al., 2011). Introduction of shift and squeeze parameters to the wavelength–detector mapping allows adjustment of the wavelength grid to better suit the spectral measurement. Stutz and Platt (1996) estimate UV spectrometers distort the wavelength measurement grid by up to a tenth of a detector element per Kelvin, due to heating and cooling effects on the detector array. With the derivation of shift and squeeze parameters, wavelength grids of reference spectra (I_0 and absorbers) are adjusted to align their wavelength grids with that of the measured spectrum I . Neglecting to ensure wavelength grids are correctly aligned in this fashion is thought to introduce large errors into the DOAS fit, on the order of 50% in strong absorption cases (Stutz and Platt, 1996).

Ring effect

As already noted, transmission of solar spectra through Earth’s atmosphere subjects light to scattering processes, including Raman scattering. Raman scattering, as a function of solar zenith angle, acts to broaden and fill in distinctive Fraunhofer solar lines, as well as those of trace gas absorption spectra in the atmosphere. The process is more commonly referred to as the Ring effect, after the first accurate descriptor of the phenomenon (Grainger and Ring, 1962). Whilst other transmission processes such as aerosol fluorescence and Rayleigh-Brillouin scattering also add to the Ring effect, Raman scattering has been confirmed as the dominant mode in UV satellite spectra (Joiner et al., 1995; Vountas et al., 1998). The Ring effect contributes to a masking of absorption features (especially for weaker absorbers such as CH_2O), manifesting in an apparent decrease in retrieved trace gas slant column densities (Fish and Jones, 1995), as well as the introduction of systematic features in retrieval residuals.

To mitigate for this underestimation in slant columns, Ring correction mod-

els have been proposed which typically apply synthetic Ring spectra as pseudo-absorbers in the DOAS fitting procedure. Differences between corrections arise in the methods used to arrive at a synthetic spectra, and the accuracy with which they are able to replicate the atmospheric situation at the time of sampling. Wagner et al. (2001) summarise several different approaches to the correction, although only the Chance and Spurr (1997) and Vountas et al. (1998) procedures are seen to be applied in any great number for satellite trace gas retrievals.

With the former model, synthetic Ring spectra are generated by convolving a high resolution solar spectrum to the instrumental slit function, followed by a further convolution of this new spectrum with N_2 and O_2 rotational Raman spectra. From the ratio of the calculated spectra, and the original solar spectrum, a cubic polynomial of the calculated spectra is subtracted to yield a close approximation of the Ring effect. This method has proven particularly successful for improving minor absorber retrievals from GOME such as BrO (Chance, 1998) and CH_2O (Thomas et al., 1998; Chance et al., 2000).

The latter method employs the SCIATRAN Radiative Transfer Model (RTM) (Rozanov et al., 2005) to calculate the radiation field for any combination of atmospheric parameters (Vountas et al., 1998). Ring spectra are then derived for the logarithms of these radiances calculated with and without rotational Raman scattering. The method's greatest strength lies in the application of a principal components analysis to several Ring spectra generated over a range of atmospheric conditions (which in the case of satellite retrievals, is simplified to SZAs), for which the first two eigenvectors effectively represent the Fraunhofer filling and molecular absorption components of the Ring effect. Compared to the Chance and Spurr (1997) method, this technique is thought to offer a superior representation of the Ring effect due to modelling of the radiative transfer, particularly in the wavelength ranges susceptible to strong Fraunhofer absorption. The increase in accuracy possible with the Vountas method is perhaps reflected by the number of recent GOME-2 trace gas retrievals utilising the method; e.g. NO_2 (Richter et al., 2011), BrO (Theys et al., 2011) and

CH₂O (De Smedt, 2011).

Sensitivity of the Ring effect is not only limited to SZA, being highly dependent on cloud (De Beek et al., 2001), aerosol (Wagner et al., 2010) and trace gas climatology (Coldewey-Egbers et al., 2005). These parameters remain a major source of error in minor trace gas retrievals, as atmospheric conditions used in the Vountas method RTM for Ring cross section generation are generally set to model mid-latitude ocean scans.

3.2.3 Slant to vertical column conversion

Dealing with scattered light observations from passively sensed upwelling radiation introduces the requirement for a description of the path radiation has taken, directly related to the quantity L in the Beer-Lambert law. Radiation losses and enhancements along the measured line of sight are introduced by Mie scattering processes from clouds, aerosols and other in-elastic scatterers. Applying knowledge of atmospheric radiative transport to trace gas measurements allows arrival at the final quantity in the DOAS scheme, the vertical column density (VCD), representing trace gas concentrations integrated for a column extending upwards perpendicular to the surface at the point of measurement. VCDs are derived through application of a scaling factor known as the Air Mass Factor (AMF), representing the proportionality between the measured SC, and the value expected were it to have been measured in the zenith. The simplest AMF takes into account measurement geometry only, whilst more advanced models integrate reflection from the ground, Mie scattering by aerosol, cloud, and trace gas absorbers themselves (Palmer et al., 2001). AMF derivation is discussed in much greater detail later in this work (Chapter 5).

3.3 Space-borne remote sensing of trace gases

The Global Ozone Monitoring Experiment 2 (GOME-2) is the latest in a line of satellite-borne instruments designed to measure ozone from UV radiation backscat-

tered by Earth’s atmosphere and surface, the heritage of which can be traced to the 1980s. Whilst early instruments such as NASA’s Solar Backscatter Ultraviolet sensor (SBUV) and Total Ozone Mapping Spectrometer (TOMS) were designed with ozone monitoring as their primary task, spectral resolutions for these instruments prevented retrieval of minor trace gas species. Since then, and prior to the launch of MetOp-A, 3 nadir sampling UV spectrometers have been placed into orbit, operating in a similar fashion to GOME-2; all of which are detailed below.

3.3.1 GOME

A UV spectrometer developed by the European Space Agency (ESA) and partners delivered the improved spectral resolution required to retrieve minor trace gases displaying only weak spectral absorption signatures (Burrows et al., 1999b). Named the Global Ozone Monitoring Experiment (GOME), the passive across track scanning spectrometer sensed in the UV between 240–790 nm at spectral resolutions between 0.2–0.4nm, and a spatial resolution of 320×40 km². The instrument was launched aboard ESA’s ERS-2 satellite in April 1995, remaining fully operational until a tape drive malfunction in June 2003 rendered data obtainable only over ground stations, before satellite de-commissioning in July 2011. GOME provided data for continuous measurements of Ozone, NO₂, BrO, SO₂, and CH₂O throughout its lifetime.

Data from the instrument has formed the basis of a large number of CH₂O investigations, with the initial retrievals of Perner et al. (1997) and Eisinger et al. (1997) preceding the first published account of GOME CH₂O observations of a biomass burning event over Indonesia in 1997 (Thomas et al., 1998). Later work with the

Instrument (Satellite)	Overpass	Spatial resolution	Swath	Spectral resolution (CH ₂ O range)
GOME (ERS-2)	10:30	320×40 km ²	960 km	0.17 nm
SCIAMACHY (ENVISAT)	10:00	60×30 km ²	960 km	0.26 nm
OMI (Terra)	13:45	24–150×13 km ²	2600 km	0.5 nm
GOME-2 (MetOp-A)	09:30	80×40 km ²	1920 km	0.26 nm

Table 3.1: Specifications of GOME-2 and comparable UV sensors. Overpass refers to local equator overpass time of the satellite.

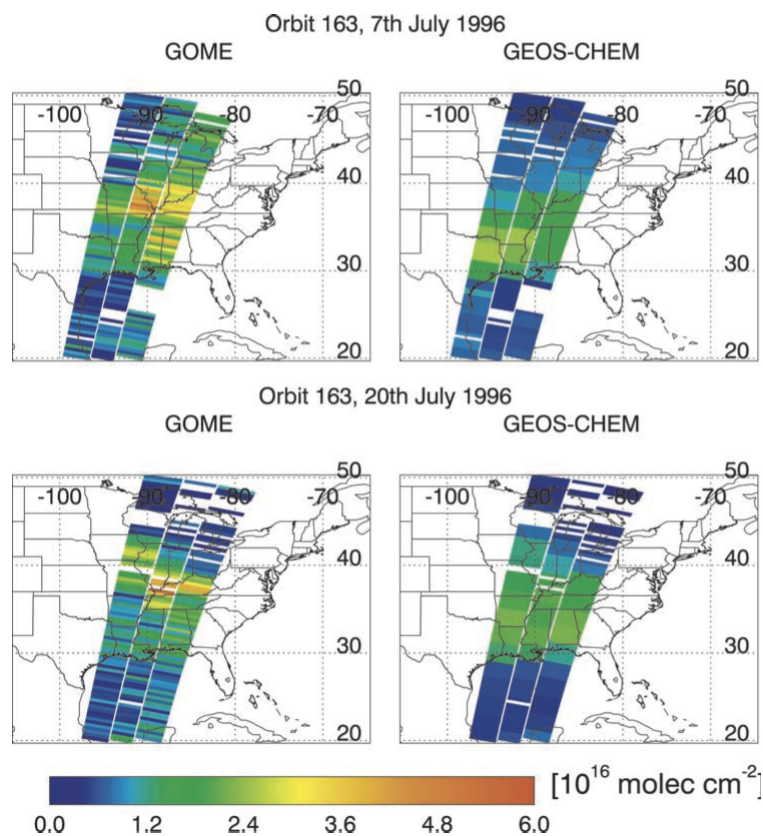


Figure 3.4: GOME-1 CH₂O vertical columns, and comparison to estimated vertical columns derived with a chemical transport model (Figure 7, Palmer et al. (2003)).

GOME dataset by Chance et al. (2000) incorporated major advances in the detection of minor absorbers, reducing fitting residuals on the CH₂O slant column fit to around 5×10^{-4} , with fitting precision of $< 0.4 \times 10^{16}$ molecules cm^{-2} . Following this reduction in retrieval error, the Chance et al. (2000) dataset found application in the work of Palmer et al. (2001), providing the first examples of a much improved air mass factor formulation (Figure 3.4). Improved conversion from slant to vertical column by the method allowed for the inversion of the GOME CH₂O dataset (Palmer et al., 2003; Shim et al., 2005) to provide continental scale top down isoprene emission estimates for North America (Palmer et al., 2006), South America (Barkley et al., 2008) and Asia (Fu et al., 2007). At a smaller scale, the instrument has found application to mapping of CH₂O shipping emissions in the Indian Ocean (Marbach et al., 2009), as well as separation of the biomass burning signal from background CH₂O (Marbach et al., 2008; Stavrou et al., 2009b).

3.3.2 SCIAMACHY

The former instrument essentially formed a precursor to the more capable SCanning Imaging Absorption SpectroMeter for Atmospheric CHartographY (SCIAMACHY) instrument, flown as part of the ENVISAT mission (Bovensmann et al., 1999). Launched in 2002, the instrument delivered data in nadir, limb and occultation scanning modes until loss of communications with the satellite ceased further activity in April 2012. Also operating in the across track scanning mode, SCIAMACHY followed GOME's specifications with a similar spectral resolution (0.2–1.5 nm) whose signal to noise ratio was greatly reduced compared to the earlier instrument in order to accommodate a faster scan for higher spatial resolution of $60 \times 30 \text{ km}^2$ in nadir mode.

Work by Wittrock (2006) and De Smedt et al. (2008) using spectral measurements from SCIAMACHY retrieved CH_2O to a precision of $\sim 1.0 \times 10^{16}$ molecules cm^{-2} for a single observation. The SCIAMACHY CH_2O product has been combined with the GOME CH_2O dataset in the work of De Smedt et al. (2008) to create a consistent 12 year dataset, which has seen its value added to in a similar fashion to that of GOME. At global scales, Stavrou et al. (2009c) inverted the dataset to produce estimates of biogenic and pyrogenic non-methane hydrocarbons, offering a comparison of emission inventories against the new dataset (Stavrou et al., 2009b). Regionally, Dufour et al. (2009) used the Wittrock et al. (2006) SCIAMACHY CH_2O columns in comparison with a chemical transport model for Europe, finding correlations in both magnitude and distributions between the datasets. Barkley et al. (2009) applied the De Smedt et al. (2008) dataset in a statistical analysis of the seasonal variability for isoprene emissions over South America, highlighting large scale leaf flushing of isoprene for rainforest vegetation in expectation of seasonal changes. The same dataset has also seen use in sensitivity studies of the error prone air mass factor calculation over South America (Barkley et al., 2011; Gonzi et al., 2011; Barkley et al., 2012a).

3.3.3 OMI

Designed and constructed by a Dutch and Finnish consortium, the Ozone Monitoring Instrument (OMI) (Levelt et al., 2006) features a CCD array of 60×1024 sensors, using the motion of its host spacecraft (NASA's Terra satellite, launched 2004) to impart along track movement. Its unique design gives a variable resolution for pixels extending away from nadir ($24 \times 13 \text{ km}^2$) to swath edges ($150 \times 13 \text{ km}^2$). At 0.5 nm, spectral resolution is poorer than that of GOME type instruments, although the instrument is still able to perform the same suite of trace gas measurements.

Retrievals with OMI data are typically made by non-linear direct fitting of radiances – a modification of the ‘classical’ DOAS technique presented above, whereby optical depth is directly fitted to measurement intensity (Chance, 2002; Kurosu et al., 2004). CH_2O slant column retrievals are available for the duration of the on-going OMI mission, with slant column uncertainties reported in the range of 40-100%. Much like the GOME and SCIAMACHY products, the OMI CH_2O product has found application to isoprene inversion schemes over North America (Millet et al., 2008), Tropical South America (Barkley et al., 2013), Africa (Marais et al., 2012) and Europe (Curci et al., 2010; Sabolis et al., 2011). OMI's high spatial resolution has also proven useful for regional pollution studies (Boeke et al., 2011), whilst OMI NO_2 datasets have been used to test significant improvements to the calculation of tropospheric AMFs for NO_2 (Zhou et al., 2009, 2010; Boersma et al., 2011; Russell et al., 2011).

3.3.4 GOME-2

Launched in October 2006, EUMETSAT's MetOp-A is the first in a series of polar-orbiting satellites expected to provide data continuity until at least 2020. As well as housing GOME-2, MetOp-A carries a suite of 12 other instruments, including the complimentary AVHRR imaging radiometer. In order to provide a continuous ozone and trace gas dataset consistent with preceding GOME and SCIAMACHY instruments, GOME-2 samples in the same spectral range, and operates in a similar



Figure 3.5: MetOp-A (source: Siddans et al. (2006))

sun synchronous orbit, circling the Earth every 101 minutes, with a local equator crossing time of 09:30 (Munro and Eisinger, 2006)

GOME-2 is a nadir viewing UV spectrometer, sampling the Earth’s backscattered radiation with 4 optical channels, and 2 Polarisation Measurement Devices (PMDs), all recorded by individual 1024 pixel silicon detector arrays, covering the 240–790 nm range (Table 3.2). Light is directed into the GOME-2 spectrometer by a cross track rotating mirror, routed via mirrors and prisms serving to diffract and redirect light into the 6 measurement channels, before gratings focus wavelength separated radiation onto their respective detectors (Figure 3.6) (Callies et al., 2000). Light is also siphoned off from the main UV-vis arrays towards the PMDs, which whilst not concerned with directly measuring Earthshine spectra, provide essential data for calibration of optical channel intensities.

The $\pm 57^\circ$ viewing angle range of GOME-2’s scan mirror permits a maximum

Channel	Spectral range (nm)	Detector pixel size (nm)	FWHM (nm)
1	240–314	0.12	0.26
2	310–403	0.12	0.27
3	397–604	0.21	0.51
4	593–790	0.21	0.48
PMD p	312–790	0.62 (312 nm)–8.8 (790 nm)	2.9 (312 nm)–37 (790 nm)
PMD s			

Table 3.2: GOME-2 spectral range and resolution (EUMETSAT, 2011b).

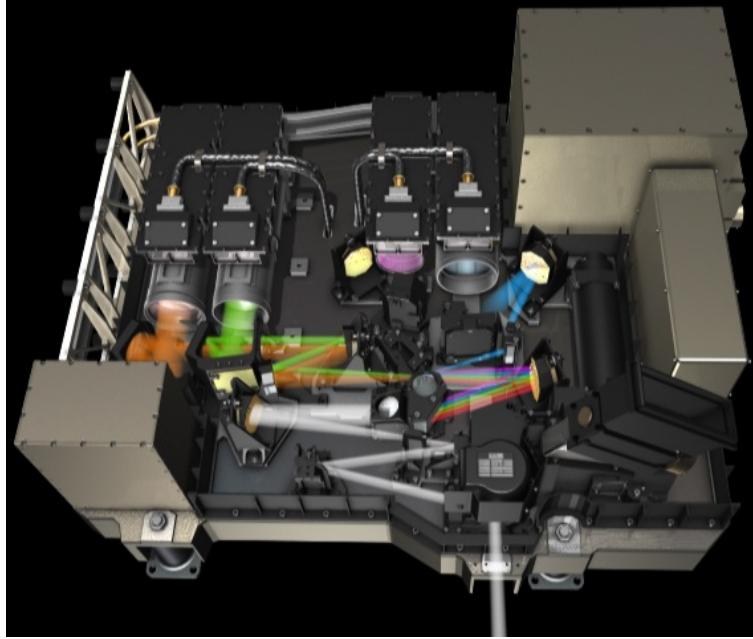


Figure 3.6: GOME-2 instrument (source: EUMETSAT (2011b)).

swath width of 1920 km, whilst adjusting detector integration times allow for variable pixel sizes depending on operational demands. In the regular nadir scanning mode, integration time is 187.5 ms for the main channels (1-4), giving a forward scan pixel size of 80 km across track, and 40 km along track, facilitated by the spacecraft's forward motion (with the exception of larger back scan pixels at $240 \times 40 \text{ km}^2$). PMD data are captured at twice the spatial resolution of the main channels, used for the instrument's cloud detection algorithm, allowing cloud discrimination at a sub pixel level (Wang et al., 2008; Loyola et al., 2011a).

Commonality in instrument design between the previous generations of European UV sensors, permitted the rapid development of a GOME-2 CH_2O product following launch. In this vein, early work by the BIRA research group (De Smedt et al., 2009; Lerot et al., 2009) built on GOME and SCIAMACHY DOAS retrievals (De Smedt et al., 2008), taking into account advances in GOME-2 BrO detection (Theys et al., 2011), as well as GOME-2's instrumental idiosyncrasies and degradation since launch, reporting SCD CH_2O fit standard deviations between $0.9\text{--}1.2 \times 10^{16} \text{ molecules cm}^{-2}$ (2007–2011). GOME-2 CH_2O data have been applied to evaluate ratios of CH_2O and the glyoxal molecule (CHOCHO), also produced

via VOC oxidation (Vrekoussis et al., 2010), confirming the co-location of both molecule’s sources and highlighting frequently enhanced CHOCHO emissions as a result of anthropogenic emissions.

3.4 Practical DOAS considerations

A number of instrumental shortcomings - inherent to all spectrometers - prevent a perfect resolution of the DOAS equation. Those applicable to GOME-2 are detailed here, along with appropriate mitigation procedures.

3.4.1 Instrument line shape

A spectrometer’s instrument line shape (ILS) represents the detector’s response to a signal of given intensity. Depending on the sensitivity of detector elements and optical dispersion elements (entrance slits and dispersion gratings), the full width half maximum (FWHM) of the ILS determines the resolution to which narrowband components of spectra can be recorded. Convolution of high resolution laboratory measured trace gas absorption cross sections with the ILS provides a representation of how the spectrometer is expected to record the absorption spectrum. Knowledge of this property is particularly important for the simulation of absorption spectra exhibiting narrowband components such as O_3 and CH_2O , which must be sampled with a high enough spectral resolution to discriminate absorption peaks from interfering absorbers.

Correct determination and application of an instrument’s ILS is a fundamental component of the DOAS procedure; use of an insufficiently characterised ILS for cross section convolution will yield erroneous DOAS fits, and inaccurate slant column densities (Van Roozendaal et al., 2002). With this in mind, the MetOp-A, B and C GOME-2 series of spectrometers were subjected to a rigorous sub-pixel ILS characterisation programme prior to launch (Siddans et al., 2006), modelling the response function of the majority of detector elements in each of its channels (Fig-

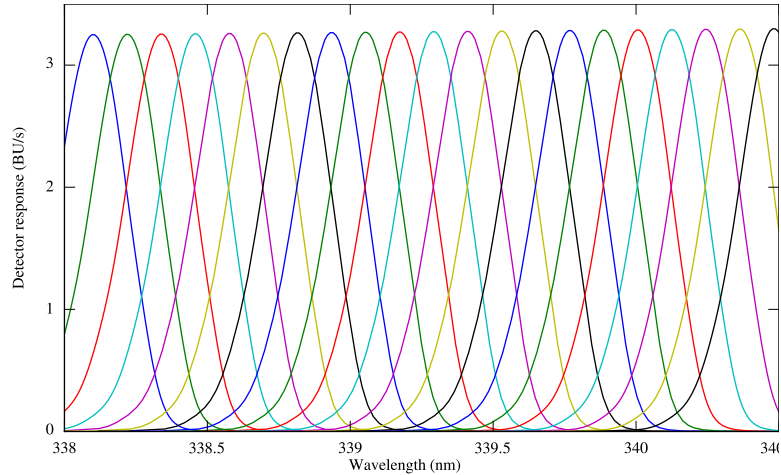


Figure 3.7: GOME-2 ILS for the inset wavelength range detailed in figure 3.8. Each line represents the response function of one detector element in the detector array, displaying approximately gaussian characteristics (colour variation is only present in order to distinguish between different detector elements).

ure 3.7). Results from this study showed the GOME-2 slit function in the CH_2O retrieval range to be asymmetric, with a wavelength dependence for both FWHM and the degree of asymmetry measured. Furthermore, significant inaccuracies in the wavelength calibration of the onboard calibration light sources (GOME-2 carries an onboard calibration lamp filled with argon and neon, whose absorption structures imprint several very well defined absorption lines upon the artificial calibration light source, with which to pinpoint detector pixel to wavelength mappings) were highlighted.

As no further in-depth spectrometer calibration is possible when the instrument is space-borne, this final finding was particularly important in addressing the need for careful calibration of the slit function in-flight. Estimating the ILS is performed in two steps, with an initial best guess slit function resolution (typically taken from Siddans et al. (2006)) used to provide a starting FWHM with which to minimise the χ^2 residual in an iterative fit between GOME-2 measured Solar irradiance, and a high resolution Solar reference (Chance and Kurucz, 2010) convolved at the estimated FWHM. This estimated FWHM is then used to define the wavelength dependent

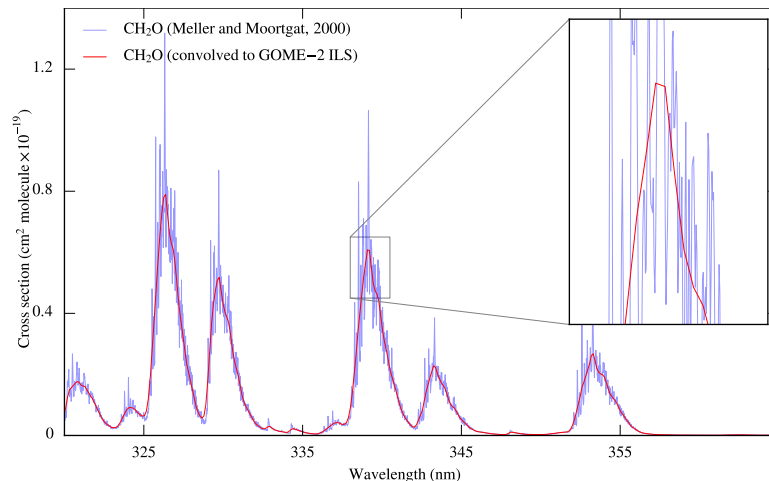


Figure 3.8: CH₂O before and after convolution to the GOME-2 ILS.

asymmetric slit function ($g(x)$), modelled by Cai et al. (2012) as:

$$g(x) = \exp\left(\frac{x^2}{((FWHM/1.66511) \times (1 \pm AF))^2}\right), \quad (3.11)$$

with x as wavelength difference and AF the dimensionless asymmetry factor representing the lean of the Gaussian, typically seen to vary in the range of ± 0.3 (De Smedt et al., 2012). An 8% reduction in slit function width has been noted between 2007–2011 using this method, suggesting slit calibration beyond the pre-flight measurement is essential to perform accurate retrievals. The current generation of space-borne UV spectrometers have spectral resolutions on the order of tens of nanometres, whilst lab measured cross sections are measured at the least to hundredths of a nanometre. Figure 3.8 shows the application of the pre-flight slit function to convolution of CH₂O absorption spectra, with high resolution CH₂O absorption spectra (in blue) down-sampled to match GOME-2’s spectral resolution, and mapped to the instrument’s wavelength grid, displaying an absence of fine scale structure previously captured.

3.4.2 Wavelength calibration

Wavelength calibration refers to the process of mapping individual detector pixels to the central wavelength of light being measured (Platt, 1994), usually derived from

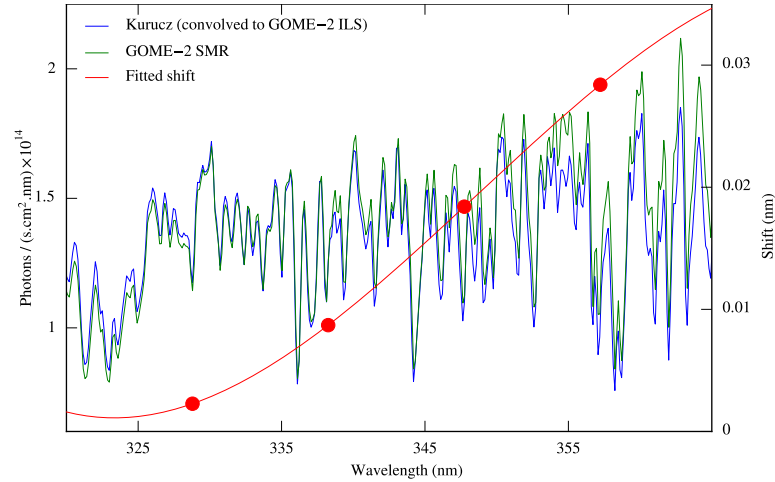


Figure 3.9: Wavelength shift calculated on the SMR for orbit 4176. Shift values are plotted as red circles (relevant to the right hand y axis), these are fitted by a linear least squares function intended to reduce the difference between GOME-2 SMR and Kurucz Solar atlas wavelength grids.

measuring well defined absorption lines in calibration light sources such as on board lamps, or from Fraunhofer lines in Solar spectra. Conducting an error assessment study on synthetic GOME-2 data at the instrument design stage, De Beek et al. (2004) identified wavelength calibration as the key source of error for trace gas retrievals with the forthcoming instrument. With a well characterised ILS, accurate wavelength calibration is essential for reducing the margin of error in DOAS retrievals, particularly for weak absorbers, where even small increases in measurement precision can translate into noticeable reductions in retrieval residuals.

It is assumed laboratory measured absorption spectra are perfectly aligned to the high resolution wavelength grid to which they are measured. This same level of wavelength grid alignment accuracy is not achievable with the space-borne UV spectrometer. Instrumental temperature variation as a function of the instrument’s illumination by the Sun along the orbital path, and degradation of spectrometer materials over the mission lifetime can lead to pixel–wavelength shifts, as found for the original GOME instrument (Coldewey-Egbers et al., 2008).

To mitigate for wavelength calibration issues, highly visible Fraunhofer structures present in the solar spectrum are used to align a high resolution solar spectrum (Chance and Kurucz, 2010) convolved to the GOME-2 ILS, to those present

in GOME-2’s interpretation of the solar spectrum. Solar spectra are measured by GOME-2 once daily at the Northern hemisphere terminator, GOME-2’s solar mean reference (SMR) is a doppler corrected mean of 32 scans taken whilst the instrument is switched to Sun observation mode (internal lights are deactivated and the solar port is opened) EUMETSAT (2011a). Originally defined for the GOME instrument (Caspar and Chance, 1997; Van Geffen and Van Oss, 2003), the recalibration process divides the fitting range of interest into several windows, each containing 30–40 pixels, whereupon a non-linear least squares fit is applied to minimise the χ^2 of the difference between GOME-2 and the convolved hi-resolution Solar spectra. Wavelength grids in each of the windows are fitted with a high order polynomial, whose first two terms represent the shift and squeeze required to align the two grids. With these two parameters estimated to the desired degree of accuracy, a reconstruction of the instrumental wavelength grid is possible from fitting a low order polynomial through the values ascertained for each fitting window, and shifting the I wavelength grid with the updated parameters (Figure 3.9).

3.4.3 I_0 effect

Absorption cross sections measured in the laboratory, are typically measured with a stable light source, therefore lacking distinctive Fraunhofer structures present in Solar and Earthshine spectra. This difference in light sources manifests in the DOAS retrieval as a series of systematic structures in the residual component of the fit (and a corresponding overall reduction in measured trace gas quantities), reflecting the omission of Fraunhofer features from fitted absorption cross sections.

Absolute mitigation for Solar I_0 effects are not possible given that both the Solar reference and Earthshine spectra are subject to the instrument’s slit function, and as such do not offer a perfect model of spectra (Aliwell et al., 2002). However, this effect can be corrected quite effectively by generating synthetic cross sections with a maximum amount of the absorber artificially included in the absorption spectrum (Johnston, 1996). A high resolution Solar reference is convolved to the instrument’s

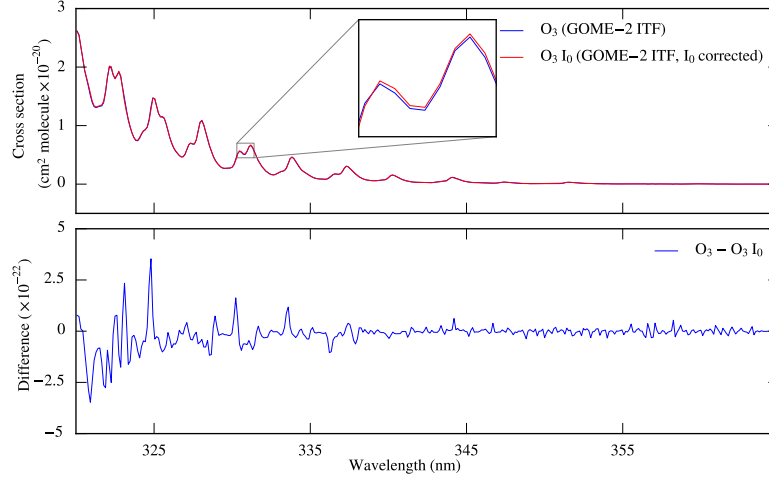


Figure 3.10: Top plot details I_0 corrected O_3 absorption cross sections, whilst the bottom plot shows the difference between I_0 corrected and uncorrected spectra.

slit function (I_0^*); the convolution is repeated for the trace gas absorption cross section of interest (I^*), incorporating a modelled quantity of the absorber (SC). Following Wagner et al. (2001); I_0 corrected cross sections (σ_{corr}) are then derived from the negative logarithm of the ratio of the two new spectra (also see Figure 3.10):

$$\sigma_{corr}(\lambda, SC) = \frac{-\ln\left(\frac{I^*(\lambda)}{I_0^*(\lambda)}\right)}{SC}. \quad (3.12)$$

3.4.4 Undersampling

With digital spectrometers limited in the spectral resolution to which they can measure, spectra are fully sampled only if the spectrum is recorded to twice the maximum wavelength frequency. If this is the case, spectra may be resampled to another wavelength grid with no reduction in information content. If these sampling conditions are not met, measurements between samples are aliased resulting in systematic fitting residuals in the DOAS retrieval – particularly in wavelength regions with a small optical depth. GOME-2 was designed to oversample spectra to 2.16 samples per FWHM; Table 3.1 shows detector pixels in channel 2 account for 0.12 nm of the spectra each, with a FWHM of 0.27 nm. The pre-flight ILS detailed in

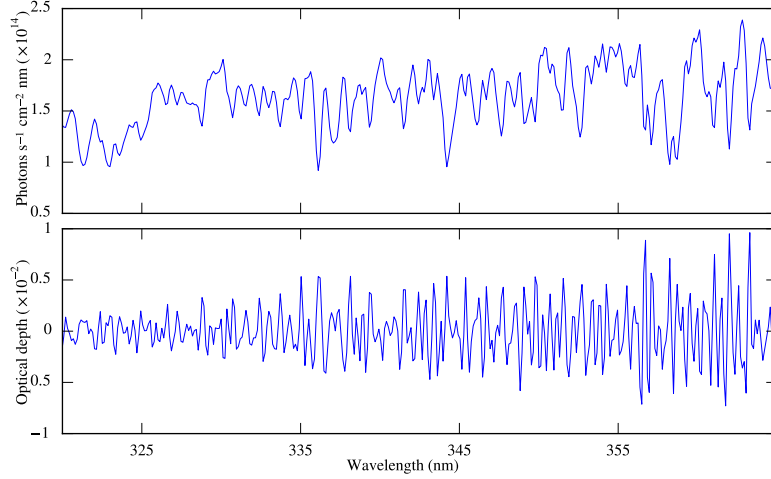


Figure 3.11: GOME-2 undersampling cross section generated following the method of Chance et al. (2005) (lower plot). Top plot shows the Solar atlas convolved to the GOME-2 slit function. As the information content of the Solar signal increase with wavelength, GOME-2 is less able to capture all the features, and so the amplitude of the undersampling spectrum correspondingly increases.

Figure 3.7 show spectral resolution over the detector range varies, in the middle of our CH_2O fit range, sampling corresponds to approximately 2.05 measurements per FWHM. Further minute wavelength shifts of the spectrometer in orbit due to spectrometer temperature variation introduce the potential for spectral undersampling, especially towards the upper limit of the CH_2O fit window where the sampling ratio approaches 2.

Chance (1998) developed a method to approximate spectrometer undersampling as a pseudo-absorber in the DOAS retrieval, detailed in Figure 3.11. Derived following the notation of (Chance et al., 2005); first a high resolution Solar atlas (Chance and Kurucz, 2010) is convolved to the spectrometer's ILS (I_0^*). This oversampled representation of the Solar spectrum is then interpolated to both the irradiance grid g_{irr} to give a fully sampled representation (I_{0irr}^*); and the instrument's wavelength grid g_{rad} , yielding an undersampled representation I_{0rad}^* . I_{0irr}^* is interpolated to the original Earthshine wavelength grid g_{rad} to obtain I'_{0rad} . The final undersampling spectrum C_u is realised as the difference of I_{0rad}^* and I'_{0rad} , scaled to the appropriate

optical depth by the mean of I_{0rad}^* :

$$C_u(\lambda) = \frac{I_{0rad}^*(\lambda) - I'_{0rad}(\lambda)}{\bar{I}_{0rad}^*(\lambda)}. \quad (3.13)$$

3.4.5 Radiometric degradation

The original GOME spectrometer suffered from severe instrument degradation due to a diffuser plate artefact affecting radiance measurements, and required application of a number of correction techniques to allow retrievals of weak absorbers (Richter and Wagner, 2001). With this in mind, GOME-2 was constructed with an improved diffuser plate – although radiance measurement degradation has still been encountered, significantly affecting the accuracy of GOME-2’s trace gas retrievals. At least two factors are combining to cause loss of light throughput from instrument degradation. De-gassing of sealants on printed circuit boards and microchips, and degradation of mirror coatings are thought to have encouraged the accumulation of an absorbing layer on internal instrument optics (Cai et al., 2012). This loss of throughput bears a strong influence on the ability to perform a precise CH₂O retrieval, reliant on the recording of a strong Earthshine spectrum to compare the very weak CH₂O absorption signal against. Further to this, the slit function is seen to alter following launch, possibly due to GOME-2’s detectors creeping towards the focal plane as a result of changing temperatures (Dikty and Richter, 2011).

Degradation of the spectrometer bears implications for what was previously a well characterised instrument line shape, causing an imperfect convolution of absorption spectra to be used in trace gas retrievals. These effects have resulted in scanner angle and wavelength dependent biases increasing from the beginning of the mission, with irradiance throughput decreasing at an average of 20% per year, further accelerated by a mid-flight decontamination test carried out in September 2009, removing an additional 15% of throughput (EUMETSAT, 2009; Dikty and Richter, 2011). Degradation is most noticeable when comparing the positive and negative scanner angles, indicating throughput on the eastern side is significantly

lower than found for the west.

EUMETSAT intend to develop an L1C GOME-2 product, removing instrument degradations (EUMETSAT, 2012), but for the time being, corrections are left to the user. To mitigate for the scan angle bias, EUMETSAT recommend the fitting of two correction factors (Eta and Zeta) measured pre-flight, as pseudo absorbers in DOAS trace gas retrievals (EUMETSAT, 2009). Following work characterising the in-orbit instrument degradation (Dikty and Richter, 2011), the recommended correction for the weakening intensity throughput is to apply a daily reference sector correction, to remove the intensity dependence of weak absorber retrievals. The method for the reference sector correction takes slant columns from a latitudinal reference strip of ‘clean’ Pacific air between 140–160° W longitude, representing a constant local time due to MetOp-A’s sun-synchronous orbit, and fitting a 3rd order polynomial through the latitudinal axis. CH₂O concentrations in this Pacific Ocean region are representative only of global background levels generated by methane oxidation, avoiding continental enhancements. Latitude-dependent fitted slant columns from this strip are then subtracted globally from each day’s measurements to serve as a daily correction. Also known as the reference sector method (RSM), the technique was originally developed for stratospheric correction of NO₂ retrievals (Martin et al., 2002; Richter and Burrows, 2002).

Aside from the general RSM technique, several research groups have developed further corrections specific to individual instrument degradation factors. Cai et al. (2012) applied a re-calibration of GOME-2 measured reflectances based on measured and radiative transfer model generated radiance differences, taking into account wavelength, scan angle and SZA dependency of degradations. This thorough modelling of radiance degradation has been applied in GOME-2 SO₂ retrievals, showing an effective reduction in scan angle dependent bias, and reducing the product’s latitudinal dependence (Nowlan et al., 2011). In addition to radiance degradation corrections, the GOME-2 ILS is recommended to be re-calibrated on a per-orbit basis; whereby fitting a new asymmetric wavelength dependent slit function corrects for a

narrowing slit function throughout GOME-2's lifetime (Cai et al., 2012; De Smedt et al., 2012). For ozone total column retrievals with GOME-2, Loyola et al. (2011b) calculated an empirical correction function based on latitudinal means of GOME-2 ozone for 2007–2008, correcting retrieved ozone values as a function of scan angle, time, and latitude; almost completely eliminating scan angle bias in the process.

3.5 Summary

Radiation emitted from the Sun undergoes a variety of scattering and absorption processes. In the photosphere, these impart a series of distinctive absorption lines in the Solar spectrum known as Fraunhofer lines. In the Earth's atmosphere, absorption and scattering by suspended molecules give rise to an Earthshine signal constructed of several absorption structures, depending on interaction with interfering molecules along a photon's path. Interfering molecules typically exhibit a unique absorption structure depending on their propensity to absorb and scatter radiation at certain wavelengths.

The Beer-Lambert law, in conjunction with this unique absorption structure, can be used to identify the absorbers in Earthshine spectra. The differential optical absorption spectroscopy technique is used to separate broadband atmospheric scattering processes such as Rayleigh scattering, from narrowband signals caused by trace gas absorption. Absorber concentrations are quantifiable with this method, applying mathematical fitting methods to minimise residual components in a DOAS retrieval to fit quantities of an absorber to best match the measured spectra. DOAS retrievals require careful selection of wavelength fitting region in order to minimise conflict with ancillary absorbers. Further consideration must be given to spectrometer characteristics, particularly pixel–wavelength mapping, and an accurate resolution of the Ring term. The final, critical component of a DOAS retrieval entails the conversion of the SC measured along the instruments line of sight, to a vertical column to allow compatibility and comparability between measurements.

Remote sensing of trace gases from space via the DOAS method, was first realised

with the original GOME UV spectrometer, launched in 1996. Since then, launch of the similar SCIAMACHY and OMI instruments have provided data to allow the construction of a continuous trace gas dataset time-series. Building on this heritage, the launch of GOME-2 in 2006, and its successors aboard MetOp's B and C over the coming years, are expected to provide data continuity until at least 2020. CH₂O columns derived with these instruments have found use in a variety of regional pollution and global VOC budget studies.

The bulk of the work presented here makes use of spectra recorded by GOME-2, for which several adaptations to the classical DOAS technique need to be made due instrumental issues. As with all spectrometers, an accurately defined instrument line shape must be applied to measurements so to best match measured Earthshine, and reference absorption spectra. Whilst GOME-2's slit function was thoroughly characterised pre-flight, there remains the necessity for constant re-calibration of the slit against a high resolution Solar spectrum to model a narrowing asymmetric slit. The wavelength-pixel mapping of GOME-2 exhibits in-orbit shifts due to temperature variation along the orbital path, which needs accurate resolution via further calibration to preclude the introduction of unwanted residuals in the DOAS due to Earthshine / absorber reference spectral mis-alignment. Solar I₀ effects and under-sampling must also be considered, especially so given the weakness of the CH₂O absorption signal when compared against the stronger absorbers in the same wavelength fit range. Mitigation is required for the significant degradation in quality of spectra from GOME-2 since launch, with a reduction in instrument throughput, and scan angle dependent biases present in recorded spectra.

Chapter 4

DOAS Parameter Testing

Despite a heritage of CH₂O monitoring from space, CH₂O column retrievals still remain less well characterised when compared to major absorbers such as ozone (e.g. Van Roozendael et al., 2002; Balis et al., 2008; Loyola et al., 2011b) and nitrogen dioxide (e.g. Boersma et al., 2004; Richter et al., 2011; Valks et al., 2011). This work attempts to address this issue by presenting a detailed assessment and characterisation of GOME-2 CH₂O retrieval uncertainties. Increased accuracy of the CH₂O column product improves confidence in its use for testing models of surface emissions.

In the analyses that follow, a default reference retrieval described in Table 4.1 is adjusted one setting at a time to determine the sensitivity of the DOAS retrieval within a range of optimised settings. Sensitivity is analysed with reference to the retrieved CH₂O column, 1σ standard deviation of the CH₂O column, and reduced χ^2 . We use the χ^2 statistic as a measure of the goodness of fit for retrievals, with χ^2 reducing towards a minimum limit of estimated noise as fit quality increases. This is output directly from QDOAS following Equation 5 in Fayt et al. (2011):

$$\chi^2(a_i) = \frac{(y(a_i) - y) \times (y(a_i) - y)}{M - N}, \quad (4.1)$$

where χ^2 is calculated as the difference between our observations (y) and the function $y(a_i)$ representing our model of the observation. a_i represents each parameter N ,

Parameter	Setting
Fit window	BrO 328.5–359 nm (Theys, 2010) CH ₂ O 328.5–346 nm (De Smedt, 2011)
Polynomial	5th order
Cross sections	BrO (223 K) (Fleischmann et al., 2004) CH ₂ O (298 K) (Meller and Moortgat, 2000) NO ₂ (220 K) (Vandaele et al., 1998) O ₃ (228 and 243 K) (Malicet et al., 1995) (I_0 corrected using 0.8×10^{19})
Linear offset	1st order
Ring	Vountas et al. (1998), Rozanov et al. (2005)
Undersampling	Chance et al. (2005)
Scan bias	Eta and zeta polarisation vectors (EUMETSAT, 2011a)
Slit function	Siddans et al. (2006)
Solar reference	GOME-2 daily solar mean reference
I_0 calibration	Caspar and Chance (1997)

Table 4.1: Default retrieval settings used in the sensitivity analysis, based on De Smedt (2011). Differences to the original retrieval are the inclusion of an undersampling cross section, and exclusion of an OCIO fit.

with M the number of data points (e.g. the number of instrument pixels providing observations within the wavelength fitting region); therefore $M - N$ accounts for the degrees of freedom allowed in the fit. This has the advantage over a basic analysis of fitting residuals in that any extra degrees of freedom allowed by the inclusion of extra fitting parameters are accounted for.

The chosen reference retrieval settings are largely based on the initial GOME-2 CH₂O characterisation of De Smedt (2011). By analysing the ensuing parameters with respect to the reference retrieval, differences in slant columns are attributed to systematic effects imparted by each parameter adjustment. The random error component of the retrieval (or the noise in GOME-2 measured Earthshine spectra) is reduced by analysing a monthly mean rather than individual orbits.

The DOAS retrieval itself is performed using the QDOAS analysis software (Fayt et al., 2011), prior to which trace gas cross sections listed in Table 4.1 are corrected to vacuum wavelengths (where appropriate), and convolved with the GOME-2 slit function measured pre-launch (Siddans et al., 2006), using the daily Solar Mean Reference (SMR) wavelength grid taken from the relevant L1B orbit file. Ozone cross sections are corrected for the I_0 effect (Aliwell et al., 2002). Shift and stretch

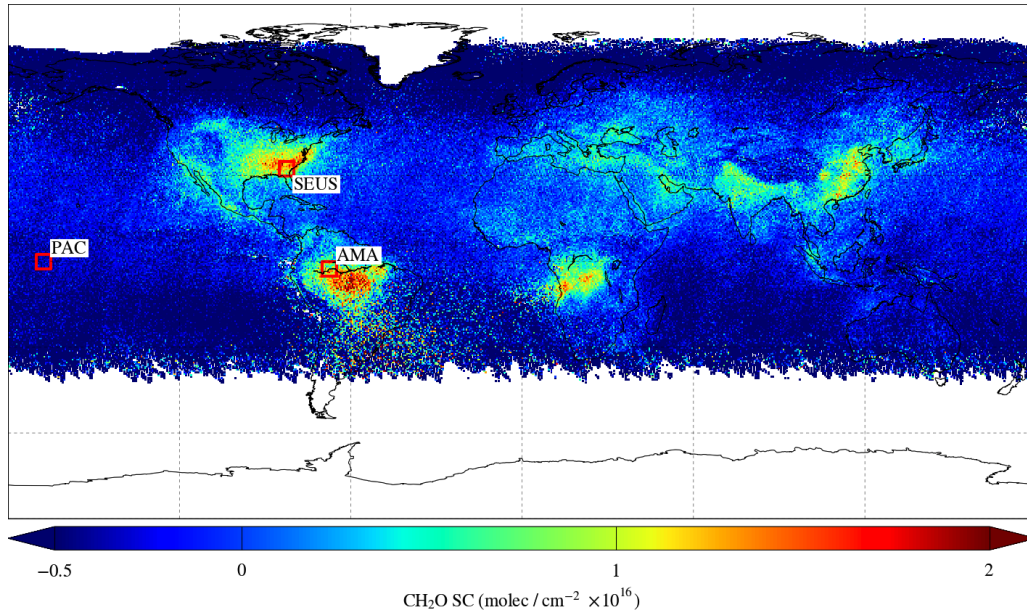


Figure 4.1: Monthly mean CH_2O slant columns for August 2007 retrieved using the default algorithm settings (Table 4.1). The data are averaged onto a $0.5^\circ \times 0.5^\circ$ grid excluding observations with cloud fraction > 0.4 and solar zenith angles $> 60^\circ$.

parameters are applied to Earthshine spectra, accounting for a very small error contribution from Doppler shift due to spacecraft and planetary motion. An improved wavelength calibration for the GOME-2 SMR I_0 reference is employed to further increase the accuracy of wavelength to pixel mapping in order to further reduce fit residuals arising from mis-alignment of Earthshine and reference absorption spectra (Caspar and Chance, 1997; Van Geffen and Van Oss, 2003). Post-processing is initially limited to discarding observations with cloud fraction > 0.4 and solar zenith angles (SZA) of $> 60^\circ$. Monthly mean CH_2O slant columns for August 2007, generated with this reference retrieval, are shown in Figure 4.1. A sample DOAS fit for a region of enhanced isoprene emissions over the southeast US (see Palmer et al., 2003) is presented in Figure 4.2. Global results are complemented by a detailed analysis for three $5^\circ \times 5^\circ$ sub-regions (detailed in Figure 4.1) to examine regional effects potentially masked in the global statistics. Sites chosen reflect the range of CH_2O column concentrations expected to be retrieved: (1) the remote Pacific Ocean (PAC) providing a clean reference in which only background concentrations of CH_2O are expected, (2) the southeast United States (SEUS) at the height of the regional growing season (August), and (3) a portion of the Amazon rainforest (AMA) where

large CH₂O enhancements due to high biogenic emissions occur (Barkley et al., 2008). Results for all sites are given as means over their respective geographic area.

4.1 DOAS parameter sensitivities

Sensitivity test results are presented towards the end of this chapter in Table 4.4, to which the reader is referred by test numbers in-line and their corresponding descriptions. The sensitivity tests are divided into three groups: (1) spectral fit range, (2) spectral fit approaches, and (3) instrumental corrections. Following this, effects due to post-processing of slant columns are discussed in Section 4.3. Analysis of each setting accompanies the description of its influence on the retrieval.

4.1.1 Spectral fit range

Selection of an appropriate fitting window is known to be a major component of achieving an accurate DOAS fit, particularly for weak absorbers (Aliwell et al., 2002). Fit problems are prone to arise when different trace gas absorption features overlap, with weakly absorbing spectra (CH₂O, BrO) masked by stronger absorbers (O₃, Ring). CH₂O is typically retrieved in the lower end of the UV between 325 and 360 nm (Wittrock et al., 2000; De Smedt et al., 2008). A large degree of overlap between absorption cross sections is evident in this region, therefore the choice of fitting window immediately presents two problems which must be overcome to effect a reliable CH₂O retrieval: (1) accurate retrieval of O₃ in the lower reaches of the fitting window, and (2) reduction of a false detection relationship between BrO and CH₂O. Here, a selection of fit windows relevant to the GOME-2 fitting range, and used throughout the literature, are tested.

BrO pre-fit

The pre-fitting technique has been used in GOME-1 and GOME-2 retrievals (Chance et al., 2000; De Smedt et al., 2012) to counter the effect of spectral similarities be-

tween BrO and CH₂O. BrO is first retrieved in a wide wavelength window (328.5–359 nm), using the same settings and spectra as found in the regular CH₂O fit. The second step of the fit fixes the BrO SCD in the CH₂O fitting window at the value retrieved in the first interval, whilst all other parameters are fitted as usual. This two step fit effects a de-correlation between the spectrally similar BrO and CH₂O absorption cross sections, with the intention of stabilising the retrieval, and increasing the signal to noise ratio in the CH₂O SCD fit (M. Van Roozendael, personal communication, 2013).

Testing the inclusion of scan bias correction terms (EUMETSAT, 2011a) in both BrO and CH₂O fit windows shows no discernible difference compared to scan correction in the BrO window alone, therefore in order to reduce the number of fitted parameters, corrections are applied to the BrO window only. Based on the GOME-2 BrO retrievals as implemented in Theys et al. (2011), a slightly narrower BrO fit window is tested here in the 332–359 nm region, both with and without inclusion of the additional absorber OCIO (as implemented in the retrieval of Theys et al. (2011)). In the first instance, test 1a adjusts the BrO fit window alone to give a global CH₂O slant column mean increase of 0.06×10^{16} molecules cm⁻², largely reflecting the increase over oceans of the same value, with a very small reducing effect on fit χ^2 . Including OCIO in test 1b increases CH₂O slant column means further ($+0.15 \times 10^{16}$ molecules cm⁻²) globally, with AMA showing a more pronounced increase than for 1a, although less so than the SEUS and PAC regions whose values are proportionally increased more by adjusting the BrO fit window. Inclusion of OCIO in both BrO and CH₂O fit windows is tested further on in the study, but it should be noted that fit quality exhibits a tendency to increase in parallel with additional fitting parameters. In the case of including OCIO here, whereby distributions of the additional absorber should be expected only on regional scales at high latitudes during the polar springtime (Kühl et al., 2006), fit quality is increased, but in an erroneous fashion.

Taking the pre-fitting concept further, Chance et al. (2000) have previously ap-

plied a three-step fitting procedure to GOME-1 data, fixing both BrO and O₃ in the CH₂O window to pre-fitted values from preferential fitting windows. Test 1c applies this method with an O₃ pre-fit in the 325–335 nm window (using the basic O₃ retrieval settings from Loyola et al., 2011a), along with the default BrO pre-fit detailed above. This two-way pre-fit offers a slight increase in CH₂O slant columns and fit χ^2 , suggesting for GOME-2 that the application of a further pre-fit is not worth the extra computation required. It should be noted, however, that the extra fit windows applied for the pre-fits are in a slightly different wavelength range to that of the CH₂O retrieval, particularly so for the extra O₃ pre-fit. Whilst slant columns for these extra absorbers are optimised with the intention of yielding a more accurate retrieval than found with the CH₂O fit window alone, the subsequent value passed into the CH₂O section of fitting is likely to be a different slant column than would have been found with the CH₂O specific window, thereby modifying the CH₂O slant column as a function of this difference. One method which may alleviate some of these issues would be the application of a weighting function DOAS (WF-DOAS) type algorithm, accounting for the wavelength dependency of the various absorbers included in the fit (Buchwitz et al., 2000). Having been successfully applied to UV retrievals of O₃ from GOME spectra (Coldewey-Egbers et al., 2005), application of WF-DOAS to minor absorbers in the UV has also shown promise, with successful retrievals of SO₂ from SCIAMACHY data proving its efficacy (Lee et al., 2008). Application of the technique to CH₂O retrievals is reserved for a future study, with the methodology requiring significant modifications to the DOAS retrieval setup in use.

Margins between differing BrO pre-fit windows are small, in terms of both retrieved CH₂O slant columns and fit residuals. Given the slightly higher CH₂O slant columns and very small increases in fit quality found with test 1a, adjusting the pre-fit window to the new range may well appear justified, in line with Theys et al. (2011) findings of an improved BrO fit in this region. In relation to the pre-fit wavelength dependence interplay, by discarding spectra taken at a SZA of $> 60^\circ$,

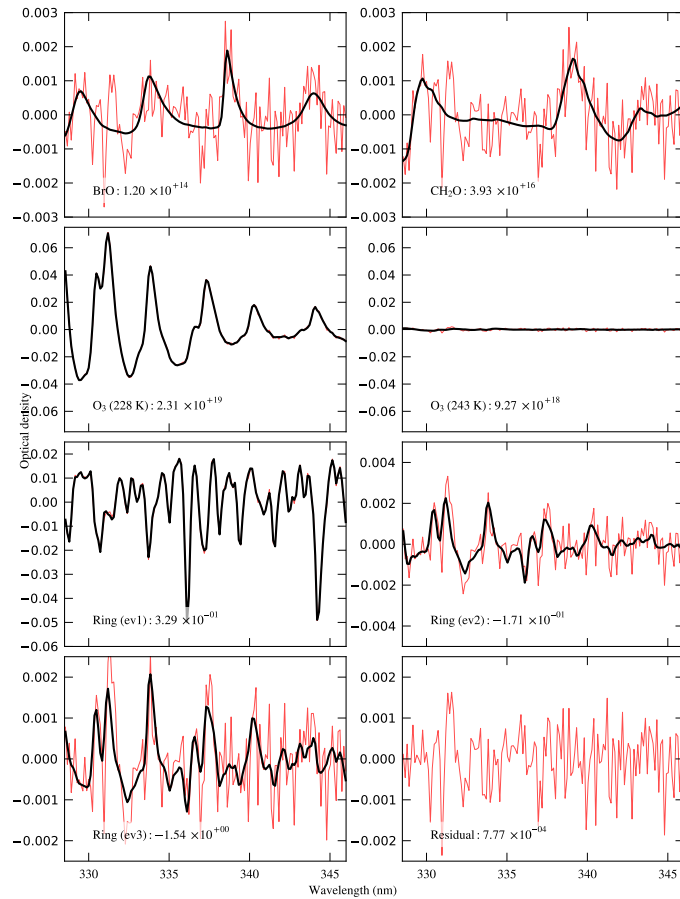


Figure 4.2: Example CH_2O fit using the reference retrieval settings for an enhanced CH_2O plume over the southeast USA on 9 August 2007 (scan 3107, orbit 4176, SZA 28.8°). NO_2 , Ring, undersampling, polynomial fit, and linear offset are omitted from the plot but included in the fit; slant column units are in molecules cm^{-2} .

the issues of spurious BrO and/or O_3 values modifying the CH_2O fit are mitigated for, given the proportionally reduced columns of these absorbers typically expected in the latitudes covered by a SZA $< 60^\circ$.

CH_2O

Shown in Figure 4.3, the dependence of retrieved slant column and its error on the chosen fit window is demonstrated by repeatedly performing a DOAS fit on a single GOME-2 scan (covering a region of strong CH_2O emissions), incrementally adjusting the upper and lower fit window limits with a 0.5 nm step. Minimised fit residuals (the remaining spectrum following the fitting of the modelled spectrum to our measured Earthshine spectrum) are found with the lower fit limit at wavelengths

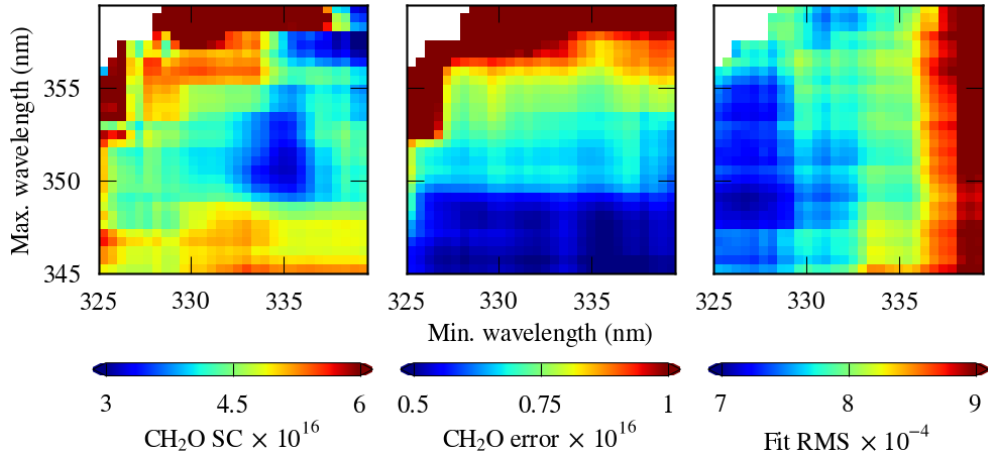


Figure 4.3: This surface plot (scan number 3107, orbit 4176) takes the reference retrieval and adjusts the upper and lower limits of the CH₂O fit window in 0.5 nm increments, revealing the large variations in slant column and concurrent errors to be found within the CH₂O fitting window. Note areas of low slant column error and fit RMS coincide well with the baseline retrieval window of 328.5–346 nm on the x and y axis, respectively. Differences between CH₂O error and fit residuals are suggested to be attributed to variation in the error covariance matrix as the fit boundary is adjusted (M. Van Roozendael, personal communication, 2012).

<329 nm, coinciding with the second major CH₂O absorption peak in the fit range, whilst slant column error serves to provide an estimate of the upper window cut-off, displaying a band of error minima in the 345–349 nm region.

In test 2a we retrieve in the 325.5–350 nm fit range used by Marbach et al. (2010), taking in the strongest CH₂O absorption peak available (326 nm) in the UV as well as an extra BrO peak towards the visible. Whilst fitting in this region is seen to substantially increase CH₂O slant columns ($+0.57 \times 10^{16}$ molecules cm⁻² globally), fitting quality becomes poorer by 1.95×10^{-7} , pointing towards significant amounts of spectral interference from the wider band of strong O₃ absorption in the lower UV. A newly proposed fit region, 332–350 nm is tested for test 2b, with the intention of avoiding the largest O₃ absorption in the lower fit range. This sees a global reduction on CH₂O slant columns of -0.08×10^{16} molecules cm⁻², along with noticeable increases in χ^2 (1.23×10^{-7} globally); suggesting exclusion of the CH₂O absorption peak around 330 nm imparts a significant negative effect on retrievals, providing an insufficient number of peaks with which to accurately discriminate CH₂O from its conflicting absorbers.

Testing similar space-borne UV spectrometer retrieval windows on GOME-2 data shows the trend in slant column reduction continues as we move to the higher end of the window further from the UV. In 2c we test the 337.5–359 nm fit window refined for use with the original GOME instrument (Chance et al., 2000; Wittrock et al., 2000). With the fit window lower limit at 337.5 nm, correlations between CH₂O and O₃ spectra should be minimised in the DOAS fit – moving into a region of greatly reduced O₃ strength compared to the CH₂O absorption spectra. However, reduction in the O₃ correlation comes at the cost of greatly reduced fit quality (-4.38×10^{-7} globally) and major reductions in CH₂O slant columns (-1.18×10^{16} molecules cm⁻²) due to increased interference from BrO and O₄. Comparable in wavelength range to GOME-2, the OMI sensor also provides spectra for CH₂O column retrievals using a GOME type spectral fitting algorithm (Chance, 2002; Kurosu et al., 2004). Test 2d applies the suggested OMI retrieval window (327.5–356.6 nm) on the GOME-2 data (in conjunction with the standard BrO pre-fit), leading to a global decrease in fit χ^2 of -2.43×10^{-7} compared to the reference retrieval, whilst we observe continental CH₂O slant column decreases of -0.26 and -0.16×10^{16} molecules cm⁻² for the AMA and SEUS regions.

From tests 2a–d, it is apparent that the differences between various spectrometers limit applications of fit windows as specific to each instrument. This has major implications for the generation of an extended CH₂O time-series from multiple sensors (e.g. De Smedt et al., 2008). Sensitivity to unknown instrumental or atmospheric absorption features towards 350 nm precludes use of the original GOME and OMI CH₂O fit windows due to their use of a higher wavelength cut-off. Nevertheless, a good retrieval is possible with the lower fitting range as applied in the reference fit, with Figure 4.3 demonstrating a minimisation of fit RMS is achieved, coupled to strongly enhanced CH₂O slant columns expected of the SEUS study site.

4.1.2 Absorber effects

Ring effect

Modelling of the Ring effect is accounted for with the inclusion of Ring spectra as pseudo-absorbers in the retrieval. In the reference retrieval, the method of Vountas et al. (1998) is applied to Ring cross sections generated with the SCIATRAN radiative transfer model (Rozanov et al., 2005), accounting for both Fraunhofer and molecular Ring effects. The widely used alternative method of Chance and Spurr (1997) applies only one pseudo-absorber in the retrieval, assuming the contribution of absorbers in Earth’s atmosphere to the Ring effect can safely be ignored. Applying this alternative Ring model (in DOAS mode) in test 3a shows large increases in CH₂O slant columns ($+0.27 \times 10^{16}$ molecules cm⁻²), coincident with dramatic reductions in fit quality for all regions demonstrated by a global χ^2 of 46.57×10^{-7} . These relatively poor results compared to the two Ring cross section method (Vountas et al., 1998), suggest the Chance and Spurr (1997) method could be better tested in the modified DOAS algorithm for which it was originally devised. This modified technique fits intensity rather than linear least squares fitting of differential optical depth, as originally intended for the method, as applied here. In either instance, further increases in fit quality can be expected with an improved Ring term, taking into account scene-specific parameters on albedo, aerosol loading, and clouds. However, given the range of variables involved in this process, this is considered beyond the scope of this study.

O₄ inclusion

When using a narrow window from 328.5–346 nm, the reference CH₂O window upper limit correlates well with an O₄ absorption minimum, which when combined with application of a 5th order polynomial, should negate significant O₄ interference in this region (De Smedt et al., 2008). Testing the inclusion of O₄ shows a minor decrease in global χ^2 , corresponding to an increase of CH₂O slant columns. The possibility of an O₄ incursion in the upper fitting region, where O₄ absorption is

strongest, has been explored for desert regions by De Smedt et al. (2008) and further tested here.

Tests 3b, c and d include the Greenblatt et al. (1990) O_4 cross section as an extra absorber. Its inclusion in the reference fit alone (test 3b) increases CH_2O slant columns for global and PAC regions by 0.14 and 0.08×10^{16} molecules cm^{-2} , respectively, with less noticeable effects for the enhanced CH_2O regions. In all O_4 tests, fit χ^2 is modulated within $\sim 1\%$ of the reference retrieval. In 3c we adjust the fit window to that of the GOME-1 fitting region, a wavelength range in which O_4 exhibits significant absorption features. Compared to test 2c (same fit region, no O_4 fitted), retrieved CH_2O slant columns increase by $\sim 0.1 \times 10^{16}$ molecules cm^{-2} , a value not dissimilar to the 0.14×10^{16} molecules cm^{-2} increase for test 3b against the reference retrieval.

In test 3d we test the effectiveness of the reference retrieval's 5th order polynomial by replacing it with a 3rd order polynomial and fitting O_4 , as previously applied to GOME-1 retrievals (albeit in a higher wavelength range) (Wittrock et al., 2000). This offers a significantly different result to the reference retrieval, not demonstrated by alternate O_4 permutations in the tests above. CH_2O slant columns are retrieved 0.94×10^{16} molecules cm^{-2} higher globally, the majority of which are accounted for by higher values over oceans, with a slightly reduced fit quality ($\sim 1.74\%$ globally). These results suggest the 5th order polynomial, in conjunction with the shift in fit region to lower wavelengths, is accounting for additional unquantified instrumental and/or atmospheric artefacts beyond the broadband atmospheric absorption processes typically modelled by a 3rd order polynomial in the fitting region.

OCIO inclusion

Including the Bogumil et al. (2003) OCIO cross section (convolved to the GOME-2 slit function) in both fit windows is seen to affect CH_2O slant columns less substantially than with O_4 , where slight decreases in fit residuals are displayed (alluded to from its inclusion in BrO pre-fit window tests), concurrent with a global reduction

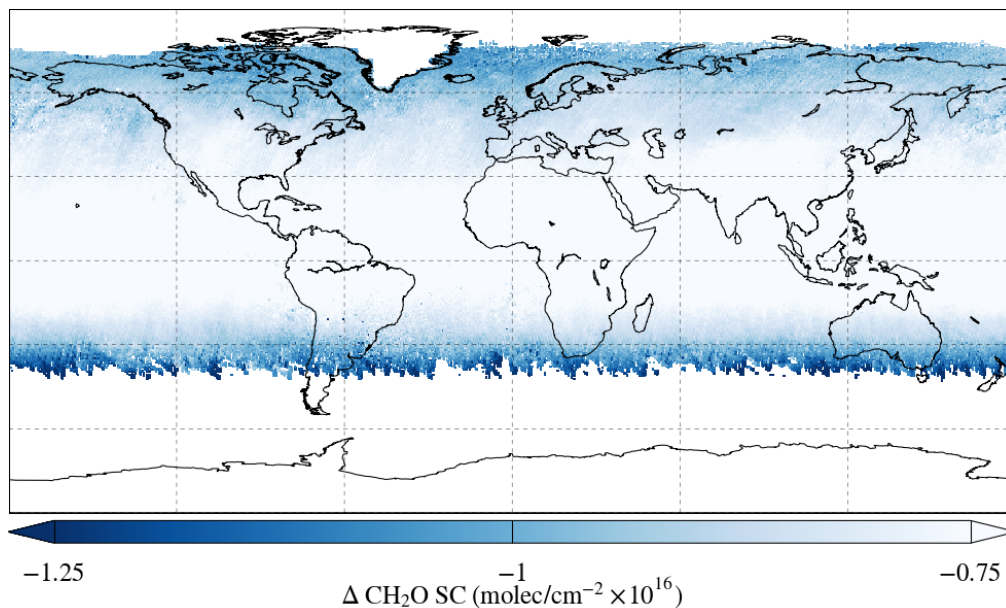


Figure 4.4: Difference plot on monthly mean for test 3f, excluding wavelength calibration. Dark fringes at the latitudinal extremes of the retrievals indicate CH_2O slant columns are strongly depressed in these regions, primarily as a function of increased O_3 interference.

in CH_2O slant columns of approximately a third. However, OCIO 's presence is inhomogeneous over the globe, being largely confined to stratospheric polar regions, and active during polar springtime (Oetjen et al., 2011). By discarding scans with $\text{SZA} > 60^\circ$, OCIO should not present a problem for CH_2O , elevated concentrations of which are largely confined to mid-latitudinal and tropical regions. However, due to similarities between CH_2O and OCIO absorption cross sections, signal contamination cannot be completely ruled out. False OCIO detection in tropical tropospheric regions will lead to a reduction in CH_2O columns, whilst an OCIO contaminated signal in poleward regions may well yield artificially enhanced CH_2O values. Test 3d includes OCIO in the DOAS fit, yielding lower CH_2O values over the Pacific Ocean (-0.16×10^{16} molecules cm^{-2}), together with slightly decreased slant columns for AMA and SEUS regions (-0.09 and 0.08×10^{16} molecules cm^{-2}) and a moderate global reduction in fit RMS (-0.04×10^{-4}).

Wavelength calibration

Although an extensive pre-flight characterisation campaign for the GOME-2 instrument (Siddans et al., 2006) has allowed for a superior operational wavelength calibration compared with its predecessor, additional wavelength calibration on reference spectra prior to application of DOAS fitting is deemed essential. To test the usefulness of this extra calibration, the wavelength calibration step is omitted from the reference retrieval in test 3f. This results in a global reduction of CH₂O slant columns by 0.81×10^{16} molecules cm⁻², coupled to an amplification in global latitudinal bias in the geographical distribution thought to be imparted by strong O₃ absorption towards the poles (see Figure 4.4). Fit quality is reduced, with χ^2 deteriorating at a global scale (by 0.55×10^{-7}). This shows the improved wavelength calibration allows for an enhanced alignment of absorption features in spectra and trace gas cross sections, crucial in improving the accuracy of O₃ and BrO fits, particularly at large SZAs.

I_0 correction

Following the methodology of Aliwell et al. (2002), O₃ cross sections included in the reference retrieval are corrected for the I_0 effect. The baseline retrieval followed here uses a slant column of 0.8×10^{19} molecules cm⁻² for the I_0 correction of O₃ cross sections prior to fitting (our reference retrieval shows O₃ retrieved in the slightly wider BrO pre-fitting window to be close enough to values retrieved in the CH₂O window to warrant using the same correction value). The slant column used for I_0 correction remains a source of error in the retrieval, typically set to the maximum retrieved slant column value of the corrected absorber. This value can be expected to exhibit wide seasonal and geographic variation. For orbit 4176, the scaling factor is adjusted in 0.1×10^{19} molecules cm⁻² steps between 0.1 and 2.3×10^{19} molecules cm⁻² to evaluate the range of retrieval effects imparted by the correction.

Figure 4.5 shows the results of this test, with a levelling off of CH₂O slant columns and errors, O₃ and fit residuals when the slant column is increased above

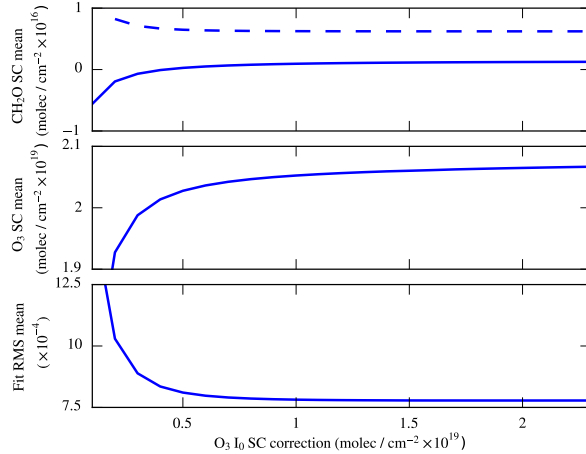


Figure 4.5: I_0 correction range test showing mean values for orbit 4176, with the O_3 column slant column adjusted at 0.1×10^{19} molecules cm^{-2} intervals along the x-axis (the reference retrieval applies an add back value of 0.8×10^{19} molecules cm^{-2}). Dashed line indicates mean CH_2O slant column error.

0.5×10^{19} molecules cm^{-2} . Assuming the retrievals from orbit 4176 are reasonably illustrative of a typical GOME-2 orbit, this indicates incorporation of an O_3 column at 0.5×10^{19} molecules cm^{-2} represents an appropriate correction factor. Extending the application of I_0 correction from just O_3 to all trace gas absorbers in test 3g (BrO at 4.5×10^{14} , CH_2O at 12×10^{16} , and NO_2 at 5×10^{17}) yields negligible global increases in CH_2O slant columns, with accompanying increases in fit quality of 0.07×10^{-7} . However, these changes are not uniform across the globe, with slant columns increases for the AMA and PAC regions, and decreases evident for SEUS. These further increases in fit quality suggest extending the I_0 correction methodology to all fitted trace gas absorbers is warranted.

Cross section temperature

Change in absorption spectra line shape and strength are encountered in parallel with temperature variations. Of relevance here, O_3 absorption cross sections show a strong relationship with temperature (Liu et al., 2007), and are therefore included in the retrieval at two temperatures, with the higher temperature orthogonalised to the lower. Tropospheric CH_2O retrievals typically fit O_3 at temperatures suitable to the stratospheric O_3 component, at around 218–228 K and 241–248 K.

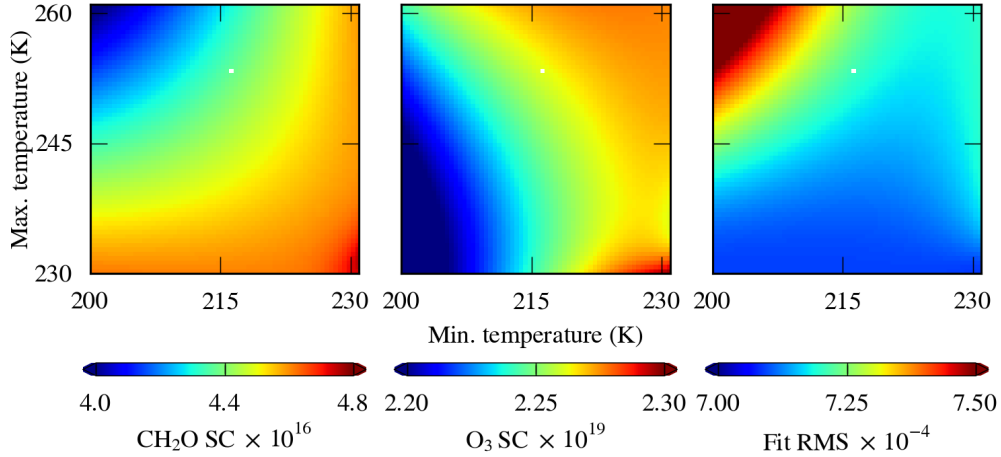


Figure 4.6: Scan number 3107 (orbit 4176) repeatedly retrieved with the reference settings, adjusting the low and high temperatures of the orthogonalised O_3 absorption spectra in increments of 0.5 K. A linear gradient is seen for slant columns (molecules cm^{-2}) and fit residuals. Whilst the range of fit residual variation is not large, the retrieved CH_2O slant column displays a non-negligible range of values.

To test the dependence of CH_2O slant column on O_3 retrieval temperature, we apply temperature coefficients given with the Liu et al. (2007) interpretation of the Malicet et al. (1995) O_3 cross sections, thus allowing derivation of O_3 absorption cross sections at any number of temperatures. As shown in Figure 4.6, the variability is assessed for a single scan over the SEUS study site, on 9th August 2007 (scan no. 3107, orbit 4176), when a high CH_2O slant column magnitude is expected. The O_3 temperature range is adjusted through 200–230 K and 230–260 K in 0.5 K intervals, altering retrieved CH_2O slant columns between $4.0\text{--}4.8 \times 10^{16}$ molecules cm^{-2} , and O_3 slant column from $2.20\text{--}2.30 \times 10^{19}$ molecules cm^{-2} . Temperature effects on fit residuals are limited to a small range of O_3 temperature combinations for < 215 K (lower) and > 245 K (upper), beyond which they flatten out around 7.1×10^{-4} . This large range of minimised fit residuals allows optimisation of the CH_2O fit according to the maximum slant columns. For CH_2O and O_3 , both suggest temperatures currently in use are entirely suitable (i.e. 228 and 243 K, respectively).

The CH_2O cross section varies throughout the UV absorption region (Brauers et al., 2007). To arrive at an appropriate error estimate for CH_2O temperature dependency, CH_2O cross sections were generated at 5 K temperature intervals between 273 and 308 K, and applied in place of the regular CH_2O cross section (298 K).

The mean temperature dependency over orbit 4176 is found to be weak, at only $\sim 0.03 \times 10^{16}$ molecules cm^{-2} over the 35 K temperature range tested, translating to an average decrease in CH_2O slant column of $0.11 \% \text{ K}^{-1}$.

Selecting two $5^\circ \times 5^\circ$ regions of high (southeastern USA) and low (Gulf of Mexico) CH_2O concentrations from the orbit provides a more detailed estimate of the temperature dependency. O_3 slant columns remain unaffected by the adjustment of CH_2O absorption cross section temperature. Corresponding to the increased cross section temperature, CH_2O slant column mean increases in a linear fashion of $+0.16 \times 10^{16}$ molecules cm^{-2} across the temperature range for the enhanced SEUS CH_2O plume, with a much smaller increase for the low CH_2O slant column case, increasing by just 0.01×10^{16} molecules cm^{-2} .

4.1.3 Polynomial degree

Fitting the GOME-2 measured Earthshine spectrum with a polynomial removes the broadband spectral component of atmospheric Rayleigh and Mie scattering prior to fitting trace gas absorbers. Work with the original GOME instrument found application of a 3rd order polynomial sufficient to remove the atmospheric scattering component (Wittrock et al., 2000). However, with the shift of the fit range further into the UV, allowing stronger O_3 absorption to increase retrieval interference, a 5th order polynomial is applied in the reference settings, based on the work of De Smedt et al. (2012). Test 4a applies a 4th order polynomial, resulting in an approximate doubling of slant columns over oceans, with gains in CH_2O slant column of 0.24×10^{16} molecules cm^{-2} for AMA, and 0.31×10^{16} molecules cm^{-2} for SEUS. Application of a 3rd order polynomial in test 4b increases the strength of the latitudinal dependency globally (reducing values at high latitudes, with increased slant columns at mid-latitudes), yielding a global CH_2O slant column increase of around 15%. Fit quality for both tests is seen to greatly reduce ($+0.23 \times 10^{-7}$ for the 4th order, and $+0.73 \times 10^{-7}$ for the 3rd globally) from the reference retrieval as we move away from the 5th order polynomial, showing lower order polynomials

Scan bias

GOME-2 exhibits a scan angle and SZA dependent bias, occurring as a function of instrument degradation since launch (Dikty and Richter, 2011; Cai et al., 2012). This is known to affect all GOME-2 retrievals, particularly those making use of short UV wavelengths (Balis et al., 2008; Antón et al., 2009; Loyola et al., 2011b). To counter this scan bias, Eta and Zeta polarisation spectra (measured pre-launch) are included in the reference retrieval BrO pre-fit window as pseudo-absorbers (EUMETSAT, 2011a; De Smedt et al., 2012). Visual inspection of individual orbits reveal the values retrieved for the Eta and Zeta parameters display distinctive east and west components. Confirmation of the corrective effect is made in test 5a by testing the retrieval without the spectra and examining individual swaths, allowing a strong cross track dependency to become apparent, highlighted by eastern slant columns retrieving between $1-2 \times 10^{16}$ molecules cm^{-2} higher than their western counterparts over clear ocean, manifesting in a globally increased CH_2O slant column mean (0.4×10^{16} molecules cm^{-2}). However, exclusion of these correction factors also serves to increase fit quality, with χ^2 values decreasing for all sites. The inclusion of the scan bias correction's overall negative effect on fit quality points to the requirement for implementation of superior retrieval-based bias correction techniques such as that derived by Loyola et al. (2011b), or empirical corrections of L1B data.

Spectral undersampling

GOME-2 samples between 2.46 and 2.25 measurements per FWHM (0.27 nm) at the lower and upper wavelength limits of the reference fitting interval. Small wavelength shifts of the spectrometer in orbit, on the order of 0.007 nm, introduce potential for undersampling of spectra, especially with a moderately decreasing FWHM towards the upper limit of the CH_2O fit window (Cai et al., 2012). Undersampling spectra are calculated for GOME-2 following Chance et al. (2005), and included as a pseudo-absorber in the reference retrieval. Testing the efficacy of the undersam-

pling correction by excluding the spectra from the fit in test 5b leads to an increase of $+0.13 \times 10^{16}$ molecules cm^{-2} in CH_2O slant columns globally, with similar increases for the study regions. Whilst the standard deviation on these columns decreases very slightly, confidence in the retrieval without an undersampling correction is undermined by significant reductions in fit quality for all sites. Loss of retrieval sensitivity from not correcting for undersampling, particularly for weak absorbers, suggests the inclusion of an undersampling correction should be strongly considered, as expected.

Offset correction

A small amount of signal measured by GOME-2 is thought to be additive from extraneous sources inherent to the imperfect nature of the instrument's design, construction and operation (e.g. stray light in the spectrometer housing, and degassing of adhesives and materials contained within the housing and unable to escape to space). These predominantly systematic artefacts can be accounted for by the addition of a linear offset term in the DOAS fit – typically taking the form of fitting a 1st order polynomial to the fit residual (as used in the reference fit here, derived following the modified offset equation detailed on page 69 of Fayt et al. (2011)). This is tested in comparison with a zero and 2nd order offset polynomial (tests 5d and 5e), as well as application of a $1/I_0$ spectrum fitted as a pseudo-absorber (in place of the standard polynomial) (Marbach et al., 2010; Valks et al., 2011). The latter method, tested in 5f, has the potential to provide a more accurate representation of the offset term, being based on the instrument's physical parameters for each daily reference spectra.

Increasing the offset polynomial to a 2nd order correction increases fit quality very slightly ($\sim 1\%$ globally), with corresponding increases in CH_2O slant column for all sites ($\sim 0.06 \times 10^{16}$ molecules cm^{-2}). Application of a zero order offset polynomial and a $1/I_0$ spectrum as the offset term both show similar significant reductions in slant columns, with fitting residuals increasing beyond that found with the reference correction term – rendering both alternatives unsuitable for further

application to the CH₂O retrieval.

4.1.5 SCD error

Slant column density errors are composed of random and systematic components De Smedt et al. (2008); Theys (2010). Random error can be approximated by the RMS of the DOAS fit, assuming it is primarily influenced by noise in the measured spectrum. Systematic errors are generated through the interference of fitted molecules, as a function of the similarity of absorption line shape and subsequent potential for mis-fit of the desired molecule. In the CH₂O fit region, absorbers are seen to be well correlated (Figure 3.1). Here the method of De Smedt et al. (2008) and Theys (2010) is used to estimate systematic errors on retrieved slant column density $\sigma^2 N_{syst}$ as a result of uncertainty on the convolved absorption cross sections:

$$\sigma^2 N_{syst} = \sum_{j=1}^m N_{s_j}^2 [\mathbf{G} \mathbf{S}_{b_j} \mathbf{G}^T]. \quad (4.2)$$

Where N_{s_j} is the fitted SCD of the j th absorber, \mathbf{S}_{b_j} is the $n \times n$ (n represents the number of wavelengths the DOAS fit is performed on) covariance matrix of errors on the j th fitted absorption cross section against the absorption cross section of interest, and the gain matrix \mathbf{G} is formed by a matrix of absorption cross sections \mathbf{K} with dimensions $n \times m$ (where m is the number of fitted absorbers):

$$\mathbf{G} = [\mathbf{K}^T \mathbf{K}]^{-1} \mathbf{K}^T. \quad (4.3)$$

Complete error budgets are unavailable for the high resolution absorption spectra in use here, therefore as in the method of De Smedt and Theys, errors are estimated by multiplying convolved absorption cross sections by the accompanying uncertainty values from each absorbers respective literature reference (BrO: 8%, CH₂O: 5%, NO₂: 3%, O₃: 3%, and Ring: 5%). An additional error source accounting for varying quality of wavelength calibration and linear offset fitting is estimated at 12%.

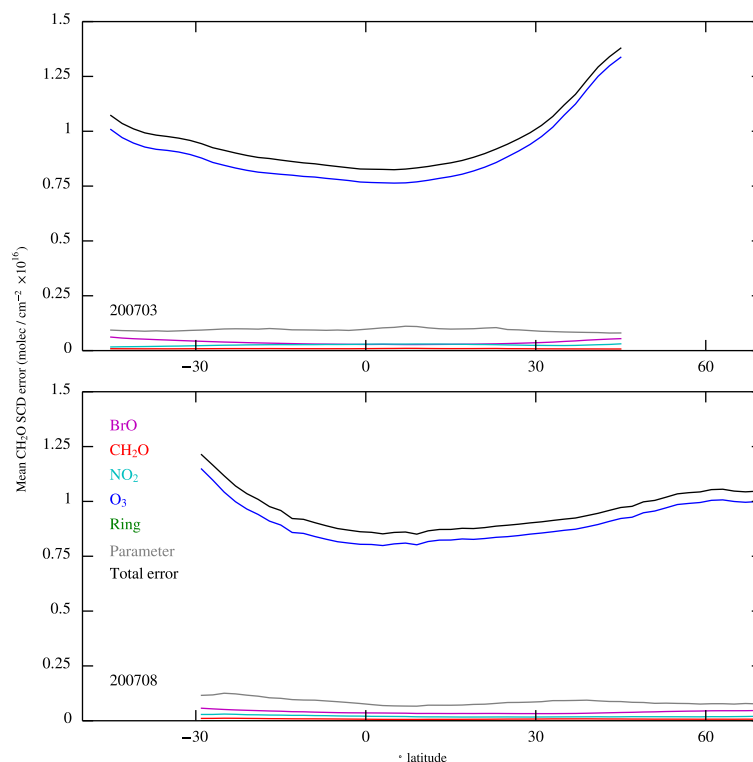


Figure 4.8: 2° latitudinal mean SCD errors calculated for 200703 and 200708.

Systematic SCD errors are calculated for March and August 2007; two months representative of the minimum and maximum expected CH₂O columns worldwide. Figure 4.8 shows the total systematic error on SCDs to be in the region of 1.1×10^{16} molecules cm^{-2} at high latitudes and 0.9×10^{16} molecules cm^{-2} towards the equator. O₃ interference in the fit is seen to be the largest contributor to total CH₂O fit uncertainty, due to the strength of ozone's absorption masking formaldehyde absorption features. Ring effect (not plotted due to y-axis differences) also plays a significant role in degrading fit quality in parallel with measurement SZA, whilst BrO induced errors are noted further towards the poles as a consequence of the molecule's relative abundance in these regions. Additional uncertainty due to fit parameters remains within a small range over all latitudes, as does the minimal interference from the NO₂ molecule. Error on the CH₂O absorption cross section itself is seen to contribute an intermediate amount to systematic SCD error. From this error budget, the difficulty of the CH₂O fit is illustrated, whereby it is apparent a much improved O₃ fit is required in order to reduce CH₂O error.

4.2 Earthshine I_0 reference

In any CH_2O DOAS fit, residual components are introduced through imprecise fitting of major absorbers present in the retrieval window. In the case of CH_2O , O_3 and Ring absorption remain as major contributors to the residual spectrum. Furthermore, a fitting bias in the CH_2O fit is evident in latitudinal means (Figure 4.10), believed to be caused by spectral fitting dependencies at high latitudes of the CH_2O fit with O_3 , Ring, BrO, and contributions from un-defined instrumental issues (De Smedt et al., 2012). In addition to the latitudinal bias, scan bias is evident from the eastern to the western portion of GOME-2's swath, which remain apparent even with inclusion of Eta and Zeta correction factors in the fit (Section 4.1.4). Corrections for this latitudinal bias typically make use of the Reference Sector Method (RSM) (Richter and Burrows, 2002). Whilst this partly mitigates for the problem, it also introduces an extra layer of complexity and error to the retrieval, coupled to further dependency on an a-priori CTM. Work is presented detailing efforts made to mitigate for latitudinal bias by reducing fit dependence on the RSM correction, and so improve the fitting portion of the retrieval further.

Ground based zenith DOAS retrievals must apply a reference background spectrum measured at a low solar zenith angle, thereby taking a measurement through the shortest atmospheric path containing a minimum of absorbers present in the reference spectrum. Application of a similar reference spectra to space-borne retrievals is tested by making use of Earthshine spectra from a clean Pacific reference sector as background reference in place of the usual extra-terrestrial solar spectrum. These already contain background concentrations of absorbers (including CH_2O), with fitted concentrations reduced by the co-incident amount of absorber present in the reference. This should confer an advantage to the retrieval from the strongest absorbers (O_3 and Ring) already being present in the I_0 reference, allowing for a reduction in the relative retrieved concentration masking absorption features of minor absorbers. O_3 and Ring both show broad latitudinal variation across the globe, whilst CH_2O concentrations are highly localised, with background concentrations

at detection minimums. Removal of background interference from strong absorbers over all latitudes should remove the latitudinal bias present in the CH₂O global mean by reducing the fitting interplay between CH₂O and stronger absorbers. Normalisation of Earthshine fitted SCDs is performed after the DOAS fit, by adding a CTM defined background CH₂O value to Earthshine fitted SCDs.

4.2.1 Earthshine I_0 selection

The clean reference sector, from which Earthshine I_0 (hereafter referred to as EI_0) are chosen, is set to the same as that defined for the RSM; -170° W to -140° W. Initial test retrievals were made for EI_0 selections only within a small 10° latitude × 10° longitude subset of the reference sector over the equator, as used for correcting diffuser plate structures in previous GOME-1 retrievals (Richter and Burrows, 2002), and with a single EI_0 to be applied to the entire days data. These were both shown to offer very poor retrievals at locations beyond their own confines; suggesting EI_0 's are required for the entire reference sector. Therefore selection of the new EI_0 is tested for the entirety of the reference sector strip for two geographic criteria; latitude and solar zenith angle. Given GOME-2's 1920 km swath width, and to avoid further unquantified scan bias contamination in the retrieval, selection in both cases is also made for scanner position in bins of two scan index width across the swath.

EI_0 spectra are sampled in 1° intervals from a latitudinal strip over the remote Pacific Ocean, and only considered for selection providing they fall below the standard cloud fraction mask of 0.4 (reducing the cloud mask further provides too few EI_0 spectra to allow useful global retrieval coverage). Significant portions of the reference sector are inevitably covered in cloud, despite use of a moderate cloud fraction screen. This negates the retrieval on any of these scanner position and latitude / SZA combinations for the rest of the day's data, leaving a stripe of no retrievals across the globe at that latitude.

To circumvent this apparent lack of EI_0 references, tests were run experimenting with a longitudinal widening of the reference sector, which was found to rapidly in-

introduce enhanced continental trace gas concentrations from Asia and North America into selected background reference spectra, defeating the object of the EI_0 retrieval. Replacing EI_0 references for the infilling of gaps due to cloud, an algorithm is implemented to initially search around the missing scan in a widening 1° band, up to $\pm 4^\circ$. If no suitable replacement is found in this search, the temporal range is then widened 1 day at a time, to a maximum of ± 4 days for the same scanner / geographic position. For SZA selection criteria, a daily solar equator is calculated based upon the point at which the Sun is directly overhead (e.g. for the 9th of August 2007, solar equator is calculated at 16.02° N), allowing splitting of data into northern and southern hemispheres relevant to solar position, and ensuring the number of EI_0 's is maximised.

Although both selection criteria should produce broadly similar EI_0 sets, the latitudinal selection method allows a greater number of EI_0 's to be selected compared to the SZA method, owing to latitudinal bands covering a narrower surface area than the 1° SZA band, permitting a higher resolution of data from which to fill gaps in with surrounding data. This impacts on the SZA selection through the introduction of larger cloud screen related gaps in the daily EI_0 set, propagating throughout the day's orbits as a longitudinal gap in retrieval coverage. Daily sets of these scan position and geo-location dependent EI_0 spectra are then applied as I_0 reference in place of the daily SMR to give differential SCs. In order to match reference spectra, trace gas absorption spectra are calibrated to the Earthshine wavelength scale in this method.

	Global			AMA			SEUS			PAC		
	Mean	$\pm 1\sigma$	χ^2	Mean	$\pm 1\sigma$	χ^2	Mean	$\pm 1\sigma$	χ^2	Mean	$\pm 1\sigma$	χ^2
Ref.	-0.30	0.57	8.96	1.01	0.33	7.64	1.14	0.32	6.40	-0.35	0.15	6.28
EI_0	0.12	0.68	11.71	1.22	0.43	13.57	1.58	0.36	8.47	0.04	0.21	9.13

Table 4.2: Results for EI_0 CH₂O DOAS retrievals, presented in the same manner as Table 4.4. Reference retrieval results are included for comparison.

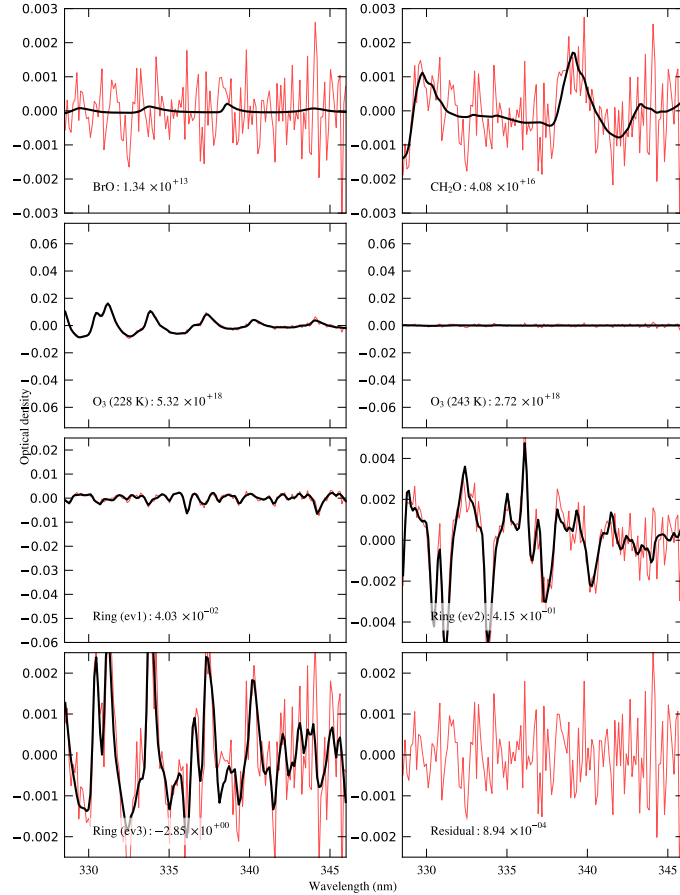


Figure 4.9: Example CH_2O fit on scan 3107, orbit 4176, performed with an EI_0 reference. Compare to Figure 4.2.

4.2.2 EI_0 retrieval results

CH_2O DOAS retrievals were performed using EI_0 references for the entirety of August 2007, using the same GOME-2 data (v4) as for the previous sensitivity tests. All settings remain the same as detailed in Table 4.1, with the following two exceptions; solar reference is switched to the appropriate EI_0 for the scan, and due to the lack of a high resolution EI_0 spectra to calibrate against inherent to the technique, wavelength calibration of spectra is disabled.

Looking first at the quality of DOAS fit achievable with an EI_0 spectrum, the sample scan 3107 from orbit 4176 is detailed in Figure 4.9. Comparing this to the regular retrieval shown in Figure 4.2, fitted concentrations of O_3 , Ring (EigenVector 1) and BrO are all significantly reduced by an order of magnitude. However Ring EV2 and EV3 are both seen to increase in the absence of EV1 detection. The Ring

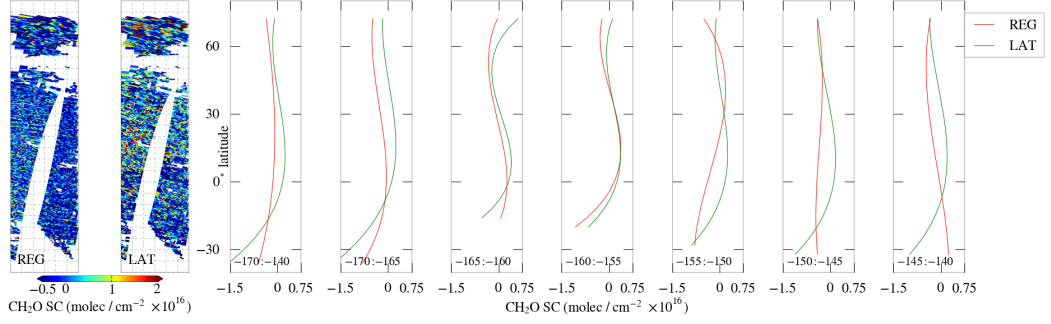


Figure 4.10: CH_2O slant column densities retrieved for the 9th August 2007 over the Pacific reference sector from which EI_0 references are taken. Plots are restricted to reference longitudes $-170^\circ \text{ W} - -140^\circ \text{ W}$. Regular (REG) and EI_0 retrievals with references selected based on the latitudinal binning scheme (LAT) are shown with scans >0.4 CF removed. Latitudinal means are presented, with the left most line plot detailing the mean over the entire reference region, and each subsequent plot representing the mean of 5° strips taken over the same region.

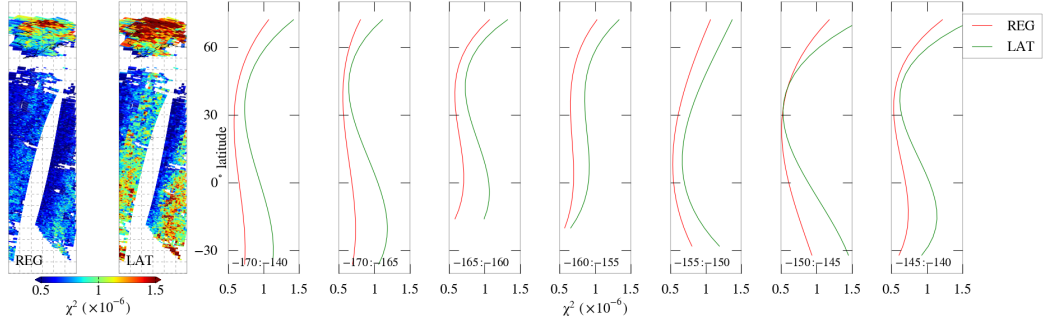


Figure 4.11: As Figure 4.10, but showing χ^2 fit quality.

issues, coupled with a degradation in quality of spectral alignment due to the lack of absolute wavelength calibration, are thought to be the driver behind the reduction in the global χ^2 fit quality by around 30% compared to the reference retrieval.

With regards to the geographic distribution of EI_0 fits, CH_2O is seen to exhibit a greater range of variation, and noise, than for its regular retrieval. The majority of fits are now positive, reflected in the global CH_2O slant column mean of $\sim 0.12 \times 10^{16}$ molecules cm^{-2} . The latitudinal CH_2O ‘hump’ is intensified with an EI_0 fit, due to amplification of latitudinal variation present in the reference sector used for EI_0 selection. Large levels of noise are not noted for O_3 and Ring fits (Figures 4.12, and 4.13), owing to the virtual elimination of these concentrations from the retrieval. CH_2O and O_3 latitudinal means for the regular retrieval demonstrate well the dependence of CH_2O concentrations on fitted O_3 ; with a depression of CH_2O

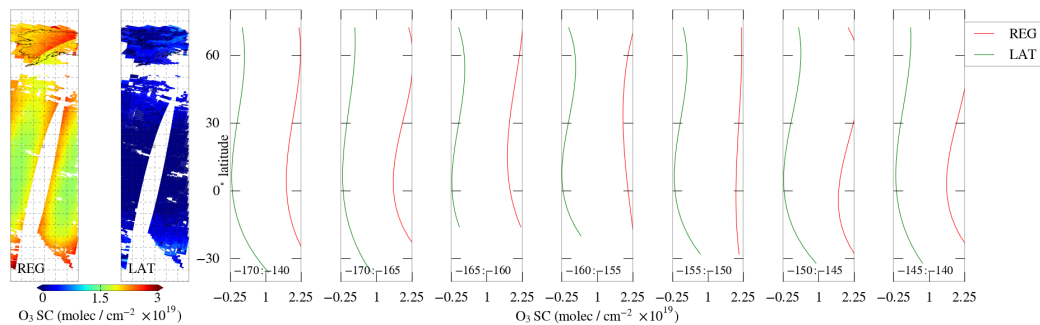


Figure 4.12: As Figure 4.10, but showing retrieved O_3 .

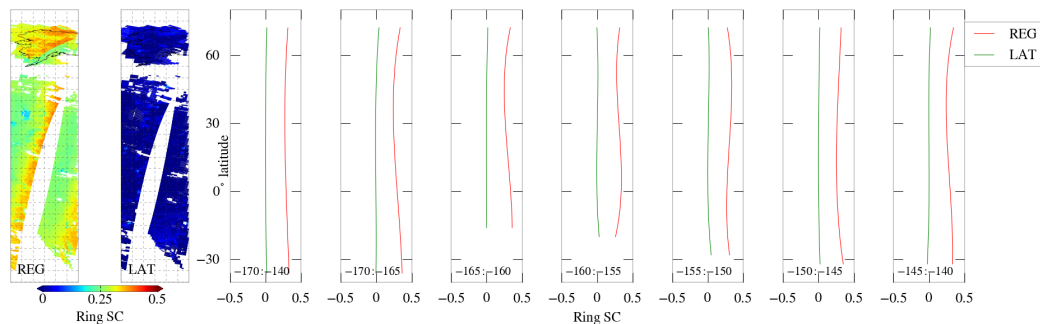


Figure 4.13: As Figure 4.10, but showing retrieved Ring (EV1).

concentrations occurring in parallel with elevated O_3 concentrations, even over what should be a homogenous region of CH_2O such as the reference sector shown.

Scan angle bias remains, albeit at a reduced level, evident in both the fit χ^2 and Ring plots. Due to the scan angle dependent nature of the reference selection and fitting, retrieval fit quality is seen to increase slightly in the western portion of the swath, offset by a reduction in fit quality on the eastern side due to amplification of degraded GOME-2 measurements.

4.2.3 EI_0 analysis

DOAS fitting with an EI_0 reference is greatly complicated by the increase in Ring EV2 and EV3 interference in the retrieval, illustrated in Figure 4.9. Referring to the original Vountas et al. (1998) description of the Ring components when derived with Principal Components Analysis; EV1 represents the Fraunhofer line filling component of the Ring effect, which is effectively removed from our retrieval. It can be assumed that use of the EI_0 reference introduces new Ring effect fit dependencies related to the filling in of atmospheric gas absorption lines, represented by EV2 and

3, both seen to significantly increase. Although further investigation is required, this could well be correlated with the presence of cloud in selected EI_0 references impacting on the measured radiances.

Further limitations in the technique arise from the lack of a stringent wavelength calibration and slit function derivation for EI_0 reference spectra, with at least part of the reduction in fit quality attributable to poor alignment of spectra, in a similar fashion to that found in sensitivity test 3f (no wavelength calibration). Mitigation for a changing slit function can be made by deriving the slit function for a regular I_0 retrieval, and applying this slit to EI_0 retrieval spectra. Positive aspects of the retrieval relate to removal of the need to apply a full reference sector correction - with EI_0 retrievals typically returning positive CH_2O slant column densities over remote areas, indicating background values are enhanced due to the co-incident reduction of retrieved O_3 and Ring slant column densities.

4.3 SCD post processing

4.3.1 Cloud fraction

For nadir mode scanning, GOME-2's detector array has an integration time set to yield a spatial resolution of $80 \times 40 \text{ km}^2$ per pixel. Whilst many entirely cloud free pixels are found in a regular GOME-2 orbit of approximately 15,000 scans, the vast majority will be at least partially contaminated with cloud. In our AMF retrieval algorithm, cloudy pixels are dealt with using the independent pixel approximation (Martin et al., 2002), as detailed in equation 5.24, leaving a margin of error on the AMF directly linked to the accuracy of input cloud data. The FRESCO+ (Fast Retrieval Scheme for Clouds from the Oxygen A band) cloud retrieval scheme used here to provide cloud information, derives cloud properties from GOME-2 PMD measurements of the O_2 A-band (759–770nm) (Wang et al., 2008). Boersma et al. (2004) summarised expected uncertainties on GOME-1 NO_2 measurements due to cloud, finding a 5% uncertainty in cloud fraction over oceans, and 20% uncertainty

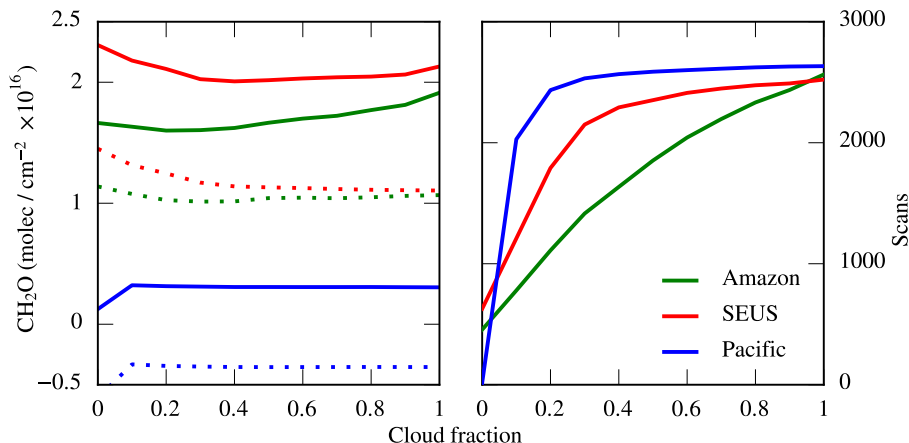


Figure 4.14: Altering the cloud fraction threshold from our reference retrieval (August 2007) shows the wide range of CH₂O slant columns (left hand plot, dotted lines), vertical columns (left hand plot, solid lines), and scan counts (right hand plot) taken into monthly means for the three detailed study sites. A cloud fraction (CF) of 1 indicates all scans are taken into account.

over land. In the AMF algorithm presented here, cloud top reflectivity is set as a Lambertian reflector with an assumed albedo of 0.8, whilst for the clear portion of the scene, we also rely on surface albedo from an external database.

Scans with an effective cloud fraction of > 0.4 are initially excluded from analysis. Here, the effect of increasing and decreasing the CF threshold for the reference retrieval is specifically examined. The high spatial sampling frequency of GOME-2 provides the opportunity to test a higher rejection rate on cloudy pixels for lower cloud fractions. This will yield less variability in monthly slant column means due to the reduction in the number of observations, for which SCD retrievals are artificially modified due to cloud scattering and absorption effects.

Figure 4.14 shows the effect this cloud fraction adjustment has on the monthly CH₂O slant columns and scan counts for August 2007. A cloud fraction of 0.4, used as the reference threshold, is seen to offer a reasonable compromise between elimination of cloudy pixels without significantly affecting SCD values. This is further illustrated in Figure 4.15, particularly for the AMA study site, where the majority of cloud can be seen to be sitting in the 300–600 hPa region. CH₂O slant and vertical columns for the PAC region are stable above a cloud fraction limit of 0.1. Minor correlations between increasing scan counts and vertical columns are

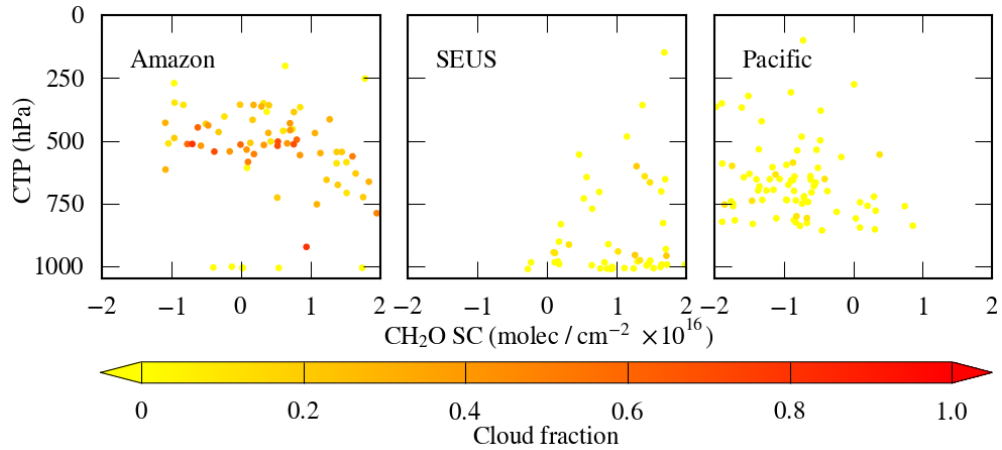


Figure 4.15: CH_2O SCD against cloud top pressure (CTP), with cloud fractions from 0–1.0 denoted by colour, for the three study sites on the 9th August 2007. The Amazon site shows the large number of high CF scans ($\text{CF} > 0.4$) expected in the area due to the regional climate, the majority of which are between 300–600 hPa, whilst the southeastern US and Pacific Ocean regions display no clear correlation between CF and CTP.

noted for the AMA region, due to an increased number of scans with higher cloud fractions increasing the reflectivity of a radiance measurement, thereby enhancing the measured CH_2O SCD (Palmer et al., 2001). For the SEUS region, slant and vertical columns decrease from cloud fractions of 0 to plateau above a cloud fraction of 0.4. The vertical column is seen to increase in parallel with an increased cloud cover at $\text{CF} > 0.4$, which is not noted for the corresponding slant columns. Whilst this offers a useful indicator of an appropriate CF threshold, it also shows the AMF is providing a sub-optimal conversion value for such scans due to an unrealistic interpretation of radiation transfer above, within, and below clouds. At higher solar zenith angles, situation is likely to be further compounded by the increasing path length of light in combination with Mie scattering effected by cloud.

Interaction between cloud and aerosol which exists over the study regions, and their representation by the AMF, may play a large part in spurious slant to vertical column conversions above certain cloud thresholds (Boersma et al., 2004). Aerosols are represented in the AMF by AODs of 6 different types supplied by the GEOS-Chem CTM (sea salt, desert dust, black carbon, water vapour and SO_2), used to modify the scattering weights implicit in AMf calculation. Biomass burning, often

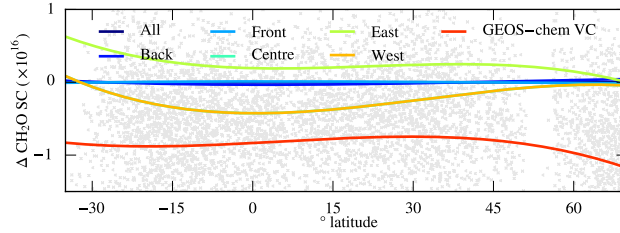


Figure 4.16: Reference sector correction for the 9 August 2007. Grey markers indicate retrieved slant column values in the reference strip from which we model our subtractive polynomial. Solid lines represent the polynomial taken from these values according to scan position. Note large differences between east and west swath corrections, illustrating bias present in retrievals according to swath position. “All” is obscured by “Back” and “Front”, whilst “Centre” is obscured by “West”.

encountered in tropical ecosystems such as the Amazon, encourages pyro-convection, with associated uplift of aerosol high into the troposphere (~ 5 km) (Gonzi and Palmer, 2010). Aerosol at these heights can act to shield incoming radiation from underlying CH_2O , effecting a decrease in the AMF and subsequent increase in CH_2O vertical columns. High clouds also affect the AMF in the same way, but possibly to a greater extent owing to their increased albedo compared to aerosols. Considering biomass burning cases, these two processes are likely to act in concert, with a greater number of aerosol molecules providing cloud formation nuclei.

4.3.2 Reference sector method

To mitigate for unresolved spectral dependencies occurring at high latitudes between CH_2O and strongly interfering BrO and O_3 molecules, a reference sector correction is performed following the standard method detailed in Section 3.4.5, developed for stratospheric correction of NO_2 retrievals (Martin et al., 2002; Richter and Burrows, 2002) and also routinely applied to CH_2O data (e.g. Palmer et al., 2006; Barkley et al., 2008; De Smedt et al., 2008).

Here, the forward scans of the GOME-2 scan packet (see Section 3.3.4) are further divided into east, centre and west components, consisting of 8 scans each, allowing investigation into the effect of the GOME-2 scan bias on the reference sector method (RSM), and final vertical columns. Figure 4.16 and Table 4.3 show

that by incorporating all scans into the correction, directional scan bias averages out over the swath, whilst including only east or west scans imparts a clear bias on the subtractive polynomial according to scan direction applied. Nevertheless, the eta/ zeta scan bias correction remains essential, with error at swath edges likely to propagate through monthly and seasonal means. Even accounting for the eta/ zeta correction, assessment of more sophisticated methods of scan bias correction mentioned in Sections 3.4.5 should be pursued for CH₂O retrievals.

4.3.3 Homogenisation of CH₂O vertical columns

To test the effect of the application of the reference sector correction on the CH₂O retrieval, differences in CH₂O slant columns are compared with their corresponding vertical columns from prior sensitivity testing (Table 4.4). From these tests, selected CH₂O vertical column results are summarised in Table 4.5. This demonstrates major reductions in differences between test retrievals and the reference retrieval, particularly so for tests with previously very large differences, bringing all global vertical column differences within 21 % of the reference, compared to a maximum slant column difference of -390% .

Despite widely varying errors in terms of fit residuals between retrievals, Table 4.6 demonstrates that application of the reference sector correction apparently causes previously disparate retrievals to converge around a broadly similar set of results. This ranges from those tests with small effects on global slant column mean (such

Scans	Global	AMA	SEUS	PAC
All	0.49	1.62	2.02	0.31
Back	0.45	1.58	1.98	0.28
Front	0.49	1.63	2.02	0.31
Centre	0.30	1.36	1.73	0.12
East	0.54	1.83	2.23	0.46
West	0.30	1.36	1.73	0.12

Table 4.3: Monthly mean CH₂O vertical columns for August 2007 (units of $\times 10^{16}$ molecules cm⁻²) derived from usage of unique directional swath components for the reference sector correction, taking the reference retrieval as source data.

Setting	Global		Amazon (AMA)		Southeast US (SEUS)		Pacific Ocean (PAC)					
	Mean	$\pm 1\sigma$	χ^2	Mean	$\pm 1\sigma$	χ^2	Mean	$\pm 1\sigma$	χ^2			
Reference retrieval	-0.30	0.57	8.96	1.01	0.33	7.64	1.14	0.32	6.40	-0.35	0.15	6.28
Spectral range												
BrO window												
1a. 332-359 nm	-0.24	0.57	8.95	1.01	0.34	7.65	1.21	0.32	6.39	-0.29	0.16	6.27
1b. 332-359 nm (+ OClO)	-0.15	0.56	8.92	1.09	0.35	7.63	1.27	0.32	6.37	-0.21	0.16	6.25
1c. Pre-fit BrO and O ₃	-0.28	0.58	9.09	1.03	0.33	7.70	1.19	0.32	6.39	-0.34	0.15	6.31
CH ₂ O window												
2a. 325.5-350 nm	0.27	0.61	10.91	1.37	0.29	8.96	1.64	0.31	7.26	0.07	0.14	7.39
2b. 332-350 nm	-0.38	0.59	10.19	0.99	0.37	8.78	1.09	0.33	7.18	-0.41	0.16	7.17
2c. 337.5-359 nm (GOME-1)	-1.48	0.75	13.34	0.02	0.47	11.95	0.03	0.38	9.73	-1.50	0.17	9.57
2d. 327.5-356.6 nm (OMI)	-0.35	0.63	11.39	0.75	0.31	9.45	0.98	0.32	7.64	-0.56	0.13	7.59
Absorber effects												
3a. Ring (Chance and Spurr, 1997)	-0.03	0.60	46.57	1.30	0.34	39.58	1.45	0.33	37.17	-0.05	0.16	41.80
3b. O ₄	-0.16	0.54	8.88	1.12	0.36	7.55	1.20	0.32	6.37	-0.22	0.16	6.22
3c. O ₄ (GOME-1 window)	-1.38	0.77	13.12	0.10	0.49	11.82	0.08	0.38	9.67	-1.41	0.18	9.46
3d. O ₄ (3rd order poly)	0.64	0.55	9.11	1.81	0.33	7.64	2.01	0.33	6.37	0.51	0.14	6.22
3e. OClO	-0.40	0.59	8.81	0.92	0.35	7.58	1.06	0.34	6.37	-0.51	0.16	6.21
3f. No wav. calibration	-1.11	0.64	9.51	0.33	0.33	7.99	0.38	0.32	6.87	-1.03	0.15	6.59
3g. I ₀ correct all abs.	-0.30	0.55	8.89	1.02	0.32	7.57	1.10	0.32	6.34	-0.32	0.15	6.22
Polynomial degree												
4a. 4th order polynomial	0.01	0.61	9.19	1.25	0.31	7.76	1.45	0.33	6.52	-0.14	0.14	6.39
4b. 3rd order polynomial	-0.35	0.72	9.69	0.89	0.30	8.09	1.23	0.34	6.63	-0.45	0.15	6.64
Instrument corrections												
5a. No scan bias correction	0.10	0.57	8.85	1.34	0.32	7.56	1.48	0.32	6.33	0.00	0.14	6.19
5b. No undersampling	-0.17	0.56	9.17	1.05	0.33	7.71	1.29	0.33	6.53	-0.31	0.16	6.36
5c. No linear offset	-1.34	0.62	10.35	0.22	0.34	8.37	0.22	0.33	7.27	-1.59	0.14	7.77
5d. 0 order offset correction	-1.13	0.62	9.78	0.38	0.34	8.15	0.42	0.33	7.00	-1.27	0.14	7.08
5e. 2nd order offset correction	-0.24	0.56	8.84	1.07	0.33	7.56	1.19	0.32	6.36	-0.30	0.15	6.25
5f. 1/I ₀ offset correction	-1.15	0.61	9.94	0.35	0.34	8.13	0.38	0.33	6.99	-1.33	0.14	7.11

Table 4.4: Parameter effects on mean CH₂O slant columns, ± 1 standard deviation, and mean χ^2 over the entire globe, Amazon, southeast US, and remote Pacific Ocean regions (as defined in Figure 4.1). Slant column units are $\times 10^{16}$ molecules cm⁻², χ^2 are $\times 10^{-7}$.

Fit window (nm)	Global		AMA		SEUS		PAC	
	Mean	$\pm 1\sigma$	Mean	$\pm 1\sigma$	Mean	$\pm 1\sigma$	Mean	$\pm 1\sigma$
Reference retrieval	0.49	0.43	1.62	0.35	2.02	0.44	0.31	0.11
Spectral range								
BrO window								
1a. 332–359	0.50	0.43	1.57	0.36	2.03	0.44	0.32	0.11
1b. 332–359 (+ OCIO)	0.48	0.42	1.56	0.36	1.98	0.44	0.31	0.12
CH ₂ O window								
2a. 325.5–350	0.57	0.48	1.54	0.31	2.05	0.44	0.30	0.10
2b. 332–350	0.49	0.44	1.70	0.40	2.07	0.46	0.33	0.11
2c. 337.5–359	0.39	0.56	1.76	0.49	1.98	0.52	0.28	0.13
2d. 327.5–356.6	0.51	0.48	1.52	0.32	1.89	0.45	0.27	0.09
Absorber effects								
3b. O ₄	0.41	0.41	1.57	0.37	1.84	0.43	0.28	0.11
3e. OCIO	0.51	0.47	1.71	0.37	2.12	0.48	0.33	0.11
3g. I ₀ correct all abs.	0.49	0.42	1.61	0.34	2.00	0.44	0.32	0.11
Polynomial degree								
4a. 4th order polynomial	0.55	0.47	1.65	0.32	2.06	0.46	0.31	0.10
4b. 3rd order polynomial	0.58	0.51	1.62	0.32	2.11	0.47	0.31	0.11
Instrument corrections								
5a. No scan bias correction	0.52	0.43	1.61	0.34	1.98	0.44	0.32	0.10
5b. No undersampling	0.52	0.44	1.64	0.35	2.07	0.45	0.32	0.11

Table 4.5: Summary of mean vertical columns (units of $\times 10^{16}$ molecules cm^{-2}) for selected tests, the range of which are in sharp contrast to the variability found with the SC precursors.

Test	Global		AMA		SEUS		PAC	
	ΔSC	ΔVC	ΔSC	ΔVC	ΔSC	ΔVC	ΔSC	ΔVC
Spectral range (nm)								
BrO window								
1a. 332–359	21	1	0	−3	6	1	17	2
1b. 332–359 (+ OCIO)	49	−2	8	−4	12	−2	40	−0
CH ₂ O window								
2a. 325.5–350	190	16	35	−5	44	2	121	−2
2b. 332–350	−27	−1	−2	5	−4	3	−16	7
2c. 337.5–359	−390	−21	−98	8	−97	−2	−328	−9
2d. 327.5–356.6	−17	3	−26	−6	−14	−6	−60	−14
Absorber effects								
3b. O ₄	−46	17	11	3	6	9	−38	8
3e. OCIO	32	−4	−9	−6	−7	−5	45	−5
3g. I ₀ correct all abs.	0	2	1	1	−3	1	−8	−2
Polynomial degree								
4a. 4th order polynomial	−105	−11	23	−2	27	−2	−60	0
4b. 3rd order polynomial	16	−17	−11	0	8	−5	28	0
Instrument corrections								
5a. No scan bias correction	133	5	32	1	30	2	99	3
5b. No undersampling	45	5	4	1	14	3	13	5

Table 4.6: Summary of the reference sector correction on the retrieved CH₂O vertical columns relative to the default reference retrieval (i.e. ΔVC). The slant column differences (ΔSC) from each test are also shown for comparison. Differences are in %.

as test 3g – I_0 correcting all absorbers, with previous slant column differences on the reference retrieval of 0.03 % converting to 1.69 % in vertical columns), to those with the largest effects (test 2c – fitting in the original GOME-1 CH_2O retrieval window whose global slant column difference of -390% is reduced to just -21%). Of note, tests 2a, 2c, 4a and 5a stand out due to the much smaller relative differences when vertical columns are considered instead of slant columns. Based on the PAC study site, the vast majority of this variability can be attributed to retrievals at or around the limit of CH_2O detection. Ocean retrievals typically return very low CH_2O slant column values, with its production determined only by CH_4 oxidation rather than the spatially limited enhanced continental isoprene sources. This homogenisation effect on the CH_2O vertical columns occurs because once the slant column bias over the Pacific Ocean is subtracted, subsequent corrected slant columns are at or close to zero. Addition of a common GEOS–Chem model CH_2O background therefore simply results in CH_2O vertical columns of similar magnitude (irrespective of the spectral fitting procedure). However, whilst the reference sector method adjusts CH_2O VCs to within similar orders of magnitude, it should be noted that the overall effect is to correct for a global offset, and latitudinal variation caused by spectral interference with ancillary absorbers at high latitudes. By not discriminating spatially, the technique maintains compatibility and comparability between the various retrievals.

4.4 Summary

This chapter presented an in-depth analysis of the parameters governing the accuracy and efficacy of GOME-2 DOAS CH_2O retrievals. Testing has shown the major parameter influencing the minimisation of fitting residuals for CH_2O fitting to be the spectral fit window, adjustment of which is shown to produce changes in retrieved slant column between 190 and -390% globally. Polynomial order, I_0 correction, fitted ancillary absorbers and offset corrections also have a significant impact on the fit residual. Subtle effects on fit quality and CH_2O slant column are also noted with instrumental corrections, such as wavelength calibration, undersampling and

scan bias correction, although these should be probably weighted with a similarly high importance, since the CH₂O retrieval is close to the limits of the instrument's sensitivity. Reference fit settings (Table 4.1) are found to provide an optimal group of parameters for global CH₂O retrievals, based on the minimisation of error each setting is seen to provide in contrast to viable alternatives.

Investigation was undertaken to examine the potential for application of a DOAS reference derived from Earthshine spectra over the remote Pacific. This technique was intended to remove the negative bias in retrievals by including an amount of the retrieved absorber in the reference. Complications related to the Ring effect and wavelength calibration prevent fitting residuals matching those of a well calibrated regular DOAS retrieval, although the technique displays some promise in the elimination of negative slant columns, reducing the dependence on the reference sector correction.

Vertical columns are shown to be much less sensitive to DOAS fitting parameters than their original slant columns, primarily due to application of the RSM technique. Analysis has shown that regardless of spectral fitting parameters, which often result in large slant column differences, addition of model CH₂O background columns to the bias corrected slant columns allows convergence of the final GOME-2 vertical column product to within a range of 16 to -21 % globally for the various CH₂O fitting windows. Cloud fraction is shown to have a large effect on both the monthly mean slant and vertical columns, the latter being affected by the relationship between the observed cloud top pressure and the CH₂O vertical distribution.

An ideal characterisation of various fitting parameters presented would make use of synthetic spectra with known trace gas concentrations and artefacts, allowing for a fully quantitative interpretation of error sources (e.g. Vogel et al. (2013)). However, the utility of an investigation focussing on real-life measurements continues to show value to improving retrievals from specific instruments, with Pinardi et al. (2013) recently conducting a large scale characterisation of CH₂O retrievals from a ground based multi axis DOAS instrument.

Further improvement to the GOME-2 DOAS retrieval beyond those characterised here are likely to take advantage of promising adjustments to the DOAS technique described in Lee et al. (2008) and Puķīte et al. (2010). The former method applies a weighting function DOAS technique to retrievals, with selected spectra included in the SCIAMACHY SO₂ retrieval being dependent on scene specific parameters (including location and ozone interference), in order to correct for latitudinal offsets imparted by major absorbers. Extension of the technique to other minor trace gases with similarly weak absorption signals in the far UV would likely warrant investigation in terms of additional computational overheads for the DOAS calculation, offset by the theoretical improvements in residual reduction available. The second method offers a reduction in fit residuals of up to an order of magnitude (when applied to SCIAMACHY BrO retrievals) by using wavelength dependent fit coefficients calculated for each spectra in a retrieval, applied as additional parameters in a standard DOAS fit. This should allow for an improved representation of strong absorber's optical depth change throughout its fitting region, allowing for a significant reduction in latitudinal retrieval bias in retrieval due to O₃ and BrO dependencies at high SZAs.

Chapter 5

Air Mass Factors

Slant column density measurements of trace gases are converted from concentrations representative of the absorber amount along the instrument's line of sight for a path length L , to a vertical measurement extending perpendicular from the surface to the top of the atmosphere. Removal of a measurement's dependence on its light path to represent that of a vertical column provides us with a geophysical quantity totally independent of viewing angle and the transmissive properties of the atmosphere. This expands the range of applications to which measurements can be applied to and compared with - ensuring comparability with other satellite platform measurements, and allowing their use in chemical transport models (e.g. isoprene inversions).

An air mass factor (AMF) is calculated for this purpose, defined as the ratio of absorber present in the slant column density (SCD), to that in a vertical column density (VCD) extending from the surface of the Earth:

$$VCD = SCD/AMF. \quad (5.1)$$

Application of a simple geometric AMF (AMF_G), for a planar atmosphere with no scattering processes accounts for looking through the atmosphere twice, with the solar zenith angle (Θ_S) and instrument line of sight (Θ_V) (Figure 5.1).

$$AMF_G = \frac{1}{\cos \Theta_S} + \frac{1}{\cos \Theta_V}. \quad (5.2)$$

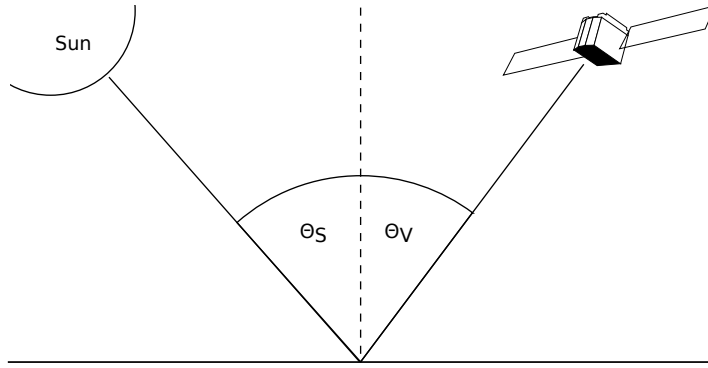


Figure 5.1: Light path and geometry for an AMF in a planar atmosphere.

Assuming the instrument is nadir viewing (applicable to GOME-2), we define AMF_G with an effective solar zenith angle Θ_E as:

$$AMF_G = \frac{1}{\cos \Theta_E} + \frac{1}{\cos 0^\circ}. \quad (5.3)$$

$$\begin{aligned} \sec \Theta_E &= \sec \Theta_S + \sec \Theta_V - 1 \\ &= AMF_G - 1. \end{aligned} \quad (5.4)$$

$$\begin{aligned} AMF_G &= 1 + \sec \Theta_E = 1 + \frac{1}{\cos \Theta_E} \\ &= \frac{1 + \cos \Theta_E}{\cos \Theta_E}. \end{aligned} \quad (5.5)$$

5.1 Air mass factors in a scattering atmosphere

The troposphere is the most chemically active region of the atmosphere. Absorption and scattering processes in this layer strongly influence paths taken by light, complicating estimates of light paths taken for satellite radiance measurements. Derivation of the light path through the atmosphere is further complicated by the sensitivity of the radiance measurement to the vertical profile of the trace gas measured.

Palmer et al. (2001) decoupled the two problems of radiative transfer in a scattering medium and its sensitivity to vertical absorber profiles, by introducing the concept of viewing the atmosphere at several levels. For each level, scattering weights are calculated by a radiative transfer model (RTM), and then integrated over the vertical height profile of our absorber of interest derived from a chemical transport

model (CTM). De-coupling the problem in this manner allows for a quantification of error sources in both parts of the AMF formulation.

We begin by considering the Beer-Lambert law, including τ_s to represent optical depth of the absorber throughout the slant column:

$$\begin{aligned}\tau_s &= \ln\left(\frac{I_0}{I}\right) \\ &= \ln I_0 - \ln I.\end{aligned}\tag{5.6}$$

As optical depth is a function of absorber amount, this allows the simplification of the AMF described as a function of the slant column and vertical column (τ_v) optical depths:

$$AMF = \frac{\tau_s}{\tau_v} = \left(\frac{\ln I_0 - \ln I}{\tau_v}\right).\tag{5.7}$$

Change in radiation intensity due to atmospheric processes of absorption and scattering ($\Delta I = I - I_0$) is re-written to approximate τ_s :

$$\ln I_0 - \ln I = \ln\left(1 - \frac{\Delta I}{I}\right).\tag{5.8}$$

And inserted into the AMF equation, appropriate for (assumed) optically thin absorbers ($\Delta I / I < 1$):

$$AMF = \frac{\ln\left(1 - \frac{\Delta I}{I}\right)}{\tau_v}.\tag{5.9}$$

This may be simplified by approximating τ_s as:

$$\ln\left(1 + \left(\frac{-\Delta I}{I}\right)\right) \simeq \frac{-\Delta I}{I},\tag{5.10}$$

and re-writing the AMF to account for this:

$$AMF = \frac{-1}{\tau_v} \frac{\Delta I}{I}\tag{5.11}$$

Change in observed radiance (∂I) is expected with a changing optical thickness ($\partial \tau$) throughout the atmosphere, represented by:

$$\Delta I = \int_0^{\tau_v} \frac{\partial I}{\partial \tau} d\tau. \quad (5.12)$$

Giving a new definition of the AMF observing this change:

$$AMF = \frac{-1}{\tau_v} \frac{1}{I} \int_0^{\tau_v} \frac{\partial I}{\partial \tau} d\tau. \quad (5.13)$$

Allowing the ratio of change in observed intensity to change in optical depth to simplify to:

$$\frac{\partial \ln I}{\partial \tau} = \frac{1}{I} \frac{\partial I}{\partial \tau}, \quad (5.14)$$

The adjustment of equation 5.13 follows:

$$AMF = \frac{-1}{\tau_v} \int_0^{\tau_v} \frac{\partial (\ln I)}{\partial \tau} d\tau. \quad (5.15)$$

Now the dependency of τ on absorbers throughout the atmospheric path length is introduced, with σ as the absorption cross section of trace gas in question, n the number density (concentration of absorber), and dz optical depth of the layer z :

$$d\tau = \sigma n dz, \quad (5.16)$$

Which inserted into equation 5.15 becomes:

$$AMF = \frac{-1}{\tau_v} \int_0^{\tau_v} \frac{\partial (\ln I)}{\partial \tau} \sigma(z) n(z) dz. \quad (5.17)$$

For the purposes of the AMF, an effective cross section (σ_e) is used, scaled to the optical depth by introducing an average concentration of absorber expected in

the vertical column (Ω_v), measured in molecules / cm^{-2} :

$$\sigma_e = \frac{1}{\Omega_v} \int_0^{\tau_v} \sigma(z) n(z) dz. \quad (5.18)$$

And allowing for the optical depth of the entire measured column:

$$\frac{1}{\tau_v} = \frac{1}{\Omega_v \sigma_e} \quad (5.19)$$

Equation 5.17 now incorporates σ_e , within which, the below decoupling of scattering weights ($w(z)$ in blue) and absorber profile as a function of the scattering weights, also known as the shape factor ($S(z)$ in green), can be identified:

$$\begin{aligned} AMF &= - \int_0^{\infty} \frac{\partial(\ln I)}{\partial \tau} \frac{1}{\Omega_v \sigma_e} \sigma(z) n(z) dz \\ &= - \int_0^{\infty} \frac{\partial(\ln I)}{\partial \tau} \frac{\sigma(z)}{\sigma_e} \left(\frac{n(z)}{\Omega_v} \right) dz. \end{aligned} \quad (5.20)$$

Scattering weights are calculated as follows:

$$w(z) = \frac{-1}{AMF_G} \frac{\partial(\ln I)}{\partial \tau} \frac{\sigma(z)}{\sigma_e}. \quad (5.21)$$

With the normalised shape factor:

$$S(z) = \int_0^{\infty} \frac{n(z)}{\Omega_v} dz. \quad (5.22)$$

Arriving at the final scattering AMF implementation applied in this work:

$$AMF = AMF_G \int_0^{\infty} w(z) S(z) dz. \quad (5.23)$$

In a clear sky situation with only Rayleigh scattering to account for, $w(z)$ is calculated as a function of viewing geometry, surface albedo from which radiation is

backscattered, and surface pressure and sensing wavelength to define the absorbing trace gas vertical profile. The provision of $w(z)$ for air masses including cloud or aerosol introduces Mie scattering, and its associated dependencies on particle size and shape to the scattering weight calculation.

The second component, shape factor (S) is derived from a vertical profile of the absorber of interest provided by an offline CTM; representing the absorber concentration on the σ pressure coordinate system. The vertical coordinate σ is used in place of z for CTM calculations, as chemical reactions are more reliably modelled as a function of pressure than optical depth. σ is defined extending from the Earth's surface pressure as the base of the coordinate, to the top of the atmosphere with a pressure of 0. As surface pressure varies across the globe, this must be accounted for in the AMF calculation with a scene specific surface pressure obtained from a digital elevation model. Scattering weights $w(z)$ are mapped to the CTM σ pressure grid to maintain consistency in the calculation by conversion with the hydrostatic equation to give $w(\sigma)$.

From this AMF definition, a few basic principles can be observed, and go some way to explaining the difficulty associated with constraining CH_2O VCD measurements, the bulk of which resides in the lower troposphere. Radiation at shorter wavelengths has a large scattering optical depth; therefore UV scattering occurs at higher altitudes than for longer wavelength light. The initial work of Palmer et al. (2001) confirmed these facts with findings summarising the scattering AMF to approximately half that of AMF_G .

Geographic variation of AMFs are accounted for by calculating the AMF based on gridded approximations of geophysical parameters influencing the observed radiance measurement. Horizontal grid resolution is determined by offline AMF inputs provided by CTMs (themselves limited by resolution of input meteorological data) and surface albedo datasets. Palmer et al. (2003) showed the generation of CH_2O from isoprene occurs within 30 minutes under temperature regimes expected for elevated isoprene emissions. In CH_2O 's source regions, a mean wind speed of 20 km / h,

limits the spatial scale over which CH_2O can be distributed to between 10–100 km. This displacement effect and associated uncertainty with source attribution limits gains to be made from increased spatial resolutions of satellite mounted detection instruments (Millet et al., 2006), with the OMI and GOME-2 instruments already operating within this threshold.

5.2 AMF implementation

The baseline University of Leicester (UoL) AMF algorithm is presented, based on the above scattering AMF definition. Beginning with the GEOS-Chem chemical transport model for provision of vertical trace gas mixing ratios (Bey et al., 2001), its choice determines the AMF’s subsequent definition of the horizontal (longitude and latitude) and vertical (pressure levels) grids, whilst scattering weights are provided by the LIDORT radiative transfer model (Spurr et al., 2001) for each observation.

5.2.1 GEOS-Chem overview

Version 8-03-01 of the GEOS-Chem global chemical transport model is used to simulate tropospheric chemistry at global and regional scales, with input data for the UoL AMF at a resolution of 4° latitude \times 5° longitude. Vertical dimensions are set to 47 pressure levels from the surface to 0.01 hPa, with the lowermost layers of the model (surface \lesssim 2 km) approximated by 14 layers, the model time-step is 1 hour. The model is driven by meteorological fields provided by NASA’s Goddard Earth Observing System version 5 (GEOS-5) atmospheric model (Rienecker et al., 2008), updated with mean 3D (those which vary between pressure levels) chemistry fields on a 1 hour time-step, and 0.5 hour mean fields for horizontal meteorology variables (z is invariant) (see Yantosca (2013) for a full description of GEOS-Chem 2D input grids). Barkley et al. (2011) (section 2.1 and references therein) provide a detailed description of model transport and chemical calculation schemes.

GEOS-Chem is a widely used and well evaluated chemical transport model rou-

tinely used in studies for global and regional calculations of CH₂O (Palmer et al., 2001, 2003; Shim et al., 2005; Palmer et al., 2006; Fu et al., 2007; Palmer et al., 2007; Barkley et al., 2008, 2011, 2012a, 2013) and NO₂ concentrations (Martin et al., 2002, 2004). Vertical profiles are calculated with GEOS-Chem taking into account aerosol and major chemical species (O₃, NO_x and VOCs) interactions. Input emission inventories are taken from the global MEGAN BVOC and EDGAR anthropogenic greenhouse gas emissions databases (Guenther et al., 2006; EDGAR, 2011); which are regionally overwritten with more detailed models for Europe (EMEP - Vestreng and Klein (2002)), Mexico (BRAVO - Kuhns et al. (2003)), South East Asia (Streets et al., 2003) and North America (United States Environmental Protection Agency (2013); Environment Canada (2013)). Regional anthropogenic emission databases are also included (see *Anthropogenic emissions - GEOS-Chem* (2013) for full details), as are pyrogenic emissions from the Global Fire Emissions Database version 2 (Randerson et al., 2007). Updates to the model from the ‘out of the box’ settings include addition of dry and wet deposition schemes for chemical species relevant to CH₂O (including isoprene). With the above settings, GEOS-Chem is used to provide daily mean vertical CH₂O mixing ratio profiles and aerosol optical depths appropriate to GOME-2’s local overpass time set to between 09:00–10:00, for each 4° × 5° grid box.

5.2.2 LIDORT overview

Scattering weights are generated with the LIDORT radiative transfer model, version 2.3 (Spurr et al., 2001; Spurr, 2001), specific to each GOME-2 scan. From the top of the atmosphere towards Earth’s surface, each atmospheric layer in the model is described as a homogeneous medium containing scattering particulates acting to re-direct, and in the case of aerosols, absorb energy. Scattering particles in the model include aerosol profiles supplied by GEOS-Chem, and number density profiles of major absorbers (O₃ and NO₂) based on the U.S. standard atmosphere climatology, interpolated to GEOS-Chem pressure levels. The model is integrated

on a layer by layer basis, bounded at the base by a reflecting surface with a pre-specified Lambertian reflectance (the reflectivity of a surface scattering equally in all directions required to provide a radiance at the top of a pure Rayleigh scattering atmosphere). Outputs are provided as scattering weights at the top of a plane parallel atmosphere in an upwelling direction, for the user defined viewing and solar zenith geometries. LIDORT outputs scattering weights on a different vertical grid to that used by GEOS-Chem, therefore requiring LIDORT scattering weights to be interpolated to the GEOS-Chem σ vertical coordinate.

The reflecting surface at the base of the RTM is specified from an albedo value derived from the Herman and Celarier (1997) Total Ozone Mapping Spectrometer (TOMS) minimum Lambert equivalent reflectance database. This simplifies the reflecting surface by describing it as an isotropic reflector, scattering uniformly in all directions, thereby ignoring angular dependencies on scattering introduced by viewing geometries. Partially cloudy scans are taken into account by the independent pixel approximation (IPA) method (Martin et al., 2002), acting to scale the AMF as a proportion of cloud present in the scene, with cloud top reflectivity treated as a Lambertian reflector with an albedo of 0.8. Cloud fraction and cloud top pressure are taken from the most recent version of the GOME-2 FRESCO+ cloud product, included in the GOME-2 L1B files (Wang et al., 2008). FRESCO+ does not calculate cloud optical thickness (COT) values, which for the purposes of our AMF necessitates all clouds to be approximated as Lambertian reflectors, a method consistent with previous work lacking COT values (Barkley et al., 2012a; De Smedt et al., 2012). Following the notation of Martin et al. (2002), AMFs representing partially cloudy scenes derived with the IPA require clear sky and cloudy AMFs (AMF_{cs} , AMF_{cld}), clear sky and cloudy albedos (ALB_{cs} , ALB_{cld}) and cloud fraction (CF) as input:

$$AMF = \frac{AMF_{CS} \times ALB_{CS} \times (1 - CF) + AMF_{CLD} \times ALB_{CLD} \times CF}{ALB_{CS} \times (1 - CF) + ALB_{CLD} \times CF}. \quad (5.24)$$

Six aerosol types (mineral dust, tropospheric sulphate, black carbon, organic carbon,

sea salt and water cloud) taken from Martin (2002) at 400 nm (appropriate to NO_2) are used to generate vertical profiles of aerosol optical depths rescaled to 340 nm. LIDORT uses these profiles in concert with pre-defined extinction coefficients, effective aerosol radii, single scattering albedos and phase functions, specific to each aerosol type, for the construction of an atmospheric model from which to derive scattering weights.

5.2.3 Baseline UoL AMF

Using the above UoL AMF input parameters, AMFs are calculated specific to GOME-2 for March and August 2007, chosen to reflect the range of expected tropospheric CH_2O concentrations. Global formaldehyde concentrations in March are at or near an annual minimum, whilst concentrations from August show evidence of seasonally elevated quantities over the South East U.S., as identified in earlier work (see Chapter 4). Figure 5.2 shows monthly mean AMFs and subsequent CH_2O VCDs for the two months, gridded to 0.25° . In the AMF plots, the coarse grid of a-priori CTM data is immediately apparent over the Western Sahara and Himalayas, whilst regions of elevated AMFs lacking the grid structure account for partly cloudy and aerosol affected scans. Formaldehyde VCDs are presented with the reference sector method applied, displaying hotspots over tropical biomes, as well as seasonal elevations of S.E. U.S. and S.E. Asian emissions.

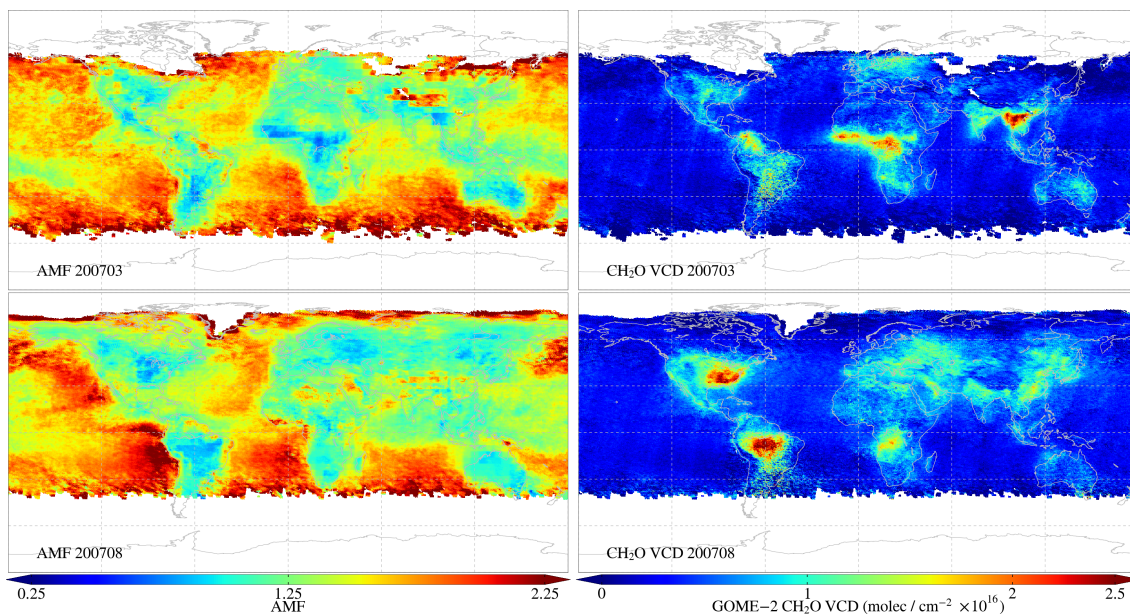


Figure 5.2: Monthly mean UoL baseline AMFs calculated with $4^\circ \times 5^\circ$ GEOS-Chem CTM gridded inputs, and subsequent CH_2O VCDs for the months of March and August 2007, gridded to 0.25° .

5.3 UoL AMF input parameter comparisons

A brief summary is provided of the state of the art in AMF calculations, looking at formaldehyde and tropospheric NO_2 retrievals, with the DOAS fit region of the latter gas (400–420 nm) especially close to the CH_2O retrieval used here (see Chapter 4). Whilst the basic method of calculation remains the same for all AMFs (e.g. that of Palmer et al. (2001)), they differ widely in temporal and spatial resolution of databases called upon to provide a priori parameters.

AMF wavelength CH_2O AMF calculations are performed at a wavelength representative of their respective slant column fitting windows, with the De Smedt et al. (2012) CH_2O retrieval calculating AMFs at 340 nm for a DOAS slant column fitting region of 328.5 – 346 nm. With the AMF calculated for a central wavelength representative of the entire fitting region, Barkley et al. (2012a) note AMF variation of approximately $\pm 5\%$ between the upper and lower window limits, demonstrated here in Figure 5.3 with a clear sky AMF calculation for a moderately high modelled CH_2O mixing ratio representative of values expected over the tropics. To this end, further accounting for strong

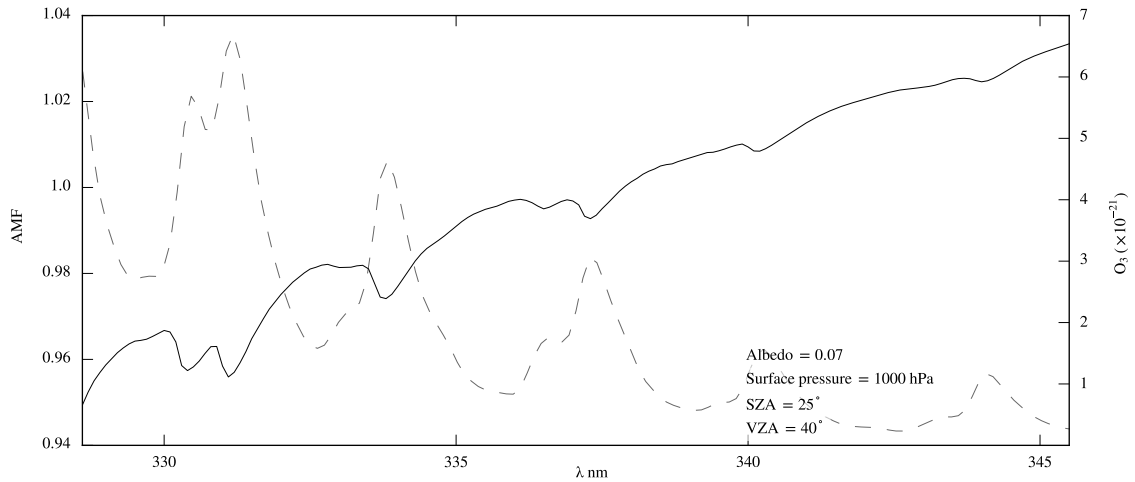


Figure 5.3: Sample clear sky (no cloud or aerosol correction) AMF plotted as a function of wavelength, with the O_3 absorption cross section at 228 K underlain (dashed line) to detail the close correlation with the latter’s absorption strength on the AMF.

UV absorption in the far UV end of the DOAS fit window, the De Smedt et al. (2012) GOME-2 slant column fit applies a series of weighting functions to the O_3 cross sections based on AMF variation due to O_3 absorption strength, tabulated as a function of SZA. Here, the AMF is calculated at 340 nm, marking a central value in the wavelength window, and maintaining consistency with the GEOS-Chem aerosol optical depth product used in scattering weight derivation.

Look up tables – All current AMF calculations detailed in the literature derive AMFs from pre-calculated look up tables (Boersma et al., 2011; Russell et al., 2011; Valks et al., 2011; De Smedt et al., 2012), the resolution of which represents an initial limiting factor in the derivation of an accurate AMF. Taking advantage of increases in computing storage and processing capacity, the implementation of the AMF algorithm shown in this work differs from those above by discarding the LUT approach; and instead calculating AMFs on a per-scan basis, removing the potential for introduction of LUT interpolation error.

Albedo database – The importance of using an accurate albedo product in AMF calculations has been cited as one of the most significant factors in reducing

AMF error (Boersma et al., 2004; Kleipool et al., 2008; Zhou et al., 2010), providing the reflecting surface to the base of the RTM. Albedo products are taken from a variety of sources, not all native to the instrument for which the AMF is calculated; no albedo datasets are yet available for GOME-2. This forces recourse to the use of either a high resolution database such as the Kleipool et al. (2008) OMI monthly product (with a local overpass time of approximately 13:30), or use of the Herman and Celarier (1997) TOMS albedo climatology product (original grid size $1^\circ \times 1.25^\circ$). Neither solution offers an ideal compromise, but in the initial AMF calculation, we apply the TOMS product (degraded to CTM grid size) for consistency with its use in the GEOS-Chem CTM. The Russell et al. (2011) OMI retrieval uses a very high resolution albedo dataset taken from a MODIS 16 day mean albedo product, acting to significantly reduce spatial and temporal bias; although inappropriate for CH_2O retrievals with the product unavailable at wavelength ranges lower than used for NO_2 retrievals (~ 410 nm).

Topography – Topography databases are required by AMF algorithms for derivation of surface pressure, providing the base of the σ pressure grid. Due to the requirement for an accurate specification of the vertical coordinates on which to calculate trace gas mixing ratios at the correct levels throughout the atmosphere, the accuracy of input terrain database is critical to the AMF. All contemporary AMF algorithms make use of high resolution terrain databases for this calculation in the range of 1 km^2 to 3 km^2 (Boersma et al., 2011; Russell et al., 2011; Valks et al., 2011; De Smedt et al., 2012), although in the initial AMF presented here, GEOS-Chem pressure values are taken directly from the CTM, derived from the GEOS-5 surface geo-potential database at model resolution.

CTM – A-priori vertical profiles are generated with CTMs, with the majority of contemporary retrievals making use of in-house models (Boersma et al., 2011; Russell et al., 2011; Valks et al., 2011; De Smedt et al., 2012), run at horizontal

resolutions between $4\text{km} \times 4\text{ km}$ and $4^\circ \times 5^\circ$, and output for between 32–35 vertical levels up to the tropopause. Groups differ widely in temporal CTM resolution, with monthly means (Valks et al., 2011) and daily profiles (Boersma et al., 2011; Russell et al., 2011; De Smedt et al., 2012; Barkley et al., 2013) both in use; with the latter expected to provide a more detailed evolution of tropospheric chemistry. Valks et al. (2011) quantified the AMF uncertainty due to monthly CTM fields by comparing against daily values calculated over the same time frame, finding monthly fields introduced a 10% error for tropospheric NO_2 AMFs.

5.4 UoL AMF development

Sensitivity of the AMF to its fundamental input parameters is well documented (Palmer et al., 2003; Boersma et al., 2004; Martin et al., 2004; Millet et al., 2006). In the initial exposition of the scattering AMF, Palmer et al. (2001) characterised the AMFs response to viewing geometry, demonstrating a 20% increase in the range of AMFs calculated for SZAs between 0 and 65° . Improvements in accuracy for the viewing geometry portion of AMF calculations are dependent on an increase of accuracy in the instrument’s ability to measure it’s own axes, and are thus unlikely to improve beyond GOME-2’s given pointing accuracy of 0.5% (Siddans et al., 2003).

Aerosol

With the AMF algorithm already accounting for cloud effects as detailed above, further light path modifications due to scattering are introduced by aerosol in the observed column. The majority of retrievals highlighted in section 5.3 rely on aerosol corrections implicit in cloud retrievals with the same instrument. This technique assumes aerosols present in the atmosphere will encourage a higher cloud fraction and lower cloud top pressure to be calculated than would be ordinarily be observed for a clean atmosphere, with the independent pixel approximation then accounting for the aerosol through a modified AMF (Boersma et al., 2004). This method is

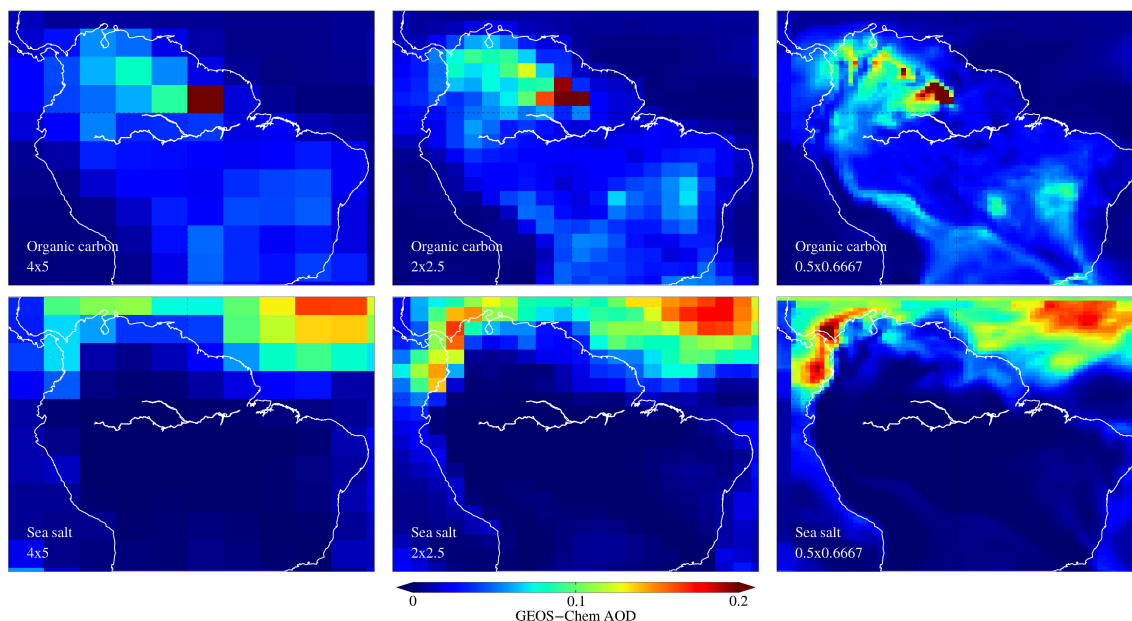


Figure 5.4: Sample model aerosol optical depths calculated with GEOS-Chem for 21st March 2007, at the three different CTM resolutions tested in this work. Also included in the AMF calculation, (but not shown here), are mineral dust, SO_2 and black carbon.

thought to be reliable because the cloud retrieval algorithm does not distinguish between clouds or aerosols in determining cloud parameters, providing a simple measure of all media acting to screen reflected radiances.

Testing this assumption, an explicit aerosol correction in the Boersma et al. (2011) NO_2 retrieval is applied, with OMI observations correlated to MODIS Aqua aerosol optical depths (AODs) measured approximately 15 minutes earlier (for clear sky scenes only). The ratio between the original AMF and an AMF calculated taking the MODIS AOD into account, is applied as a correction factor, showing AMFs calculated without the explicit aerosol correction go some way to correcting for aerosols. However in high aerosol loading situations the simplified $\text{O}_2\text{-O}_2$ CF aerosol correction fails to account for as much as 20% of the aerosol modified AMF. Similar work conducted for GOME-2 shows this also to be the case for cloud retrievals with the FRESCO+ algorithm, with cloud free scans yielding a cloud fraction found to be representative of aerosol fraction (Wang et al., 2012).

In this work, the method of Palmer et al. (2003) is followed in accounting for aerosol effects, passing vertical aerosol optical depth (AOD) profiles of pre-specified

aerosol types to the LIDORT RTM to be used in generation of the model atmosphere (Figure 5.4); scattering weights are then calculated taking this extra scattering source into account. AOD profiles from the GEOS-Chem model are applied, generated with the same GEOS-5 meteorological database as used for trace gas mixing ratio vertical columns. Untested modifications to the aerosol correction as applied here are currently limited to the replacement of aerosol data-sets from GEOS-Chem derived to the ECMWF MACC aerosol re-analysis product (Morcrette et al., 2009; Benedetti et al., 2009). As the MACC product is derived in a similar fashion to that of GEOS-Chem, albeit utilising ECMWF meteorological fields in place of the GEOS-5 database, the product is subject to a similar set of error sources in its calculation as already encountered with the GEOS product. For this reason, testing of the MACC aerosol product in the UoL AMF is intended for future work, noting varying results may arise as a result of differing MACC input emission inventories. The optimum solution would be to use collocated aerosol observations as for the Boersma et al. (2011) correction. The AATSR sensor onboard MetOp-A is suited to these types of aerosol measurements with successful aerosol retrievals made for the SYNAER product from GOME-1 and SCIAMACHY (Holzer-Popp et al., 2008), although to date an equivalent GOME-2 product has yet to be published.

Trace gas vertical profiles

For NO_2 and CH_2O , the accuracy of CTM generated vertical profiles has been investigated (Martin et al., 2004; Millet et al., 2006; Barkley et al., 2012a). In both instances, authors were able to compare shape factors calculated from trace gas column observations made in field campaigns over the South East U.S.A. and North Atlantic to those calculated with CTM provided values. Consistency between observed and modelled AMFs is high over regions investigated, validating the use of CTM provided input data for AMF generation over North America, particularly given the paucity of ground and aircraft based measurements. Further work in profile validation is required for the rest of the globe however, with uncertainties remain-

ing for bias and differences between profiles calculated away from North America. Clear sky AMFs calculated for these comparisons inspire confidence in application of standard AMF (Palmer et al., 2001), with modelled shape factors imparting a bias of $\sim 5\%$ on the AMF over the U.S.A. (Millet et al., 2006), and an estimated 20% error on AMFs over the Amazon (Barkley et al., 2012a).

Angular albedo effects

A complicating factor in the application of surface albedo as a reflecting surface on which to base the RTM, is the behaviour of the surface depending on the relationship between incident radiation and viewing angles. Albedo data in use for this work, and for other highlighted research group's AMF retrievals, all simplify the surface representation to that of a Lambertian reflector. Wide angle viewing geometries encountered with high resolution instruments such as GOME-2 and OMI, inevitably encounter shadow and illumination effects away from nadir as a function of their swath, not represented by the albedo database value passed to the LIDORT RTM. Known as surface reflectance anisotropy, or the bi-directional reflectance distribution function (BRDF), Zhou et al. (2010) accounted for this effect in a study comparing the utility of various albedo datasets, as applied to OMI NO₂ VCD retrievals. Results with the BRDF specifically accounted for indicated VCD changes of 0–3% in July for northern Europe. However conclusions from the research demonstrated the dominant control on surface reflectance VCD modulation to be choice of albedo dataset, changing the VCD by $\sim 15\%$ on the same VCD retrievals as used in the BRDF tests. Extending this study to tropical CH₂O retrievals may provide further improvements to the accuracy of the AMF calculation, although currently no BRDF or high temporal resolution albedo datasets appropriate to the GOME-2 CH₂O SCD fitting range and overpass time of MetOp-A exist.

UoL AMF improvements

Improvements to the UoL AMF algorithm are tested by implementing the following modifications:

- Increase grid resolution of CTM a-priori inputs to the AMF, in an attempt to reduce spatial artefacts such as evidence of the original CTM grid (Figure 5.2).
- Area weight grid inputs for individual scans.
- Update albedo database to high resolution wavelength dependent input.
- Introduce a high resolution topography database required for reducing bias in mountainous terrain following the method of Zhou et al. (2009).
- Incorporate the instrumental slit function to the scattering weight calculation, and account for the temperature dependency of absorption cross sections.
- O₃ vertical mixing ratio climatology to replace fixed values in scattering weight calculations.

5.4.1 A-priori input grid resolution

GEOS-Chem CTM data at $4^\circ \times 5^\circ$ are used in the baseline AMF calculations here primarily for computational efficiency. Low resolution input databases are known to lead to inaccurate AMF calculations due to misrepresentation of sub grid scale inhomogeneities – particularly for strongly geographically varying regions such as land / sea boundaries (Heckel et al., 2011). A GOME-2 pixel observes an $80 \text{ km} \times 40 \text{ km}$ footprint on the Earth’s surface; and with 4° longitude at the equator equivalent to $\sim 450 \text{ km}$, significant sampling errors are likely to be introduced. Reducing these sampling errors requires the use of higher resolution a-priori grid inputs for the AMF calculation, to the point where the satellite instrument pixel size is matched by the size of a-priori grids. Figure 5.5 illustrates this point with GEOS-Chem CH₂O VCD outputs for the Amazon nested grid region, calculated at the 3 available CTM grid

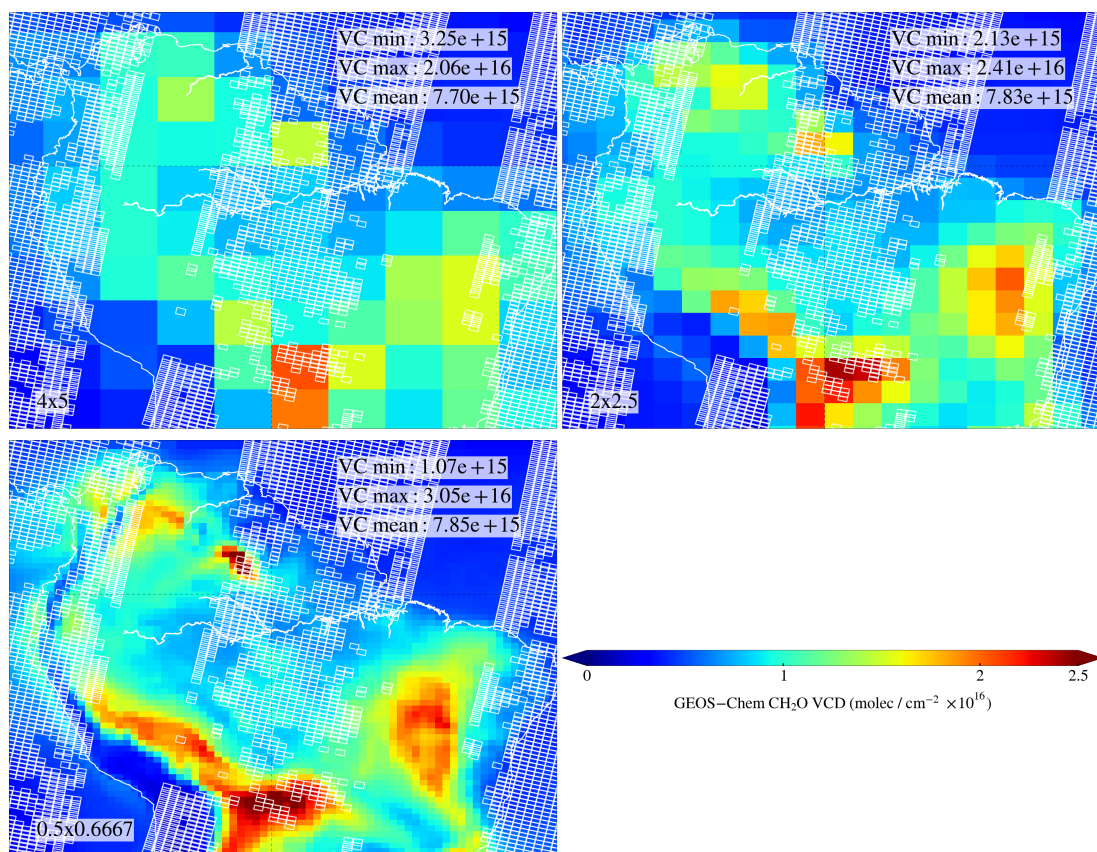


Figure 5.5: GEOS-Chem CH₂O model VCDs calculated for 21st March 2007 at the three a-priori CTM resolutions. GOME-2 forward scan pixels are overlain, illustrating the suitability (or lack) of a-priori grid sizes, with only the 0.5°×0.667° grid adequately matching a GOME-2 pixel's dimensions. Mean CH₂O VCD concentrations for the region presented are seen to rise with a reduction in CTM grid size.

sizes, and the GOME-2 scan grid (forward pixels only) overlain. For the three grid sizes, two facts are immediately apparent; only the nested grid resolution comes close to approximating the GOME-2 pixel size, and a higher resolution grid imparts a greater range of model CH₂O VCDs, due to a reduction in averaging effects.

Gridded GEOS-Chem meteorological drivers are degraded to model resolution from high resolution GEOS-5 meteorological data at 0.5°×0.667°. In addition to the 4°×5° AMF already demonstrated, CTM a-priori data is also available at 2°×2.5° and the original 0.5°×0.667° resolutions. Due to computational expense, running GEOS-Chem at the highest resolution is only possible for a subset of South America (a nested grid covering -85°W to -33.33°W longitude and 25.75°S to 14.25°N), allowing grid effects at these scales to be tested only over the Amazonian nested grid

domain. Boundary conditions for nested grid model calculations are provided by $4^\circ \times 5^\circ$ model data. Figure 5.6 compares monthly mean AMFs for March 2007 calculated with the baseline $4^\circ \times 5^\circ$ a-priori CTM inputs (top left plot) against AMFs calculated with the two higher resolution CTM datasets. The AMF differences presented in the right hand column demonstrate the capacity for higher resolution a-priori grids to better model geographic variation, with largest AMF changes evident over the Andes and coastal regions. For example, the CH_2O point source located just above the equator (see Figure 5.5), towards the mid-east of the continent, is also well represented in the higher resolution AMF, manifesting as an area of reduced AMF compared to the baseline CTM driven version. Although August 2007 AMFs are not shown here, temporal variation in CTM drivers between the two tested months show higher AMFs for March across the Amazon basin than in August. Temporal variations are driven by changes in albedo, a-priori model inputs (CH_2O mixing ratio, AOD, surface pressure and temperature), and to a lesser extent, differences in GOME-2 viewing geometry between the months.

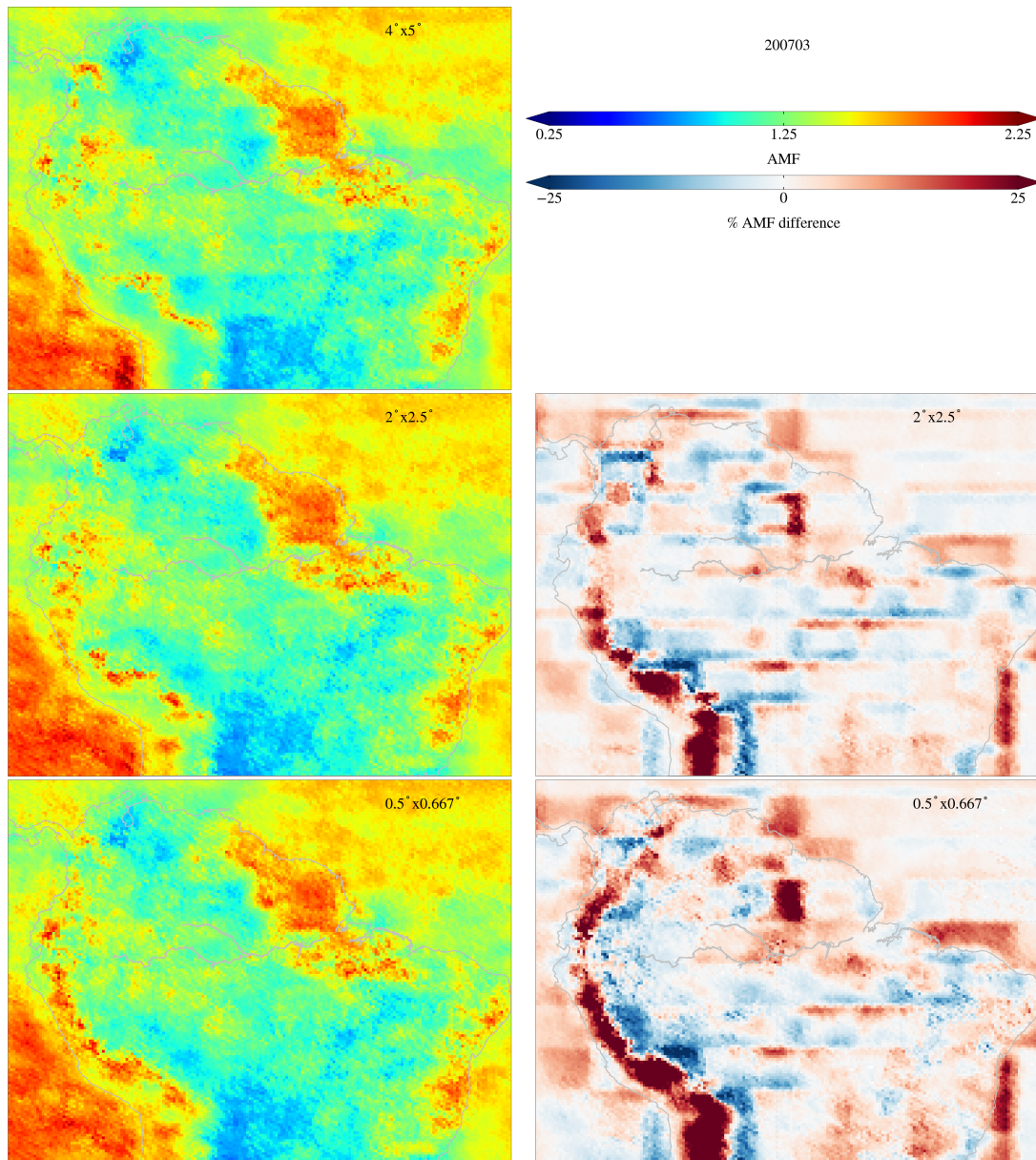


Figure 5.6: Monthly mean AMFs gridded to 0.25° for March 2007 (left hand column) at $4^\circ \times 5^\circ$, $2^\circ \times 2.5^\circ$ and $0.5^\circ \times 0.667^\circ$, with % differences of the baseline retrieval AMFs against those calculated with the two higher resolution a-priori grid inputs in the right hand columns.

Summarising a-priori grid effects, the use of higher resolution grids for AMF parameter input varies the AMF in a range of $\pm 25\%$, with Figure 5.6 showing the bulk of differences are to be found at the edges of coarse grid cells, coastline, and mountainous regions. AMFs do not show a uniform spatial response to increasing a-priori grid resolution, although finer grids clearly allow for AMF calculations with smoother horizontal gradients, acting to reduce obvious grid artefacts associated with low resolution input data. Spatial change in AMFs between CTM resolutions

is being driven by better model representation of albedo and vertical CH_2O and AOD profiles, accounting for an AMF change of around $\pm 25\%$ for strongly varying geography, whilst central Amazonian regions see more modest changes in the region of $\pm 5\%$. Were computing resources to permit availability of nested grid CTM inputs at a high resolution for the rest of the globe, their application in an upgraded AMF algorithm would be beneficial. However, as global GEOS-Chem model runs are currently only feasible at a maximum of the $2^\circ \times 2.5^\circ$ resolution, this a-priori dataset (with a halving of spatial resolution compared to the baseline UoL algorithm) represents an obvious upgrade for application in an improved AMF calculation.

5.4.2 Weighted pixel means

Testing AMF differences between the three a-priori grid resolutions is extended by incorporating area weighting of GEOS-Chem CTM inputs to provide a GOME-2 pixel averaged value, accounting for sub-pixel inhomogeneities overlooked by a pure grid cell selection algorithm (hereafter referred to as IJ). The baseline UoL retrieval (and the majority of other research group's AMF calculations) locate a satellite observation's coincident a-priori grid cell by degrading central longitude and latitude coordinates for a scan to match those of the CTM grid, and selecting the closest value from the grid. A weighted pixel mean value for each scan represents a unique averaged value for every individual GOME-2 observation based on the areal proportions of grid cells underlying the scan. Yielding a spatially constrained average of the grid cells beneath the scan should allow for a better representation of the surface the grid is attempting to simulate, particularly over regions of strong geographic variability.

Weighted pixel means are calculated by deriving the spherical polygon area of a GOME-2 scan, using the observation's four Cartesian corner co-ordinates to define polygon edges as great circle segments (see Chamberlain and Duquette (2007) for a full mathematical description). CTM grid longitude and latitude vertices whose cells enclose the GOME-2 scan are also used to derive spherical polygon areas for the

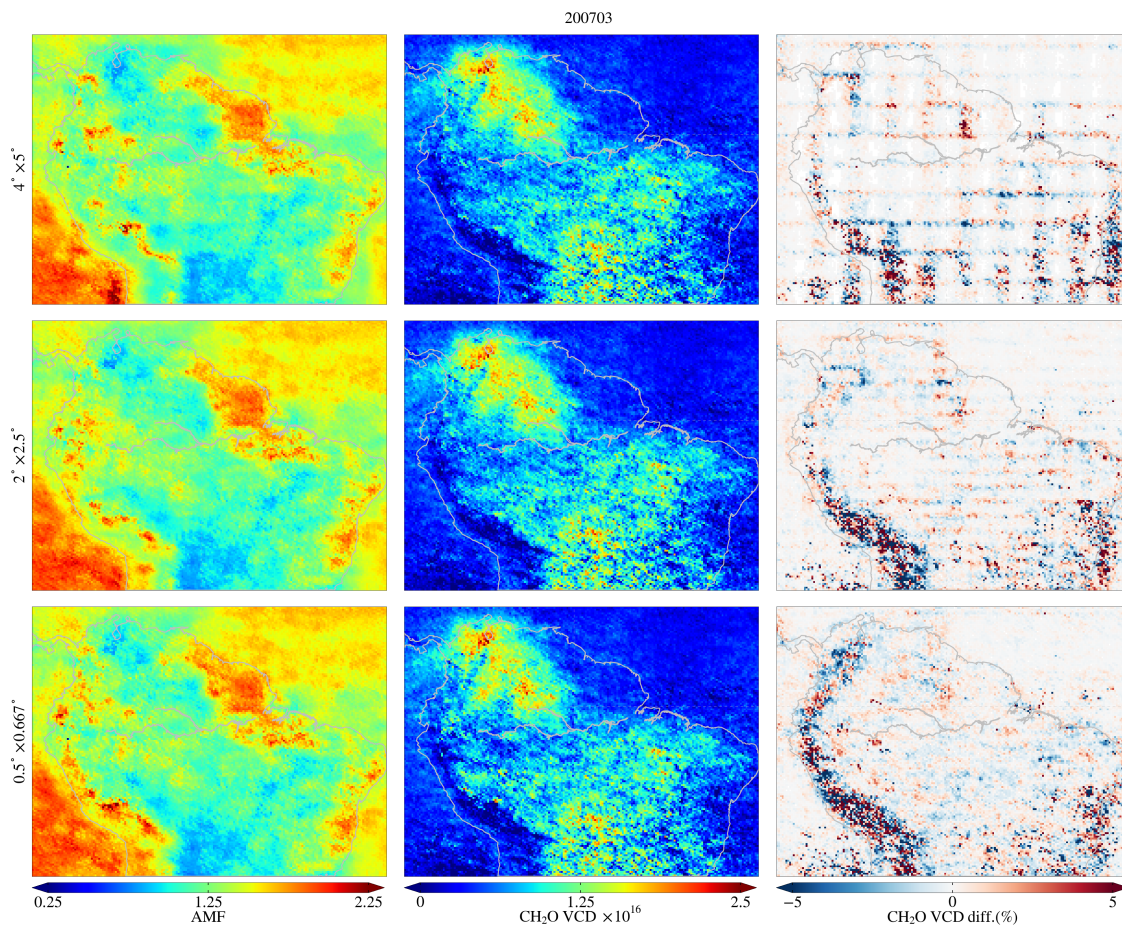


Figure 5.7: Gridded to 0.25° , the effect of the pixel mean algorithm applied to all gridded inputs is displayed on AMFs (leftmost column) for March 2007 and CH_2O VCDs (central). % CH_2O VCD differences on their respective IJ VCD (rightmost column) correlate exactly to adjustments in AMF due to pixel area weighting. Coarse CTMs show most change at grid cell edges, whilst fine scale grids display less systematic gridded change, but better account for CTM variation due to mountainous terrain. Results for August 2007, not shown here, display a similar distribution and magnitude of AMF adjustment as found for the earlier month.

underlying CTM grids in the same manner. The values of each contributing CTM cell to the GOME-2 scan polygon are then added together and divided by the cell area weight to arrive at an area weighted pixel mean value specific to each GOME-2 observation. Weighted pixel means are tested here by applying the technique on all gridded inputs to the AMF algorithm for each GOME-2 scan: albedo, topography, surface pressure, temperature profiles and CH_2O and AOD profiles. Monthly mean differences (gridded to 0.25°) between IJ AMFs and pixel mean AMFs are presented in Figure 5.7 for the Amazon region covered by the highest resolution nested grid CTM.

Examining VCD differences from the pixel mean method compared to original IJ values, a clear reduction in grid bias is evident, particularly for the low and medium resolution a-priori CTM data. Values crossing the edges of grid boxes into a neighbouring cell are better approximated with the pixel mean technique, providing an AMF as a weighted sum of grid cells, whilst values from the centre of large grid cells, particularly for the coarsest grids, are left unchanged. The above results show pixel mean algorithms work best when applied to data whose resolution is several times higher than that of a GOME-2 scan, allowing for an accurate representation of the sum of sub pixel heterogeneity not accessible with larger grid sizes. For higher resolution a-priori grids, the overall effect of the pixel mean is more subtle than found for the coarse grid, with a mixed spatial pattern of increases and decreases in calculated AMF, within a small range of $\pm 5\%$. At these scales gridding effects are less noticeable as the CTM grid size reduces towards surpassing the observation size, with the majority of differences evident for mountainous regions whereby pixel means can better represent CTM variability caused by terrain inhomogeneity.

5.4.3 Updated surface albedo

Dimensionless surface albedo exhibits variation according to surface type, generally within a range of 0.01 to 0.2, except for very bright surfaces such as snow / ice and cloud tops where values are >0.8 . High albedo values imply more radiation is reflected from the surface, with a corresponding increase in AMF to represent an increased average optical path length (Leitão et al., 2010). Surface albedo does not exhibit rapid temporal fluctuations on decadal scales for most regions, especially at the scan size of the GOME-2 data in use here, permitting the use of temporally averaged products for global AMF calculations. For OMI NO₂ retrievals, high temporal and spatial resolution MODIS albedo products have been tested, accounting for scene variation across the instrument's small scan size (Heckel et al., 2011; Russell et al., 2011); although such albedo products do not extend far enough into the UV to find applicability to CH₂O retrievals. The baseline UoL AMF algorithm uses

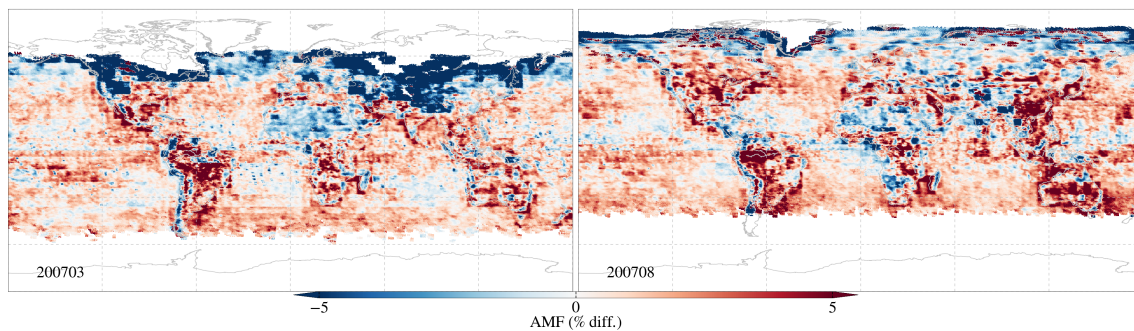


Figure 5.8: AMF differences (%) produced by the introduction of the OMI albedo database at $0.5^\circ \times 0.5^\circ$ resolution on the baseline $4^\circ \times 5^\circ$ UoL AMF. The blocky nature of the differences result from the significantly finer resolution of the OMI albedo product offering a more rapidly spatially varying reflecting surface than is possible with the baseline GEOS-Chem albedo.

a Lambert equivalent reflectivity (LER) database of monthly averages for 14.5 years of TOMS radiance data (Herman and Celarier, 1997) measured between 340–380 nm. This dataset is re-gridded from its original 1° latitude \times 1.25° longitude to match the corresponding a-priori CTM grid size.

Use of an LER database assumes the surface the albedo is attempting to model scattering equally in all directions. Work by Zhou et al. (2010) investigated the implications for assuming an LER surface through comparisons with a BRDF modified reflecting surface, finding variation of $<5\%$. More important than BRDF effects, the choice of albedo database offered up to 20% variation for the OMI NO_2 retrievals tested (November values). These findings are tested here, extrapolating to the CH_2O fitting range by taking advantage of the $0.5^\circ \times 0.5^\circ$ Kleipool et al. (2008) OMI albedo database calculated at 335 nm. Using the reference UoL AMF algorithm at $4^\circ \times 5^\circ$, the original Herman and Celarier (1997) albedo product is replaced with the high resolution Kleipool database.

A mixed pattern of differences in the AMF are seen for application of the OMI albedo when compared against those calculated with the baseline TOMS albedo. Ocean albedos are generally higher with the OMI product, but now take into account reductions colocated with changes in ocean colour extending from the coasts of western Africa and South America. Over land, albedos are also generally higher, with the exceptions of the Sahara, South Africa, and much of the boreal landmass.

As shown in figure 5.8, the albedo differences encourage a general increase in AMF of $\sim 5\%$, although reductions are noted for the previously mentioned regions with reduced albedo. These AMF changes affect CH_2O VCDs with the same spatial variation, with notable reductions in VCD for regions of enhanced CH_2O emissions.

The fine resolution of the Kleipool albedo product prevents significant gains being made for accuracy of monthly mean CH_2O values through application of the pixel mean algorithm, with spatial variability of the albedo already well captured at a sub GOME-2 scan size scale. However, pixel mean benefits will be noticed when parsing the GOME-2 VCD dataset on a scan by scan basis, by reducing the dependence of the measurement sensitivity to averaging processes designed to filter out small scale variation. Introduction of the fine scale albedo product helps to reduce gridding artefacts imparted by the coarse a-priori inputs, although in regions of enhanced CH_2O emissions, the CTM vertical profiles still clearly represent the dominant variable in the AMF calculation.

A further enhancement to albedo representation is made by applying a temporal linear interpolation on the OMI albedo product over the measurement date's two adjacent months, as applied in the OMI DOMINO NO_2 algorithm (Boersma et al., 2011b). Producing a very subtle modulation of inter-month albedo values (and consequently AMF), use of the method serves to reduce temporal bias between one month's albedo database and the next.

5.4.4 Pressure correction

Accurate surface pressure values are a critical component in the generation of CTM vertical profiles, defining the base from which CTM mixing ratios extend from. As noted in the previous a-priori grid size testing work, input parameter grid resolution carries significant potential to bias the AMF in regions of high geographic variability. Zhou et al. (2009) presented a modification to the AMF algorithm designed to mitigate for terrain bias in mountainous regions due to inadequate simulation of topography imparted by coarse input CTM grid size; applied for OMI NO_2 retrievals

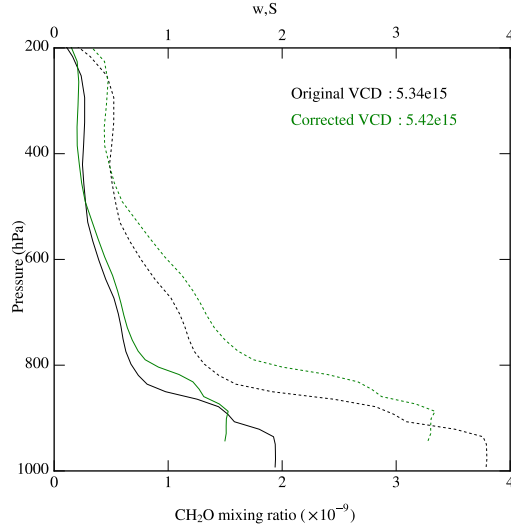


Figure 5.9: Effect of the vertical profile pressure correction for a scan over the Colombian coastline at approximately 4.5° north; with CH_2O mixing ratios (solid line) along the bottom x axis and corresponding calculated shape factor S (dotted line) on the top axis. The corrected CH_2O profile is shifted upwards and reduced in magnitude as a result of the lower surface pressure value on which to base the profile. Scattering weights are accordingly reduced, acting to reduce the AMF for this scan, and subsequently increase the CH_2O VCD.

over the European Alps. Replacing low resolution terrain inputs in the AMF model with pixel mean high resolution topography data enables application of the hypsometric equation to derive a new surface pressure value for the observed scene. The CTM σ pressure coordinates are adjusted to represent the atmosphere extending from a base defined by the new surface pressure, followed by a re-scaling of the parameters mapped to it.

The pressure correction is implemented here for CH_2O , replacing the GEOS-Chem surface pressure database derived from GEOS-5 surface geo-potential (Rienecker et al., 2008) at CTM resolution, with the $0.0083^\circ \times 0.0083^\circ$ GMTED2010 digital elevation model (Danielson and Gesch, 2011). Following the terminology of Zhou et al. (2009), this high resolution topography dataset is run through the same pixel mean algorithm previously outlined, to arrive at an area weighted effective terrain height for the GOME-2 scan h_{eff} . Corresponding CTM values of surface temperature (T_{surf}), surface pressure (p_{CTM}) and CTM terrain height (h_{CTM}) are also area weighted to provide a mean value for the observation. An effective surface

pressure p_{eff} is first derived:

$$p_{eff} = p_{CTM} \times \left(\frac{T_{surf}}{T_{surf} + \Gamma \times (h_{CTM} - h_{eff})} \right)^{-g/r\Gamma}, \quad (5.25)$$

with Γ the adiabatic lapse rate of 6.5 K / km, g as gravitational acceleration at 9.8 m/s⁻², and r dry air gas constant of 287 J kg⁻¹K⁻¹. Based on this, the tops and bottoms of layers l are defined for p_{eff} and p_{CTM} , using the original GEOS-Chem η vertical coordinate:

$$\begin{aligned} p_{CTM_b}(l) &= \eta_A(l) + p_{CTM} \times \eta_B(l) \\ p_{CTM_t}(l) &= \eta_A(l+1) + p_{CTM} \times \eta_B(l+1) \\ p_{eff_b}(l) &= \eta_A(l) + p_{eff} \times \eta_B(l) \\ p_{eff_t}(l) &= \eta_A(l+1) + p_{eff} \times \eta_B(l+1). \end{aligned} \quad (5.26)$$

With the new vertical co-ordinates, a scaling factor is calculated:

$$p_{eff_{scl}}(l) = \frac{p_{eff_b}(l) - p_{eff_t}(l)}{p_{CTM_b}(l) - p_{CTM_t}(l)}. \quad (5.27)$$

Vertical temperature profiles and CH₂O mixing ratios are then transferred to the new p_{eff} grid, and scaled with $p_{eff_{scl}}$, whilst total column AODs are preserved by interpolating values to the new grid. Figure 5.9 details a sample CH₂O profile before and after application of the pressure correction, with shape and amount of the vertical profile changing as a function of the scaling value derived for the new pressure grid.

Individual GOME-2 orbits are presented in Figure 5.10 to illustrate the effect of the pressure correction on a scan by scan basis, with differences between the coarse CTM and GMTED terrain grids immediately apparent. To evaluate the effect of the pressure correction against uncorrected values, corrected values are analysed with respect to AMFs calculated with area weighted CTM inputs (Figure 5.11), thereby isolating pressure correction as the only variable. From this, we can see that incorporation of high resolution terrain data into the AMF calculation highlights $\pm 5\%$

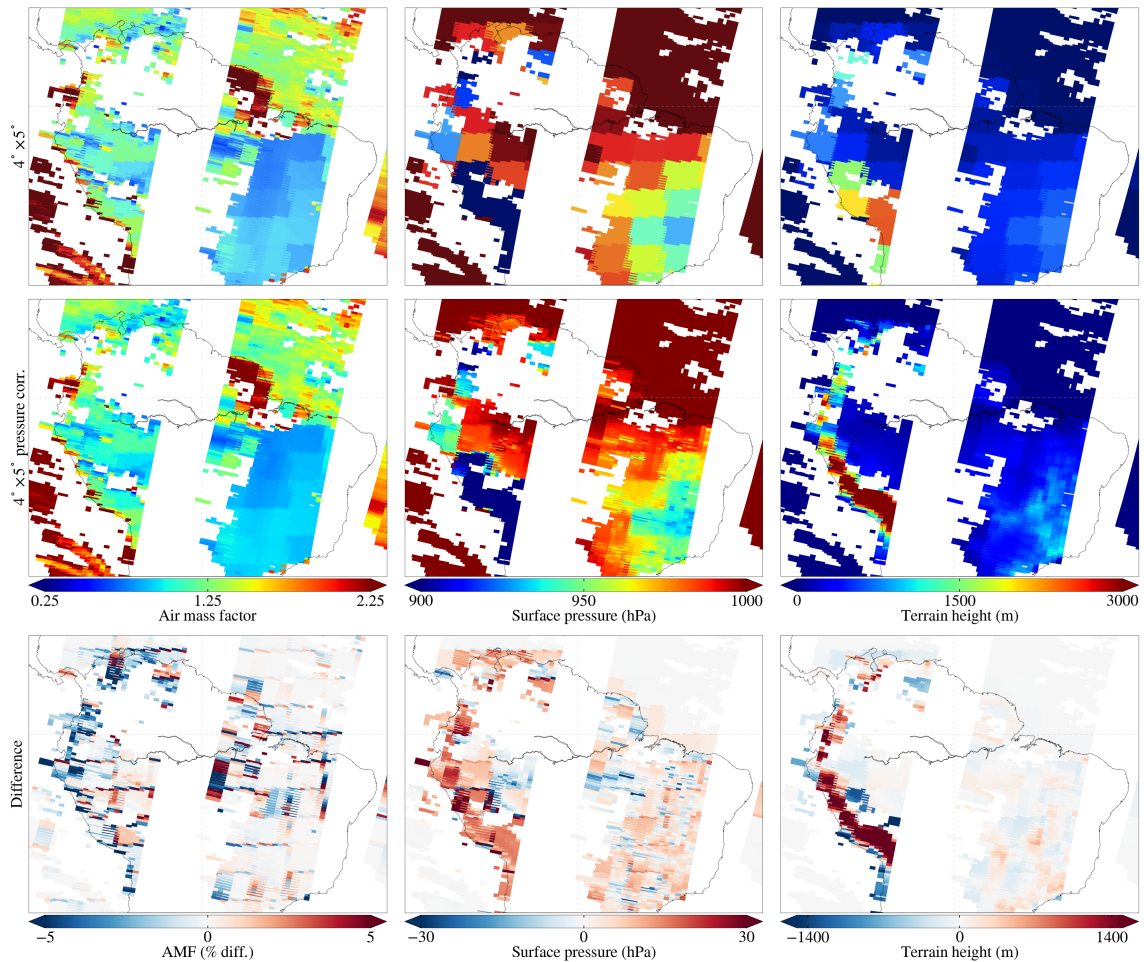


Figure 5.10: Orbits over the nested Amazon region for August 8th 2007, scans with a CF >0.4 are excluded. The effect of the pixel mean algorithm is apparent when comparing the top row of baseline $4^\circ \times 5^\circ$ IJ AMFs with the middle row's pressure corrected values. The bottom row details differences as a result of the pressure correction over elevated terrain, and to a lesser extent coastlines.

discrepancies between coarse resolution CTM terrain (and pressure grids) and the surface it is attempting to simulate, with pixel mean effects noted along CTM grid boundaries. Mountainous regions, for which the technique was originally intended to correct vertical profiles for, exhibit the largest change in AMF regardless of month, displaying typical AMF reductions of $\sim 5\%$, translating to an increase in observed CH_2O VCD. Given the importance of CH_2O profile shape for scattering weight calculations throughout the model atmosphere, this pressure correction and scaling of the profile to a more realistic value than provided with the CTM alone, represents an important component in efforts to reduce terrain and grid related errors.

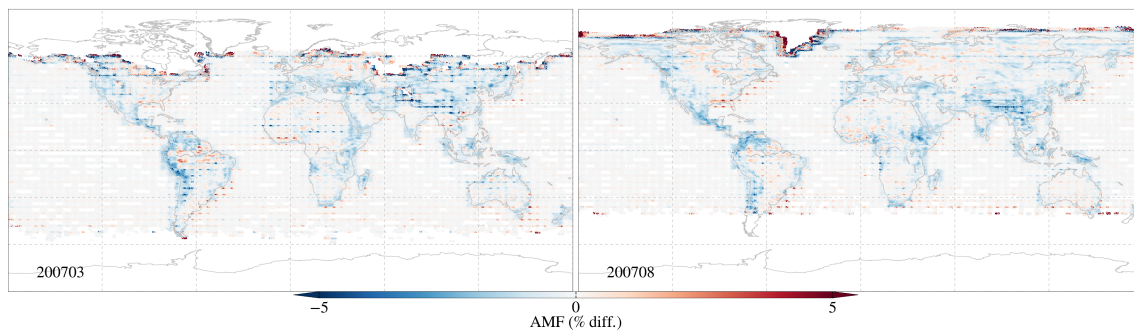


Figure 5.11: Effect of the Zhou et al. (2009) pressure correction illustrated as the difference against a fully area weighted set of AMF inputs. In this case, differences between the two tests are exclusively due to the pressure correction routine. As such, the correction is most noticeable over mountainous terrain, effecting a reduction in AMFs in the region of -5%. Noticeable gridding artefacts occur along the edges of the $4^\circ \times 5^\circ$ CTM grids, where the pressure correction causes difference in AMFs between pixel mean only pressure, and terrain corrected values.

5.4.5 LIDORT absorption cross sections

Accurate representation of absorption cross sections plays a large role in reducing fitting residuals for the DOAS fitting portion of the retrieval (Chapter 4). Applying the same philosophy to the generation of scattering weights with the LIDORT RTM, absorption spectra used in this calculation are carried through from the DOAS fitting procedure to the AMF calculation. The baseline AMF implementation generates scattering weights with CH_2O absorption spectra recorded by Cantrell et al. (1990), convolved to an arbitrary OMI slit function for an unknown orbit. This is improved on by passing Meller and Moortgat (2000) CH_2O absorption spectra convolved to the current orbit's asymmetric slit function, identical to that applied in the SCD portion of the retrieval.

Benefits of basing RTM calculations on the same cross sections as applied in the SCD portion of the retrieval should arise from the inclusion of time dependent slit function degradation throughout the instrument's lifetime. Furthermore, temperature dependency of formaldehyde is now accounted for throughout the extent of the LIDORT model atmosphere by applying temperature coefficients supplied with the original high resolution CH_2O spectra. Formaldehyde absorption cross sections and temperature coefficients are convolved to the GOME-2 slit function specific to the observation's parent orbit. These are both passed to a modified LIDORT cross

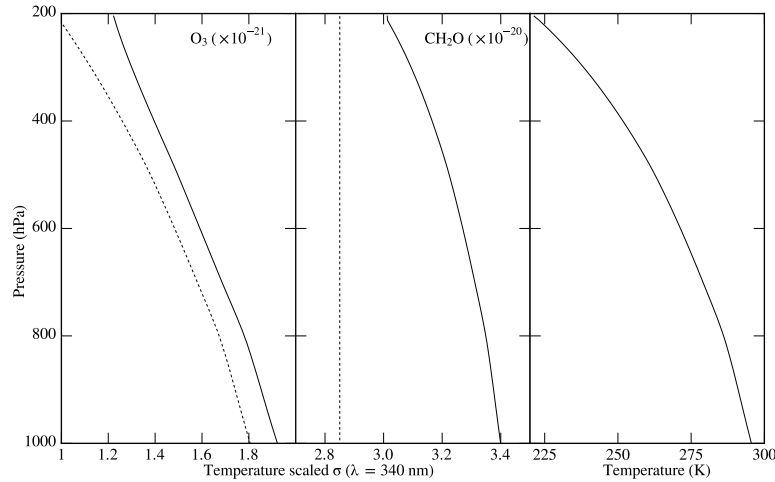


Figure 5.12: RTM absorption cross section optical depths showing original hard-coded values (dashed line), and GOME-2 orbit convolved values (solid line). Variation in σ throughout the depth of the atmosphere is due to temperature (column 3), now accounted for in the CH_2O cross section.

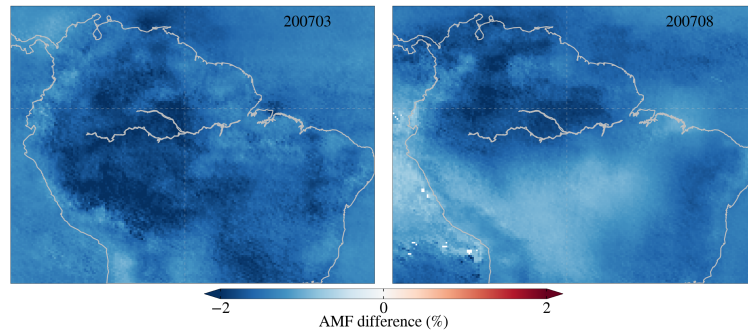


Figure 5.13: Monthly mean AMF differences on nested Amazon AMFs caused by the introduction of orbit specific CH_2O and O_3 absorption cross sections, with the former incorporating temperature dependence into the scattering weight calculation for the first time.

section generator, outputting a temperature adjusted CH_2O absorption cross section value for the calculated AMF wavelength (Figure 5.12). The same theory is applied to O_3 cross sections (although the baseline AMF RTM implementation does already account for temperature dependency of this absorber). Figure 5.12 details the effect of this change on both cross sections, as well as illustrating the fixed U.S. standard atmosphere vertical temperature profile on which the cross section temperature dependency is based.

Figure 5.13 shows a slight reduction in monthly mean AMFs of approximately -2% arising from the introduction of orbit specific absorption spectra into the RTM scattering weight calculation. Due to the close correlation with CTM CH_2O vertical profiles (e.g. Figure 5.5), the main driver of geographic variability for these

AMF differences is thought to be the modulation of RTM scattering weight generation through the introduction of the temperature dependent CH_2O cross section. With LIDORT cross sections updated to account for temperature throughout the atmosphere, a corresponding adjustment of the DOAS portion of the retrieval to incorporate a temperature dependency could well further enhance the accuracy of the first portion of the retrieval.

5.4.6 O_3 vertical mixing ratios

Profiles of CH_2O mixing ratios are provided as output from the GEOS-Chem CTM, intended to represent a geographically heterogeneous latitudinal variation of the trace gas. In the baseline UoL AMF algorithm, O_3 vertical mixing ratios are fixed to a single profile representing the U.S. standard summertime atmosphere; ignoring major spatial variation in O_3 concentration and profile. With the strength of O_3 absorption so important for scattering weight generation in the lower UV region CH_2O is fitted, the fixed O_3 VMR is likely to introduce significant errors. This is tested with the incorporation of a temporally and latitudinally dependent O_3 VMR climatology.

Using the TOMS version 8 O_3 climatology (Bhartia, 2002) as applied in the SCIATRAN v2.2 radiative transfer model (Rozanov et al., 2005), monthly ozone VMRs are provided in one of eighteen 10° latitude bands for 61 atmospheric levels, appropriate to the observation's month of year. Further tailoring of the O_3 VMR is implemented by scaling the new VMR values to coincident GOME-2 O_3 total column concentration from the DLR retrieval (Loyola et al., 2011a). These VMRs are passed to LIDORT to be applied in scattering weight generation in place of the original U.S. standard atmosphere values.

Results of the O_3 VMR substitution are presented in Figure 5.14, where large scale spatial variation is visible in the differences on the baseline retrieval for both months, with the difference closely matching the spatial distribution of O_3 . March 2007 AMFs are seen to be generally depressed in the northern hemisphere, coincident

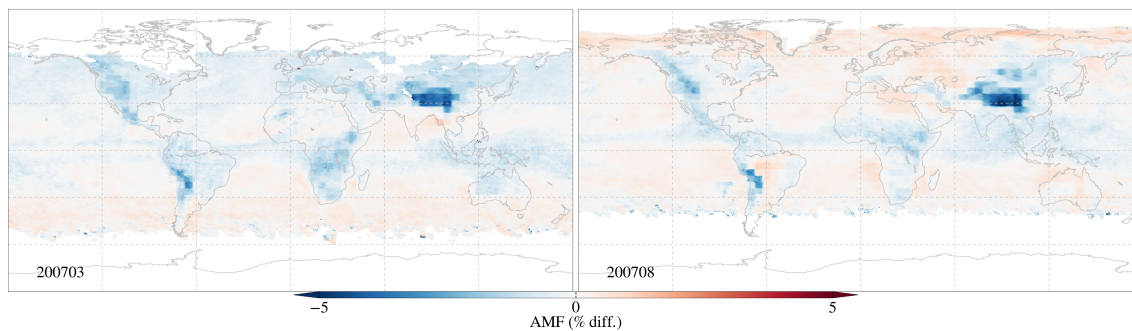


Figure 5.14: Differences imparted on the $4^{\circ} \times 5^{\circ}$ IJ retrieval by the inclusion of the TOMS O_3 climatology. As the climatology is latitudinally and temporally dependent, the two tested months exhibit differences in the distribution and magnitude of adjusted AMF as a function of the upgraded GOME-2 scaled O_3 VMRs.

with seasonally elevated total O_3 columns around the poles. For August, the same effect is not as prominent in the southern hemisphere, owing to the SZA limit on observations preventing incorporation of very low latitude observations in monthly means. Consistently reduced for both months by up to -5%, updated AMFs over mountainous terrain reflect the reduced ozone columns retrieved by the DLR product acting to scale the VMR with a dependence on topographical effects on O_3 for these regions. The AMF is shown to be highly responsive to the upgraded O_3 VMR correction; with the TOMS v8 climatology offering a control on temporal and broad scale latitudinal ozone trends, whilst small scale regional ozone features are modulated with the DLR O_3 column scaling.

5.5 Updated AMF algorithm

An improved AMF algorithm has been generated based on a combination of the above tested AMF developments. A-priori CTM inputs are increased in grid size from $4^{\circ} \times 5^{\circ}$ to $2^{\circ} \times 2.5^{\circ}$, having been shown to reduce CTM grid artefacts by way of providing a closer representation of localised CH_2O vertical profiles. The surface albedo database is updated to the Kleipool et al. (2008) OMI product at $0.5^{\circ} \times 0.5^{\circ}$, derived for 335 nm and so closely matching the AMF wavelength calculated here, with the finer spatial resolution better simulating spatial variability in albedo. Unique albedo values are provided with the OMI database on a per-

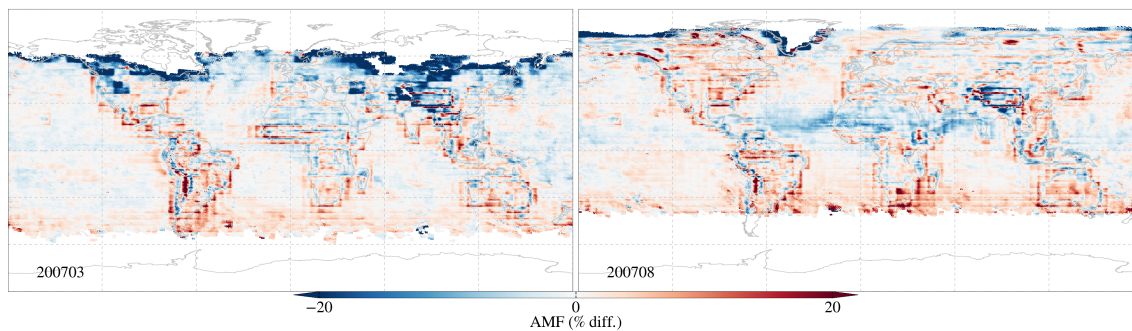


Figure 5.15: Differences between monthly mean AMFs calculated with the baseline UoL AMF, and the final UoL AMF algorithm taking into account upgrades tested and presented. The finer grid of the $2^{\circ} \times 2.5^{\circ}$ CTM provides the majority of change in AMF distribution, with the O_3 climatology correction also evident in the August plot. Changes in AMF magnitude are noted around coastlines and significant mountain ranges, in part effected by the pressure correction of vertical profiles, and to a lesser extent, pixel averaging of coarse gridded CTM inputs in these areas.

observation basis, as area weighted means for the present AMF calculation. This better reflects sub-pixel scene inhomogeneity, particularly over coastlines; additionally, a temporal interpolation is performed to reflect inter-month albedo change (Boersma et al., 2011b). The Zhou et al. (2009) pressure correction for AMFs over mountainous terrain is included, necessitating the use of weighted pixel means for all CTM inputs, and so providing a better approximation of terrain variability by scaling absorber profiles to match a surface pressure value, newly derived with enhanced accuracy from the high resolution DEM. CH_2O and O_3 absorption cross sections convolved to each orbit's asymmetric slit function are carried through from the DOAS portion of the retrieval for use as RTM inputs for scattering weight calculation, also taking into account the temperature dependency of CH_2O . TOMS ozone VMR climatology values replace the previously hardcoded O_3 VMRs, which in conjunction with observation specific scaling to the GOME-2 measured O_3 column, adjust the AMFs through use of ozone scattering weights appropriate to the measurement's time and location.

Differences of the improved UoL AMF against the baseline implementation are illustrated in Figure 5.15. Change in CTM grid size represents the largest driver of global AMF change comparing new to old, with the upgrade to a $2^{\circ} \times 2.5^{\circ}$ CTM manifesting in a gridded appearance. Upgrading the albedo database to the high

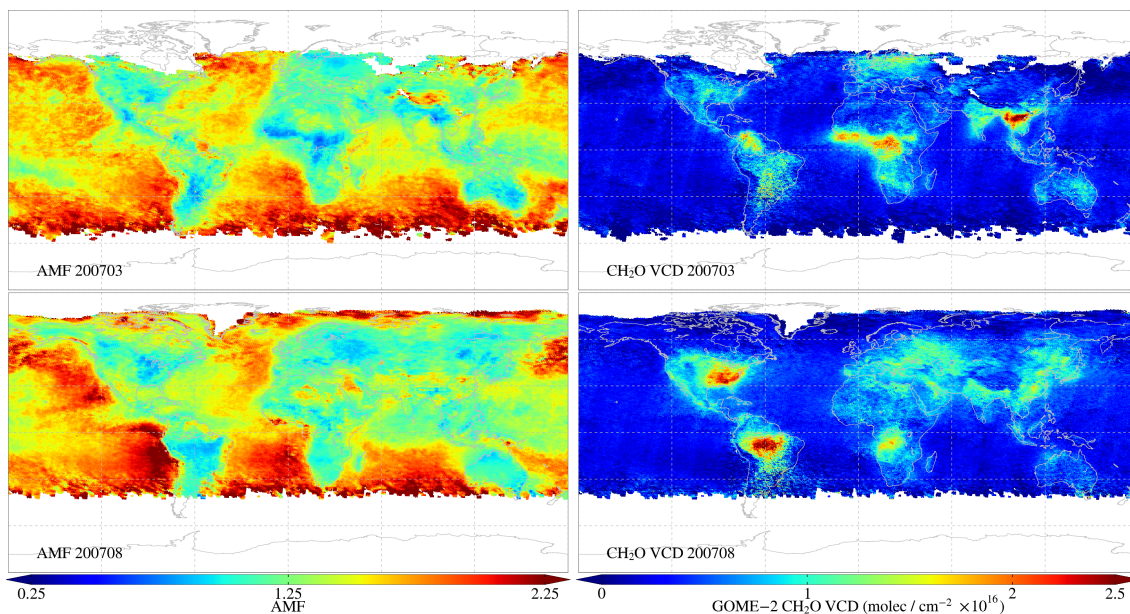


Figure 5.16: Calculated with the AMF algorithm taking into account all of the implemented upgrades, monthly mean AMFs and subsequent CH_2O VCDs are presented for March and August 2007, gridded to 0.25° .

resolution OMI product represents the other major change on global AMF calculations, with its use correlating to general AMF increases. Pressure corrections over mountainous terrain force reductions in the AMF of $\sim 5\%$, due to the rescaling of CTM vertical profiles – proving particularly relevant for elevated Amazonian CH_2O emissions directly eastwards of the Andes. Impacting AMFs in mountain regions are the updated O_3 vertical mixing ratios, visible in both month’s difference plots with reduced AMFs over the Himalayas and Andes. The ozone correction also acts to provide a more subtle global AMF modulation in concert with the latitudinal and temporal variation of the TOMS climatology. Finally, AMF reductions of $\sim 2\%$ are included due to the application of orbit specific absorption cross sections for scattering weight generation, affecting the AMF through the introduction of a temperature dependence on CH_2O VMRs. Figure 5.16 displays monthly mean AMFs and subsequent CH_2O VCDs calculated with the upgraded UoL AMF algorithm, for the tested months. CTM gridding artefacts are entirely removed from a combination of the upgraded CTM resolution, and application of pixel mean area weighting for gridded inputs. A slight reduction in CH_2O VCDs is noted for regions of elevated emissions, although the improved AMF allows for a much improved discrimination

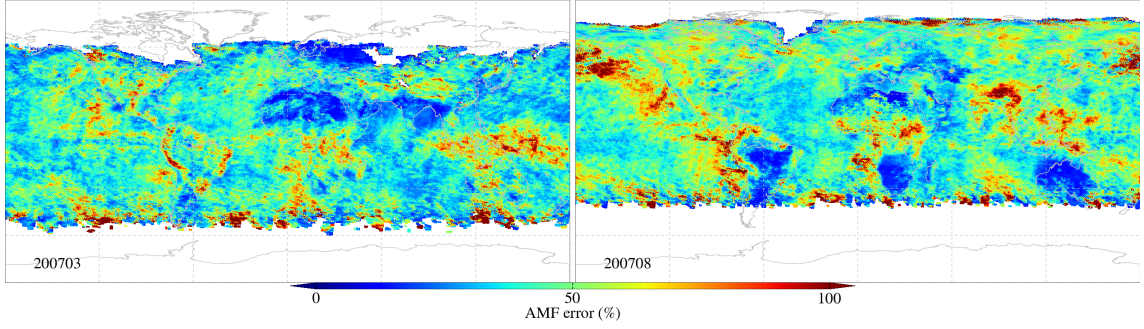


Figure 5.17: Monthly mean AMF error for March and August 2007, gridded to 0.25° .

of regional and point emission sources.

5.6 AMF error

AMF error is calculated following the method of Boersma et al. (2004) for NO_2 AMF error calculation, and validated for CH_2O retrievals by De Smedt et al. (2008). This estimation takes into account sensitivity of the AMF due to uncertainties in cloud fraction, cloud top pressure, albedo, and absorber profile. Following the notation of De Smedt et al. (2008), AMF errors (σ^2) are derived for each scan as follows:

$$\sigma^2 AMF = \left(\frac{\partial AMF}{\partial a_s} \sigma_{a_s} \right)^2 + \left(\frac{\partial AMF}{\partial CF} \sigma_{CF} \right)^2 + \left(\frac{\partial AMF}{\partial CTP} \sigma_{CTP} \right)^2 + \left(\frac{\partial AMF}{\partial S} \sigma_S \right)^2. \quad (5.28)$$

With ∂AMF indicating the AMF change due to perturbation of the denominator variable, by the denominator variable's assumed error. Assumed error for surface albedo a_s (0.02), CF (0.05) and CTP (60 hPa) are all taken from the respective variable's maximum error as detailed in its corresponding literature. Absorber profile error (S) is calculated by perturbing CH_2O profile values below the altitude of the two layers above the CH_2O mixing ratio peak by +25%, whilst layers above this are perturbed by -25%.

Therefore error estimates are presented in Figure 5.17 as monthly means for the two months selected for AMF parameter testing, both providing representative values for elevated and background CH_2O emissions for all locations of interest.

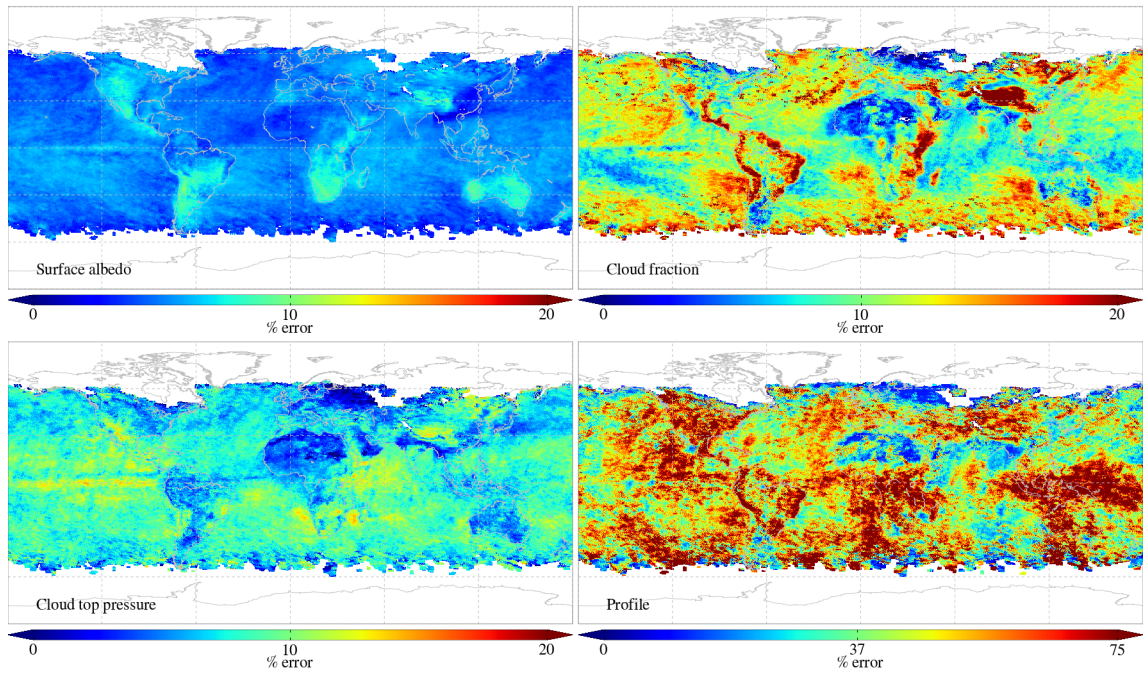


Figure 5.18: Monthly mean contributions of constituent errors to total AMF error for March 2007, gridded to 0.25° .

Errors contributing to the total AMF error are presented in Figure 5.18, showing albedo and CTP contribute $<15\%$ globally, with contributions from CF increasing to $\sim 20\%$ in the worst cases. Absorber profile errors are frequently cited as the largest error source in AMFs (Boersma et al., 2004; De Smedt et al., 2008), with errors here ranging from 30–60%. For GOME-2 in particular, errors on the absorber profile are thought to be magnified due to the mid-morning overpass time (09:30) of MetOp-A. Demonstrated in Figure 5.19, the majority of CH_2O would be expected to be in the very lowest levels of the troposphere for regions of high formaldehyde concentration. When perturbed for error estimation, the profile will exhibit a distinctive ‘kick’, giving rise to significant errors in the region.

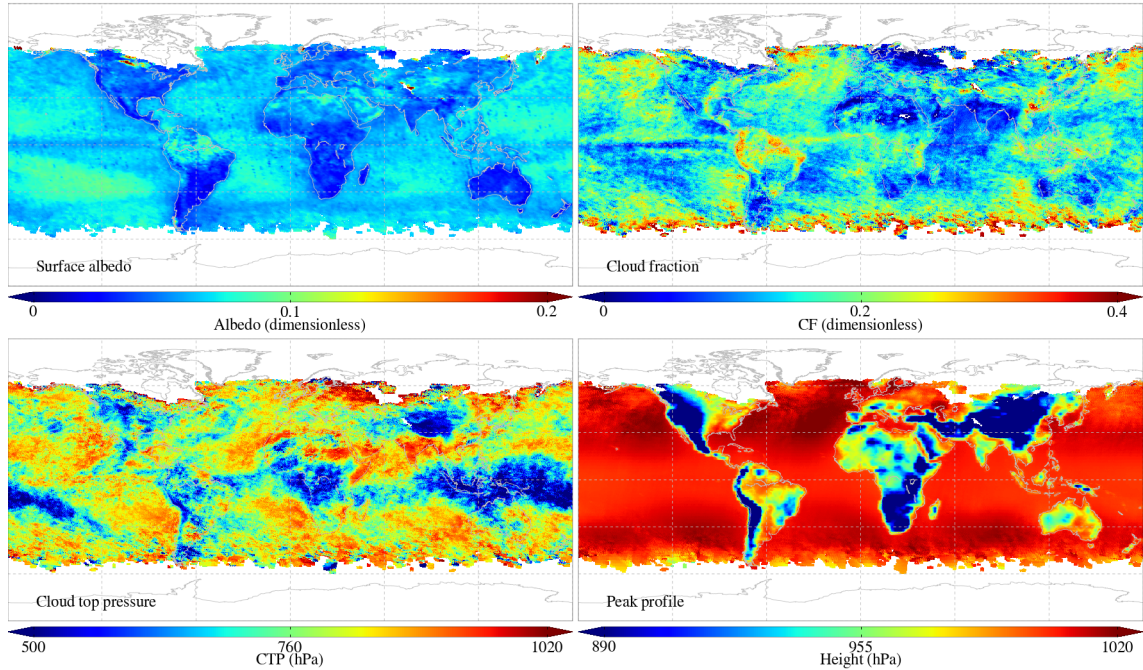


Figure 5.19: Monthly mean geophysical parameters used for above AMF error calculations.

5.7 Summary

Previous AMF calculations beginning with Palmer et al. (2001) made use of coarser resolution a-priori data, partly due to computational restrictions on the running of CTMs at the time, and partly for the close matching of these coarse grids to GOME-1 pixel sizes. With increases in both of these elements, the need for a coincident adjustment of a-priori databases to better match increased GOME-2 scan resolutions is apparent. A reference UoL AMF algorithm based on the work of Barkley et al. (2011) for CH_2O retrievals is presented, utilising GEOS-Chem CTM a-priori input data at $4^\circ \times 5^\circ$. This is upgraded by incorporating recent developments proposed for NO_2 AMF calculations, as well as several novel improvements to the AMF algorithm. Major changes to the AMF are found with use of a higher resolution $2^\circ \times 2.5^\circ$ GEOS-Chem a-priori, and the OMI albedo product at $0.5^\circ \times 0.5^\circ$. More subtle modifications to the AMF are effected with pressure correction of VMRs over mountainous terrain, and pixel mean weighting of gridded inputs better representing sub-pixel inhomogeneity. Use of a temporally and spatially dependent O_3 climatology, and incorporation of orbit specific temperature dependent absorp-

tion cross sections allows for a more accurate estimation of atmospheric scattering weights, translating to enhanced accuracy in the AMF.

Further improvements to the updated AMF are envisaged, with a need for co-located aerosol data to improve scattering weight calculations specific to each observation. Additional fixes to the GEOS-Chem CTM have been proposed by Sabolis et al. (2011), aiming to reduce the prominent CH_2O hotspot over the Mediterranean Sea in summertime via the reduction of Saharan model dust emissions. Were an appropriate BRDF database to become available extending to the fitting region of GOME-2, an improved albedo term could be included in the AMF calculation. Similarly, use of an albedo database derived with GOME-2 should reduce AMF bias due to instrumental and temporal sampling differences between GOME-2 and OMI. Cloud optical thickness and cloud top albedo data from complimentary sensors mounted onboard MetOp-A could be used in the derivation of AMFs for cloudy scenes, greatly improving over the current fixed cloud representations.

Chapter 6

VCD Evaluation and Comparison

Following large scale DOAS parameter sensitivity testing for the slant column retrieval (Chapter 4), and assessment and implementation of several improvements to the air mass factor algorithm (Chapter 5), this chapter focusses on the application of these optimised retrieval settings for the derivation of a 5 year CH₂O vertical column product from the GOME-2 instrument. Seasonal means and regional time-series are presented for CH₂O columns generated for this new product. The consistency of GOME-2 CH₂O VCDs to GEOS-Chem modelled VCDs is analysed. Finally, correlations are drawn against complimentary environmental parameters (aerosol optical depth, rain rate, land surface temperature and chlorophyll fluorescence) to investigate year to year variations.

6.1 Five year CH₂O VCD product

Approximately 309,600 GOME-2 orbits were processed to generate a 5 year CH₂O VCD product spanning 2007–2011 (inclusive). An optimised processing stream was developed for use on the University of Leicester’s high performance computing cluster. With a mixture of Bash shell scripting, Python and Fortran programming languages, one year’s VCDs can be generated in approximately 24 hours, using 439 CPU cores (Intel Xeon X5550 at 2.67 GHz). Processing time is divided into three roughly equal portions, with pre-processing covering the extraction of relevant ra-

diance and geo-location parameters from the native GOME-2 L1B product, cross section convolution followed by SCD generation with a modified version of QDOAS, and reference sector method application and AMF calls completing the data processing chain.

6.1.1 VCD seasonal means

In the following discussion, seasonal GOME-2 VCD means are presented spanning 2007–2011. GOME-2 is timetabled to record observations at an enhanced ‘zoom’ spatial resolution of $10 \text{ km} \times 40 \text{ km}$ on the middle day of each month, and for selected other orbits as per mission requirements. All zoom orbits are removed from processing in order to reduce a distinctive striping effect imparted on the mean along zoom orbit tracks. GOME-2 back-scan measurements (with a larger scan footprint of $240 \text{ km} \times 40 \text{ km}$) are included in means, with the area weighting of the gridding procedure distributing portions of larger scans as a function of area. South Atlantic Anomaly affected scans also remain in the mean, with monthly and seasonal averages largely acting to remove the random pattern of bad pixels. Scans with a cloud fraction >0.4 and $\text{SZA} >60^\circ$ are not included in the mean (see Chapter 4). Seasonal CH_2O means processed with the above criteria for 2007–2011 are presented in Figure 6.1.

Means for DJF reflect the southern hemisphere summertime, with Australia exhibiting VCD concentrations of around $1.0 \times 10^{16} \text{ molecules cm}^{-2}$, which then drop off to background levels of $\sim 0.5 \times 10^{16} \text{ molecules cm}^{-2}$ for the rest of the year. In the northern hemisphere spring (MAM), emissions over south east Asia and India rapidly reach a peak, followed by a global surge in concentrations during JJA, with the majority of the Earth’s landmasses experiencing a northern hemisphere summertime. In autumn (SON), northern hemisphere emissions recede to similar values to MAM, whilst the Amazon and South America reach an emission peak.

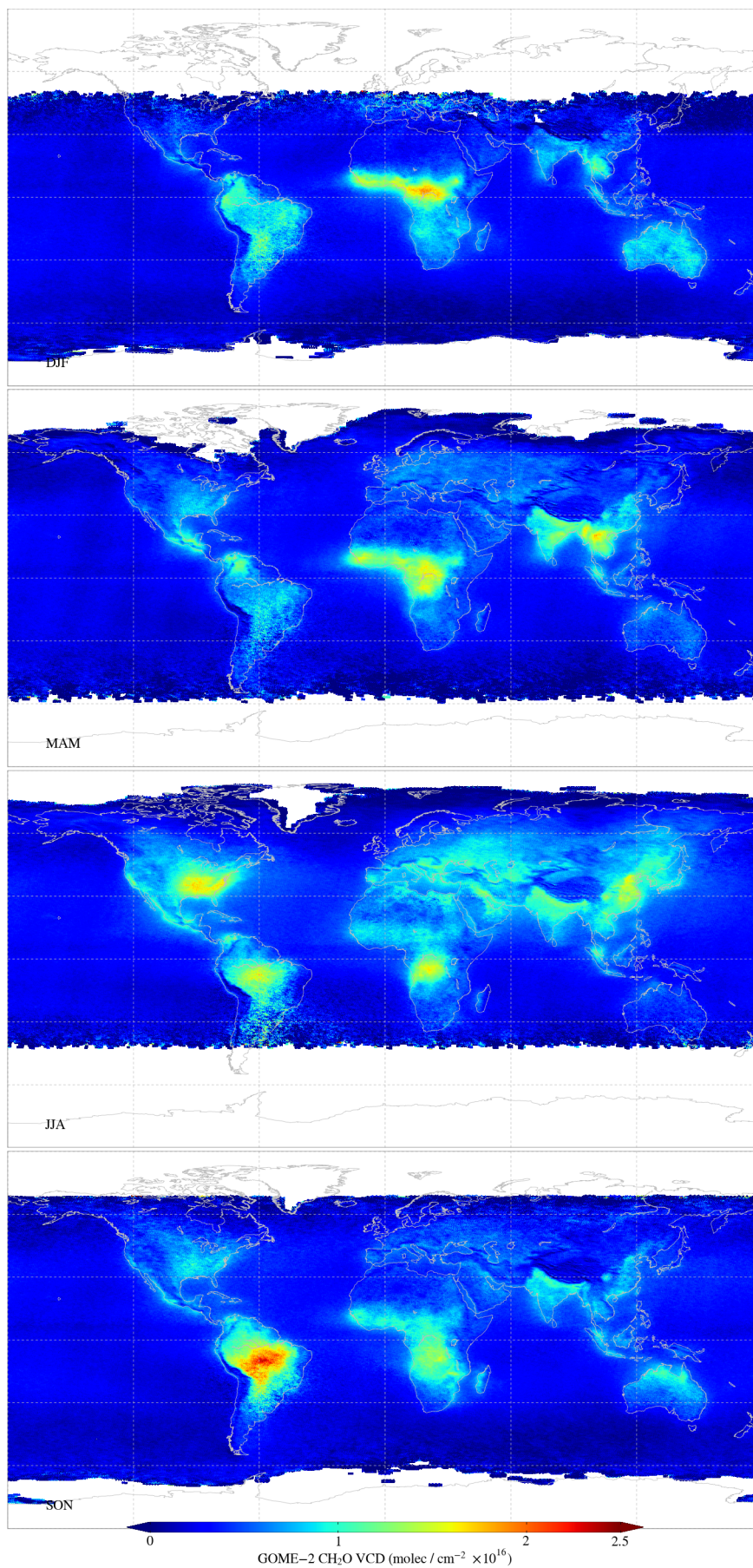


Figure 6.1: GOME-2 CH₂O VCD seasonal means for 2007–2011, gridded to 0.1°, no smoothing of data is applied. Scans with CF>0.4 and SZA >60° are excluded.

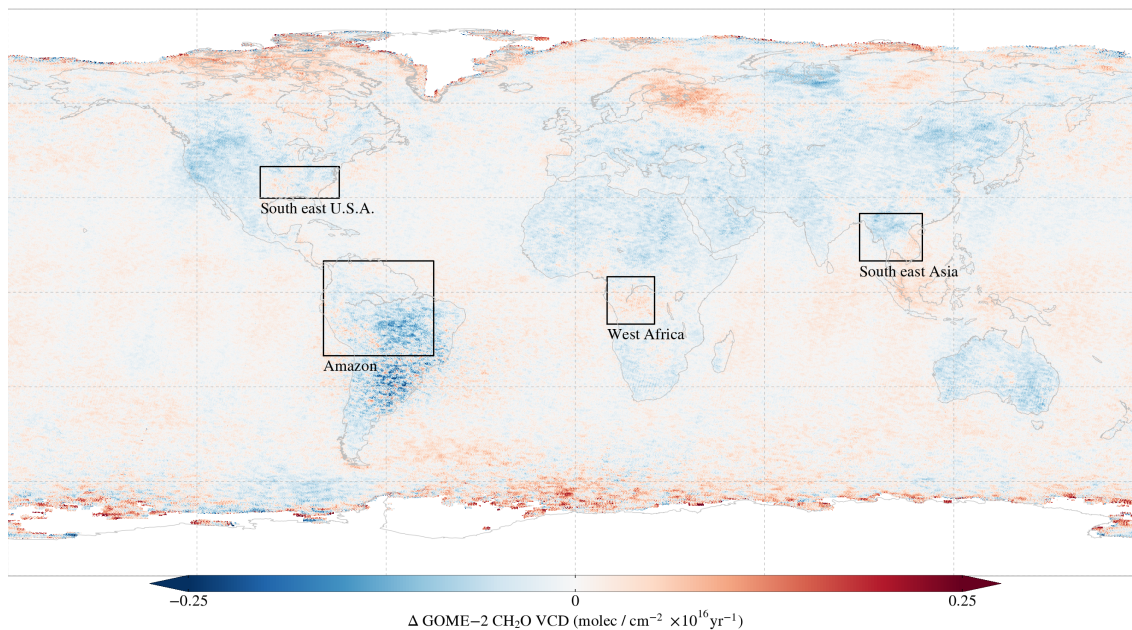


Figure 6.2: Mean annual GOME-2 CH₂O VCD change between 2007–2011, gridded to 0.1°. Also plotted are the extent of regions subsequently used for monthly mean analysis.

6.1.2 VCD trend

To analyse changes in global CH₂O concentrations over the course of the 5 year product, mean annual trend is calculated following the method of Richter et al. (2005) for NO₂ trend analysis. Annual CH₂O global means are calculated from UoL GOME-2 VCDs on a 0.1° grid for each year in the available time-series. A linear regression is applied to each cell (straight line fit with residual minimisation) through the 5 years of data, to calculate the average annual gradient for each sampled grid point on the globe, shown in Figure 6.2.

There exists a possibility for skewing of trends at higher latitudes, for which GOME-2 data is sampled only on a seasonal basis due to the inclination of MetOp-A's orbit. With only a 5 year time-series to perform gradient calculations on, it is also acknowledged that single anomalous years for any location could bias a trend. Spatial patterns evident suggest a general decrease in CH₂O emissions over most landmasses, with regional exceptions of increasing emissions over Finland and western Russia. These increases are likely attributed to the exceptional series of wildfires experienced in these regions in 2010 (Huijnen et al., 2012). Slightly larger decreases

are noted for parts of southern South America, although with the region being strongly affected by the South Atlantic Anomaly, attribution of this feature to an increased strength of SAA effects as a function of instrument degradation is possible. West Africa and parts of northern South America show slight CH_2O column increases, as does much of Indonesia and Papua New Guinea. Further instrumental bias is seen over oceans, where a faint east / west scan bias manifests itself as alternating patches of minor increases and decreases, in line with MetOp-A's orbital path. Based on these gradients, CH_2O emissions exhibit a mixture of spatial patterns for the time-series, with general decreases over landmasses with the exception of increases over some of the equatorial tropics.

6.1.3 Model comparisons

Comparisons are drawn with GEOS-Chem CTM formaldehyde VCDs, generated with model settings detailed in Section 5.2.1. In GEOS-Chem's case, many of the chemical parameters relevant to generation of model CH_2O columns are derived from the MEGAN BVOC model (Guenther et al., 2006). GEOS-Chem CH_2O VCDs are calculated from area weighted mean vertical mixing ratios used for AMF calculation, specific to each observation. With CTM VCDs calculated for the same viewing geometry and scene specific parameters as applied for the derivation of its corresponding GOME-2 VCD, use of an averaging kernel (Eskes and Boersma, 2003) is not necessary, with the relationship between modelled and measured columns implicit in the companion CTM VCDs. Nevertheless, averaging kernels are calculated for each observation and included in the final GOME-2 CH_2O product for users wishing to compare results to external CH_2O databases.

Figure 6.3 shows monthly means over the extent of the product for GOME-2 and GEOS-Chem CH_2O VCDs. In addition to global means, four sub-regions of elevated formaldehyde concentrations are presented, whose spatial coverage are plotted on Figure 6.2. Observed global CH_2O means generally reflect the CH_2O background due to methane oxidation represented in GEOS-Chem columns very well. For the four

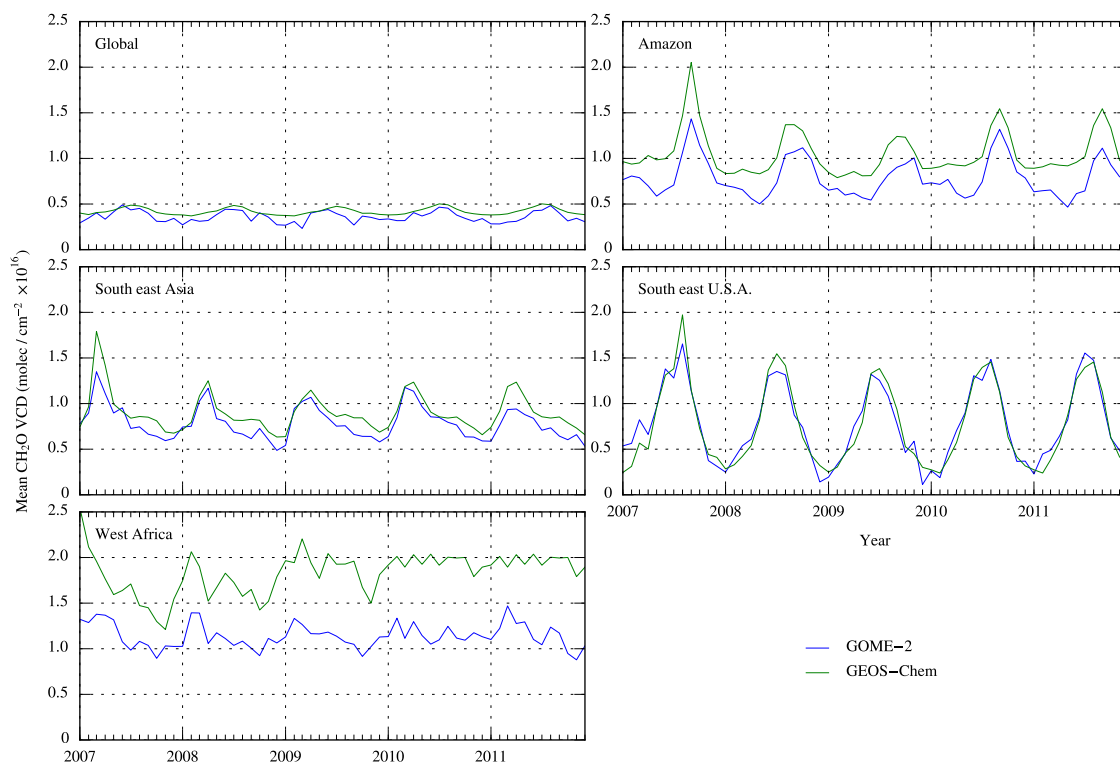


Figure 6.3: Monthly mean CH_2O VCDs from GOME-2 and GEOS-Chem. Both dataset's temporal patterns are very similar, although magnitude is seen to vary somewhat for west African and Amazon regions.

sub-regions, temporal patterns of CH_2O concentrations compare very favourably from model to observation, particularly so for the south east U.S.A. and south east Asia. Figure 6.4 shows the correlation between modelled and measured columns, confirming the close matching of both datasets in trend and magnitude. Bias exists for the Amazon and west African regions, with CTM VCDs consistently 0.25 and 0.8×10^{16} molecules cm^{-2} higher respectively, also shown in Barkley et al. (2013) for SCIAMACHY and OMI observations over the Amazon. Causes for this disparity may be related to a relative paucity of in-situ observations for these regions leading to less well evaluated model concentrations, particularly when compared to the relatively data-rich south-east U.S.A. (Frost et al., 2002; Fried et al., 2008; Parrish et al., 2012). With further reference to the CTM VCDs, a better model representation over the U.S.A. is likely due to a better understood NO_x chemistry for high NO_x concentrations over the U.S.A. (Sillman and He, 2002; Martin et al., 2003) than for more remote tropical regions with lower NO_x quantities (e.g. Pike et al. (2010)).

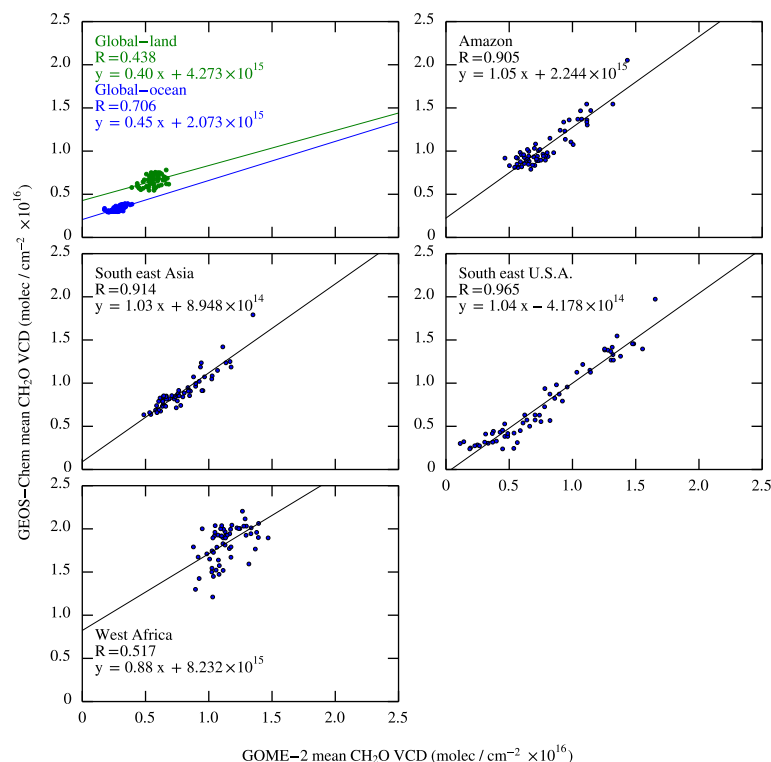


Figure 6.4: Correlation between monthly mean CH_2O VCDs from GOME-2 and GEOS-Chem. Mean bias between the two datasets is shown to be small in all cases, with excellent agreement for the south east Asia and south east U.S.A. regions.

In the monthly mean time-series the Amazon region is seen to almost double its CH_2O emission peak in 2007 and 2010 compared to adjacent years, tying in with noted Amazon drought years (Lewis et al., 2011; Saatchi et al., 2013). Furthermore, Amazon model formaldehyde columns reach their peak 1–2 months early compared with GOME-2 observations for the summers of 2008 and 2009.

6.1.4 Fire screening

Biomass burning is known to contribute large amounts of formaldehyde to the atmosphere over short spaces of time (Gonzi et al., 2011). The intense heat associated with major wildfire events serves to rapidly elevate trace gas and aerosol burning products into the troposphere (Andreae and Merlet, 2001). A fire screening procedure is applied to UoL CH_2O VCDs in order to remove the signal due to biomass burning, leaving a better representation of biogenic only emissions. To do so, the method of Barkley et al. (2013) is applied, using daily $0.5^\circ \times 0.667^\circ$ grids of MODIS

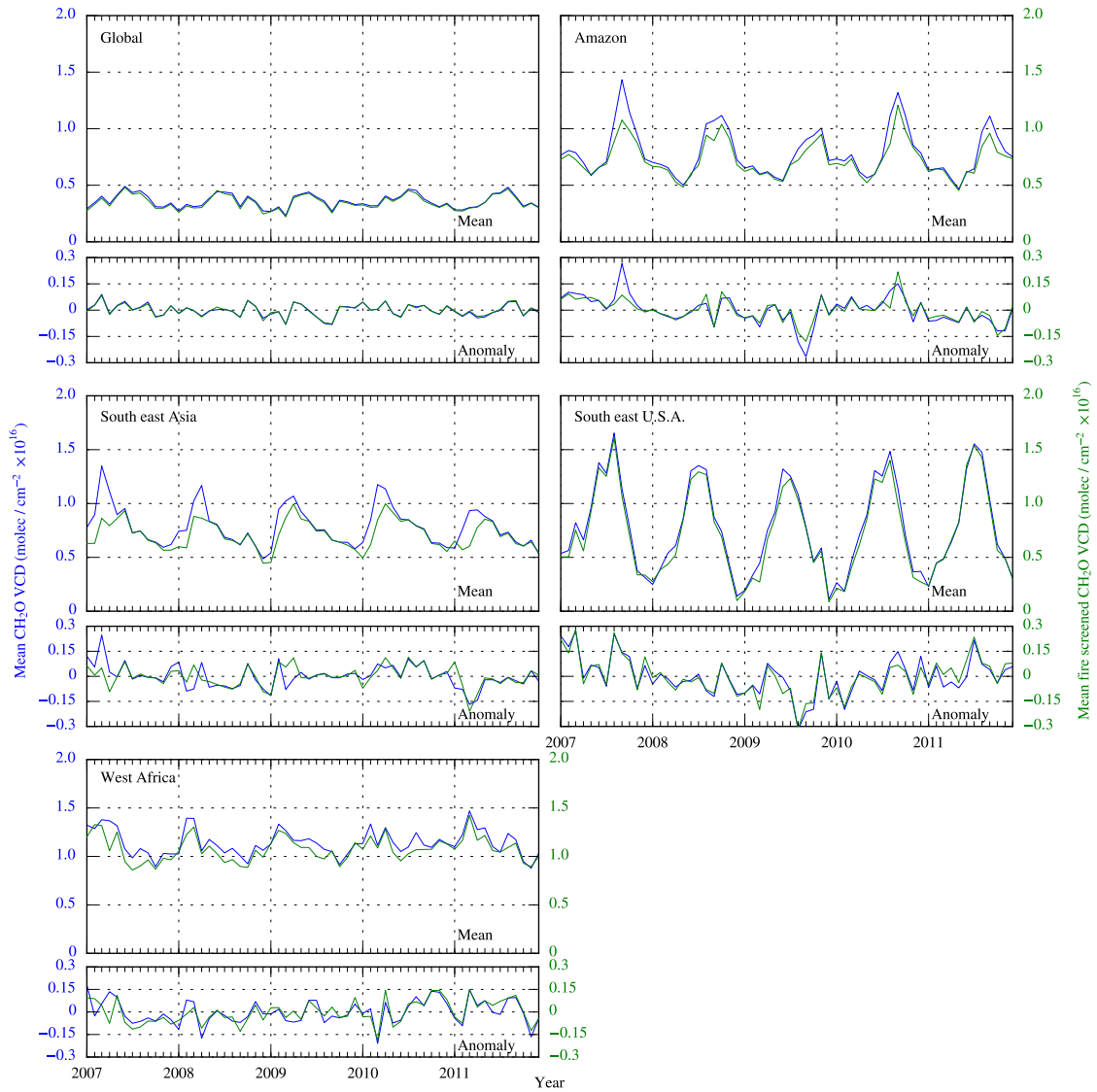


Figure 6.5: Monthly mean time series of fire-screened CH_2O columns plotted alongside un-screened columns for the entirety of the UoL product.

Terra, MODIS Aqua (Giglio et al., 2003) and ENVISAT AATSR (Arino et al., 2005) fire counts to remove any VCD measurements falling within a 1 grid cell radius of fire affected cells. The technique removes 9.423% of GOME-2 observations for the entire dataset, with the screened monthly means presented in Figure 6.5. Anomalies on the total VCD trend are also given in the subplots, representing the variation in monthly means with seasonal variation removed. These are calculated by deriving 12 total monthly mean values covering the observation period (2007–2011), followed by subtracting the relevant total monthly mean from each ‘normal’ monthly mean value.

Biomass burning emissions contribute significant amounts of CH_2O to the global budget, evidenced by the 0.25×10^{16} molecules cm^{-2} reduction in measured formaldehyde concentrations when fire screened. Amazon and S.E. Asian regions experience significant biomass burning events, reflected in the reduction of monthly mean columns when CH_2O VCDs are fire screened. VCD time series over the south east U.S.A. are not greatly effected by fire screening, with the region being well managed by humans and so experiencing little in the way of massive burning events. Fire screening has a only a small effect on monthly VCDs for West Africa, with the prevalence of wildfire and its effects on CH_2O columns expected to be slightly northwards of the region examined (Marais et al., 2012).

6.1.5 Retrieval comparisons

Further evaluation of the new UoL CH_2O product is possible through comparison with the Belgian Institute for Space Aeronomy (BIRA) GOME-2 formaldehyde VCD product (De Smedt et al., 2012). The BIRA product is retrieved in the same two step fashion as for the work presented here; with slant columns derived through DOAS fitting of GOME-2 radiances to absorption cross sections, followed by conversion to vertical columns with an AMF. Settings for the first step in the retrieval are similar between UoL and BIRA retrievals (Hewson et al., 2013), therefore the majority of variation is expected to arise from the SCD–VCD conversion.

Monthly means and correlations between UoL and BIRA products are presented in Figures 6.6 and 6.7. The BIRA monthly mean time series is seen to be slightly smoother than for the UoL product in the global mean, although the UoL product has a small mean global difference of $+1.696 \times 10^{15}$ molecules cm^{-2} . This closeness of temporal patterns and small difference is continued for all regional means (with the exception of a very small negative difference for south east Asia). For the south east U.S.A. noticeable differences exist for annual minima and maxima, with the UoL product retrieving approximately 0.3×10^{16} molecules cm^{-2} higher concentrations at the peak of the growing season, offset by slightly lower concentrations during

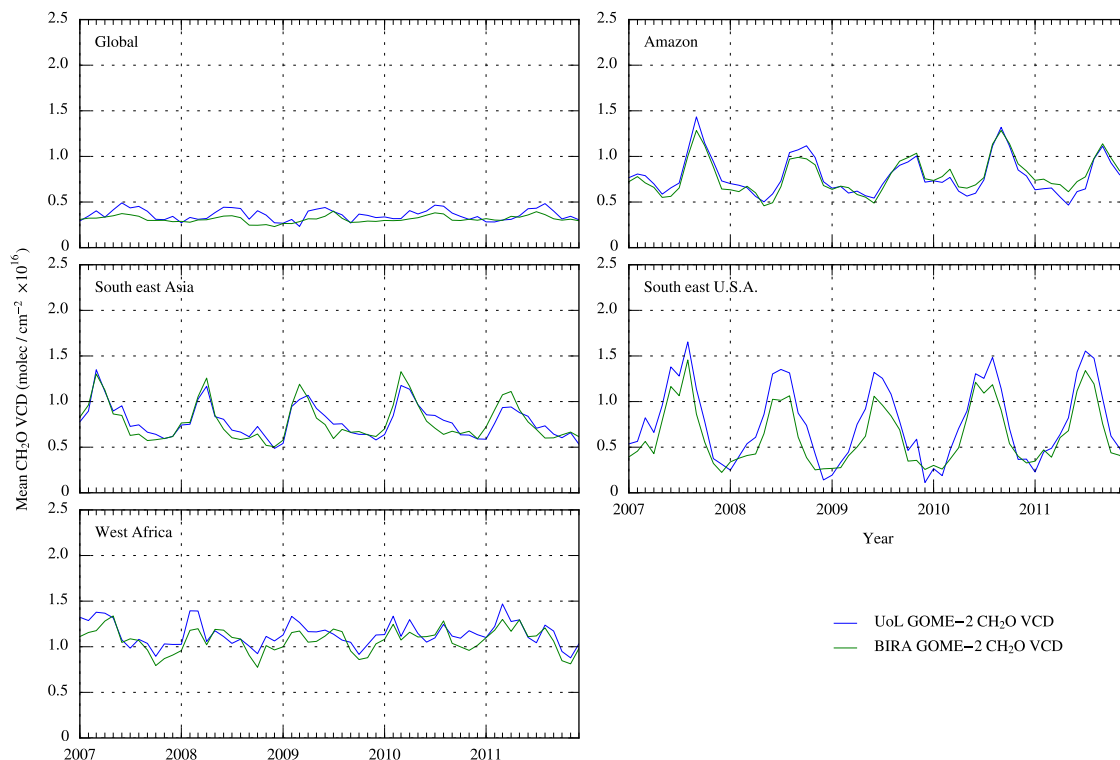


Figure 6.6: Monthly mean UoL CH₂O VCDs from retrievals presented in this work, plotted alongside the BIRA GOME-2 formaldehyde product (De Smedt et al., 2012). UoL concentrations and temporal patterns closely match those of the BIRA product.

wintertime.

Without a thorough inter-comparison of AMF calculation inputs for the two retrievals, reasoning for differences between both products are only speculated upon. However, with both AMFs using the 0.5° OMI albedo product (although UoL applies area weighted values) and FRESCO+ cloud product, variation is likely caused by CTM choice (GEOS-Chem and IMAGES – also affecting the ‘added back’ reference sector method concentrations), use of an aerosol correction (BIRA do not explicitly correct for aerosol) and further UoL specific corrections detailed in Section 5.5. A more thorough parallel validation of UoL and BIRA VCDs against in-situ measurements of CH₂O concentrations should allow for a better analysis of the small differences present, nevertheless current agreement between the two datasets inspires confidence in the new UoL retrieval. Such work is not pursued here due to the lack of available in-situ CH₂O column measurements.

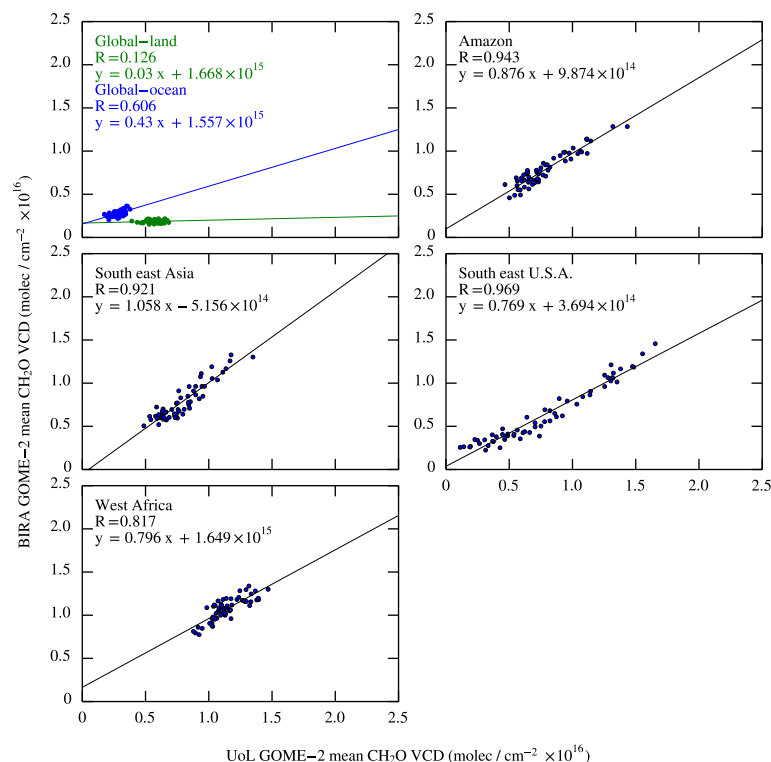


Figure 6.7: Scatterplots of UoL and BIRA CH_2O , with R values indicating strong agreement between the two datasets for all regional cases. A small positive bias is evident for the new UoL retrieval compared against BIRA VCDs. Note global BIRA data spans 2007-2010 only, therefore UoL global data is cropped to match this.

6.2 Environmental correlations

Cycles of formaldehyde VCD concentrations throughout the year (detailed in Section 6.1) are now examined with respect to several closely linked environmental parameters. GOME-2 formaldehyde time-series are compared with GEOS-Chem aerosol, TRMM monthly mean precipitation rate (inferring water availability to isoprene emitting vegetation), AATSR land surface temperature (heat tolerance of plants), and the new GOME-2 fluorescence product. Land surface temperature and GOME-2 fluorescence datasets in the following section are relevant to land based parameters only, therefore for these comparisons GOME-2 CH_2O VCD means are masked to remove ocean cells which may otherwise introduce bias from the CH_4 background source.

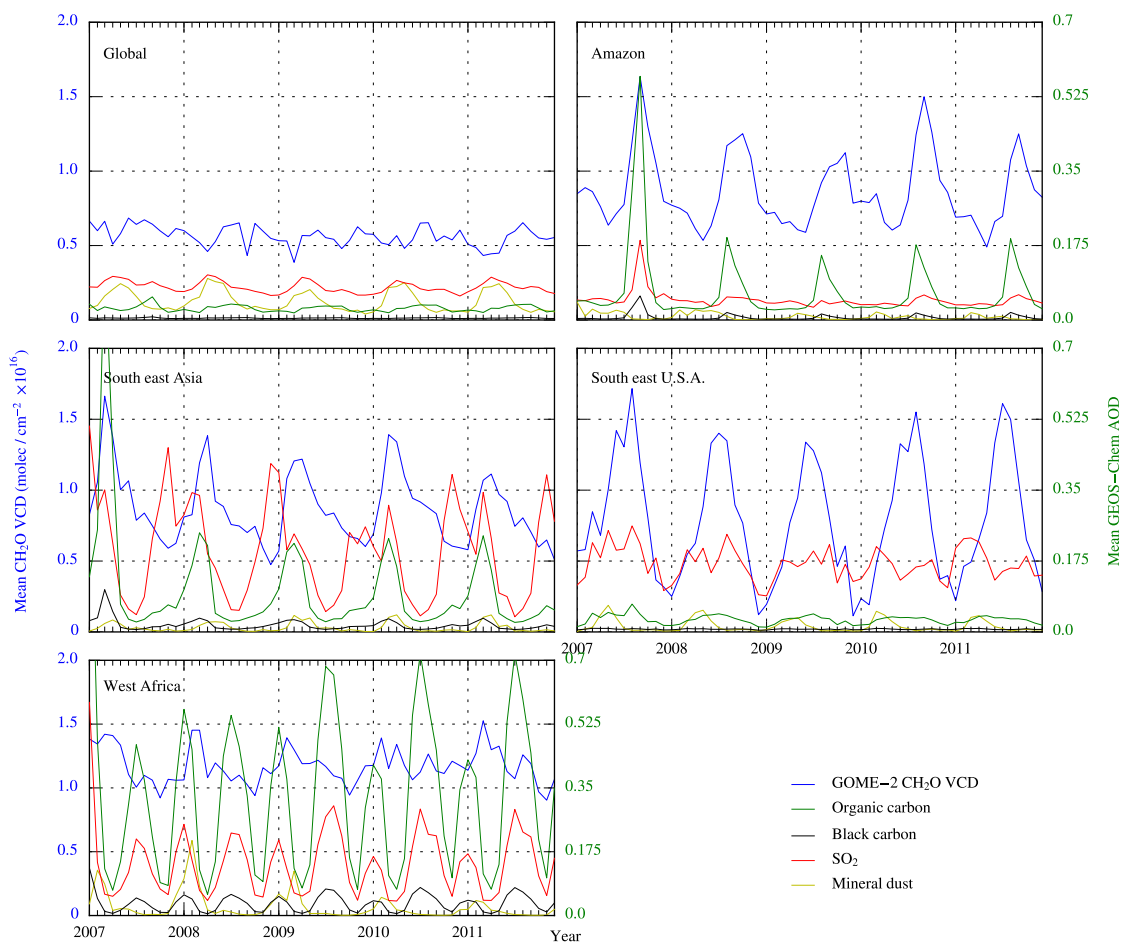


Figure 6.8: Monthly mean plots of UoL CH_2O VCDs and GEOS-Chem AODs for four significant aerosol types.

6.2.1 Aerosol

Total column aerosol optical depths (AOD) calculated by GEOS-Chem for inclusion in the AMF scattering weight calculation are used for investigation of correlation between calculated CH_2O VCDs and aerosol effects. With six aerosol types represented (mineral dust, SO_2 , black carbon, organic carbon, sea salt and water cloud), some correlation is expected with formaldehyde – particularly for the black and organic carbon types, frequently associated with biomass burning events (Gonzi and Palmer, 2010; Gonzi et al., 2011).

Large amounts of mineral dust are known to be transported from the Sahara over the Atlantic Ocean providing fertilisation for the Amazon basin (Bristow et al., 2010), although correlations between mineral dust AODs at 340 nm and CH_2O VCDs in the region are not significant ($R = -0.423$). Closer inspection of Figure

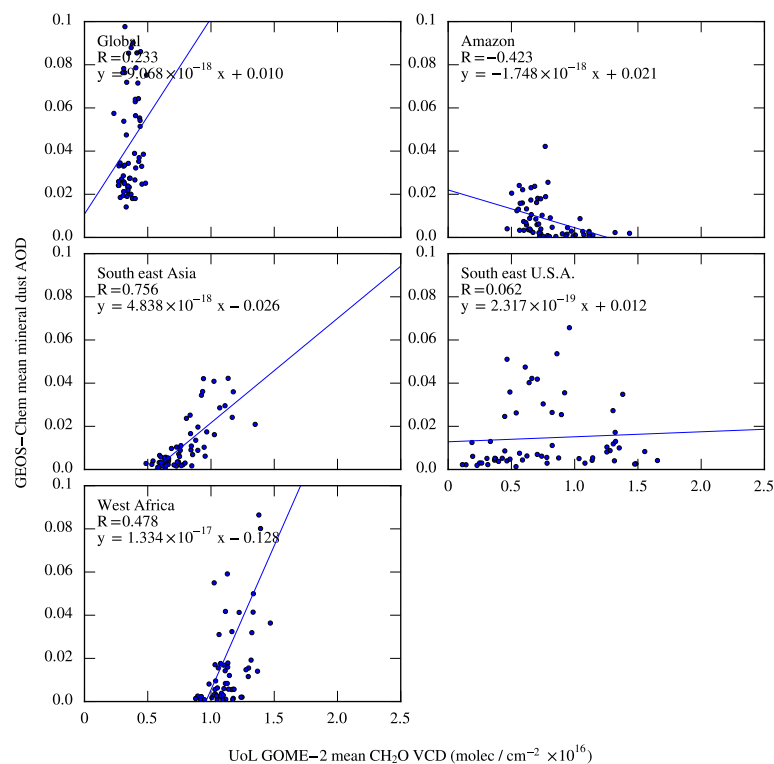


Figure 6.9: Correlations between monthly mean UoL CH₂O VCDs and GEOS-Chem mineral dust AODs.

6.9 reveals a distinctive grouping of elevated monthly mean AODs matching low (for the region) VCD values of $0.5\text{--}1.0 \times 10^{16}$ molecules cm^{-2} . Time series plots show an increase in mineral dust AODs for the Amazon 2–3 months prior to major formaldehyde concentration peaks, although year round values are low compared to the other regions examined. South east U.S.A. and south east Asia experience large increases in mineral dust AODs around the same time as for the Amazon, but show larger AOD peaks. Mineral dust AODs for West Africa exhibit larger peaks up to 2010 (AOD=0.5), after which values return to similar levels as for other regions (AOD=0.1–0.2). The adjacency of West Africa to Saharan mineral dust sources, in concert with meteorological conditions for years with larger AOD peaks would be the most probable cause for enhanced AODs.

SO₂ AODs are seen to be largely region dependent - with the Amazon showing only one peak in mid 2007 coinciding with the major CH₂O VCD peak, before returning to an almost constant value for the rest of the observation period. For other regions, SO₂ AODs show a more regular cycle. South east Asia has an annual SO₂

AOD peak late in the year, preceding formaldehyde emission peaks by 1–2 months. U.S.A. values are less variable in their annual cycle, although clear correlations with summertime CH_2O concentration maxima are evident. Twice yearly SO_2 peaks for West Africa do not show significant correlation with CH_2O cycles for the region.

Over West Africa black carbon emissions are particularly strong in comparison to other regions examined, exhibiting a regular biannual cycle, likely reflecting the temporal regime of biomass burning seasons. South east Asia and the Amazon also show minor black carbon peaks, correlating with elevated organic carbon peaks in these regions. For all regions bar the south east U.S.A. organic and black carbon emissions are very closely matched in their timing and relative increases against their respective background trends, suggesting the same cause is responsible for both emissions. Looking back to Figure 6.5, large VCD reductions are evident in VCDs for 2007 when fire screened. These factors allow identification of 2007 as a major year for biomass burning events, with formaldehyde VCDs, organic and black carbon all increasing to levels well beyond regular annual emission peaks. Correlations between sea salt and CH_2O VCDs are low, and therefore not plotted, with the two parameters showing little in the way of coincident variation.

Testing the relationship between monthly mean GOME-2 cloud fraction and the 6 aerosol optical depth parameters showed little to no correlation between variables for monthly means. A more detailed investigation of individual orbits is required for the CF / aerosol correction effect to be fully validated for GOME-2 CH_2O measurements. For this to take place, a complimentary set of cloud and aerosol measurements is required (Boersma et al., 2011), which for GOME-2 is currently unavailable.

6.2.2 Precipitation

Precipitation affects vegetation health through partially controlling water availability for uptake via the roots of vegetation, so bearing a large impact on the operation of the biosphere (Rodriguez-Iturbe, 2000). A connection between formaldehyde and precipitation is expected to exist in the spatial, and to a greater extent, temporal

domains, given plant health, and consequently isoprene's emission dependence on water availability to vegetation (Müller et al., 2008).

Satellite measurements of precipitation

Launched in 1997, the JAXA / NASA Tropical Rainfall Measuring Mission (TRMM) provides rainfall data from its suite of microwave instruments specifically designed for precipitation monitoring (for a comprehensive description of the instrument see Huffman et al. (2007)). The orbit of the TRMM spacecraft covers only the tropics ($50^{\circ}\text{S} - 50^{\circ}\text{N}$), precluding a global analysis, although the sub-regions selected for analysis all fall within this domain. Rain rate is a precipitation intensity measurement defined as the amount of rain in mm falling on a given location per hour. For comparison with CH_2O VCDs, the TRMM monthly mean level 3 rain rate product at 0.25° (3B43) was obtained through the NASA Giovanni data service (Acker and Leptoukh, 2007). 3B43 is derived primarily with TRMM data, but also takes into account ancillary data from other satellite microwave instruments, all of which are weighted by ground based rain gauge measurements before arriving at a monthly best estimate rainfall rate.

TRMM monthly mean precipitation : comparison to GOME-2 CH_2O

Regional means of TRMM rain rate data are shown in Figure 6.10 alongside GOME-2 CH_2O VCDs. Anomalies on the monthly means are shown in the smaller subplots relevant to each region, calculated following the method outlined for fire screen anomalies. The nature of TRMM observations means no cloud screening is performed, whilst UoL CH_2O have a significant number of cloud affected scans removed from the mean. This may lead to a mis-match between dataset sampling, however for spectroscopic observations of CH_2O , there currently exists no alternative to mitigate for cloud screening problems.

The Amazon rainfall time-series exhibits a noticeable reduction in peak monthly rainfall at the beginning of the GOME-2 measurement period (MAM 2007), and

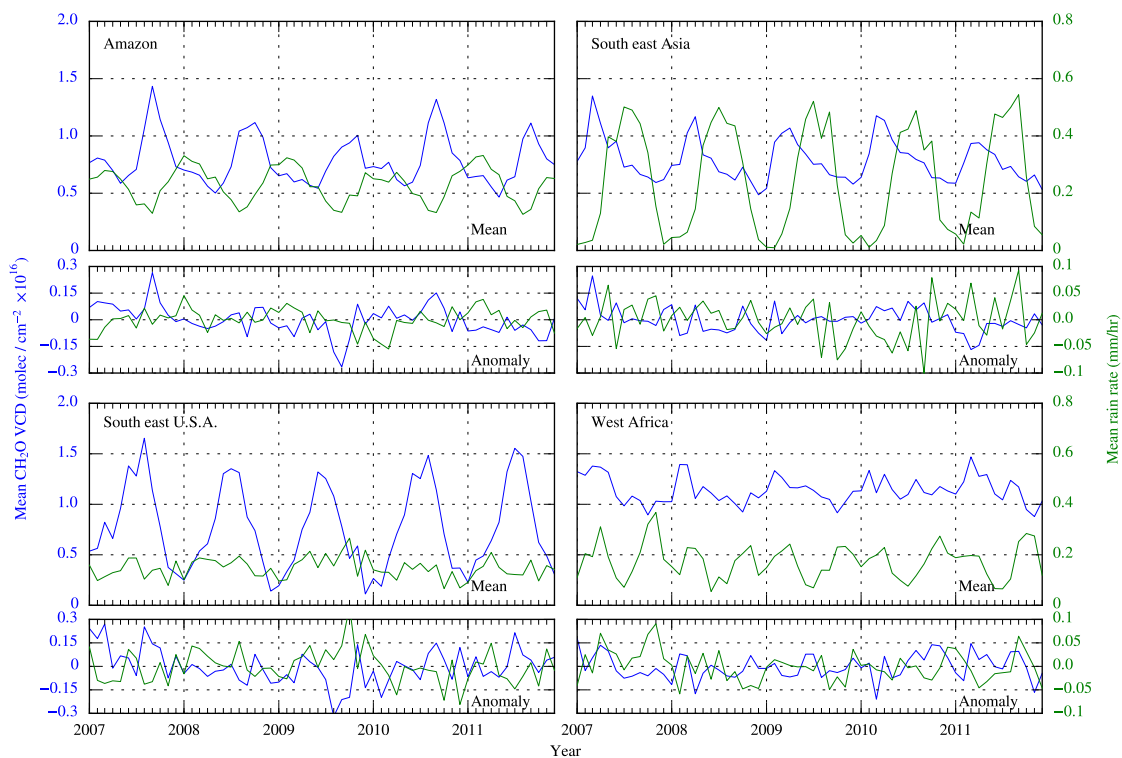


Figure 6.10: Monthly mean time series of UoL GOME-2 CH_2O VCDs (in blue) and TRMM hourly rain rate (in green). Lower subplots for each region display the anomaly on the mean.

for DJF–MAM 2010. Anomalies over the Amazon region confirm concentrations of CH_2O were elevated above the observation period trend in 2007, with TRMM rain rate preceding this high value with low values in the anomalies noted at the beginning of the observation period. With a similar pattern noted in 2011, there appears to be a correlation for the Amazon between elevated periods of rainfall preceding seasons of depressed CH_2O concentrations compared to the observation trend. South east Asia shows the highest and lowest monthly mean values, corresponding with monsoon type weather systems noted for the region (Romatschke et al., 2010).

Apart from the south east U.S.A., studied regions show significant swings in monthly mean rain rates throughout the year, corresponding to seasonal variation of the ITCZ. For the south east U.S.A., situated too far north to be drastically affected in this fashion, rain rates show much less of a cycle, remaining within a small range of 0.05–0.2 mm / hr all year round. Patterns in U.S.A. anomalies are harder to discern, although an anti-correlation between increased rain rate and CH_2O concentrations

is noted for 2009. West African monthly means are consistently high for CH₂O and TRMM rain rate, showing less variation than other study regions. Time series and anomalies for the region show a noticeable anti-correlation between the two datasets – when the rain rate is high, CH₂O concentrations are low, whilst the opposite is true for periods of low rainfall. These linkages can be caused by the fact that both CH₂O concentrations and rain rate are driven by a common third parameter (e.g. meteorological dynamics), thereby offering a coincidental correlation between the parameters through seasonal cycles.

6.2.3 Land surface temperature

Vegetation has previously been shown to exhibit a response to temperature with increased isoprene emissions (Rinne et al., 2002; Millet et al., 2008). Using data from the Advanced Along Track Scanning Radiometer (AATSR) satellite instrument, a University of Leicester and Norwegian Institute for Air Research group have developed a high resolution land surface temperature (LST) product (Ghent et al., in preparation). This data is compared and correlated with GOME-2 CH₂O VCDs to assess the dependency of formaldehyde emissions on temperature at global and regional scales.

AATSR LST method

Land surface temperature measured from space makes use of radiometric observations in the infra-red region, taking measurements from two adjacent channels whose central wavelengths are close. LST is estimated via the linear relationship between measured radiances, based on the assumption that the difference in radiances can be modelled as a function of the Planck function and atmospheric absorption due to water vapour (Prata, 2002). AATSR, mounted on-board the ENVISAT instrument provides data covering the GOME-2 CH₂O VCD time-series here, with observations recorded at a local overpass time of 10:00 providing a reasonably matched set of observations for comparison with GOME-2 (local overpass 09:30). The LST product

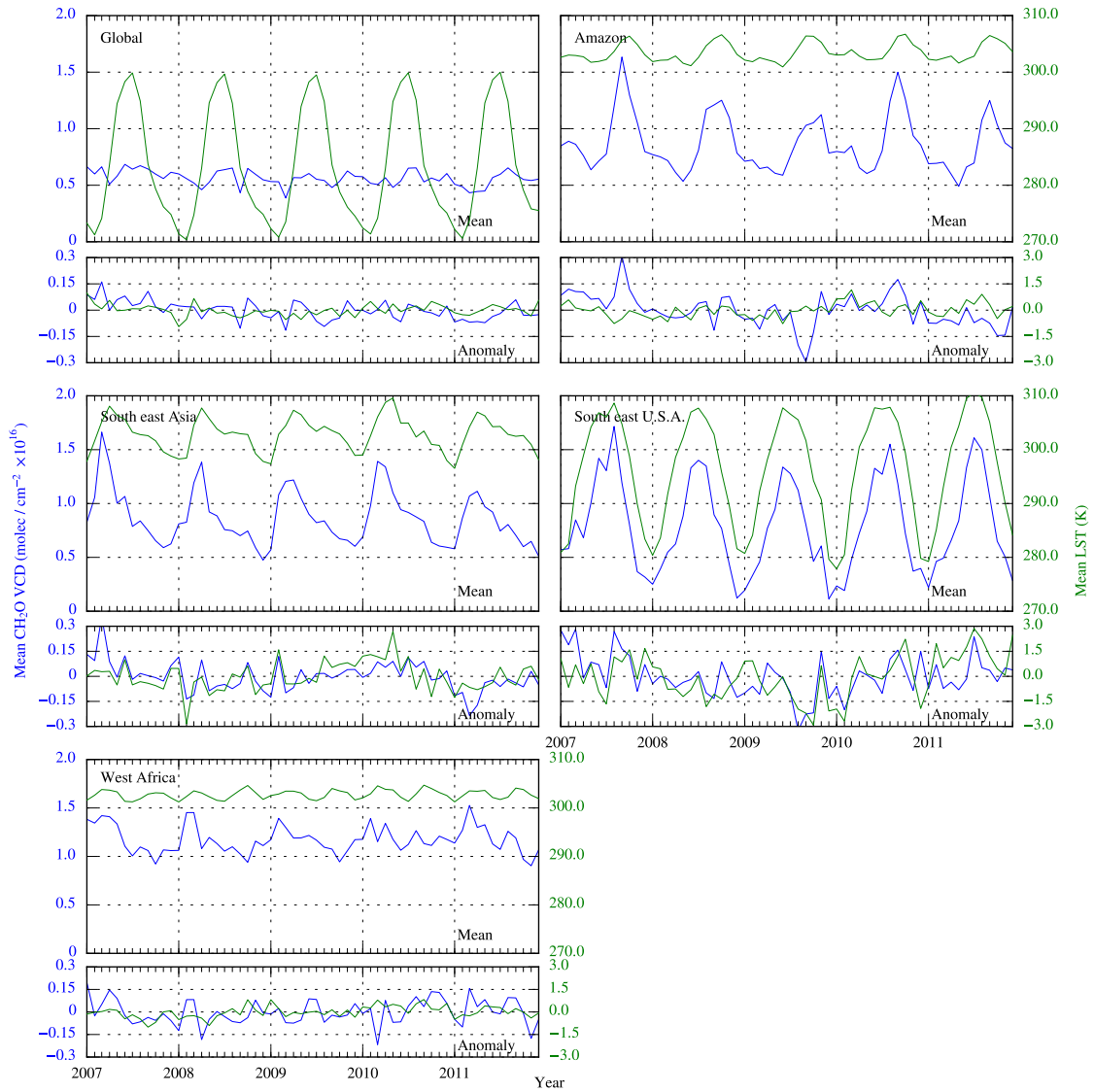


Figure 6.11: Monthly mean time series of CH₂O VCDs and AATSR LST. Left hand axis and blue line represents GOME-2 formaldehyde VCDs, right hand axis is AATSR LST. Anomalies are shown in the lower subplots, derived in the same manner as detailed in Figure 6.10.

is provided as gridded monthly means at 0.25°, generated from AATSR orbits cloud screened to include completely cloud free scans only.

AATSR LST : comparison and correlations to GOME-2 CH₂O

Figure 6.11 shows monthly mean time series of GOME-2 CH₂O and AATSR LST plotted together. Global LST exhibits significant year round changes from variation in insolation receipt for landmasses predominantly in the northern hemisphere, whereas formaldehyde emissions show less variation at a global scale, modulated

instead by a stable CH_4 background. For the Amazon, elevated CH_2O peaks agree with the seasonal shift in LST, although maximum mean LST lags behind maximum mean CH_2O by 1–2 months. For the two maximum Amazon emission years (2007 and 2010), the year’s first mini LST peak (February – March) is seen to be slightly higher than for adjacent years, although examination of the anomalies suggests variation in temperature is minimal.

Formaldehyde emission and LST patterns for south east Asia and south east U.S.A. are both very similar. In both cases, LST and CH_2O monthly means and anomalies are very well matched, with neither parameter significantly departing from the trend without the other doing so also. Patterns are harder to discern over west Africa due to year round high temperatures correlating with year round elevated CH_2O emissions. This region appears to offer a dual peak of LST, reflecting the movement of the inter-tropical convergence zone, with the springtime peak matching elevated formaldehyde, and the autumn peak anti-correlating with emissions.

6.2.4 Chlorophyll fluorescence

With concentrations of formaldehyde linked to plant productivity and health via isoprene emissions, CH_2O vertical columns are now compared with measurements of vegetation photosynthesis. Chlorophyll fluorescence observations provide direct measurements of photosynthetic efficiency from vegetation (Meroni et al., 2009). The link between light emission by chlorophyll and photosynthesis arises from a proportion of radiation absorbed by chlorophyll undergoing excitation in the plant, and being re-emitted at longer wavelengths. This fluorescence process acts in competition with photosynthesis for the application of a plant’s absorbed radiation budget. Meroni et al. (2009) note a complicated relationship between photosynthesis and fluorescence based on light and plant stress factors (water availability and heat tolerance).

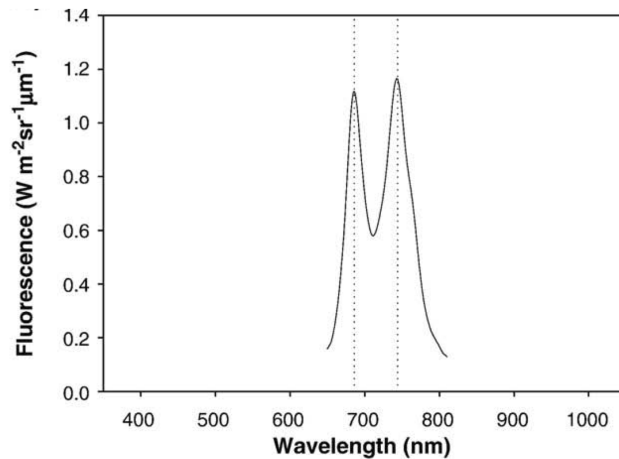


Figure 6.12: Fluorescence spectrum of a sugar beet leaf (Figure 1a, Meroni et al. (2009)).

Measurement method

Investigation of spectroscopic measurements of vegetation fluorescence reveals two characteristic chlorophyll emission peaks at 690 and 740 nm (Figure 6.12). Fluorescence emission signatures are detectable in passively sensed backscattered radiation, through the addition of these fluorescence peaks to the reflected solar spectrum. Although the additive signal is very weak at approximately 1–5% of an observed spectrum (Meroni et al., 2009; Guanter et al., 2010), by viewing the Fraunhofer lines (areas of reduced irradiance in the solar spectrum due to absorption in the Sun’s photosphere and Earth’s atmosphere), the chlorophyll re-emission signal is more readily detected.

For passive remote sensing applications, three Fraunhofer lines are commonly used in the visible and near infra-red - $H\alpha$ at ~ 656 nm, O_2-B at ~ 687 nm, and O_2-A at ~ 760 nm. A very narrow Fraunhofer feature width (on the order of 0.5 – 2 nm, with O_2 bands at the higher end of the scale), places a requirement for sampling of the radiance spectrum at very high spectral resolution for applicability to fluorescence measurements. The basic principle behind remote sensing of chlorophyll fluorescence examines these Fraunhofer lines for the amount of infilling from an assumed re-emission of radiation by vegetation.

Passive sensing of fluorescence is typically made using the O_2 bands, being closest

to chlorophyll emission signatures illustrated in Figure 6.12. Sensing in the O₂ bands presents fluorescence retrieval problems from the susceptibility of the windows to atmospheric interferences and the bi-directional reflectance distribution function, as well as the requirement for very high resolution spectrometers with which to accurately discern the amount of infilling.

These problems combine to make retrieval of fluorescence from space difficult, with the user required to account for scattered sunlight in the standard air mass factor scheme, as well as mitigation for the attenuation of the desired fluorescence measurement in the reflected spectrum. Early simulations by Sioris et al. (2003) examining the possibility of space-borne fluorescence observations with the current generation of spectrometers found Fraunhofer filling by chlorophyll emissions to be on the same order as effected by rotational Raman scattering (Ring effect), confirming the viability of the measurement.

Satellite chlorophyll fluorescence

Due to the requirement for radiance measurements to be made with high spectral resolution spectrometers, space-borne monitoring of chlorophyll fluorescence has only recently become a reality, with the launch of the Greenhouse gases Observing Satellite (GOSAT), a Fourier transform spectrometer designed to discern narrow absorption lines of atmospheric trace gases. Frankenberg et al. (2011a) initially explored the application of radiance data at typical space borne spectrometer resolutions to the technique outlined above, proving its suitability for chlorophyll fluorescence measurement with a series of theoretical radiative transfer experiments. Application to actual GOSAT data, ideal for its high spectral resolution, demonstrated the utility of space-borne fluorescence measurements, providing a first global view of the parameter (Joiner et al., 2011; Frankenberg et al., 2011b). However the low spatial sampling imparted by GOSAT's 82 km² circular scan footprint render global coverage of the instrument coarse at best, suitable for providing monthly means on 2° × 2° grids.

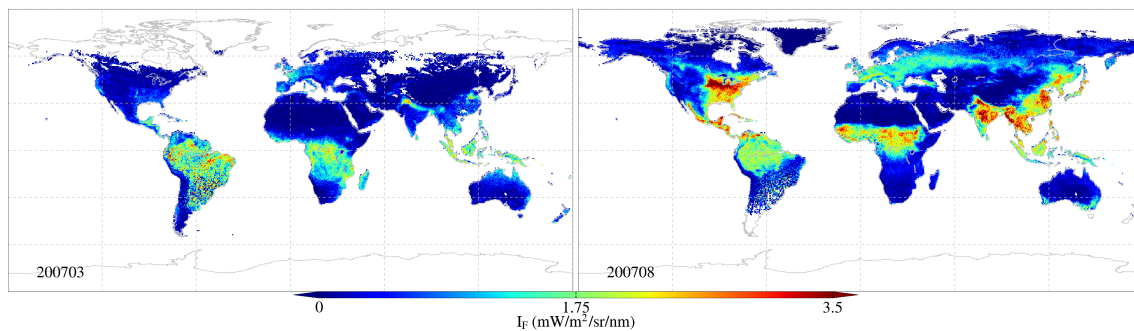


Figure 6.13: Sample GOME-2 fluorescence monthly global means for March and August 2007. Elevated I_F values correlate closely to seasonal variation in vegetation phenology.

Extending the fluorescence fitting range to make use of 866 nm Ca II Fraunhofer line filling, (Joiner et al., 2012) pioneered measurement compatibility with the lower spectral resolution, but far higher spatial resolution measurements of SCIAMACHY, although noting the move away from the traditional ~ 700 nm fitting range is expected to impact on measurement precision. A development of the fluorescence retrieval for GOME-2 has applied radiative transfer modelling to spectral measurements covering the O₂ A-band, separating absorption by the atmosphere, reflectance from the surface, and radiance due to fluorescence (I_F) (for full retrieval details see Joiner et al. (2013)). Advantages of this updated methodology have shown GOME-2 data can overcome the spatial limitations of the GOSAT retrieval, whilst mitigating for the measurement precision losses of the SCIAMACHY retrieval. GOME-2 I_F retrievals for March and August 2007 are shown in Figure 6.13, with spatial distribution closely matching that seen for CH₂O as a result of biogenic emissions.

GOME-2 fluorescence : comparisons to GOME-2 CH₂O

In this work, the chlorophyll fluorescence dataset of Joiner et al. (2013) is applied. Quality control on the dataset prior to user distribution includes cloud fraction filtering (<0.4) and SZA filtering ($<70^\circ$). Whilst the SZA filter for the GOME-2 I_F product is 10° higher than for the UoL CH₂O product, the quantity, quality and validity of the extra data at these latitudes is not significant for CH₂O, therefore GOME-2 I_F is cropped to match UoL CH₂O. These GOME-2 I_F data are averaged

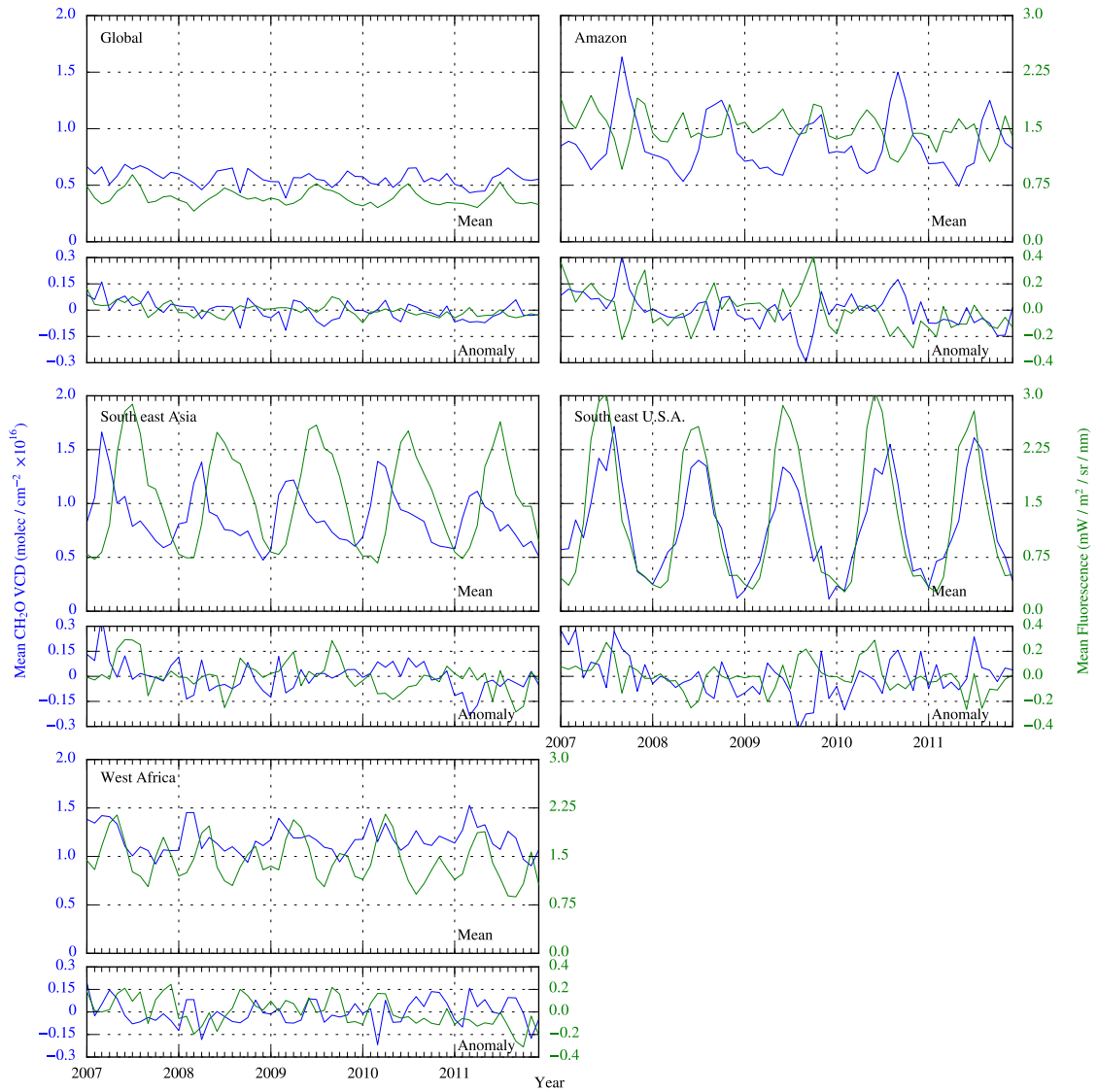


Figure 6.14: Monthly mean GOME-2 I_F and UoL CH_2O VCDs for the entire study period.

to global 0.25° monthly grids for comparison with UoL CH_2O measurements.

Figure 6.14 shows monthly mean variation in GOME-2 I_F alongside GOME-2 CH_2O VCDs, masked to land cells only. The global GOME-2 I_F mean contrasts with formaldehyde by exhibiting only one major annual peak, as opposed to formaldehyde's slightly muted second annual peak. Monthly GOME-2 I_F means for the Amazon show an annual pattern of a springtime (MAM) peak, followed by drops in fluorescence for the summer, and ending the year with another, smaller I_F peak. Figure 6.15 confirms a distinctive anti-correlation between Amazon CH_2O and I_F , with the largest CH_2O concentration peaks coinciding with major drops for I_F (e.g.

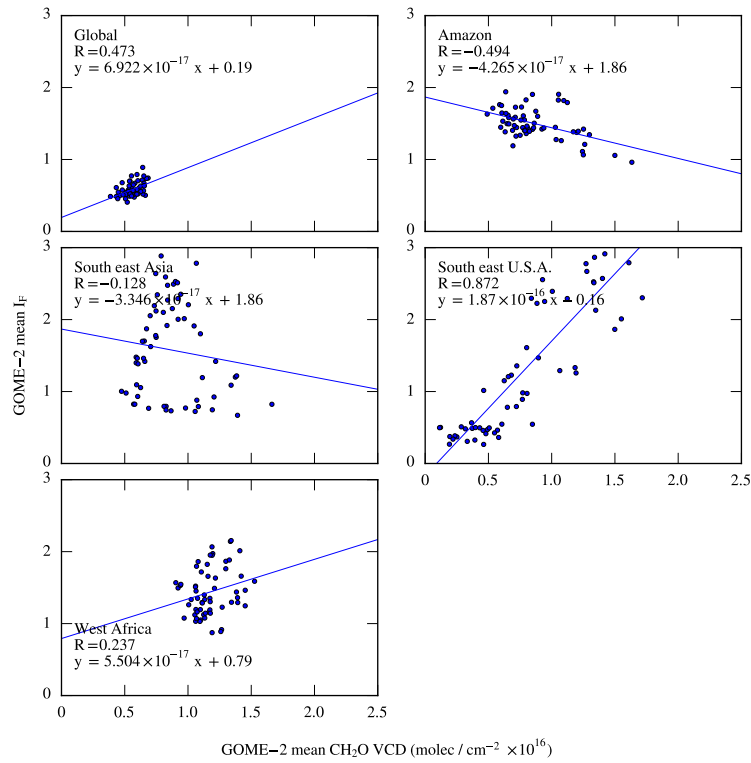


Figure 6.15: Correlation between 2007–2011 monthly mean GOME-2 I_F and UoL CH_2O VCDs.

JJA 2007 and 2010). Conversely, I_F peaks are matched by major dips in CH_2O columns, reflected in an R value of -0.494. Results for south east Asia and south east U.S.A. show a clearer picture, with the two parameters closely tracking one another throughout the year. Maximum south east Asian I_F values occur approximately 4 months after the CH_2O peak, whilst south eastern U.S.A. fluorescence data match formaldehyde with an R of 0.872. As with the Amazon region, west African agreement of CH_2O and I_F exhibits a bi-annual cycle of peaks early in the year, followed by a mis-match later on. Although fluorescence itself is a time dependent parameter in much the same fashion as CH_2O , these results show that fluorescence can provide a useful parameter for monitoring plant health, and by extension, CH_2O emissions, particularly for the Amazon region where biomass stores are high.

6.3 Summary

A 5 year atmospheric formaldehyde concentration product is generated from the processing of GOME-2 radiance data spanning 2007–2011. The product makes use of optimised spectroscopic parameters, and a significantly updated air mass factor algorithm, both detailed in the previous two chapters. Trend analysis for the observation period is performed on the entire dataset, exhibiting general small decreases over land with the exception of equatorial regions, and increases over oceans. Comparison against GEOS-Chem modelled CH_2O columns shows very strong agreement between the two datasets. Comparison to the existing BIRA GOME-2 CH_2O product also details similarity in retrieved columns, with variation between the two thought to arise from differing AMF routines. Validation against in-situ datasets would be preferable, although a current lack of relevant ground and aircraft based measurements covering the study period for regions of significantly elevated CH_2O columns precludes this for the time being.

Comparisons and correlations are drawn with four environmental parameters, demonstrating the utility of CH_2O as an atmospheric variable relevant to more detailed studies of biogenic interactions, particularly for the tropical regions. A mixed picture of regional correlations are found, with those regions exhibiting large swings in temperature (south east U.S.A.) also showing similar variation in CH_2O concentration – suggesting here temperature is one of the primary drivers for CH_2O . For regions less affected by seasonal temperature variation (e.g. Amazon, West Africa) correlations are not as clear, with a variety of factors likely to be contributing to seasonal cycles. In these instances, there exists a possibility for the use of CH_2O columns in combination with fluorescence measurements to provide an index of biomass health. It is acknowledged rain rate may not represent the best hydrological parameter to investigate with reference to isoprene emission, and by extension, vegetation studies, due to the fact these parameters are more likely to be affected by moisture availability to roots than instantaneous rainfall measurements. However, given the coverage issues associated with soil moisture products (e.g. Pradhan et al.

(2011), Wagner et al. (2013)), the availability of the TRMM product outweighed the problems associated with generating a new soil moisture climatology solely for this small study.

Fluorescence measurements from GOME-2 (Joiner et al., 2013) are also compared with the CH₂O product, exhibiting a mixed pattern of coincident variation between the two datasets. Peak formaldehyde concentrations are seen to correlate with low fluorescence values for some regions (Amazon, West Africa), with similar activity, albeit on a smaller scale, shown for south east Asia and south east U.S.A. General patterns drawn from these environmental correlations indicate an anti-correlation of formaldehyde concentrations with rain rate. Data from the Amazon region suggests reductions in monthly mean CH₂O concentrations (e.g. JJA 2009), are preceded by above average periods of rainfall (e.g. MMA 2009), whilst the opposite is true for periods of elevated CH₂O concentrations. Anomalies on the annual observation trend show temperature fluctuations to agree less well with CH₂O variation, indicating for the regions studied, water availability plays a larger role in isoprene emission than temperature.

Chapter 7

Discussion and Conclusions

This chapter presents an overview of work conducted for the project, together with further analysis, suggestions for improvements, and future work. Radiance data from the GOME-2 instrument flying aboard the MetOp-A satellite have been used to generate a new 5 year retrieval of tropospheric formaldehyde vertical columns, which are analysed to better understand variations in biogenic emissions.

Split into two main components, the retrieval consists of spectroscopic fitting of absorption cross sections to the GOME-2 radiances to derive line of sight CH_2O concentrations, and a calculation of a conversion factor to vertical column concentrations. Difficulties in the DOAS fitting portion are related to the very weak CH_2O absorption signal in comparison to other fitted absorbers, and accounting for GOME-2 instrumental degradation over the lifetime of the mission. The satellite DOAS community have developed a range of methods to mitigate for these effects (Vountas et al., 1998; Aliwell et al., 2002; Van Roozendael et al., 2002; Cai et al., 2012). The first objective of this work was to derive an optimised CH_2O retrieval by parameterising these error sources in an extensive series of sensitivity tests on actual GOME-2 data.

7.1 DOAS parameter testing

Split into 4 parameter groups, DOAS fit settings of importance were identified from the literature and previous satellite spectrometer CH₂O retrievals. The spectral fit range was determined as bearing the largest effect on retrievals, specifying the encroachment interfering absorption cross sections are able to make on the retrieval. Inclusion and exclusion of certain absorbers is also seen to carry a large impact on retrieved SCD and fit error, with some absorbers simulating the CH₂O absorption cross section and thereby artificially reducing retrieved CH₂O SCDs (e.g. BrO). Accounting for broad-band atmospheric effects in the DOAS fit is carried out by the subtraction of a fitted polynomial to radiances, the level of accuracy with which this can be performed depending on the ability of the polynomial to model these effects. In the small wavelength fit range used for CH₂O, a 5th order polynomial is shown to be most appropriate for removal of slowly fluctuating atmospheric absorption from the fit, in contrast to previous GOME-1 retrievals with wider fitting ranges, where 3rd order polynomials were found sufficient (Wittrock et al., 2006). Parameter testing for this work also served to identify the homogenisation of slant columns processed with the reference sector method to account for retrieval bias. Despite various DOAS fit parameters producing different slant column CH₂O concentrations, subsequent application of the RSM largely homogenised vertical columns to within an approximate range of 16–21% globally.

Absorption cross sections

Advances in O₃ and Ring retrieval accuracy are needed to significantly improve the CH₂O retrieval by reducing interference from these major absorbers in the formaldehyde fitting range. The availability of recently re-calibrated pre-launch measured O₃ GOME-2 cross sections (Chehade et al., 2013), and new high resolution cross sections intended for spectroscopic applications (Gorshelev et al., 2013) points towards an awareness of these needs in the DOAS community. However, early applications of these updated O₃ spectra have shown little to no reduction in fit residuals from an

improved ozone fit, so important for increasing the signal available for the CH₂O fit, with the Malicet et al. (1995) cross sections apparently remaining the optimal choice. Updated CH₂O absorption cross sections (Chance and Orphal, 2011) have become available since work for Chapter 4 was conducted, although exploratory retrievals with these for GOME-2 have not found improvements on the Meller and Moortgat (2000) cross sections. Mitigation for the Ring effect remains a major uncertainty in CH₂O retrievals, being the second most effective absorber in the formaldehyde fitting range after O₃, further highlighted in the *EI*₀ work here. The Vountas et al. (1998) Ring correction method offers an adequate representation of the Ring effect, although integrating scene specific variables, such as wavelength dependence of Fraunhofer filling in due to multiple scattering caused by aerosol and cloud, should offer an improved Ring correction term (Langford et al., 2007).

Instrument corrections

Whilst problems with accuracy of absorption cross sections are relevant to all DOAS applications, GOME-2 inflicts several instrument specific nuances on the retrieval which increase fit residuals. Although largely removed in monthly means, the east-west swath bias evident upon examination of individual orbits remains a significant problem for using small temporal windows of GOME-2 data. This scan degradation is thought to be caused by a layer of outgassed material coming to rest on the scan mirror (Dikty and Richter, 2011). The current EUMETSAT recommended fix of applying polarisation vectors does not provide a sufficient correction. To this end, several groups are pursuing their own empirical radiance correction models based on several years worth of retrievals, generating temporally dependent scan angle correction factors after the retrieval is conducted (Loyola et al., 2011b). An optimised solution would entail a thorough characterisation and modelling of the layers of matter in the spectrometer which are causing problems, allowing for a pre-retrieval correction of radiances. Such studies have been successful in the past, offering mitigation for SCIAMACHY's radiometric throughput issues (Snel and Krijger, 2009;

Krijger, 2013).

South Atlantic anomaly (SAA) affected areas encompass a large part of the Amazon basin, affecting retrieval accuracy for this major region of CH₂O emissions. Observations subject to an SAA event yield spurious values in the retrieval, for which current solutions are to remove the affected scan entirely, or expand this to ignore all scans within a pre-defined SAA affected region. Neither of these are implemented in the UoL retrieval, as monthly means serve to largely remove SAA effects due to the averaging process successfully accounting for outliers. However, an explicit SAA correction would be preferable in order to ensure scan counts are maximised over the SAA region. For their GOME-2 NO₂ retrieval, Richter et al. (2011) implement a procedure to detect anomalous spikes in individual Earthshine spectra, which in conjunction with an error weighted DOAS fit, serves to largely remedy affected scans. With the UoL retrieval not making use of DOAS error weighting, the method was adapted to ignore bad pixels all together by adding gaps to the fit over bad pixels, proving unsuccessful. Reasons for the failure are thought to be related to SAA affected scans in the CH₂O fitting range impacting on a greater number of pixels per scan than for the higher wavelength NO₂ fit, resulting in numerical instability in the DOAS procedure. It is thought implementation of error weighting in the DOAS procedure could alleviate these problems to a certain extent.

Future research directions

The QDOAS software retrieved approximately 164,250,000 CH₂O SCDs for the 5 year retrieval, offering a ready-made, stable, and well supported DOAS solution for CH₂O retrievals. However, despite QDOAS's heritage of validation and evaluation, constructing an in-house UoL DOAS algorithm would offer significant benefits for future work. These would include the ability to rapidly update the code in order to include new features such as WF-DOAS (taking into account radiance changes due to absorber profile), radiance error weighting on fits, and inclusion of scan specific geo-physical parameters such as atmospheric temperature for temperature

dependent cross sections. The prospect of an instrument specific DOAS retrieval would allow total integration of the SCD and VCD processing streams, greatly speeding up extended retrievals from the current scheme's dependence on several different pieces of software working in harmony.

7.2 Air mass factors

For development of the air mass factor, several parts of the algorithm were identified whose input parameter resolution could be upgraded thanks to the availability of new databases, and an improved version of the CTM. The addition of area weighting of gridded inputs enables a true per-observation AMF retrieval. Allowing for the inclusion of pressure correction of coarse CTM vertical absorber profiles over mountainous terrain brought about a general reduction in AMF for these regions, acting to increase the retrieved CH₂O VCD. Novel additions to the AMF algorithm are concerned with the accuracy of radiative transfer modelling, by applying orbit specific absorption cross sections carried through from the DOAS fit to scattering weight generation in order to account for instrument degradation and better matching initial spectroscopy. Improved representation of O₃ vertical mixing ratios for scattering weight generation is also included by scaling TOMS v8 ozone climatology data to each observation's DLR retrieved O₃ concentration.

AMF error characterisation is presented for two months proving the viability of error product generation for each scan, however in further work, an error product covering the full time-series of observations would be desirable. Spatial resolution of input databases and CTMs are now much more in line with the increased spatial resolution of a GOME-2 scan, with pixel area weighting serving to reduce grid induced bias further. Expanding the nested CTM from the Amazon region to global coverage would therefore be likely to provide the next significant step forward for AMF accuracy. Despite accounting for aerosol effects by way of CTM aerosol data, the possibility for a double aerosol correction is acknowledged, whereby both an explicit CTM aerosol correction, and an aerosol modified O₂ – O₂ CF serve to modify

the AMF at scattering weight generation, and independent pixel approximation stages. Mitigation for this would make use of a future GOME-2 aerosol product in conjunction with independent, but co-located cloud observations (Leitão et al., 2010).

Use of the high resolution OMI albedo product is seen to bear a large effect on calculated AMFs, due to the improved resolution on previous products. There exists a 3 hour time window in between OMI and GOME-2 local overpass time (13:30 and 09:30 respectively), in which differences in surface albedo are likely to occur. With GOME-2 still operational at time of writing there now exists an almost seven year record of GOME-2 radiance data – were a new albedo database to be generated with GOME-2 data utilising the instrument’s enhanced spatial resolution, further significant changes to AMFs could possibly be expected. On this theme, testing CH₂O AMFs for BRDF sensitivity may produce a different set of findings to the small changes found for the Zhou et al. (2009) NO₂ retrieval.

Future research directions

Although presented for CH₂O, the UoL retrieval should be easily extensible to tropospheric glyoxal (CHOCHO) and NO₂ retrievals. The AMF program is set up in such a way to allow this extension by the simple change of AMF calculation wavelength. Representing a slightly larger challenge for changing the observed trace gas, the DOAS portion of the retrieval would need a more thorough period of characterisation, optimisation and validation, particularly given the paucity of existing glyoxal retrievals (Wittrock, 2006; Lerot et al., 2009). Application of the AMF to existing and upcoming satellite instruments (e.g. TROPOMI) would be a trivial operation, with the primary concern being matching of DOAS fit window wavelengths to the stipulated AMF wavelength and associated wavelength dependent input grids (albedo and aerosol). An improved AMF cloud correction should also take into account available DLR OCRA/ROCINN cloud parameters (Loyola et al., 2011a), offering retrieved values of cloud top albedo and cloud optical thickness for

input to the scattering weight generation.

7.3 CH₂O VCD evaluation and comparisons

The penultimate chapter presented a 5 year CH₂O VCD generated with techniques detailed in the previous two chapters. This was compared to model CH₂O VCDs, demonstrating excellent agreement with GEOS-Chem data and so lending confidence to the new retrieval. Trend analysis was performed on the entire dataset in an effort to discern long term spatial variation, showing a slight reduction in columns over landmasses, and a very slight increase over oceans. In addition to GEOS-Chem, UoL VCDs show good agreement with the BIRA GOME-2 formaldehyde VCD product, with differences between the retrievals likely attributable to post SCD steps in the retrieval. Application of a MODIS / AATSR fire screen is intended to remove the influence of biomass burning affected scans from the dataset, discarding 9% of all GOME-2 scans with a strict screening algorithm. VCD trends remain the same with fire affected data removed, although major CH₂O concentration peaks in 2007 and 2010 were reduced.

Comparison of formaldehyde VCDs with the associated environmental variables of aerosol, rainfall rate, land surface temperature and fluorescence were then drawn. Few comparisons of this kind are noted in the literature, with mechanisms describing CH₂O formaldehyde emission response to external parameters at a global scale still requiring exploration. Aerosol optical depth from GEOS-Chem and VCD comparisons are made, with both showing similar temporal patterns for emissions, but providing an inconclusive picture as to the relationship between the two due. TRMM rain rate data correlate with CH₂O VCDs in a general sense of annual cycles as well, however a clearer picture of CH₂O concentration reliance on moisture may well be garnered from soil moisture datasets, whose values can be more reliably linked to vegetation health. Similarly, land surface temperature shows general agreement with observed columns globally and for studied regions, expected given the knowledge of isoprene's emission dependence on the parameter. New GOME-2 fluorescence

data gives an indication of the photosynthetic efficiency of vegetation, exhibiting a complicated relationship with formaldehyde VCDs. Some studied regions (south east U.S.A. and Asia) showed strong matching of time series for both annual cycles and magnitude, whilst for others (Amazon and west Africa) there exists clear anti-correlations. This suggests further research needs conducting investigating the matching dependencies of these closely related variables in order to ascertain causes.

Future research directions

The local overpass time of MetOp-A (09:30) means GOME-2 precedes the CH₂O peak by 3–4 hours, although use of the data in tandem with those observing the peak (e.g. OMI) provides an important component in analysing the temporal evolution of the formaldehyde column. Further validation of the product against in-situ datasets is required in order to increase confidence in the retrieval further than its excellent agreement with model and satellite datasets. There is currently a scarcity of such real world data, largely due to the inaccessibility and associated expense of conducting measurement campaigns in the tropics where CH₂O is most prevalent. This is exemplified by regional studies in this work of west Africa and the Amazon, which both show excellent agreement with CTM CH₂O VCD temporally whilst disagreeing on magnitudes. Despite this, previous work has shown good agreement between in-situ measurements and satellite observed columns (Martin et al., 2004; Millet et al., 2006; Vigouroux et al., 2009).

Given the high spatial resolution of GOME-2, coupled to the extended time-series of data available, a detailed analysis of CH₂O columns at local scales should provide an interesting compliment to regional analysis here. Gridded to 0.1° monthly means, the dataset is entirely applicable to examination of emissions from megacities and industrial centres - although it is acknowledged extra aerosol and haze generally associated with these regions may prevent a reliable discrimination of the CH₂O signal. To this end, a more thorough examination of CH₂O's interaction with regional aerosol concentrations could provide further insights into isoprene's role

in secondary organic aerosol production, whilst increasing accuracy of the highly sensitive aerosol correction in AMF calculations (Leitão et al., 2010; Veefkind et al., 2011). On a similar theme, investigating the relationship of CH₂O concentrations to various environmental and meteorological parameters should provide a better insight into the role of the trace gas at local and regional scales, with well validated trace gases such as NO₂ already receiving such attention (Zhou et al., 2012).

7.4 Conclusions

In an effort to ensure optimal retrieval settings are in use, tropospheric DOAS retrievals of formaldehyde with the GOME-2 instrument have been thoroughly characterised by an extensive suite of sensitivity tests in the first portion of this work. Air mass factors were calculated for each observation in a 5 year GOME-2 dataset using an upgraded AMF algorithm taking into account advances in spatial resolution of input databases and several novel additions to improve the representation of scattering weights in the calculation. Both DOAS retrievals and AMF calculations were combined in the final chapter for the generation of a continuous five year global dataset spanning 2007–2011. Following evaluation against model and other group’s satellite CH₂O columns, exploratory correlations were drawn against several external environmental parameters.

For a development of work with the new 5 year UoL formaldehyde dataset presented here, its application to isoprene inversions would represent the next logical step. The confidence in this dataset inspired by the thorough description of algorithms and testing gone into its construction for this work should allow for an improvement in the understanding of isoprene’s effects on tropospheric chemistry. The relevance of such retrievals as presented here can only increase as the climate adjusts in response to anthropogenic forcing, providing extremely valuable data with which to validate the spatial and temporal components of the growing number of Earth system models accounting for atmospheric chemistry.

References

- Abbot, D. S., Palmer, P. I., Martin, R. V., Chance, K. V., Jacob, D. J. and Guenther, A.: 2003, Seasonal and interannual variability of North American isoprene emissions as determined by formaldehyde column measurements from space, *Geophysical Research Letters* **30**(17), ASC 5-1 – 5-4.
- Acker, J. G. and Leptoukh, G.: 2007, Online analysis enhances use of NASA Earth science data, *Eos, Transactions American Geophysical Union* **88**(2), 14–17.
- Aghedo, A. M., Bowman, K. W., Worden, H. M., Kulawik, S. S., Shindell, D. T., Lamarque, J. F., Faluvegi, G., Parrington, M., Jones, D. B. A. and Rast, S.: 2011, The vertical distribution of ozone instantaneous radiative forcing from satellite and chemistry climate models, *Journal of Geophysical Research: Atmospheres* **116**(D1).
- Ainsworth, E. A., Yendrek, C. R., Sitch, S., Collins, W. J. and Emberson, L. D.: 2012, The effects of tropospheric ozone on net primary productivity and implications for climate change, *Annual Review of Plant Biology* **63**(1), 637–661.
- Aliwell, S. R., Van Roozendaal, M., Johnston, P. V., Richter, A., Wagner, T., Arlander, D. W., Burrows, J. P., Fish, D. J., Jones, R. L., Tørnkvist, K. K., Lambert, J., Pfeilsticker, K. and Pundt, I.: 2002, Analysis for BrO in zenith-sky spectra: An intercomparison exercise for analysis improvement, *Journal of Geophysical Research: Atmospheres* **107**(14), 10-1–10-20.
- Andreae, M. O. and Merlet, P.: 2001, Emission of trace gases and aerosols from biomass burning, *Global Biogeochemical Cycles* **15**(4), 955–966.
- Andrews, E. S., Theis, N. and Adler, L. S.: 2007, Pollinator and herbivore attraction to Cucurbita floral volatiles, *Journal of Chemical Ecology* **33**(9), 1682–1691.
- Anthropogenic emissions - GEOS-Chem*: 2013.
URL: wiki.seas.harvard.edu/geos-chem/index.php/Anthropogenic_emissions
- Antón, M., Loyola, D., López, M., Vilaplana, J. M., Bañón, M., Zimmer, W. and Serrano, A.: 2009, Comparison of GOME-2/MetOp total ozone data with Brewer spectroradiometer data over the Iberian Peninsula, *Annales Geophysicae* **27**(4), 1377–1386.
- Apel, E. C., Olson, J. R., Crawford, J. H., Hornbrook, R. S., Hills, A. J., Cantrell, C. A., Emmons, L. K., Knapp, D. J., Hall, S., Mauldin III, R. L., Weinheimer, A. J., Fried, A., Blake, D. R., Crouse, J. D., Clair, J. M. S., Wennberg, P. O., Diskin, G. S., Fuelberg, H. E., Wisthaler, A., Mikoviny, T., Brune, W. and Riemer, D. D.: 2012, Impact of the deep convection of isoprene and other reactive trace species on radicals and ozone in the upper troposphere, *Atmospheric Chemistry and Physics* **12**(2), 1135–1150.
- Archibald, A. T., Cooke, M. C., Utembe, S. R., Shallcross, D. E., Derwent, R. G.

- and Jenkin, M. E.: 2010, Impacts of mechanistic changes on HO_x formation and recycling in the oxidation of isoprene, *Atmospheric Chemistry and Physics* **10**(17), 8097–8118.
- Archibald, A. T., Levine, J. G., Abraham, N. L., Cooke, M. C., Edwards, P. M., Heard, D. E., Jenkin, M. E., Karunaharan, A., Pike, R. C., Monks, P. S., Shallcross, D. E., Telford, P. J., Whalley, L. K. and Pyle, J. A.: 2011, Impacts of HO_x regeneration and recycling in the oxidation of isoprene: Consequences for the composition of past, present and future atmospheres, *Geophysical Research Letters* **38**(5), n/a–n/a.
- Arino, O., Plummer, S. and Defrenne, D.: 2005, Fire disturbance: the ten years time series of the ATSR world fire atlas, *Proceedings of the MERIS-AATSR workshop 2005*, Frascati, Italy.
- Arneth, A., Harrison, S. P., Zaehle, S., Tsigaridis, K., Menon, S., Bartlein, P. J., Feichter, J., Korhola, A., Kulmala, M., O'Donnell, D., Schurgers, G., Sorvari, S. and Vesala, T.: 2010, Terrestrial biogeochemical feedbacks in the climate system, *Nature Geosci.* **3**(8), 525–532.
- Arneth, A., Monson, R. K., Schurgers, G., Niinemets, U. and Palmer, P. I.: 2008, Why are estimates of global terrestrial isoprene emissions so similar (and why is this not so for monoterpenes)?, *Atmospheric Chemistry and Physics* **8**(16), 4605–4620.
- Arneth, A., Niinemets, U., Pressley, S., Bäck, J., Hari, P., Karl, T., Noe, S., Prentice, I. C., Serça, D., Hickler, T., Wolf, A. and Smith, B.: 2007, Process-based estimates of terrestrial ecosystem isoprene emissions: incorporating the effects of a direct CO₂-isoprene interaction, *Atmospheric Chemistry and Physics* **7**(1), 31–53.
- Arneth, A., Schurgers, G., Lathiere, J., Duhl, T., Beerling, D. J., Hewitt, C. N., Martin, M. and Guenther, A.: 2011, Global terrestrial isoprene emission models: sensitivity to variability in climate and vegetation, *Atmospheric Chemistry and Physics* **11**(15), 8037–8052.
- Ashmore, M. R.: 2005, Assessing the future global impacts of ozone on vegetation, *Plant, Cell & Environment* **28**(8), 949–964.
- Atkinson, R.: 2000, Atmospheric chemistry of VOCs and NO_x, *Atmospheric Environment* **34**(12-14), 2063–2101.
- Atkinson, R. and Arey, J.: 2003, Atmospheric degradation of volatile organic compounds, *Chemical reviews* **103**(12), 4605–4638.
- Baldwin, I. T., Halitschke, R., Paschold, A., Von Dahl, C. C. and Preston, C. A.: 2006, Volatile signaling in plant-plant interactions: "Talking trees" in the genomics era, *Science* **311**(5762), 812–815.
- Baldwin, I. T. and Shultz, J. C.: 1983, Rapid Changes in Tree Leaf Chemistry Induced by Damage: Evidence for Communication Between Plants, *Science* **221**(4607), 277–279.
- Balis, D., Koukouli, M., Loyola, D., Valks, P. and Hao, N.: 2008, Second validation report of GOME-2 total ozone products (OTO/O3, NTO/O3) processed with GDP4.2, *Report SAF/O3M/AUTH/GOME-2VAL/RP/02*, O3M-SAF.
- Barkley, M. P., De Smedt, I., Van Roozendael, M., Kurosu, T. P., Chance, K., Arneth, A., Hagberg, D., Guenther, A., Paulot, F., Marais, E. A. and Mao, J.:

- 2013, Top-down isoprene emissions over tropical South America inferred from SCIAMACHY and OMI formaldehyde columns, *Journal of Geophysical Research: Atmospheres* **118**(12), 6849–6868.
- Barkley, M. P., Kurosu, T. P., Chance, K., De Smedt, I., Van Roozendael, M., Arneth, A., Hagberg, D. and Guenther, A.: 2012a, Assessing sources of uncertainty in formaldehyde air mass factors over tropical South America: Implications for top-down isoprene emission estimates, *Journal of Geophysical Research: Atmospheres* **117**(D13).
- Barkley, M. P., Palmer, P. I., De Smedt, I., Karl, T., Guenther, A. and Van Roozendael, M.: 2009, Regulated large-scale annual shutdown of Amazonian isoprene emissions?, *Geophysical Research Letters* **36**(4).
- Barkley, M. P., Palmer, P. I., Ganzeveld, L., Arneth, A., Hagberg, D., Karl, T., Guenther, A., Paulot, F., Wennberg, P. O., Mao, J., Kurosu, T. P., Chance, K., Müller, J. ., De Smedt, I., Van Roozendael, M., Chen, D., Wang, Y. and Yantosca, R. M.: 2011, Can a "state of the art" chemistry transport model simulate Amazonian tropospheric chemistry?, *Journal of Geophysical Research: Atmospheres* **116**(16).
- Barkley, M. P., Palmer, P. I., Kuhn, U., Kesselmeier, J., Chance, K., Kurosu, T. P., Martin, R. V., Helmig, D. and Guenther, A.: 2008, Net ecosystem fluxes of isoprene over tropical South America inferred from Global Ozone Monitoring Experiment (GOME) observations of HCHO columns, *Journal of Geophysical Research: Atmospheres* **113**(20).
- Beerling, D. J., Fox, A., Stevenson, D. S. and Valdes, P. J.: 2011, Enhanced chemistry-climate feedbacks in past greenhouse worlds, *Proceedings of the National Academy of Sciences of the United States of America* **108**(24), 9770–9775.
- Beerling, D. J., Hewitt, C. N., Pyle, J. A. and Raven, J. A.: 2007, Critical issues in trace gas biogeochemistry and global change, *Philosophical Transactions of the Royal Society A: Mathematical, Physical and Engineering Sciences* **365**(1856), 1629–1642.
- Benedetti, A., Morcrette, J.-J., Boucher, O., Dethof, A., Engelen, R. J., Fisher, M., Flentje, H., Huneeus, N., Jones, L., Kaiser, J. W., Kinne, S., Mangold, A., Razinger, M., Simmons, A. J. and Suttie, M.: 2009, Aerosol analysis and forecast in the European Centre for Medium-Range Weather Forecasts Integrated Forecast System: 2. Data assimilation, *Journal of Geophysical Research: Atmospheres* **114**(D13).
- Bertram, T. H., Heckel, A., Richter, A., Burrows, J. P. and Cohen, R. C.: 2005, Satellite measurements of daily variations in soil NO_x emissions, *Geophysical Research Letters* **32**(24).
- Bey, I., Jacob, D. J., Yantosca, R. M., Logan, J. A., Field, B. D., Fiore, A. M., Li, Q., Liu, H. Y., Mickley, L. J. and Schultz, M. G.: 2001, Global modeling of tropospheric chemistry with assimilated meteorology: Model description and evaluation, *Journal of Geophysical Research: Atmospheres* **106**(D19), 23073–23095.
- Bhartia, P. K.: 2002, TOMS-V8 Total O₃ Algorithm Theoretical Basis Document, *OMI Algorithm Theoretical Basis Document*, NASA Goddard Space Flight Center, Greenbelt, Maryland, USA.
- Boeke, N. L., Marshall, J. D., Alvarez, S., Chance, K. V., Fried, A., Kurosu, T. P.,

- Rappenglück, B., Richter, D., Walega, J., Weibring, P. and Millet, D. B.: 2011, Formaldehyde columns from the Ozone Monitoring Instrument: Urban versus background levels and evaluation using aircraft data and a global model, *Journal of Geophysical Research: Atmospheres* **116**(5).
- Boersma, K. F., Braak, R. and van der A, R. J.: 2011b, Dutch OMI NO₂ (DOMINO) data product v2.0, *User Manual*, KNMI.
- Boersma, K. F., Eskes, H. J. and Brinksma, E. J.: 2004, Error analysis for tropospheric NO₂ retrieval from space, *Journal of Geophysical Research: Atmospheres* **109**(4), D04311 1–20.
- Boersma, K. F., Eskes, H. J., Dirksen, R. J., van der A, R. J., Veefkind, J. P., Stammes, P., Huijnen, V., Kleipool, Q. L., Sneep, M., Claas, J., Leitão, J., Richter, A., Zhou, Y. and Brunner, D.: 2011, An improved tropospheric NO₂ column retrieval algorithm for the Ozone Monitoring Instrument, *Atmospheric Measurement Techniques* **4**(9), 1905–1928.
- Bogumil, K., Orphal, J., Homann, T., Voigt, S., Spietz, P., Fleischmann, O., Vogel, A., Hartmann, M., Kromminga, H., Bovensmann, H., Frerick, J. and Burrows, J.: 2003, Measurements of molecular absorption spectra with the sciamachy pre-flight model: instrument characterization and reference data for atmospheric remote-sensing in the 230–2380 nm region, *Journal of Photochemistry and Photobiology A: Chemistry* **157**(2–3), 167 – 184.
- Bovensmann, H., Burrows, J. P., Buchwitz, M., Frerick, J., Noël, S., Rozanov, V. V., Chance, K. V. and Goede, A. P. H.: 1999, Sciamachy: Mission objectives and measurement modes, *Journal of the Atmospheric Sciences* **56**(2), 127–150.
- Brasseur, G. P., Kiehl, J. T., Müller, J. ., Schneider, T., Granier, C., Tie, X. and Hauglustaine, D.: 1998, Past and future changes in global tropospheric ozone: Impact on radiative forcing, *Geophysical Research Letters* **25**(20), 3807–3810.
- Brauers, T., Bossmeyer, J., Dorn, H., Schlosser, E., Tillmann, R., Wegener, R. and Wahner, A.: 2007, Investigation of the formaldehyde differential absorption cross section at high and low spectral resolution in the simulation chamber saphir, *Atmospheric Chemistry and Physics* **7**(13), 3579–3586.
- Bristow, C. S., Hudson-Edwards, K. A. and Chappell, A.: 2010, Fertilizing the Amazon and equatorial Atlantic with West African dust, *Geophysical Research Letters* **37**(14).
- Brunekreef, B. and Holgate, S. T.: 2002, Air pollution and health, *Lancet* **360**(9341), 1233–1242.
- Buchwitz, M., Rozanov, V. V. and Burrows, J. P.: 2000, A near-infrared optimized DOAS method for the fast global retrieval of atmospheric CH₄, CO, CO₂, H₂O, and N₂O total column amounts from SCIAMACHY Envisat-1 nadir radiances, *Journal of Geophysical Research: Atmospheres* **105**(D12), 15231–15245.
- Burrows, J. P., Weber, M., Buchwitz, M., Rozanov, V., Ladstätter-Weissenmayer, A., Richter, A., Debeek, R., Hoogen, R., Bramstedt, K., Eichmann, K., Eisinger, M. and Perner, D.: 1999b, The Global Ozone Monitoring Experiment (GOME): Mission concept and first scientific results, *Journal of the Atmospheric Sciences* **56**(2), 151–175.
- Cai, Z., Liu, Y., Liu, X., Chance, K., Nowlan, C. R., Lang, R., Munro, R. and Suleiman, R.: 2012, Characterization and correction of Global Ozone Monitoring

- Experiment 2 ultraviolet measurements and application to ozone profile retrievals, *Journal of Geophysical Research: Atmospheres* **117**(D7).
- Callies, J., Corpaccioli, E., Eisinger, M., Hahne, A. and Lefebvre, A.: 2000, GOME-2 – Metop’s Second-Generation Sensor for Operational Ozone Monitoring, *ESA Bulletin*, Vol. 102, pp. 28–36.
- Calvert, J. G., Alistair Kerr, J., Demerjian, K. L. and McQuigg, R. D.: 1972, Photolysis of formaldehyde as a hydrogen atom source in the lower atmosphere, *Science* **175**(4023), 751–752.
- Cantrell, C. A., Davidson, J. A., McDaniel, A. H., Shetter, R. E. and Calvert, J. G.: 1990, Temperature-dependent formaldehyde cross sections in the near-ultraviolet spectral region, *Journal of Physical Chemistry* **94**(10), 3902–3908.
- Carlton, A. G., Wiedinmyer, C. and Kroll, J. H.: 2009, A review of Secondary Organic Aerosol (SOA) formation from isoprene, *Atmospheric Chemistry and Physics* **9**(14), 4987–5005.
- Carpenter, L. J., Fleming, Z. L., Read, K. A., Lee, J. D., Moller, S. J., Hopkins, J. R., Purvis, R. M., Lewis, A. C., Müller, K., Heinold, B., Herrmann, H., Fomba, K. W., Pinxteren, D., Müller, C., Tegen, I., Wiedensohler, A., Müller, T., Niedermeier, N., Achterberg, E. P., Patey, M. D., Kozlova, E. A., Heimann, M., Heard, D. E., Plane, J. M. C., Mahajan, A., Oetjen, H., Ingham, T., Stone, D., Whalley, L. K., Evans, M. J., Pilling, M. J., Leigh, R. J., Monks, P. S., Karunaharan, A., Vaughan, S., Arnold, S. R., Tschritter, J., Pöhler, D., Frieß, U., Holla, R., Mendes, L. M., Lopez, H., Faria, B., Manning, A. J. and Wallace, D. W. R.: 2010, Seasonal characteristics of tropical marine boundary layer air measured at the Cape Verde Atmospheric Observatory, *Journal of Atmospheric Chemistry* **67**(2-3), 87–140.
- Caspar, C. and Chance, K.: 1997, GOME wavelength calibration using solar and atmospheric spectra, *European Space Agency, (Special Publication) ESA SP* (414 PART 2), 609–612.
- Chamberlain, R. G. and Duquette, W. H.: 2007, Some algorithms for polygons on a sphere, *Emerging Computational Techniques and Technologies in GeoComputation*, Association of American Geographers, Jet Propulsion Laboratory, Pasadena, California, U.S.A.
- Chameides, W. L., Lindsay, R. W., Richardson, J. and Kiang, C. S.: 1988, The role of biogenic hydrocarbons in urban photochemical smog: Atlanta as a case study, *Science* **241**(4872), 1473–1475.
- Chameides, W. L., Xingsheng, L., Xiaoyan, T., Xiuji, Z., Luo, C., Kiang, C. S., St. John, J., Saylor, R. D., Liu, S. C., Lam, K. S., Wang, T. and Giorgi, F.: 1999, Is ozone pollution affecting crop yields in China?, *Geophysical Research Letters* **26**(7), 867–870.
- Chance, K.: 1998, Analysis of BrO measurements from the Global Ozone Monitoring Experiment, *Geophysical Research Letters* **25**(17), 3335–3338.
- Chance, K.: 2002, OMI Trace Gas Algorithms, *OMI Algorithm Theoretical Basis Document*, Smithsonian Astrophysical Observatory, Cambridge, MA, USA.
- Chance, K., Kurosu, T. P. and Sioris, C. E.: 2005, Undersampling correction for array detector-based satellite spectrometers, *Appl. Optics* **44**(7), 1296–1304.
- Chance, K. and Kurucz, R. L.: 2010, An improved high-resolution solar refer-

- ence spectrum for earth's atmosphere measurements in the ultraviolet, visible, and near infrared, *Journal of Quantitative Spectroscopy and Radiative Transfer* **111**(9), 1289–1295.
- Chance, K. and Orphal, J.: 2011, Revised ultraviolet absorption cross sections of H₂CO for the HITRAN database, *Journal of Quantitative Spectroscopy and Radiative Transfer* **112**(9), 1509–1510.
- Chance, K., Palmer, P. I., Spurr, R. J. D., Martin, R. V., Kurosu, T. P. and Jacob, D. J.: 2000, Satellite observations of formaldehyde over North America from GOME, *Geophysical Research Letters* **27**(21), 3461–3464.
- Chance, K. and Spurr, R. J. D.: 1997, Ring effect studies: Rayleigh scattering, including molecular parameters for rotational Raman scattering, and the Fraunhofer spectrum, *Appl. Optics* **36**(21), 5224–5230.
- Chapman, S.: 1932, Discussion of memoirs. on a theory of upper-atmospheric ozone, *Quarterly Journal of the Royal Meteorological Society* **58**(243), 11–13.
- Chehade, W., Gür, B., Spietz, P., Gorshelev, V., Serdyuchenko, A., Burrows, J. P. and Weber, M.: 2013, Temperature dependent ozone absorption cross section spectra measured with the GOME-2 FM3 spectrometer and first application in satellite retrievals, *Atmospheric Measurement Techniques* **6**(7), 1623–1632.
- Chen, J., Avise, J., Guenther, A., Wiedinmyer, C., Salathe, E., Jackson, R. B. and Lamb, B.: 2009, Future land use and land cover influences on regional biogenic emissions and air quality in the United States, *Atmospheric Environment* **43**(36), 5771 – 5780.
- Cicerone, R. J. and Oremland, R. S.: 1988, Biogeochemical aspects of atmospheric methane, *Global Biogeochemical Cycles* **2**(4), 299–327.
- Claeys, M., Graham, B., Vas, G., Wang, W., Vermeylen, R., Pashynska, V., Cafmeyer, J., Guyon, P., Andreae, M. O., Artaxo, P. and Maenhaut, W.: 2004, Formation of secondary organic aerosols through photooxidation of isoprene, *Science* **303**(5661), 1173–1176.
- Coldewey-Egbers, M., Slijkhuis, S., Aberle, B. and Loyola, D.: 2008, Long-term analysis of GOME in-flight calibration parameters and instrument degradation, *Appl. Opt.* **47**(26), 4749–4761.
- Coldewey-Egbers, M., Weber, M., Lamsal, L. N., de Beek, R., Buchwitz, M. and Burrows, J. P.: 2005, Total ozone retrieval from GOME UV spectral data using the weighting function DOAS approach, *Atmospheric Chemistry and Physics* **5**(4), 1015–1025.
- Collins, W. D., Ramaswamy, V., Schwarzkopf, M. D., Sun, Y., Portmann, R. W., Fu, Q., Casanova, S. E. B., Dufresne, J.-L., Fillmore, D. W., Forster, P. M. D., Galin, V. Y., Gohar, L. K., Ingram, W. J., Kratz, D. P., Lefebvre, M.-P., Li, J., Marquet, P., Oinas, V., Tsushima, Y., Uchiyama, T. and Zhong, W. Y.: 2006, Radiative forcing by well-mixed greenhouse gases: Estimates from climate models in the Intergovernmental Panel on Climate Change (IPCC) Fourth Assessment Report (AR4), *Journal of Geophysical Research: Atmospheres* **111**(D14).
- Collins, W. J., Derwent, R. G., Johnson, C. E. and Stevenson, D. S.: 2002, The Oxidation of Organic Compounds in the Troposphere and their Global Warming Potentials, *Climatic Change* **52**(4).

- Collins, W. J., Sitch, S. and Boucher, O.: 2010, How vegetation impacts affect climate metrics for ozone precursors, *Journal of Geophysical Research: Atmospheres* **115**(D23).
- Colomb, A., Gros, V., Alvain, S., Sarda-Esteve, R., Bonsang, B., Moulin, C., Klpfel, T. and Williams, J.: 2009, Variation of atmospheric volatile organic compounds over the Southern Indian Ocean (30–49°S), *Environmental Chemistry* **6**(1), 70–82.
- Conrad, R.: 1996, Soil microorganisms as controllers of atmospheric trace gases (H₂, CO, CH₄, OCS, N₂O, and NO), *Microbiological reviews* **60**(4), 609–640.
- Cooke, M. C., Utembe, S. R., Gorrotxategi Carbajo, P., Archibald, A. T., Orr-Ewing, A. J., Jenkin, M. E., Derwent, R. G., Lary, D. J. and Shallcross, D. E.: 2010, Impacts of formaldehyde photolysis rates on tropospheric chemistry, *Atmospheric Science Letters* **11**(1), 33–38.
- Curci, G., Palmer, P. I., Kurosu, T. P., Chance, K. and Visconti, G.: 2010, Estimating European volatile organic compound emissions using satellite observations of formaldehyde from the Ozone Monitoring Instrument, *Atmospheric Chemistry and Physics* **10**(23), 11501–11517.
- Danielson, J. and Gesch, D.: 2011, Global Multi-resolution Terrain Elevation Data 2010 (GMTED2010), *Open-File Report 2011-1073*, U.S. Geological Survey.
- De Arellano, J. V. ., Patton, E. G., Karl, T., Van Den Dries, K., Barth, M. C. and Orlando, J. J.: 2011, The role of boundary layer dynamics on the diurnal evolution of isoprene and the hydroxyl radical over tropical forests, *Journal of Geophysical Research: Atmospheres* **116**(7).
- De Beek, R., Vountas, M., Rozanov, V. V., Richter, A. and Burrows, J. P.: 2001, The Ring effect in the cloudy atmosphere, *Geophysical Research Letters* **28**(4), 721–724.
- De Beek, R., Weber, M., Rozanov, V. V., Rozanov, A., Richter, A. and Burrows, J. P.: 2004, Trace gas column retrieval - an error assessment study for GOME-2, *Advances in Space Research* **34**(4), 727–733.
- De Smedt, I.: 2011, *Long-Term Global Observations of Tropospheric Formaldehyde Retrieved from Spaceborne Nadir UV Sensors*, PhD thesis, Universite Libre De Bruxelles, Laboratoire de Chimie Quantique et Photophysique, Faculté de Sciences Appliquées.
- De Smedt, I., Müller, J., Stavrou, T., Van Der A, R., Eskes, H. and Van Roozendael, M.: 2008, Twelve years of global observations of formaldehyde in the troposphere using GOME and SCIAMACHY sensors, *Atmospheric Chemistry and Physics* **8**(16), 4947–4963.
- De Smedt, I., Stavrou, J., Müller, J.-F., Hao, N., Valks, P., Loyola, D. and Van Roozendael, M.: 2009, H₂CO Columns Retrieved From GOME-2: First Scientific Results And Progress Towards The Development Of An Operational Product, *Proceedings of the EUTMETSAT conference, 2009*.
- De Smedt, I., Van Roozendael, M., Stavrou, T., Müller, J.-F., Lerot, C., Theys, N., Valks, P., Hao, N. and van der A, R.: 2012, Improved retrieval of global tropospheric formaldehyde columns from GOME-2/MetOp-A addressing noise reduction and instrumental degradation issues, *Atmospheric Measurement Techniques* **5**(11), 2933–2949.

- Diffey, B. L.: 1991, Solar ultraviolet radiation effects on biological systems, *Physics in Medicine and Biology* **36**(3), 299.
- Dikty, S. and Richter, A.: 2011, Support for Analysis of GOME-2 In-Orbit Degradation and Impacts on Level 2 Data Products, *Technical Report ITT 09/10000262*, EUMETSAT, Insitute of Remote Sensing, University of Bremen.
- Dufour, G., Wittrock, F., Camredon, M., Beekmann, M., Richter, A., Aumont, B. and Burrows, J. P.: 2009, SCIAMACHY formaldehyde observations: Constraint for isoprene emission estimates over Europe?, *Atmospheric Chemistry and Physics* **9**(5), 1647–1664.
- Duncan, B. N., Logan, J. A., Bey, I., Megretskaia, I. A., Yantosca, R. M., Novelli, P. C., Jones, N. B. and Rinsland, C. P.: 2007, Global budget of CO, 1988–1997: Source estimates and validation with a global model, *Journal of Geophysical Research: Atmospheres* **112**(D22).
- Duncan, B. N., Yoshida, Y., Damon, M. R., Douglass, A. R. and Witte, J. C.: 2009, Temperature dependence of factors controlling isoprene emissions, *Geophysical Research Letters* **36**(5).
- EDGAR: 2011, *Emission Database for Global Atmospheric Research (EDGAR), release version 4.2*, European Commission, Joint Research Centre (JRC)/Netherlands Environmental Assessment Agency (PBL).
URL: <http://edgar.jrc.ec.europa.eu>
- Edlén, B.: 1966, The refractive index of air, *Metrologia* **2**(2), 71–80.
- Eerdeken, G., Ganzeveld, L., Vilà-Guerau de Arellano, J., Klüpfel, T., Sinha, V., Yassaa, N., Williams, J., Harder, H., Kubistin, D., Martinez, M. and Lelieveld, J.: 2009, Flux estimates of isoprene, methanol and acetone from airborne PTR-MS measurements over the tropical rainforest during the GABRIEL 2005 campaign, *Atmospheric Chemistry and Physics* **9**(13), 4207–4227.
- Eisinger, M., Burrows, J. P., Richter, A. and Ladstätter-Weissenmayer, A.: 1997, SO₂, OClO, BrO, and other minor trace gases from the Global Ozone Monitoring Experiment (GOME), *Proceedings of the 3rd ERS-2 Symposium, Florence, Italy*, ESA, <http://earth.esa.int/workshops/ers97/papers/eisinger/>.
- Environment Canada: 2013, Environment Canada - Pollution and Waste - NPRI Datasets.
URL: <http://www.ec.gc.ca/inrp-npri/default.asp?lang=en&n=0EC58C98->
- Eskes, H. J. and Boersma, K. F.: 2003, Averaging kernels for DOAS total-column satellite retrievals, *Atmospheric Chemistry and Physics* **3**(5), 1285–1291.
- EUMETSAT: 2009, GOME-2 FM3 Long-Term In-Orbit Degradation - Status After 2nd Throughput Test, *Technical Report EUM/OPS-EPS/TEN/09/0318*, EUMETSAT, Am Kavalleriesand 31, D-64295 Darmstadt, Germany.
- EUMETSAT: 2011a, GOME-2 Product Generation Statement, *Technical Report EPS.SYS.SPE.990011*, EUMETSAT.
- EUMETSAT: 2011b, GOME-2 Product Guide, *Technical Report EUM/OPS-EPS/MAN/07/0445*, EUMETSAT.
- EUMETSAT: 2012, GOME-2 / Metop-A Reprocessed L1B-R2 Data-Set User Guide, *Technical Report EUM/OPS-EPS/DOC/09/0618*, EUMETSAT, EUMETSAT Allee 1, D-64295 Darmstadt, Germany.

- Farman, J. C., Gardiner, B. G. and Shanklin, J. D.: 1985, Large losses of total ozone in Antarctica reveal seasonal ClO_x / NO_x interaction, *Nature* **315**(6016), 207–210.
- Fayt, C., De Smedt, I., Letocart, V., Merlaud, A., Pinardi, G. and Van Roozendaal, M.: 2011, *QDOAS software user manual*, 1.00 edn, Belgian Institute for Space Aeronomy.
- Finlayson-Pitts, B. J. and Pitts, J. N.: 2000, Chapter 1 - overview of the chemistry of polluted and remote atmospheres, *Chemistry of the Upper and Lower Atmosphere*, Academic Press, San Diego, pp. 1 – 14.
- Fiore, A. M., Levy II, H. and Jaffe, D. A.: 2011, North American isoprene influence on intercontinental ozone pollution, *Atmospheric Chemistry and Physics* **11**(4), 1697–1710.
- Fish, D. J. and Jones, R. L.: 1995, Rotational Raman scattering and the ring effect in zenith-sky spectra, *Geophysical Research Letters* **22**(7), 811–814.
- Fleischmann, O. C., Hartmann, M., Burrows, J. P. and Orphal, J.: 2004, New ultraviolet absorption cross-sections of BrO at atmospheric temperatures measured by time-windowing Fourier transform spectroscopy, *J. Photochem. Photobiol. A Chem.* **168**(1-2), 117–132.
- Forster, P., Ramaswamy, V., Artaxo, P., Berntsen, T., Betts, R., Fahey, D., Haywood, J., Lean, J., Lowe, D., Myhre, G., Nganga, J., Prinn, R., Raga, G., Schulz, M. and Van Dorland, R.: 2007, Changes in Atmospheric Constituents and in Radiative Forcing, in S. Solomon, D. Qin, M. Manning, Z. Chen, M. Marquis, K. Avery, M. Tignor and H. Miller. (eds), *Climate Change 2007: The Physical Science Basis. Contribution of Working Group I to the Fourth Assessment Report of the Intergovernmental Panel on Climate Change*, Cambridge University Press, Cambridge, United Kingdom and New York, NY, USA., chapter 2.
- Fowler, D., Pilegaard, K., Sutton, M. A., Ambus, P., Raivonen, M., Duyzer, J., Simpson, D., Fagerli, H., Fuzzi, S., Schjoerring, J. K., Granier, C., Neftel, A., Isaksen, I. S. A., Laj, P., Maione, M., Monks, P. S., Burkhardt, J., Daemmgen, U., Neirynek, J., Personne, E., Wichink-Kruit, R., Butterbach-Bahl, K., Flechard, C., Tuovinen, J. P., Coyle, M., Gerosa, G., Loubet, B., Altimir, N., Gruenhage, L., Ammann, C., Cieslik, S., Paoletti, E., Mikkelsen, T. N., Ro-Poulsen, H., Cellier, P., Cape, J. N., Horváth, L., Loreto, F., Niinemets, U., Palmer, P. I., Rinne, J., Misztal, P., Nemitz, E., Nilsson, D., Pryor, S., Gallagher, M. W., Vesala, T., Skiba, U., Brüggemann, N., Zechmeister-Boltenstern, S., Williams, J., O’Dowd, C., Facchini, M. C., de Leeuw, G., Flossman, A., Chaumerliac, N. and Erisman, J. W.: 2009, Atmospheric composition change: Ecosystems-Atmosphere interactions, *Atmospheric Environment* **43**(33), 5193–5267.
- Frankenberg, C., Butz, A. and Toon, G. C.: 2011a, Disentangling chlorophyll fluorescence from atmospheric scattering effects in O_2 A-band spectra of reflected sun-light, *Geophysical Research Letters* **38**(3).
- Frankenberg, C., Fisher, J. B., Worden, J., Badgley, G., Saatchi, S. S., Lee, J.-E., Toon, G. C., Butz, A., Jung, M., Kuze, A. and Yokota, T.: 2011b, New global observations of the terrestrial carbon cycle from GOSAT: Patterns of plant fluorescence with gross primary productivity, *Geophysical Research Letters* **38**(17).
- Fried, A., Walega, J. G., Olson, J. R., Crawford, J. H., Chen, G., Weibring, P., Richter, D., Roller, C., Tittel, F. K., Heikes, B. G., Snow, J. A., Shen, H.,

- O'Sullivan, D. W., Porter, M., Fuelberg, H., Halland, J. and Millet, D. B.: 2008, Formaldehyde over North America and the North Atlantic during the summer 2004 INTEX campaign: Methods, observed distributions, and measurement-model comparisons, *Journal of Geophysical Research: Atmospheres* **113**(D10).
- Frost, G. J., Fried, A., Lee, Y.-N., Wert, B., Henry, B., Drummond, J. R., Evans, M. J., Fehsenfeld, F. C., Goldan, P. D., Holloway, J. S., Hübler, G., Jakoubek, R., Jobson, B. T., Knapp, K., Kuster, W. C., Roberts, J., Rudolph, J., Ryerson, T. B., Stohl, A., Stroud, C., Sueper, D. T., Trainer, M. and Williams, J.: 2002, Comparisons of box model calculations and measurements of formaldehyde from the 1997 North Atlantic Regional Experiment, *Journal of Geophysical Research: Atmospheres* **107**(D8).
- Fu, T. ., Jacob, D. J., Palmer, P. I., Chance, K., Wang, Y. X., Barletta, B., Blake, D. R., Stanton, J. C. and Pilling, M. J.: 2007, Space-based formaldehyde measurements as constraints on volatile organic compound emissions in east and south Asia and implications for ozone, *Journal of Geophysical Research: Atmospheres* **112**(6).
- Fuhrer, J.: 2003, Agroecosystem responses to combinations of elevated CO₂, ozone, and global climate change, *Agriculture, Ecosystems & Environment* **97**(1–3), 1 – 20.
- Fuhrer, J., Skärby, L. and Ashmore, M. R.: 1997, Critical levels for ozone effects on vegetation in Europe, *Environmental Pollution* **97**(1-2), 91–106.
- Ghent, D., Corlett, G., Sembhi, H., Prata, F., Zeller, O. and Remedios, J.: in preparation, Advancing the AATSR land surface temperature retrieval with higher resolution auxiliary datasets: Part A – derivation of coefficients, *Remote Sensing of Environment* .
- Giglio, L., Descloitres, J., Justice, C. O. and Kaufman, Y. J.: 2003, An Enhanced Contextual Fire Detection Algorithm for MODIS, *Remote Sensing of Environment* **87**(2–3), 273 – 282.
- Gold, D. R., Litonjua, A., Schwartz, J., Lovett, E., Larson, A., Nearing, B., Allen, G., Verrier, M., Cherry, R. and Verrier, R.: 2000, Ambient pollution and heart rate variability, *Circulation* **101**(11), 1267–1273.
- Goldan, P. D., Parrish, D. D., Kuster, W. C., Trainer, M., McKeen, S. A., Holloway, J., Jobson, B. T., Sueper, D. T. and Fehsenfeld, F. C.: 2000, Airborne measurements of isoprene, CO, and anthropogenic hydrocarbons and their implications, *Journal of Geophysical Research: Atmospheres* **105**(D7), 9091–9105.
- Gonzi, S. and Palmer, P. I.: 2010, Vertical transport of surface fire emissions observed from space, *Journal of Geophysical Research: Atmospheres* **115**(D2).
- Gonzi, S., Palmer, P. I., Barkley, M. P., De Smedt, I. and Van Roozendaal, M.: 2011, Biomass burning emission estimates inferred from satellite column measurements of HCHO: Sensitivity to co-emitted aerosol and injection height, *Geophysical Research Letters* **38**(14).
- Gorshelev, V., Serdyuchenko, A., Weber, M., Chehade, W. and Burrows, J. P.: 2013, High spectral resolution ozone absorption cross-sections - Part 1: Measurements, data analysis and comparison with previous measurements around 293 K, *Atmospheric Measurement Techniques Discussions* **6**(4), 6567–6611.
- Grainger, J. F. and Ring, J.: 1962, Anomalous fraunhofer line profiles, *Nature*

193(4817), 762.

- Greenblatt, G. D., Orlando, J. J., Burkholder, J. B. and Ravishankara, A. R.: 1990, Absorption measurements of oxygen between 330 and 1140 nm, *Journal of Geophysical Research: Atmospheres* **95**(D11), 18,577–18,582.
- Guanter, L., Alonso, L., Gómez-Chova, L., Meroni, M., Preusker, R., Fischer, J. and Moreno, J.: 2010, Developments for vegetation fluorescence retrieval from spaceborne high-resolution spectrometry in the O₂-A and O₂-B absorption bands, *Journal of Geophysical Research: Atmospheres* **115**(D19).
- Guenther, A.: 1995, A global model of natural volatile organic compound emissions, *Journal of Geophysical Research: Atmospheres* **100**(D5), 8873–8892.
- Guenther, A. B., Jiang, X., Heald, C. L., Sakulyanontvittaya, T., Duhl, T., Emons, L. K. and Wang, X.: 2012, The Model of Emissions of Gases and Aerosols from Nature version 2.1 (MEGAN2.1): an extended and updated framework for modeling biogenic emissions, *Geoscientific Model Development* **5**(6), 1471–1492.
- Guenther, A., Baugh, W., Davis, K., Hampton, G., Harley, P., Klinger, L., Vierling, L., Zimmerman, P., Allwine, E., Dilts, S., Lamb, B., Westberg, H., Baldocchi, D., Geron, C. and Pierce, T.: 1996, Isoprene fluxes measured by enclosure, relaxed eddy accumulation, surface layer gradient, mixed layer gradient, and mixed layer mass balance techniques, *Journal of Geophysical Research: Atmospheres* **101**(13), 18555–18567.
- Guenther, A., Geron, C., Pierce, T., Lamb, B., Harley, P. and Fall, R.: 2000, Natural emissions of non-methane volatile organic compounds, carbon monoxide, and oxides of nitrogen from north america, *Atmospheric Environment* **34**(12-14), 2205–2230.
- Guenther, A., Karl, T., Harley, P., Wiedinmyer, C., Palmer, P. I. and Geron, C.: 2006, Estimates of global terrestrial isoprene emissions using megan (model of emissions of gases and aerosols from nature), *Atmospheric Chemistry and Physics* **6**(11), 3181–3210.
- Guo, H., Ling, Z. H., Simpson, I. J., Blake, D. R. and Wang, D. W.: 2012, Observations of isoprene, methacrolein (MAC) and methyl vinyl ketone (MVK) at a mountain site in Hong Kong, *Journal of Geophysical Research: Atmospheres* **117**(D19).
- Hallquist, M., Wenger, J. C., Baltensperger, U., Rudich, Y., Simpson, D., Claeys, M., Dommen, J., Donahue, N. M., George, C., Goldstein, A. H., Hamilton, J. F., Herrmann, H., Hoffmann, T., Iinuma, Y., Jang, M., Jenkin, M. E., Jimenez, J. L., Kiendler-Scharr, A., Maenhaut, W., McFiggans, G., Mentel, T. F., Monod, A., Prévôt, A. S. H., Seinfeld, J. H., Surratt, J. D., Szmigielski, R. and Wildt, J.: 2009, The formation, properties and impact of secondary organic aerosol: current and emerging issues, *Atmospheric Chemistry and Physics* **9**(14), 5155–5236.
- Hanson, R. S. and Hanson, T. E.: 1996, Methanotrophic bacteria, *Microbiological reviews* **60**(2), 439–471.
- Hardacre, C. J., Palmer, P. I., Baumanns, K., Rounsevell, M. and Murray-Rust, D.: 2013, Probabilistic estimation of future emissions of isoprene and surface oxidant chemistry associated with land-use change in response to growing food needs, *Atmospheric Chemistry and Physics* **13**(11), 5451–5472.
- Harley, P., Otter, L., Guenther, A. and Greenberg, J.: 2003, Micrometeorologi-

- cal and leaf-level measurements of isoprene emissions from a southern African savanna, *Journal of Geophysical Research: Atmospheres* **108**(D13).
- Heald, C. L., Henze, D. K., Horowitz, L. W., Feddema, J., Lamarque, J. ., Guenther, A., Hess, P. G., Vitt, F., Seinfeld, J. H., Godstein, A. H. and Fung, I.: 2008, Predicted change in global secondary organic aerosol concentrations in response to future climate, emissions, and land use change, *Journal of Geophysical Research D: Atmospheres* **113**(5).
- Heckel, A., Kim, S.-W., Frost, G., Richter, A., Trainer, M. and Burrows, J.: 2011, Influence of low spatial resolution a priori data on tropospheric NO₂ satellite retrievals, *Atmospheric Measurement Techniques* **4**, 1805 – 1820.
- Heckel, A., Richter, A., Tarsu, T., Wittrock, F., Hak, C., Pundt, I., Junkermann, W. and Burrows, J. P.: 2005, MAX-DOAS measurements of formaldehyde in the Po-Valley, *Atmospheric Chemistry and Physics* **5**(4), 909–918.
- Heggestad, H. E. and Middleton, J. T.: 1959, Ozone in High Concentrations as Cause of Tobacco Leaf Injury, *Science* **129**(3343), 208–210.
- Helmig, D., Balsley, B., Davis, K., Kuck, L. R., Jensen, M., Bogner, J., Smith Jr., T., Arrieta, R. V., Rodríguez, R. and Birks, J. W.: 1998, Vertical profiling and determination of landscape fluxes of biogenic nonmethane hydrocarbons within the planetary boundary layer in the Peruvian Amazon, *Journal of Geophysical Research: Atmospheres* **103**(D19), 25519–25532.
- Henze, D. K. and Seinfeld, J. H.: 2006, Global secondary organic aerosol from isoprene oxidation, *Geophysical Research Letters* **33**(9).
- Herman, J. R. and Celarier, E. A.: 1997, Earth surface reflectivity climatology at 340–380 nm from TOMS data, *Journal of Geophysical Research: Atmospheres* **102**(D23), 28003–28011.
- Herndon, S. C., Zahniser, M. S., Nelson, D. D., Shorter, J., McManus, J. B., Jiménez, R., Warneke, C. and de Gouw, J. A.: 2007, Airborne measurements of HCHO and HCOOH during the New England Air Quality Study 2004 using a pulsed quantum cascade laser spectrometer, *Journal of Geophysical Research: Atmospheres* **112**(D10).
- Hewitt, C. N., Lee, J. D., MacKenzie, A. R., Barkley, M. P., Carslaw, N., Carver, G. D., Chappell, N. A., Coe, H., Collier, C., Commane, R., Davies, F., Davison, B., DiCarlo, P., Di Marco, C. F., Dorsey, J. R., Edwards, P. M., Evans, M. J., Fowler, D., Furneaux, K. L., Gallagher, M., Guenther, A., Heard, D. E., Helfter, C., Hopkins, J., Ingham, T., Irwin, M., Jones, C., Karunaharan, A., Langford, B., Lewis, A. C., Lim, S. F., MacDonald, S. M., Mahajan, A. S., Malpass, S., McFiggans, G., Mills, G., Misztal, P., Moller, S., Monks, P. S., Nemitz, E., Nicolas-Perea, V., Oetjen, H., Oram, D. E., Palmer, P. I., Phillips, G. J., Pike, R., Plane, J. M. C., Pugh, T., Pyle, J. A., Reeves, C. E., Robinson, N. H., Stewart, D., Stone, D., Whalley, L. K. and Yin, X.: 2010, Overview: oxidant and particle photochemical processes above a south-east Asian tropical rainforest (the OP3 project): introduction, rationale, location characteristics and tools, *Atmospheric Chemistry and Physics* **10**(1), 169–199.
- Hewson, W., Bösch, H., Barkley, M. P. and De Smedt, I.: 2013, Characterisation of GOME-2 formaldehyde retrieval sensitivity, *Atmospheric Measurement Techniques* **6**(2), 371–386.

- Holloway, T., Levy, H. and Kasibhatla, P.: 2000, Global distribution of carbon monoxide, *Journal of Geophysical Research: Atmospheres* **105**(D10), 12123–12147.
- Holton, J. R., Haynes, P. H., McIntyre, M. E., Douglass, A. R., Rood, R. B. and Pfister, L.: 1995, Stratosphere-troposphere exchange, *Reviews of Geophysics* **33**(4), 403–439.
- Holzer-Popp, T., Schroedter-Homscheidt, M., Breitkreuz, H., Martynenko, D. and Klüser, L.: 2008, Improvements of synergetic aerosol retrieval for ENVISAT, *Atmospheric Chemistry and Physics* **8**(24), 7651–7672.
- Hoyle, C. R., Berntsen, T., Myhre, G. and Isaksen, I. S. A.: 2007, Secondary organic aerosol in the global aerosol – chemical transport model oslo ctm2, *Atmospheric Chemistry and Physics* **7**(21), 5675–5694.
- Hsu, J. and Prather, M. J.: 2009, Stratospheric variability and tropospheric ozone, *Journal of Geophysical Research D: Atmospheres* **114**(6).
- Huffman, G. J., Bolvin, D. T., Nelkin, E. J., Wolff, D. B., Adler, R. F., Gu, G., Hong, Y., Bowman, K. P. and Stocker, E. F.: 2007, The TRMM Multisatellite Precipitation Analysis (TMPA): Quasi-Global, Multiyear, Combined-Sensor Precipitation Estimates at Fine Scales, *Journal of Hydrometeorology* **8**(1), 38–55.
- Huijnen, V., Flemming, J., Kaiser, J. W., Inness, A., Leitão, J., Heil, A., Eskes, H. J., Schultz, M. G., Benedetti, A., Hadji-Lazarou, J., Dufour, G. and Eremenko, M.: 2012, Hindcast experiments of tropospheric composition during the summer 2010 fires over western Russia, *Atmospheric Chemistry and Physics* **12**(9), 4341–4364.
- IPCC: 2001, *IPCC Third Assessment Report: Climate Change 2001, Working Group I: The Scientific Basis*, Cambridge University Press.
- Isaksen, I., Granier, C., Myhre, G., Berntsen, T., Dalsøren, S., Gauss, M., Klimont, Z., Benestad, R., Bousquet, P., Collins, W., Cox, T., Eyring, V., Fowler, D., Fuzzi, S., Jöckel, P., Laj, P., Lohmann, U., Maione, M., Monks, P., Prevot, A., Raes, F., Richter, A., Rognerud, B., Schulz, M., Shindell, D., Stevenson, D., Storelvmo, T., Wang, W.-C., van Weele, M., Wild, M. and Wuebbles, D.: 2009, Atmospheric composition change: Climate–Chemistry interactions, *Atmospheric Environment* **43**(33), 5138 – 5192.
- Jacob, D.: 2000, Heterogeneous chemistry and tropospheric ozone, *Atmospheric Environment* **34**(12–14), 2131 – 2159.
- Jacob, D. J. and Wofsy, S. C.: 1988, Photochemistry of biogenic emissions over the amazon forest, *Journal of Geophysical Research: Atmospheres* **93**(D2), 1477–1486.
- Jacobi, H.-W., Frey, M. M., Hutterli, M. A., Bales, R. C., Schrems, O., Cullen, N. J., Steffen, K. and Koehler, C.: 2002, Measurements of hydrogen peroxide and formaldehyde exchange between the atmosphere and surface snow at Summit, Greenland, *Atmospheric Environment* **36**(15–16), 2619 – 2628.
- Jaegle, L., Steinberger, L., Martin, R. V. and Chance, K.: 2005, Global partitioning of NO_x sources using satellite observations: Relative roles of fossil fuel combustion, biomass burning and soil emissions, *Faraday Discuss.* **130**, 407–423.
- Jardine, K. J., Monson, R. K., Abrell, L., Saleska, S. R., Arneth, A., Jardine, A., Ishida, F. Y., Serrano, A. M. Y., Artaxo, P., Karl, T., Fares, S., Goldstein, A.,

- Loreto, F. and Huxman, T.: 2011, Within-plant isoprene oxidation confirmed by direct emissions of oxidation products methyl vinyl ketone and methacrolein, *Global Change Biology* **18**(3), 973–984.
- Jenkin, M. E. and Clemitshaw, K. C.: 2000, Ozone and other secondary photochemical pollutants: Chemical processes governing their formation in the planetary boundary layer, *Atmospheric Environment* **34**(16), 2499–2527.
- Johnston, P. V.: 1996, Making UV/Vis Cross Sections, Reference Fraunhofer and Synthetic Spectra. Private communication (March, 2011) - original notes.
- Joiner, J., Bhartia, P. K., Cebula, R. P., Hilsenrath, E., McPeters, R. D. and Park, H.: 1995, Rotational Raman scattering (Ring effect) in satellite backscatter ultraviolet measurements, *Appl. Opt.* **34**(21), 4513–4525.
- Joiner, J., Guanter, L., Lindstrot, R., Voigt, M., Vasilkov, A. P., Middleton, E. M., Huemmrich, K. F., Yoshida, Y. and Frankenberg, C.: 2013, Global monitoring of terrestrial chlorophyll fluorescence from moderate spectral resolution near-infrared satellite measurements: methodology, simulations, and application to GOME-2, *Atmospheric Measurement Techniques Discussions* **6**(2), 3883–3930.
- Joiner, J., Schoeberl, M. R., Vasilkov, A. P., Oreopoulos, L., Platnick, S., Livesey, N. J. and Levelt, P. F.: 2009, Accurate satellite-derived estimates of the tropospheric ozone impact on the global radiation budget, *Atmospheric Chemistry and Physics* **9**(13), 4447–4465.
- Joiner, J., Yoshida, Y., Vasilkov, A. P., Middleton, E. M., Campbell, P. K. E., Yoshida, Y., Kuze, A. and Corp, L. A.: 2012, Filling-in of near-infrared solar lines by terrestrial fluorescence and other geophysical effects: simulations and space-based observations from SCIAMACHY and GOSAT, *Atmospheric Measurement Techniques* **5**(4), 809–829.
- Joiner, J., Yoshida, Y., Vasilkov, A. P., Yoshida, Y., Corp, L. A. and Middleton, E. M.: 2011, First observations of global and seasonal terrestrial chlorophyll fluorescence from space, *Biogeosciences* **8**(3), 637–651.
- Jones, C. E., Hopkins, J. R. and Lewis, A. C.: 2011, In situ measurements of isoprene and monoterpenes within a south-east Asian tropical rainforest, *Atmospheric Chemistry and Physics* **11**(14), 6971–6984.
- Kanakidou, M., Seinfeld, J. H., Pandis, S. N., Barnes, I., Dentener, F. J., Facchini, M. C., Van Dingenen, R., Ervens, B., Nenes, A., Nielsen, C. J., Swietlicki, E., Putaud, J. P., Balkanski, Y., Fuzzi, S., Horth, J., Moortgat, G. K., Winterhalter, R., Myhre, C. E. L., Tsigaridis, K., Vignati, E., Stephanou, E. G. and Wilson, J.: 2005, Organic aerosol and global climate modelling: A review, *Atmospheric Chemistry and Physics* **5**(4), 1053–1123.
- Karl, M., Tsigaridis, K., Vignati, E. and Dentener, F.: 2009, Formation of secondary organic aerosol from isoprene oxidation over Europe, *Atmospheric Chemistry and Physics* **9**(18), 7003–7030.
- Kesselmeier, J., Kuhn, U., Wolf, A., Andreae, M. O., Ciccioli, P., Brancaleoni, E., Frattoni, M., Guenther, A., Greenberg, J., De Castro Vasconcellos, P., De Oliva, T., Tavares, T. and Artaxo, P.: 2000, Atmospheric volatile organic compounds (VOC) at a remote tropical forest site in central Amazonia, *Atmospheric Environment* **34**(24), 4063–4072.
- Kesselmeier, J. and Staudt, M.: 1999, Biogenic Volatile Organic Compounds (VOC):

An Overview on Emission, Physiology and Ecology, *Journal of Atmospheric Chemistry* **33**, 23–88.

- Kessler, A., Halitschke, R., Diezel, C. and Baldwin, I. T.: 2006, Priming of plant defense responses in nature by airborne signaling between *Artemisia tridentata* and *Nicotiana attenuata*, *Oecologia* **148**(2), 280–292.
- Khare, P., Satsangi, G. S., Kumar, N., Kumari, K. M. and Srivastava, S. S.: 1997, Surface measurements of formaldehyde and formic and acetic acids at a subtropical semiarid site in India, *Journal of Geophysical Research: Atmospheres* **102**(D15), 18997–19005.
- Kim, C. S., Alexis, N. E., Rappold, A. G., Kehrl, H., Hazucha, M. J., Lay, J. C., Schmitt, M. T., Case, M., Devlin, R. B., Peden, D. B. and Diaz-Sanchez, D.: 2011, Lung function and inflammatory responses in healthy young adults exposed to 0.06 ppm ozone for 6.6 hours, *American Journal of Respiratory and Critical Care Medicine* **183**(9), 1215–1221.
- Kleipool, Q. L., Dobber, M. R., de Haan, J. F. and Levelt, P. F.: 2008, Earth surface reflectance climatology from 3 years of OMI data, *Journal of Geophysical Research: Atmospheres* **113**(D18).
- Kost, C. and Heil, M.: 2006, Herbivore-induced plant volatiles induce an indirect defence in neighbouring plants, *Journal of Ecology* **94**(3), 619–628.
- Krijger, J.: 2013, Let's get dirty again: More contaminated mirrors in space, Atmospheric Composition, Validation and Evolution, ESA, ESA-ESRIN, Frascati, Italy.
- Kroll, J. H. and Seinfeld, J. H.: 2008, Chemistry of secondary organic aerosol: Formation and evolution of low-volatility organics in the atmosphere, *Atmospheric Environment* **42**(16), 3593 – 3624.
- Kühl, S., Wilms-Grabe, W., Frankenberg, C., Grzegorski, M., Platt, U. and Wagner, T.: 2006, Comparison of OCIO nadir measurements from SCIAMACHY and GOME, *Advances in Space Research* **37**(12), 2247–2253.
- Kuhn, U., Andreae, M. O., Ammann, C., Araújo, A. C., Brancaleoni, E., Ciccioli, P., Dindorf, T., Frattoni, M., Gatti, L. V., Ganzeveld, L., Kruijt, B., Lelieveld, J., Lloyd, J., Meixner, F. X., Nobre, A. D., Pöschl, U., Spirig, C., Stefani, P., Thielmann, A., Valentini, R. and Kesselmeier, J.: 2007, Isoprene and monoterpene fluxes from Central Amazonian rainforest inferred from tower-based and airborne measurements, and implications on the atmospheric chemistry and the local carbon budget, *Atmospheric Chemistry and Physics* **7**(11), 2855–2879.
- Kuhns, H., Green, M. and Etyemezian, V.: 2003, Big Bend Regional Aerosol and Visibility Observational (BRAVO) Study Emissions Inventory, *Technical report*, Desert Research Institute.
- Kurosu, T. P., Chance, K. and Sioris, C. E.: 2004, Preliminary results for HCHO and BrO from the EOS-aura ozone monitoring instrument, *Proceedings of SPIE - The International Society for Optical Engineering*, Vol. 5652, pp. 116–123.
- Kuzma, J. and Fall, R.: 1993, Leaf isoprene emission rate is dependent on leaf development and the level of isoprene synthase, *Plant Physiology* **101**(2), 435–440.
- Langford, A. O., Schofield, R., Daniel, J. S., Portmann, R. W., Melamed, M. L.,

- Miller, H. L., Dutton, E. G. and Solomon, S.: 2007, On the variability of the Ring effect in the near ultraviolet: Understanding the role of aerosols and multiple scattering, *Atmospheric Chemistry and Physics* **7**(3), 575–586.
- Lashof, D. A. and Ahuja, D. R.: 1990, Relative contributions of greenhouse gas emissions to global warming, *Nature* **344**(6266), 529–531.
- Lathi ere, J., Hewitt, C. N. and Beerling, D. J.: 2010, Sensitivity of isoprene emissions from the terrestrial biosphere to 20th century changes in atmospheric CO₂ concentration, climate, and land use, *Global Biogeochemical Cycles* **24**(1).
- Lee, C., Richter, A., Weber, M. and Burrows, J. P.: 2008, SO₂ Retrieval from SCIAMACHY using the Weighting Function DOAS (WFDOAS) technique: comparison with Standard DOAS retrieval, *Atmospheric Chemistry and Physics* **8**(20), 6137–6145.
- Leit ao, J., Richter, A., Vrekoussis, M., Kokhanovsky, A., Zhang, Q. J., Beekmann, M. and Burrows, J. P.: 2010, On the improvement of NO₂ satellite retrievals – aerosol impact on the airmass factors, *Atmospheric Measurement Techniques* **3**(2), 475–493.
- Lelieveld, J., Butler, T. M., Crowley, J. N., Dillon, T. J., Fischer, H., Ganzeveld, L., Harder, H., Lawrence, M. G., Martinez, M., Taraborrelli, D. and Williams, J.: 2008, Atmospheric oxidation capacity sustained by a tropical forest, *Nature* **452**(7188), 737–740.
- Lelieveld, J., Crutzen, P. J. and Dentener, F. J.: 1998, Changing concentration, lifetime and climate forcing of atmospheric methane, *Tellus, Series B: Chemical and Physical Meteorology* **50**(2), 128–150.
- Lelieveld, J. and Dentener, F. J.: 2000, What controls tropospheric ozone?, *Journal of Geophysical Research D: Atmospheres* **105**(D3), 3531–3551.
- Lerot, C., De Smedt, I., Stavrou, T., M uller, J.-F. and Van Roozendael, M.: 2009, Combined formaldehyde and glyoxal observations from GOME-2 backscattered light measurements, number SP-676, ESA, Barcelona, Spain.
- Levelt, P. F., Van Den Oord, G. H. J., Dobber, M. R., M alkki, A., Visser, H., De Vries, J., Stammes, P., Lundell, J. O. V. and Saari, H.: 2006, The ozone monitoring instrument, *IEEE Transactions on Geoscience and Remote Sensing* **44**(5), 1093–1100.
- Lewis, S. L., Brando, P. M., Phillips, O. L., van der Heijden, G. M. F. and Nepstad, D.: 2011, The 2010 Amazon Drought, *Science* **331**(6017), 554.
- Li, Y., Shao, M., Lu, S., Chang, C.-C. and Dasgupta, P. K.: 2010, Variations and sources of ambient formaldehyde for the 2008 Beijing Olympic games, *Atmospheric Environment* **44**(21–22), 2632 – 2639.
- Liakakou, E., Vrekoussis, M., Bonsang, B., Donousis, C., Kanakidou, M. and Mihalopoulos, N.: 2007, Isoprene above the Eastern Mediterranean: Seasonal variation and contribution to the oxidation capacity of the atmosphere, *Atmospheric Environment* **41**(5), 1002 – 1010.
- Liu, X., Chance, K., Sioris, C. E. and Kurosu, T. P.: 2007, Impact of using different ozone cross sections on ozone profile retrievals from Global Ozone Monitoring Experiment (GOME) ultraviolet measurements, *Atmospheric Chemistry and Physics* **7**(1), 971–993.

- Liu, Y. J., Herdinger-Blatt, I., McKinney, K. A. and Martin, S. T.: 2012, Production of methyl vinyl ketone and methacrolein via the hydroperoxyl pathway of isoprene oxidation, *Atmospheric Chemistry and Physics Discussions* **12**(12), 33323–33358.
- Logan, J. A., Prather, M. J., Wofsy, S. C. and McElroy, M. B.: 1981, Tropospheric chemistry: a global perspective., *Journal of Geophysical Research* **86**(C8), 7210–7254.
- Loreto, F. and Velikova, V.: 2001, Isoprene produced by leaves protects the photosynthetic apparatus against ozone damage, quenches ozone products, and reduces lipid peroxidation of cellular membranes, *Plant Physiology* **127**(4), 1781–1787.
- Loyola, D. G., Koukouli, M. E., Valks, P., Balis, D. S., Hao, N., Van Roozendaal, M., Spurr, R. J. D., Zimmer, W., Kiemle, S., Lerot, C. and Lambert, J. C.: 2011b, The gome-2 total column ozone product: Retrieval algorithm and ground-based validation, *Journal of Geophysical Research: Atmospheres* **116**(D7).
- Loyola, D., Valks, P., Hao, N., Rix, M. and Slijkhuis, S.: 2011a, Algorithm Theoretical Basis Document for GOME-2 Total Column Products of Ozone, NO₂, tropospheric NO₂, BrO, SO₂, H₂O, HCHO, OClO and Cloud Properties., *Technical Report DLR/GOME-2/ATBD/01*, EUMETSAT.
- MacDonald, S. M., Oetjen, H., Mahajan, A. S., Whalley, L. K., Edwards, P. M., Heard, D. E., Jones, C. E. and Plane, J. M. C.: 2012, DOAS measurements of formaldehyde and glyoxal above a south-east Asian tropical rainforest, *Atmospheric Chemistry and Physics* **12**(13), 5949–5962.
- Malicet, J., Daumont, D., Charbonnier, J., Parisse, C., Chakir, A. and Brion, J.: 1995, Ozone UV spectroscopy. II. Absorption cross-sections and temperature dependence, *Journal of Atmospheric Chemistry* **21**(3), 263–273.
- Marais, E. A., Jacob, D. J., Kurosu, T. P., Chance, K., Murphy, J. G., Reeves, C., Mills, G., Casadio, S., Millet, D. B., Barkley, M. P., Paulot, F. and Mao, J.: 2012, Isoprene emissions in Africa inferred from OMI observations of formaldehyde columns, *Atmospheric Chemistry and Physics* **12**(14), 6219–6235.
- Marbach, T., Beirle, S., Liu, C., Platt, U. and Wagner, T.: 2008, Biomass burning emissions from satellite observations: Synergistic use of formaldehyde (HCHO), fire counts, and surface temperature, Vol. 7089.
- Marbach, T., Beirle, S., Penning de Vries, M., Liu, C. and Wagner, T.: 2010, Sources and trends of Tropospheric Formaldehyde (HCHO) derived from GOME-1 and -2, Living Planet Symposium, ESA.
- Marbach, T., Beirle, S., Platt, U., Hoor, P., Wittrock, F., Richter, A., Vrekoussis, M., Grzegorski, M., Burrows, J. P. and Wagner, T.: 2009, Satellite measurements of formaldehyde linked to shipping emissions, *Atmospheric Chemistry and Physics* **9**(21), 8223–8234.
- Martin, R. V.: 2002, *Satellite Observations of Tropospheric Chemistry: Retrievals and Interpretation*, PhD thesis, Harvard University, Cambridge, Massachusetts.
- Martin, R. V., Chance, K., Jacob, D. J., Kurosu, T. P., Spurr, R. J. D., Bucsela, E., Gleason, J. F., Palmer, P. I., Bey, I., Fiore, A. M., Li, Q., Yantosca, R. M. and Koелеmeijer, R. B. A.: 2002, An improved retrieval of tropospheric nitrogen dioxide from GOME, *Journal of Geophysical Research: Atmospheres* **107**(20).

- Martin, R. V., Jacob, D. J., Yantosca, R. M., Chin, M. and Ginoux, P.: 2003, Global and regional decreases in tropospheric oxidants from photochemical effects of aerosols, *Journal of Geophysical Research: Atmospheres* **108**(3), ACH 6–1 – ACH 6–14.
- Martin, R. V., Parrish, D. D., Ryerson, T. B., Nicks, D. K., Chance, K., Kurosu, T. P., Jacob, D. J., Sturges, E. D., Fried, A. and Wert, B. P.: 2004, Evaluation of GOME satellite measurements of tropospheric NO₂ and HCHO using regional data from aircraft campaigns in the southeastern United States, *Journal of Geophysical Research: Atmospheres* **109**(24), 1–11.
- Meller, R. and Moortgat, G. K.: 2000, Temperature dependence of the absorption cross sections of formaldehyde between 223 and 323 K in the wavelength range 225–375 nm, *Journal of Geophysical Research: Atmospheres* **105**(D6), 7089–7101.
- Meroni, M., Rossini, M., Guanter, L., Alonso, L., Rascher, U., Colombo, R. and Moreno, J.: 2009, Remote sensing of solar-induced chlorophyll fluorescence: Review of methods and applications, *Remote Sensing of Environment* **113**(10), 2037 – 2051.
- Mikaloff Fletcher, S. E., Tans, P. P., Bruhwiler, L. M., Miller, J. B. and Heimann, M.: 2004, CH₄ sources estimated from atmospheric observations of CH₄ and its ¹³C/¹²C isotopic ratios: 1. Inverse modeling of source processes, *Global Biogeochemical Cycles* **18**(4).
- Millet, D. B., Jacob, D. J., Boersma, K. F., Fu, T. ., Kurosu, T. P., Chance, K., Heald, C. L. and Guenther, A.: 2008, Spatial distribution of isoprene emissions from North America derived from formaldehyde column measurements by the OMI satellite sensor, *Journal of Geophysical Research: Atmospheres* **113**(2).
- Millet, D. B., Jacob, D. J., Turquety, S., Hudman, R. C., Wu, S., Fried, A., Walega, J., Heikes, B. G., Blake, D. R., Singh, H. B., Andersen, B. E. and Clarke, A. D.: 2006, Formaldehyde distribution over North America: Implications for satellite retrievals of formaldehyde columns and isoprene emission, *Journal of Geophysical Research: Atmospheres* **111**(24).
- Monks, P. S.: 2005, Gas-phase radical chemistry in the troposphere, *Chem. Soc. Rev.* **34**, 376–395.
- Monks, P. S., Granier, C., Fuzzi, S., Stohl, A., Williams, M. L., Akimoto, H., Amann, M., Baklanov, A., Baltensperger, U., Bey, I., Blake, N., Blake, R. S., Carslaw, K., Cooper, O. R., Dentener, F., Fowler, D., Fragkou, E., Frost, G. J., Generoso, S., Ginoux, P., Grewe, V., Guenther, A., Hansson, H. C., Henne, S., Hjorth, J., Hofzumahaus, A., Huntrieser, H., Isaksen, I. S. A., Jenkin, M. E., Kaiser, J., Kanakidou, M., Klimont, Z., Kulmala, M., Laj, P., Lawrence, M. G., Lee, J. D., Liousse, C., Maione, M., McFiggans, G., Metzger, A., Mieville, A., Moussiopoulos, N., Orlando, J. J., O’Dowd, C. D., Palmer, P. I., Parrish, D. D., Petzold, A., Platt, U., Pöschl, U., Prévôt, A. S. H., Reeves, C. E., Reimann, S., Rudich, Y., Sellegri, K., Steinbrecher, R., Simpson, D., ten Brink, H., Theloke, J., van der Werf, G. R., Vautard, R., Vestreng, V., Vlachokostas, C. and von Glasow, R.: 2009, Atmospheric composition change - global and regional air quality, *Atmospheric Environment* **43**(33), 5268–5350.
- Monson, R. K., Jaeger, C. H., Adams III, W. W., Driggers, E. M., Silver, G. M. and Fall, R.: 1992, Relationships among isoprene emission rate, photosynthesis,

- and isoprene synthase activity as influenced by temperature, *Plant Physiology* **98**(3), 1175–1180.
- Monson, R. K., Trahan, N., Rosenstiel, T. N., Veres, P., Moore, D., Wilkinson, M., Norby, R. J., Volder, A., Tjoelker, M. G., Briske, D. D., Karnosky, D. F. and Fall, R.: 2007, Isoprene emission from terrestrial ecosystems in response to global change: minding the gap between models and observations, *Philosophical Transactions of the Royal Society A: Mathematical, Physical and Engineering Sciences* **365**(1856), 1677–1695.
- Morcrette, J.-J., Boucher, O., Jones, L., Salmond, D., Bechtold, P., Beljaars, A., Benedetti, A., Bonet, A., Kaiser, J. W., Razinger, M., Schulz, M., Serrar, S., Simmons, A. J., Sofiev, M., Suttie, M., Tompkins, A. M. and Untch, A.: 2009, Aerosol analysis and forecast in the European Centre for Medium-Range Weather Forecasts Integrated Forecast System: Forward modeling, *Journal of Geophysical Research: Atmospheres* **114**(D6).
- Morgan, W. T., Allan, J. D., Bower, K. N., Esselborn, M., Harris, B., Henzing, J. S., Highwood, E. J., Kiendler-Scharr, A., McMeeking, G. R., Mensah, A. A., Northway, M. J., Osborne, S., Williams, P. I., Krejci, R. and Coe, H.: 2010, Enhancement of the aerosol direct radiative effect by semi-volatile aerosol components: Airborne measurements in north-western europe, *Atmospheric Chemistry and Physics* **10**(17), 8151–8171.
- Müller, J. ., Stavrakou, T., Wallens, S., De Smedt, I., Van Roozendael, M., Potosnak, M. J., Rinne, J., Munger, B., Goldstein, A. and Guenther, A. B.: 2008, Global isoprene emissions estimated using MEGAN, ECMWF analyses and a detailed canopy environment model, *Atmospheric Chemistry and Physics* **8**(5), 1329–1341.
- Munro, R., Anderson, C., Callies, J., Corpaccioli', E., Eisinger, M., Lang, R., Lefebvre, A., Livschitz, Y. and Albiñana, A. P.: 2006, GOME-2 on MetOp, *European Space Agency, (Special Publication) ESA SP*.
- Munro, R. and Eisinger, M.: 2006, *GOME-2 Level 1 Product Generation Specification*, 6:1 edn, EUMETSAT, Am Kavalleriesand 31, Postfach D-64295 Darmstadt, Germany.
- Murphy, J. G., Oram, D. E. and Reeves, C. E.: 2010, Measurements of volatile organic compounds over West Africa, *Atmospheric Chemistry and Physics* **10**(12), 5281–5294.
- Niinemets, U., Kuhn, U., Harley, P. C., Staudt, M., Arneth, A., Cescatti, A., Ciccioli, P., Copolovici, L., Geron, C., Guenther, A., Kesselmeier, J., Lerdau, M. T., Monson, R. K. and Peñuelas, J.: 2011, Estimations of isoprenoid emission capacity from enclosure studies: measurements, data processing, quality and standardized measurement protocols, *Biogeosciences* **8**(8), 2209–2246.
- Niinemets, U., Monson, R. K., Arneth, A., Ciccioli, P., Kesselmeier, J., Kuhn, U., Noe, S. M., Peñuelas, J. and Staudt, M.: 2010, The leaf-level emission factor of volatile isoprenoids: caveats, model algorithms, response shapes and scaling, *Biogeosciences* **7**(6), 1809–1832.
- Nowlan, C. R., Liu, X., Chance, K., Cai, Z., Kurosu, T. P., Lee, C. and Martin, R. V.: 2011, Retrievals of sulfur dioxide from the Global Ozone Monitoring Experiment 2 (GOME-2) using an optimal estimation approach: Algorithm and initial validation, *Journal of Geophysical Research: Atmospheres* **116**(D18).

- Oetjen, H., Wittrock, F., Richter, A., Chipperfield, M. P., Medeke, T., Sheode, N., Sinnhuber, B. ., Sinnhuber, M. and Burrows, J. P.: 2011, Evaluation of stratospheric chlorine chemistry for the Arctic spring 2005 using modelled and measured OClO column densities, *Atmospheric Chemistry and Physics* **11**(2), 689–703.
- Pacifico, F., Harrison, S. P., Jones, C. D. and Sitch, S.: 2009, Isoprene emissions and climate, *Atmospheric Environment* **43**(39), 6121–6135.
- Palmer, P. I., Abbot, D. S., Fu, T. ., Jacob, D. J., Chance, K., Kurosu, T. P., Guenther, A., Wiedinmyer, C., Stanton, J. C., Pilling, M. J., Pressley, S. N., Lamb, B. and Sumner, A. L.: 2006, Quantifying the seasonal and interannual variability of North American isoprene emissions using satellite observations of the formaldehyde column, *Journal of Geophysical Research: Atmospheres* **111**(12).
- Palmer, P. I., Barkley, M. P., Kurosu, T. P., Lewis, A. C., Saxton, J. E., Chance, K. and Gatti, L. V.: 2007, Interpreting satellite column observations of formaldehyde over tropical South America, *Philosophical Transactions of the Royal Society A: Mathematical, Physical and Engineering Sciences* **365**(1856), 1741–1751.
- Palmer, P. I., Jacob, D. J., Chance, K., Martin, R. V., Spurr, R. J. D., Kurosu, T. P., Bey, I., Yantosca, R., Fiore, A. and Li, Q.: 2001, Air mass factor formulation for spectroscopic measurements from satellites: Application to formaldehyde retrievals from the Global Ozone Monitoring Experiment, *Journal of Geophysical Research: Atmospheres* **106**(D13), 14539–14550.
- Palmer, P. I., Jacob, D. J., Fiore, A. M., Martin, R. V., Chance, K. and Kurosu, T. P.: 2003, Mapping isoprene emissions over North America using formaldehyde column observations from space, *Journal of Geophysical Research: Atmospheres* **108**(6), ACH 2–1 – 2–13.
- Paredes-Miranda, G., Arnott, W. P., Jimenez, J. L., Aiken, A. C., Gaffney, J. S. and Marley, N. A.: 2009, Primary and secondary contributions to aerosol light scattering and absorption in Mexico City during the MILAGRO 2006 campaign, *Atmospheric Chemistry and Physics* **9**(11), 3721–3730.
- Parrish, D. D., Ryerson, T. B., Mellqvist, J., Johansson, J., Fried, A., Richter, D., Walega, J. G., Washenfelder, R. A., De Gouw, J. A., Peischl, J., Aikin, K. C., McKeen, S. A., Frost, G. J., Fehsenfeld, F. C. and Herndon, S. C.: 2012, Primary and secondary sources of formaldehyde in urban atmospheres: Houston Texas region, *Atmospheric Chemistry and Physics* **12**(7), 3273–3288.
- Paulot, F., Henze, D. K. and Wennberg, P. O.: 2012, Impact of the isoprene photochemical cascade on tropical ozone, *Atmospheric Chemistry and Physics* **12**(3), 1307–1325.
- Peñuelas, J., Guenther, A., Rappardini, F., Llusia, J., Filella, I., Seco, R., Estiarte, M., Mejia-Chang, M., Ogaya, R., Ibañez, J. et al.: 2013, Intensive measurements of gas, water, and energy exchange between vegetation and troposphere during the MONTES campaign in a vegetation gradient from short semi-desertic shrublands to tall wet temperate forests in the NW Mediterranean Basin, *Atmospheric Environment* **75**, 348–364.
- Perner, D., Hegels, E., Klüpfel, T. and Martinez-Walter, M.: 1997, First results on tropospheric observations by the Global Ozone Monitoring Experiment, GOME, on ERS-2, *Proceedings of the 3rd ERS-2 Symposium, Florence, Italy*, ESA.
- Peters, E., Wittrock, F., Großmann, K., Frieß, U., Richter, A. and Burrows, J. P.:

- 2012, Formaldehyde and nitrogen dioxide over the remote western Pacific Ocean: SCIAMACHY and GOME-2 validation using ship-based MAX-DOAS observations, *Atmospheric Chemistry and Physics* **12**(22), 11179–11197.
- Pichersky, E. and Gershenson, J.: 2002, The formation and function of plant volatiles: perfumes for pollinator attraction and defense, *Current Opinion in Plant Biology* **5**(3), 237 – 243.
- Pike, R. C., Lee, J. D., Young, P. J., Carver, G. D., Yang, X., Warwick, N., Moller, S., Misztal, P., Langford, B., Stewart, D., Reeves, C. E., Hewitt, C. N. and Pyle, J. A.: 2010, NO_x and O₃ above a tropical rainforest: an analysis with a global and box model, *Atmospheric Chemistry and Physics* **10**(21), 10607–10620.
- Pinardi, G., Van Roozendaal, M., Abuhassan, N., Adams, C., Cede, A., Clémer, K., Fayt, C., Frieß, U., Gil, M., Herman, J., Hermans, C., Hendrick, F., Irie, H., Merlaud, A., Navarro Comas, M., Peters, E., Pitters, A. J. M., Puentedura, O., Richter, A., Schönhardt, A., Shaiganfar, R., Spinei, E., Strong, K., Takashima, H., Vrekoussis, M., Wagner, T., Wittrock, F. and Yilmaz, S.: 2013, MAX-DOAS formaldehyde slant column measurements during CINDI: intercomparison and analysis improvement, *Atmospheric Measurement Techniques* **6**(1), 167–185.
- Platt, U.: 1994, Differential optical absorption spectroscopy (DOAS), in M. Sigrist (ed.), *Air Monitoring by Spectroscopic Techniques*, Vol. 127 of *Chemical Analysis Series*, John Wiley and Sons, Inc., chapter 2.
- Platt, U., Perner, D. and Paetz, H. W.: 1979, Simultaneous Measurement of Atmospheric CH₂O, O₃, and NO₂ by Differential Optical Absorption, *Journal of Geophysical Research: Atmospheres* **84**(C10), 6329–6335.
- Platt, U. and Stutz, J.: 2008, *Differential Optical Absorption Spectroscopy*, Physics of Earth and Space Environments, Springer, Berlin.
- Potosnak, M. J., Baker, B. M., LeSturgeon, L., Disher, S. M., Griffin, K. L., Bret-Harte, M. S. and Starr, G.: 2013, Isoprene emissions from a tundra ecosystem, *Biogeosciences* **10**(2), 871–889.
- Pradhan, Y., Brookes, D. M. and Saunders, R.: 2011, ESCAT soil moisture climatology, *Report 551*, Met Office.
- Prata, F.: 2002, Land Surface Temperature Measurement from Space - AATSR Algorithm Theoretical Basis Document, *Technical report*, CSIRO, CSIRO Atmospheric Research, Aspendale, Australia.
- Price, C., Penner, J. and Prather, M.: 1997, NO_x from lightning 1. Global distribution based on lightning physics, *Journal of Geophysical Research D: Atmospheres* **102**(5), 5929–5941.
- Prinn, R.: 2003, 4.01 - Ozone, Hydroxyl Radical, and Oxidative Capacity, in E. in Chief: Heinrich D. Holland and K. K. Turekian (eds), *Treatise on Geochemistry*, Pergamon, Oxford, pp. 1 – 19.
- Puķite, J., Kūhl, S., Deutschmann, T., Platt, U. and Wagner, T.: 2010, Extending differential optical absorption spectroscopy for limb measurements in the uv, *Atmospheric Measurement Techniques* **3**(3), 631–653.
- Randerson, J., Van Der Werf, G. R., Giglio, L., G.J., C. and Kasibhatla, P.: 2007, Global fire emissions database, version 2.1. data set.
URL: [doi:10.3334/ORNLDAAC/849](https://doi.org/10.3334/ORNLDAAC/849)

- Redeker, K. R., Wang, N.-Y., Low, J. C., McMillan, A., Tyler, S. C. and Cicerone, R. J.: 2000, Emissions of methyl halides and methane from rice paddies, *Science* **290**(5493), 966–969.
- Reich, P. B. and Amundson, R. G.: 1985, Ambient levels of ozone reduce net photosynthesis in tree and crop species, *Science* **230**(4725), 566–570.
- Richter, A., Begoin, M., Hilboll, A. and Burrows, J. P.: 2011, An improved NO₂ retrieval for the GOME-2 satellite instrument, *Atmospheric Measurement Techniques* **4**(6), 1147–1159.
- Richter, A. and Burrows, J. P.: 2002, Tropospheric NO₂ from GOME measurements, *Advances in Space Research* **29**(11), 1673–1683.
- Richter, A., Burrows, J. P., Nusz, H., Granier, C. and Niemeier, U.: 2005, Increase in tropospheric nitrogen dioxide over China observed from space, *Nature* **437**(7055), 129–132.
- Richter, A. and Wagner, T.: 2001, Diffuser plate spectral structures and their influence on GOME slant columns, *Technical note*.
URL: http://www.iup.uni-bremen.de/gome/data/diffuser_gome.pdf
- Rienecker, M., Suarez, M., Todling, R., Bacmeister, J., Takacs, L., Liu, H., Gu, W., Sienkiewicz, M., Koster, R., Gelaro, R., Stajner, I. and Nielsen, J.: 2008, The GEOS-5 Data Assimilation System – Documentation of Versions 5.0.1, 5.1.0, and 5.2.0, *Technical Report 27*, NASA Goddard Space Flight Center, NASA Goddard Space Flight Center, Greenbelt, Maryland.
- Rinne, H., Guenther, A., Greenberg, J. and Harley, P.: 2002, Isoprene and monoterpene fluxes measured above Amazonian rainforest and their dependence on light and temperature, *Atmospheric Environment* **36**(14), 2421 – 2426.
- Rodriguez-Iturbe, I.: 2000, Ecohydrology: A hydrologic perspective of climate-soil-vegetation dynamics, *Water Resources Research* **36**(1), 3–9.
- Romatschke, U., Medina, S. and Houze, R. A.: 2010, Regional, seasonal, and diurnal variations of extreme convection in the south asian region, *Journal of Climate* **23**(2), 419–439.
- Rottenberger, S., Kuhn, U., Wolf, A., Schebeske, G., Oliva, S. T., Tavares, T. M. and Kesselmeier, J.: 2004, Exchange of short-chain aldehydes between Amazonian vegetation and the atmosphere, *Ecological Applications* **14**(4 SUPPL.), S247–S262.
- Rowland, F.: 2006, Stratospheric ozone depletion, *Philosophical Transactions of the Royal Society B: Biological Sciences* **361**(1469), 769–790.
- Royal Society: 2008, *Ground-level ozone in the 21st century: future trends, impacts and policy implications*, Vol. 15/08, The Royal Society.
- Rozanov, A., Rozanov, V., Buchwitz, M., Kokhanovsky, A. and Burrows, J. P.: 2005, SCIATRAN 2.0 - A new radiative transfer model for geophysical applications in the 175–2400 nm spectral region, *Advances in Space Research* **36**(5), 1015–1019.
- Russell, A. R., Perring, A. E., Valin, L. C., Bucsel, E., Browne, E. C., Min, K. ., Wooldridge, P. J. and Cohen, R. C.: 2011, A high spatial resolution retrieval of NO₂ column densities from OMI: Method and evaluation, *Atmospheric Chemistry and Physics* **11**(4), 12411–12440.
- Ryerson, T. B., Trainer, M., Angevine, W. M., Brock, C. A., Dissly, R. W., Fehsenfeld, F. C., Frost, G. J., Goldan, P. D., Holloway, J. S., Hübler, G., Jakoubek,

- R. O., Kuster, W. C., Neuman, J. A., Nicks, D. K., Parrish, D. D., Roberts, J. M., Sueper, D. T., Atlas, E. L., Donnelly, S. G., Flocke, F., Fried, A., Potter, W. T., Schaubler, S., Stroud, V., Weinheimer, A. J., Wert, B. P., Wiedinmyer, C., Alvarez, R. J., Banta, R. M., Darby, L. S. and Senff, C. J.: 2003, Effect of petrochemical industrial emissions of reactive alkenes and NO_x on tropospheric ozone formation in Houston, Texas, *Journal of Geophysical Research: Atmospheres* **108**(D8).
- Saatchi, S., Asefi-Najafabady, S., Malhi, Y., Aragão, L. E. O. C., Anderson, L. O., Myneni, R. B. and Nemani, R.: 2013, Persistent effects of a severe drought on Amazonian forest canopy, *Proceedings of the National Academy of Sciences* **110**(2), 565–570.
- Sabolis, A., Meskhidze, N., Curci, G., Palmer, P. I. and Gantt, B.: 2011, Interpreting elevated space-borne HCHO columns over the Mediterranean Sea using the OMI sensor, *Atmospheric Chemistry and Physics* **11**(24), 12787–12798.
- Samet, J. M., Dominici, F., Curriero, F. C., Coursac, I. and Zeger, S. L.: 2000, Fine particulate air pollution and mortality in 20 u.s. cities, 1987-1994, *New England Journal of Medicine* **343**(24), 1742–1749.
- Sanderson, M. G., Jones, C. D., Collins, W. J., Johnson, C. E. and Derwent, R. G.: 2003, Effect of climate change on isoprene emissions and surface ozone levels, *Geophysical Research Letters* **30**(18).
- Seinfeld, J. and Pandis, S.: 2006, *Atmospheric Chemistry and Physics: From Air pollution To Climate Change*, Wiley.
- Sharkey, T. D. and Loreto, F.: 1993, Water stress, temperature, and light effects on the capacity for isoprene emission and photosynthesis of kudzu leaves, *Oecologia* **95**(3), 328–333.
- Sharkey, T. D. and Singsaas, E. L.: 1995, Why plants emit isoprene, *Nature* **374**(6525), 769.
- Sharkey, T. D., Singsaas, E. L., Vanderveer, P. J. and Geron, C.: 1996, Field measurements of isoprene emission from trees in response to temperature and light, *Tree Physiology* **16**(7), 649–654.
- Sharkey, T. D., Wiberley, A. E. and Donohue, A. R.: 2008, Isoprene emission from plants: Why and how, *Annals of Botany* **101**(1), 5–18.
- Sharkey, T. D. and Yeh, S.: 2001, Isoprene emission from plants, *Annual Review of Plant Biology* **52**, 407–436.
- Shim, C., Wang, Y., Choi, Y., Palmer, P. I., Abbot, D. S. and Chance, K.: 2005, Constraining global isoprene emissions with Global Ozone Monitoring Experiment (GOME) formaldehyde column measurements, *Journal of Geophysical Research: Atmospheres* **110**(24), 1–14.
- Siddans, Latter, B., Kerridge, B., Weber, M., de Beek, R., Burrows, J. P., Aben, I., Tanzi, P., Hartmann, W. and Wickett, M.: 2003, Gome-2 error assessment study, *Technical report*.
- Siddans, R., Kerridge, B. and Latter, B.: 2006, Analysis of GOME-2 slit function measurements, *Executive Summary Eumetsat Contract No. EUM/CO/04/1298/RM*, Rutherford Appleton Laboratory.
- Sillman, S. and He, D.: 2002, Some theoretical results concerning O₃-NO_x-VOC

- chemistry and NO_x-VOC indicators, *Journal of Geophysical Research: Atmospheres* **107**(D22).
- Sillman, S. et al.: 1999, The relation between ozone, nox and hydrocarbons in urban and polluted rural environments, *Atmospheric Environment* **33**(12), 1821–1846.
- Singsaas, E. L., Lerdau, M., Winter, K. and Sharkey, T. D.: 1997, Isoprene increases thermotolerance of isoprene-emitting species, *Plant Physiology* **115**(4), 1413–1420.
- Singsaas, E. L. and Sharkey, T. D.: 2000, The effects of high temperature on isoprene synthesis in oak leaves, *Plant, Cell & Environment* **23**(7), 751–757.
- Sioris, C. E., Bazalgette Courrèges-Lacoste, G. and Stoll, M.-P.: 2003, Filling in of Fraunhofer lines by plant fluorescence: Simulations for a nadir-viewing satellite-borne instrument, *Journal of Geophysical Research: Atmospheres* **108**(D4).
- Sitch, S., Cox, P. M., Collins, W. J. and Huntingford, C.: 2007, Indirect radiative forcing of climate change through ozone effects on the land-carbon sink, *Nature* **448**(7155), 791–794.
- Siwko, M. E., Marrink, S. J., de Vries, A. H., Kozubek, A., Schoot Uiterkamp, A. J. M. and Mark, A. E.: 2007, Does isoprene protect plant membranes from thermal shock? a molecular dynamics study, *Biochimica et Biophysica Acta - Biomembranes* **1768**(2), 198–206.
- Smith, B., Prentice, I. C. and Sykes, M. T.: 2001, Representation of vegetation dynamics in the modelling of terrestrial ecosystems: comparing two contrasting approaches within European climate space, *Global Ecology and Biogeography* **10**(6), 621–637.
- Snel, R. and Krijger, J.: 2009, An Improved Scanner Model for SCIAMACHY, Atmospheric Science Conference, Barcelona, Spain., ESA, ESA.
- Spurr, R. J. D.: 2001, *LIDORT - User's Guide to Version 2.3*, Harvard-Smithsonian Center for Astrophysics, 60 Garden Street, Cambridge, MA 02138, USA.
- Spurr, R. J. D., Kurosu, T. P. and Chance, K. V.: 2001, A linearized discrete ordinate radiative transfer model for atmospheric remote-sensing retrieval, *J. Quant. Spectrosc. Ra.* **68**(6), 689–735.
- Squire, O. J., Archibald, A. T., Beerling, D. J., Hewitt, C. N., Lathièrè, J., Pike, R. C., Telford, P. J. and Pyle, J. A.: 2013, Influence of future climate and cropland expansion on isoprene emissions and tropospheric ozone, *Atmospheric Chemistry and Physics Discussions* **13**(7), 18307–18344.
- Stavrakou, T., Müller, J. ., De Smedt, I., Van Roozendaal, M., Van Der Werf, G. R., Giglio, L. and Guenther, A.: 2009c, Global emissions of non-methane hydrocarbons deduced from SCIAMACHY formaldehyde columns through 2003–2006, *Atmospheric Chemistry and Physics* **9**(11), 3663–3679.
- Stavrakou, T., Müller, J., De Smedt, I., Van Roozendaal, M., Van Der Werf, G. R., Giglio, L. and Guenther, A.: 2009b, Evaluating the performance of pyrogenic and biogenic emission inventories against one decade of space-based formaldehyde columns, *Atmospheric Chemistry and Physics* **9**(3), 1037–1060.
- Stevenson, D. S., Dentener, F. J., Schultz, M. G., Ellingsen, K., van Noije, T. P. C., Wild, O., Zeng, G., Amann, M., Atherton, C. S., Bell, N., Bergmann, D. J., Bey, I., Butler, T., Cofala, J., Collins, W. J., Derwent, R. G., Doherty, R. M., Drevet, J., Eskes, H. J., Fiore, A. M., Gauss, M., Hauglustaine, D. A., Horowitz, L. W.,

- Isaksen, I. S. A., Krol, M. C., Lamarque, J. ., Lawrence, M. G., Montanaro, V., Müller, J. ., Pitari, G., Prather, M. J., Pyle, J. A., Rast, S., Rodriguez, J. M., Sanderson, M. G., Savage, N. H., Shindell, D. T., Strahan, S. E., Sudo, K. and Szopa, S.: 2006, Multimodel ensemble simulations of present-day and near-future tropospheric ozone, *Journal of Geophysical Research D: Atmospheres* **111**(8).
- Stevenson, D. S., Young, P. J., Naik, V., Lamarque, J.-F., Shindell, D. T., Voulgarakis, A., Skeie, R. B., Dalsoren, S. B., Myhre, G., Berntsen, T. K., Folberth, G. A., Rumbold, S. T., Collins, W. J., MacKenzie, I. A., Doherty, R. M., Zeng, G., van Noije, T. P. C., Strunk, A., Bergmann, D., Cameron-Smith, P., Plummer, D. A., Strode, S. A., Horowitz, L., Lee, Y. H., Szopa, S., Sudo, K., Nagashima, T., Josse, B., Cionni, I., Righi, M., Eyring, V., Conley, A., Bowman, K. W. and Wild, O.: 2012, Tropospheric ozone changes, radiative forcing and attribution to emissions in the Atmospheric Chemistry and Climate Model Inter-comparison Project (AC-CMIP), *Atmospheric Chemistry and Physics Discussions* **12**(10), 26047–26097.
- Stone, D., Evans, M. J., Edwards, P. M., Commane, R., Ingham, T., Rickard, A. R., Brookes, D. M., Hopkins, J., Leigh, R. J., Lewis, A. C., Monks, P. S., Oram, D., Reeves, C. E., Stewart, D. and Heard, D. E.: 2011, Isoprene oxidation mechanisms: Measurements and modelling of OH and HO₂ over a South-East Asian tropical rainforest during the OP3 field campaign, *Atmospheric Chemistry and Physics* **11**(13), 6749–6771.
- Streets, D. G., Bond, T. C., Carmichael, G. R., Fernandes, S. D., Fu, Q., He, D., Klimont, Z., Nelson, S. M., Tsai, N. Y., Wang, M. Q., Woo, J.-H. and Yarber, K. F.: 2003, An inventory of gaseous and primary aerosol emissions in Asia in the year 2000, *Journal of Geophysical Research: Atmospheres* **108**(D21).
- Stutz, J. and Platt, U.: 1996, Numerical analysis and estimation of the statistical error of differential optical absorption spectroscopy measurements with least-squares methods, *Appl. Opt.* **35**(30), 6041–6053.
- Sumner, A. L. and Shepson, P. B.: 1999, Snowpack production of formaldehyde and its effect on the Arctic troposphere, *Nature* **398**(6724), 230–233.
- Taraborrelli, D., Lawrence, M. G., Crowley, J. N., Dillon, T. J., Gromov, S., Grosz, C. B. M., Vereecken, L. and Lelieveld, J.: 2012, Hydroxyl radical buffered by isoprene oxidation over tropical forests, *Nature Geoscience* **5**(3), 190–193.
- Tawfik, A. B., Stöckli, R., Goldstein, A., Pressley, S. and Steiner, A. L.: 2012, Quantifying the contribution of environmental factors to isoprene flux interannual variability, *Atmospheric Environment* **54**(0), 216 – 224.
- Theys, N.: 2010, *Atmospheric Bromine Monoxide: multi-platform observations and model calculations*, PhD thesis, Université Libre De Bruxelles, Laboratoire de Chimie Quantique et Photophysique, Faculté de Sciences Appliquées.
- Theys, N., Van Roozendaal, M., Hendrick, F., Yang, X., De Smedt, I., Richter, A., Begoin, M., Errera, Q., Johnston, P. V., Kreher, K. and De Mazière, M.: 2011, Global observations of tropospheric BrO columns using GOME-2 satellite data, *Atmospheric Chemistry and Physics* **11**(4), 1791–1811.
- Thomas, W., Hegels, E., Slijkhuis, S., Spurr, R. and Chance, K.: 1998, Detection of biomass burning combustion products in Southeast Asia from backscatter data taken by the GOME spectrometer, *Geophysical Research Letters* **25**(9), 1317–1320.

- United States Environmental Protection Agency: 2013, 2005 National Emissions Inventory Data & Documentation.
URL: <http://www.epa.gov/ttnchie1/net/2005inventory.html>
- Valks, P., Pinardi, G., Richter, A., Lambert, J.-C., Hao, N., Loyola, D., Van Roozendael, M. and Emmadi, S.: 2011, Operational total and tropospheric NO₂ column retrieval for GOME-2, *Atmospheric Measurement Techniques* **4**(7), 1491–1514.
- van Donkelaar, A., Martin, R. V., Park, R. J., Heald, C. L., Fu, T. ., Liao, H. and Guenther, A.: 2007, Model evidence for a significant source of secondary organic aerosol from isoprene, *Atmospheric Environment* **41**(6), 1267–1274.
- Van Geffen, J. H. G. M. and Van Oss, R. F.: 2003, Wavelength calibration of spectra measured by the Global Ozone Monitoring Experiment by use of a high-resolution reference spectrum, *Appl. Optics* **42**(15), 2739–2753.
- Van Roozendael, M., Soebijanta, V., Fayt, C. and Lambert, J.-C.: 2002, Investigation of doas issues affecting the accuracy of the GDP version 3.0 total ozone product, *Technical report*, Space Aeronomy Institute of Belgium.
- Vandaele, A. C., Hermans, C., Simon, P. C., Carleer, M., Colin, R., Fally, S., Mérienne, M. F., Jenouvrier, A. and Coquart, B.: 1998, Measurements of the NO₂ absorption cross-section from 42 000 cm⁻¹ to 10 000 cm⁻¹ (238-1000 nm) at 220 K and 294 K, *J. Quant. Spectrosc. Ra.* **59**(3-5), 171–184.
- Veefkind, J. P., Boersma, K. F., Wang, J., Kurosu, T. P., Krotkov, N., Chance, K. and Levelt, P. F.: 2011, Global satellite analysis of the relation between aerosols and short-lived trace gases, *Atmospheric Chemistry and Physics* **11**(3), 1255–1267.
- Vestreng, V. and Klein, H.: 2002, Emission data reported to UNECE/EMEP: Quality Assurance and Trend Analysis & Presentation of WebDab., *Status report*, Norwegian Meteorological Institute.
- Vigouroux, C., Hendrick, F., Stavrakou, T., Dils, B., De Smedt, I., Hermans, C., Merlaud, A., Scolas, F., Senten, C., Vanhaelewyn, G., Fally, S., Carleer, M., Metzger, J.-M., Müller, J.-F., Van Roozendael, M. and De Mazière, M.: 2009, Ground-based FTIR and MAX-DOAS observations of formaldehyde at Réunion Island and comparisons with satellite and model data, *Atmospheric Chemistry and Physics* **9**(24), 9523–9544.
- Vogel, L., Sihler, H., Lampel, J., Wagner, T. and Platt, U.: 2013, Retrieval interval mapping: a tool to visualize the impact of the spectral retrieval range on differential optical absorption spectroscopy evaluations, *Atmospheric Measurement Techniques* **6**(2), 275–299.
- Vountas, M., Rozanov, V. V. and Burrows, J. P.: 1998, Ring effect: Impact of rotational Raman scattering on radiative transfer in Earth’s atmosphere, *J. Quant. Spectrosc. Radiat. Transfer* **60**(6), 943–961.
- Vrekoussis, M., Wittrock, F., Richter, A. and Burrows, J. P.: 2010, GOME-2 observations of oxygenated VOCs: what can we learn from the ratio glyoxal to formaldehyde on a global scale?, *Atmospheric Chemistry and Physics* **10**(21), 10145–10160.
- Wagner, T., Beirle, S., Deutschmann, T. and Penning de Vries, M.: 2010, A sensitivity analysis of Ring effect to aerosol properties and comparison to satellite observations, *Atmospheric Measurement Techniques* **3**(6), 1723–1751.
- Wagner, T., Chance, K., Frieß, U., Gil, M., Goutail, F., Hönniger, G., Johnston,

- P. V., Karlsen-Tørnkvist, K., Kostadinov, I., Leser, H., Petritoli, A., Richter, A., Van Roozendael, M. and Platt, U.: 2001, Correction of the Ring effect and I₀ effect for DOAS observations of scattered sunlight, *Proceedings of the 1st DOAS Workshop, Heidelberg, Germany*.
- Wagner, W., Hahn, S., Kidd, R., Melzer, T., Bartalis, Z., Hasenauer, S., Figa-Saldana, J., de Rosnay, P., Jann, A., Schneider, S., Komma, J., Kubu, G., Brügger, K., Aubrecht, C., Zuger, J., Gangkofner, U., Kienberger, S., Brocca, L., Wang, Y., Bloschl, G., Eitzinger, J., Steinnocher, K., Zeil, P. and Rubel, F.: 2013, The ASCAT Soil Moisture Product: A Review of its Specifications, Validation Results, and Emerging Applications, *Meteorologische Zeitschrift* **22**(1), 5–33.
- Wang, J.-L., Chew, C., Chang, C.-Y., Liao, W.-C., Lung, S.-C. C., Chen, W.-N., Lee, P.-J., Lin, P.-H. and Chang, C.-C.: 2013, Biogenic isoprene in subtropical urban settings and implications for air quality, *Atmospheric Environment* **79**, 369–379.
- Wang, P., Stammes, P., van der A, R., Pinardi, G. and van Roozendael, M.: 2008, FRESCO+: an improved O₂ A-band cloud retrieval algorithm for tropospheric trace gas retrievals, *Atmospheric Chemistry and Physics* **8**(21), 6565–6576.
- Wang, P., Tuinder, O. N. E., Tilstra, L. G., de Graaf, M. and Stammes, P.: 2012, Interpretation of FRESCO cloud retrievals in case of absorbing aerosol events, *Atmospheric Chemistry and Physics* **12**(19), 9057–9077.
- Warneke, C., McKeen, S. A., de Gouw, J. A., Goldan, P. D., Kuster, W. C., Holloway, J. S., Williams, E. J., Lerner, B. M., Parrish, D. D., Trainer, M., Fehsenfeld, F. C., Kato, S., Atlas, E. L., Baker, A. and Blake, D. R.: 2007, Determination of urban volatile organic compound emission ratios and comparison with an emissions database, *Journal of Geophysical Research: Atmospheres* **112**(10).
- Wayne, R.: 1990, Atmospheric Chemistry, *Science Progress* **74**, 379–409.
- Wex, H., Petters, M. D., Carrico, C. M., Hallbauer, E., Massling, A., McMeeking, G. R., Poulain, L., Wu, Z., Kreidenweis, S. M. and Stratmann, F.: 2009, Towards closing the gap between hygroscopic growth and activation for secondary organic aerosol: Part 1-evidence from measurements, *Atmospheric Chemistry and Physics* **9**(12), 3987–3997.
- Whiting, G. J. and Chanton, J. P.: 1993, Primary production control of methane emission from wetlands, *Nature* **364**(6440), 794–795.
- Wiedinmyer, C., Friedfeld, S., Baugh, W., Greenberg, J., Guenther, A., Fraser, M. and Allen, D.: 2001, Measurement and analysis of atmospheric concentrations of isoprene and its reaction products in central Texas, *Atmospheric Environment* **35**(6), 1001 – 1013.
- Wittrock, F.: 2006, *The retrieval of oxygenated volatile organic compounds by remote sensing techniques*, PhD thesis, Universität Bremen.
- Wittrock, F., Richter, A., Ladstätter-Weißmayer, A. and Burrows, J. P.: 2000, Global observations of formaldehyde, *European Space Agency, (Special Publication) ESA SP*, pp. 1358–1362.
- Wittrock, F., Richter, A., Oetjen, H., Burrows, J. P., Kanakidou, M., Myriokefalitakis, S., Volkamer, R., Beirle, S., Platt, U. and Wagner, T.: 2006, Simultaneous global observations of glyoxal and formaldehyde from space, *Geophysical Research Letters* **33**(16).

- Wuebbles, D. J. and Hayhoe, K.: 2002, Atmospheric methane and global change, *Earth-Science Reviews* **57**(3-4), 177–210.
- Yantosca, R. M.: 2013, List of GEOS-5 met fields.
URL: http://wiki.seas.harvard.edu/geos-chem/index.php/List_of_GEOS-5_met_fields
- Young, P. J., Arneth, A., Schurgers, G., Zeng, G. and Pyle, J. A.: 2009, The CO₂ inhibition of terrestrial isoprene emission significantly affects future ozone projections, *Atmospheric Chemistry and Physics* **9**(8), 2793–2803.
URL: <http://www.atmos-chem-phys.net/9/2793/2009/>
- Zhang, L., Jacob, D. J., Liu, X., Logan, J. A., Chance, K., Eldering, A. and Bojkov, B. R.: 2010, Intercomparison methods for satellite measurements of atmospheric composition: Application to tropospheric ozone from TES and OMI, *Atmospheric Chemistry and Physics* **10**(10), 4725–4739.
- Zhou, X., Lee, Y.-N., Newman, L., Chen, X. and Mopper, K.: 1996, Tropospheric formaldehyde concentration at the Mauna Loa Observatory during the Mauna Loa Observatory Photochemistry Experiment 2, *Journal of Geophysical Research: Atmospheres* **101**(D9), 14711–14719.
- Zhou, Y., Brunner, D., Boersma, K. F., Dirksen, R. and Wang, P.: 2009, An improved tropospheric NO₂ retrieval for OMI observations in the vicinity of mountainous terrain, *Atmospheric Measurement Techniques* **2**(2), 401–416.
- Zhou, Y., Brunner, D., Hueglin, C., Henne, S. and Staehelin, J.: 2012, Changes in OMI tropospheric NO₂ columns over Europe from 2004 to 2009 and the influence of meteorological variability, *Atmospheric Environment* **46**, 482–495.
- Zhou, Y., Brunner, D., Spurr, R. J. D., Boersma, K. F., Sneep, M., Popp, C. and Buchmann, B.: 2010, Accounting for surface reflectance anisotropy in satellite retrievals of tropospheric NO₂, *Atmospheric Measurement Techniques* **3**(5), 1185–1203.

Peer reviewed publication

W. Hewson, H. Bösch, M. P. Barkley, and I. De Smedt. Characterisation of GOME-2 formaldehyde retrieval sensitivity. *Atmospheric Measurement Techniques*, 6(2):371–386, 2013.